DOE/ER-0046/15

J. Scott (PPL 4-13-84

APR 1 C 1984

Damage Analysis and Fundamental Studies

Quarterly Progress Report
July-September 1983

November 1983

U.S. Department of Energy
Office of Energy Research
Office of Fusion Energy
Washington, DC 20545

NOTICE

Printed in the United States of America
Available from
National Technical Information Service
U.S. Department of Commerce
5285 Port Royal Road
Springfield, VA 22161

NTIS price codes
Printed copy: A 07
Microfiche copy: A01

DOE/ER-0046/15
UC-20,20c

Damage Analysis and Fundamental Studies

Quarterly Progress Report
July-September 1983

November 1983

U.S. Department of Energy
Office of Energy Research
Office of Fusion Energy
Washington, DC 20545

FOREWORD

This report is the twenty-third in a series of Quarterly Technical Progress Reports on ***Damage Analysis and Fundamental Studies*** (DAFS), which is one element of the Fusion Reactor Materials Program, conducted in support of the Magnetic Fusion Energy Program of the U.S. Department of Energy (DOE). The first eight reports in this series were numbered DOE/ET-0065/1 through 8. Other elements of the Fusion Materials Program are:

- Alloy Development for Irradiation Performance (ADIP)
- Plasma-Materials Interaction (PMI)
- Special Purpose Materials (SPM).

The DAFS program element is a national effort composed of contributions from a number of National Laboratories and other government laboratories, universities, and industrial laboratories. It was organized by the Materials and Radiation Effects Branch, DOE/Office of Fusion Energy, and a Task Group on ***Damage Analysis and Fundamental Studies,*** which operates under the auspices of that branch. The purpose of this series of reports is to provide a working technical record of that effort for the use of the program participants, the fusion energy program in general, and the DOE.

This report is organized along topical lines in parallel to a Program Plan of the same title so that activities and accomplishments may be followed readily, relative to that Program Plan. Thus, the work of a given laboratory may appear throughout the report. Note that a new chapter has been added on Reduced Activation Materials to accommodate work on a topic not included in the early program plan. The Contents is annotated for the convenience of the reader.

This report has been compiled and edited under the guidance of the Chairman of the Task Group on ***Damage Analysis and Fundamental Studies,*** D. G. Doran, Hanford Engineering Development Laboratory (HEDL). His efforts, those of the supporting staff of HEDL, and the many persons who made technical contributions are gratefully acknowledged. T. C. Reuther, Materials and Radiation Effects Branch, is the DOE counterpart to the Task Group Chairman and has responsibility for the DAFS program within DOE.

G. M. Haas, Chief
Reactor Technologies Branch
Office of Fusion Energy

CONTENTS

CHAPTER 1

IRRADIATION TEST FACILITIES

RTNS-II IRRADIATIONS AND OPERATIONS

C.M. Logan and D. W. Heikkinen
Lawrence Livenmre National Laboratory

1.0 jective

The objectives of this work are operation of RTNS-II (a 14-MeV neutron source facility), mchine developnent, and support of the experimental program that utilizes this facility. Experimenter services include dosimetry, handling, scheduling, coordination, and reporting. RTNS-II is dedicated to mterials research for the fusion power program. Its primry use is to aid in the development of models of high-energy neutron effects. Such models are needed in interpreting and projecting to the fusion environment, engineering data obtained in other spectra.

2.0 Summary

Irradiations were performed for 12 different experimenters during this quarter. Fifty centimter targets will be used on the right machine in the near future. Ion source development is being done on the right mchine. Upgrade of the right mchine extraction power supply began.

3.0 Program

Title: RTNS-II operations (WZJ-16)
Principal Investigator: C. M. Logan
Affiliation: Lawrence Livenmre National Laboratory

4.0 Relevant DAFS Program Plan Task/Subtask

TASK II,A,2,3,4,
TASK II,B,3,4
TASK II,C,1,2,6,11,18,

5.0 Irradiati - M. rman, D. W. Heikkinen and M. W. Guinan

During this quarter, irradiations (both dedicated and add-on) were done for the following people.

Experimenter	P or A*	Sample Irradiated
J. Fowler (LANL)	P	MACOR - changes in electrical and mechanical properties
P. Hahn (Vienna)	A	Nb-Ti - measure fluxoid pinning strength of superconductors
C. Logan (LLNL)	A	Cu alloys - activation analysis
C. Violet (LLNL)	A	W - Mossbauer effect source

5.0 (Continued)

Experimenter	P or A*	Sample Irradiated
R. Borg (LLNL)	A	1. NiRh - magnetic properties 2. Geological samples - inert gas production and diffusion
P. Cannon (HEDL)	P	EMIT instrumentation
D. Heikkinen (LLNL)	A	Nb - dosimetry calibration
T. vercelli (LLNL)	A	Carbon fiber/epoxy - tensile strength
Y. Tabata (Tokyo)	A	Polymer materials - tensile strength
M. Guinan (LLNL), T. Okada (Osaka), and K, Suzuki (Tohoku)	P	Nb_3Sn, Cu and Mo-Si amorphous alloy - critical current, resistivity and rmgnetoresistance
T. Okada (Osaka)	A	Epoxys - mechanical strength and thermal contraction coefficient
C. Ichihara (Kyoto)	A	1. Si - gama-ray spectrum analysis 2. Li^6Cl, Li^7Cl, Ta, Au, Nb, Cu, Ni, Co, Fe and Ti - neutron energy spectrum 3. AU, Nb, Fe and Ni - dosimetry comparison

*P - primary, A = Add-on

5.1 RTNS-II Status - M. Logan and D. W. Heikkinen

The ion source system for the right machine is being checked and tested for efficiency and possible improvement. Preparations are being rmde to convert the right nwchine for 50-cm target operation by late October. The right nwchine extraction power supply is being upgraded for higher voltage and current capabilities. Tne left mchine has teen operating five days a week, twenty-four hours a day to accommodate the Guinan/Okada/Suzuki experiment.

6.0 Future Work

Irradiations will be continued for J. Fowler (LANL), R. Borg, (LLNL), T. Vercelli (LLNL), and Y. Tabata (Tokyo). Also during this period, irradiations for N. Itoh (Nagoya), K. Saneyoshi (Tokyo), C. Ichihara (Kyoto) and K. Abe (Tohoku) will be made.

CHAPTER 2

DOSIMETRY AND DAMAGE PARAMETERS

FISSION REACTOR DOSIMETRY - HFIR - T2 and RB1

L. R. Greenwood (Argonne National Laboratory)

1.0 Objective

To characterize neutron irradiation facilities in terms of neutron flux, spectra, and damage parameters (dpa, gas production, transmutation) and to measure these exposure parameters during fusion materials irradiations.

2.0 Sunmary

Dosimetry measurements and damage calculations are sunmarized for the T2 and RB1 irradiations in HFIR. The status of all other experiments is summarized in Table 1.

TABLE 1 .

STATUS OF DOSIMETRY EXPERIMENTS

	Facility/Experiment	Status/Comments
ORR	- MFE 1	Completed 12/79
	- MFE 2	Completed 06/81
	- MFE 4A1	Completed 12/81
	- MFE 4A2	Completed 11/82
	- MFE 4B	Samples Received 09/83
	- MFE 4C	Irradiation in Progress
	- TBC 07	Completed 07/80
	- TRIO-Test	Completed 07/82
	- TRIO-1	Samples Received 09/83
HFIR	- CTR 32	Completed 04/82
	- CTR 31, 34, 35	Completed 04/83
	- CTR 30	Irradiation in Progress
	- T2, RB1	Completed 09/83
	- T1, CTR 39	Samples Counted 06/83
	- RB2, RB3, T3	Irradiations in Progress
	- CTR 40-49	Irradiations in Progress
Omega West	- Spectral Analysis	Completed 10/80
	- HEDL1	Completed 05/81
	- HEDL2	Samples Sent 05/83
EBR II	- X287	Completed 09/81
IPNS	- Spectral Analysis	Completed 01/82
	- LANL1 (Hurley)	Completed 06/82
	- Hurley	Completed 02/83
	- Coltman	Completed 08/83

3.0 Program

Title: Dosimetry and Damage Analysis
Principal Investigator: L. R. Greenwood
Affiliation: Argonne National Laboratory

4.0 Relevant OAFS Program Plan Task/Subtask

Task II.A.1 Fission Reactor Dosimetry

5.0 Accomplishments and Status

Neutron activation dosimetry measurements and damage parameter calculations have been completed for the T2 and RB1 experiments in the High Flux Isotopes Reactor (HFIR) at Oak Ridge National Laboratory. The irradiation histories are, as follows:

Irradiation	Reactor Position	Dates	Exposure, MWD
T2	Target	2/81 to 5/81	**6,616**
RB1	Be	11/81 to 7/82	23,386

Dosimetry capsules were placed at two heights in T2 and five heights in the RB1 subassembly. The T2 capsules contained Fe, Co, Ti, Mn-Cu, and Cu wires. The RB1 capsules did not have the Mn-Cu and Cu samples. The measured activation rates are listed in Table 2.

TABLE 2

ACTIVATION RATES MEASURED IN HFIR-T2, RB1
(Values Normalized to 100-MW Power Level)

Reaction	Activation Rate, atom/atom-s				
	Height, cm:	7.22		16.95	
T2 Experiment					
$^{58}Fe(n,\gamma)^{59}Fe$	(10^{-9})	--		2.08	
$^{59}Co(n,\gamma)^{60}Co$	(10^{-8})	--		6.32	
$^{54}Fe(n,p)^{54}Mn$	(10^{-11})	5.83		4.50	
$^{46}Ti(n,p)^{46}Sc$	(10^{-12})	8.58		6.31	
$^{55}Mn(n,2n)^{54}Mn$	(10^{-13})	1.79		1.43	
$^{63}Cu(n,\alpha)^{60}Co$	(10^{-13})	4.87		3.04	
RB1 Experiment					
	Height, cm:	-23.02	-5.40	+2.02	+10.72	+21.15
$^{59}Co(n,\gamma)^{60}Co$	(10^{-8})	1.27	3.51	3.68	2.80	1.67
$^{58}Fe(n,\gamma)^{59}Fe$	(10^{-10})	--	--	10.12	7.69	4.77
$^{54}Fe(n,p)^{54}Mn$	(10^{-11})	--	--	1.38	1.21	0.81
$^{46}Ti(n,p)^{46}Sc$	(10-121	--	--	2.17	1.86	1.20

The T2 data in the target position close to the PTP is similar to our previous measurements in the PTP.[1] Consequently, we assume that the flux gradients are also described by our previous equations, namely:

$$f(z) = a(1 + bz + cz^2) \quad (1)$$

where z is the height above midplane (cm), b = 0.195 x 10^{-3}, c = -0.975 x 10^{-3}, and a is the flux or damage rate at midplane. The midplane fluence and damage rates are listed in Table 3. In order to find a given fluence or damage rate at any other height, the user should simply take the midplane value in Table 3 for a and use Eq. (1) for the desired value of z.

The RB1 experiment was conducted in the removable beryllium position of HFIR with a different flux spectrum and vertical gradient than encountered in the PTP. The spectrum was taken from a report by Kam and Swanks.? The gradients were also described by Eq. (1) except that the b and c parameters are slightly different than in the PTP. A least-squares fit to the data in Table 2 gives b = -9.18 x 10^{-5} and c = -1.175 x 10^{-3}. The midplane values are also listed in Table 3.

TABLE 3

FLUENCE AND DAMAGE PARAMETERS FOR HFIR-T2, RB1
Values are listed at midplane; for gradients use Eq. (1) in text where for T2: $b = 1.95 \times 10^{-4}$, $c = -9.75 \times 10^{-4}$, and for RB1: $b = -9.18 \times 10^{-5}$, $c = -1.175 \times 10^{-3}$

Neutron Fluence, $\times 10^{22}$ n/cm^2	T2	RB1
Total	3.20	3.89
Thermal (<.5 eV)[a]	1.55	2.21
Fast (>.11 MeV)	0.722	0.685

	T2		RB1	
Element	DPA	He	OPA	He
Al	9.37	4.37	8.66	4.12
Ti	5.95	2.87	5.49	2.43
V	6.68	0.15	6.20	0.15
Cr	5.84	1.00	5.35	0.91
Mn[b]	6.59	0.88	6.32	0.83
Fe	5.15	1.76	4.68	1.61
Co[b]	6.97	0.87	7.27	0.81
Ni[c] Fast	5.61	22.84	5.24	19.40
Ni[c] ^{59}Ni	3.89	2206.	6.82	3865.
Ni[c] Total	9.50	2230.	12.06	3884.
cu	5.06	1.58	4.67	1.48
Nb	4.99	0.32	4.56	0.29
Mo	3.73	--	3.45	--
316 ss	5.83	291.	5.64	506.

[a] The 2200 m/s value is equal to 0.886 times the total <.5 eV.

[b] The thermal (n,γ) damage is 8% for Mn and 28% for Co; however, self-shielding effects must be considered.

[c] Nickel gradients for He must be done differently; see Table 4 and Ref. 3.

[d] 316 ss: Fe (0.645), Ni (0.13), Cr (0.18), Mn (0.019), Mo (0.026)

The spectral and gradient differences between the PTP, target, and Be positions are illustrated in Fig. 1. As can be seen the spectra become considerably softer as we move out from the core, as expected. The gradients are only slightly steeper in the Be position.

The helium production and damage in nickel and stainless steel requires a more detailed calculation, as discussed in recent publications.[3,4] Due to the complexity of this calculation, detailed gradients are listed in Table 4. The thermal two-step reaction and fast reactions are summed in the table and the extra OPA from the ^{56}Fe recoils (He/567) is also included.4

Helium calculations were made using newly evaluated cross sections for ^{59}Ni[5] averaged over our adjusted neutron spectra. This procedure appears to agree quite closely with helium measurements made at Rockwell International, as discussed elsewhere in this report.3 With over 45 separate measurements in HFIR, ORR, and EBR II, the measurements and calculations have an average ratio of 0.982 ± 0.064, and the maximum difference was only 11%.

6.0 References

1. L. R. Greenwood, "Fission Reactor Dosimetry," Damage Analysis and Fundamental Studies Quarterly Progress Report, DOE/ER-0046/14, pp. 9-18, August 1983.

2. F. B. K. Kam and J. H. Swanks, "Neutron Flux Spectrum in the HFIR Target Region," ORNL-TM-3322, 1971.

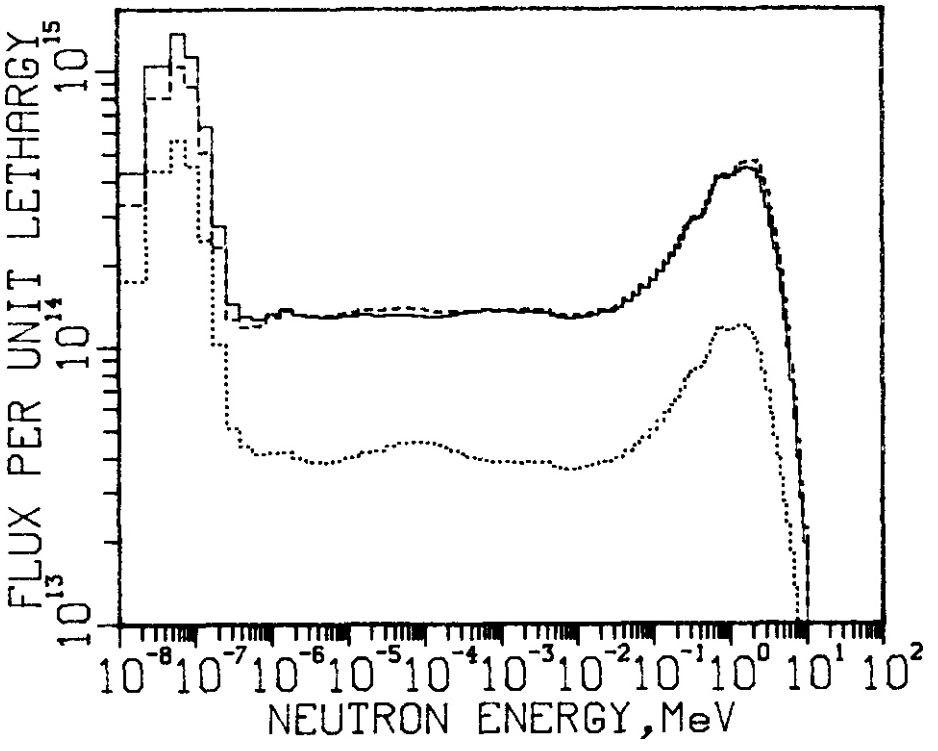

Fig. 1. Neutron flux spectra are compared at different locations in HFIR. The dashed line is the PTP (CTR 32), the solid line is for the target position (T2), and the dotted line is for the removable beryllium position (RB1).

TABLE 4

HELIUM (appm) AND DPA GRADIENTS FOR NICKEL IN HFIR-T2, RB1
Helium values include $^{59}Ni(n,\alpha)$ and fast reactions.
DPA values include thermal effects (He/567).
Gradients are nearly symmetric about midplane.

	T2		RB1	
Height, cm	He	DPA	He	DPA
0	2230.	9.50	3884	12.06
3	2195.	9.39	3823.	11.90
6	2105.	9.09	3628.	11.38
9	1950.	8.57	3330.	10.58
12	1746.	7.88	2909.	9.45
15	1488.	6.99	2393.	8.05
18	1188.	5.93	1793.	6.37
21	869.	4.74	1172.	4.57
24	547.	3.44	574.	2.68

3. D. W. Kneff and L. R. Greenwood, "Comparison of Measured and Calculated Helium Production in Nickel," this report.

4. L. R. Greenwood, "A New Calculation of Thermal Neutron Damage and Helium Production in Nickel," J. Nucl Mater. 115, 137-142 (1983).

5. F. M. Mann, "^{59}Ni+n Cross Section Evaluation," Damage Analysis and Fundamental Studies Quarterly Progress Report, DOE/ER-0046/12, pp. 35-36 (1983).

7.0 Future Work

Samples have been gamma counted from the CTR39 and T1 irradiations in HFIR and analysis is now in progress. Samples have been received from the MFE4B irradiation in DRR. Data in the present report is being added to our DOSFILE program on the NMFECC computer for rapid access by experimenters.

8.0 Publications

The following papers have been accepted for publication in the proceedings of the Third Topical Meeting of Fusion Reactor Materials in Albuquerque, New Mexico, on September 19-22, 1983.

1. L. R. Greenwood, D. W. Kneff, R. P. Skowronski, and F. M. Mann, Comparison of Measured and Calculated Helium Production in Nickel Using Newly Evaluated Neutron Cross Sections for ^{59}Ni.

2. L. R. Greenwood, Recent Developments in Neutron Dosimetry and Radiation Damage Calculations for Fusion Materials Studies

EXPERIMENTS AT THE IPNS SPALLATION NEUTRON SOURCE

L. R. Greenwood (Argonne National Laboratory)

1.0 Objective

To characterize the IPNS irradiation facilities and to provide dosimetry measurements and damage parameter calculations for fusion materials experiments.

2.0 Sumnary

Dosimetry measurements and damage calculations are reported for a cryogenic (4°K) irradiation of copper for R. Coltman (ORNL) at the IPNS on March 25 to April 5, 1983. The maximum neutron fluence was 7.1 x 10^{17} n/cm^2 producing a total dose of 1.6 x 10^7 rads in copper.

3.0 Program

Title: Dosimetry and Damage Analysis
Principal Investigator: L. R. Greenwood
Affiliation: Argonne National Laboratory

4.0 Relevant DAFS Program Plan Task/Subtask

Task II.A.2 High-Energy Neutron Dosimetry

5.0 Accomplishments and Status

Copper stabilizer materials were irradiated for R. Coltman (ORNL) at the Intense Pulsed Neutron Source (IPNS) at Argonne National Laboratory on March 25-April 5, 1983. The samples were irradiated in the VT2 position of the Radiation Effects Facility at liquid helium temperatures (4°K). The total proton current on the depleted uranium target was 3.43 x 10^{19} at an energy of 450 MeV.

Neutron dosimetry wires consisting of Co-Al, Ti, Fe, and Ni were coirradiated with the samples. The wires measured about 3 inches long with diameters of 10-20 mils. Following the irradiation, each wire was cut into four pieces and activities were measured by Ge(Li) gamma spectroscopy. The measured activation rates are listed in Table 1. As can be seen, the vertical flux gradients are rather small since the samples were centered on the proton beam axis. The fast flux gradients are <10% and the thermal <3%. Radial gradients are not important since the copper samples were wound around the average position of our dosimeters.

The maximum centerline activities were used to adjust the neutron spectrum determined previously[1,2] with a much larger number of reactions. A least-squares procedure was followed using the STAVSL computer code. The adjusted fluence values are listed in Table 2. The total fluence of 7.1 x 10^{17} n/cm^2 corresponds to 0.021 n/cm^2 per proton.

Damage parameter calculations were performed using our SPECTER[3] code package, now available on the NMFECC computer at Lawrence Livermore National Laboratory. The total dose in copper was 1.61 x 10^7 rads. The damage parameters are listed in Table 3.

TABLE 1

ACTIVATION RATES MEASURED AT IPNS-REF-VT2
450 MeV; 3.43 x 10^{19} protons; accuracy ±1.5%
Each sample measures about 0.7 inches in length

	Activation rate (x 10^{-28} atomlatom-proton)			
Reaction	Sample: 1 (top)	2	3	4
$^{58}Fe(n,\gamma)^{59}Fe$	4.63	4.63	4.77	4.68
$^{59}Co(n,\gamma)^{60}Co$	221.	222.	224.	224.
$^{58}Ni(n,p)^{58}Co$	6.81	7.24	7.41	7.04
$^{54}Fe(n,p)^{54}Mn$	9.81	10.47	10.82	10.21
$^{46}Ti(n,p)^{46}Sc$	3.35	3.64	3.64	3.52

TABLE 2

NEUTRON FLUENCE VALUES MEASURED AT IPNS

Energy, MeV	Fluence, x 10^{17} n/cm^2	Error, %
Total	7.07	10
>0.1 MeV	4.76	12
Thermal (<.5 eV)	0.092	20
0.5 eV - 0.1 MeV	2.20	14
0.1 - 1	2.78	15
1 - 5	1.67	16
5 - 10	0.146	13
10 - 20	0.046	14
>20	0.130	12

TABLE 3

CALCULATED DAMAGE AND GAS PRODUCTION IN COPPER AT IPNS

Rads =	1.61 x 10^{7}
DPA =	2.89 x 10^{-4}
Hydrogen =	5.03 x 10^{-3} appm
Helium =	1.02 x 10^{-3} appm
PKA Energy =	8.69 keV
Damage Energy =	6.87 keV

6.0 References

1. L. R. Greenwood and R. J. Popek, "Characterization of Spallation Neutron Sources," DOE/ER-0046/7, pp. 17-23, November 1981.

2. R. C. Birtcher, T. H. Blewitt, M. A. Kirk, T. L. Scott, B. S. Brown, and L. R. Greenwood. J. Nucl. Mater. 108, 3 (1982).

3. L. R. Greenwood, "Recent Developments in Neutron Oosimetry and Radiation Damage Calculations for Fusion Materials Studies," Proceedings of the Third Topical Meeting on Fusion Reactor Materials, Albuquerque, NM, September 19-22, 1983, to be published.

7.0 Future Work

Additional irradiations are being planned for the IPNS facility. Other fusion-related work is being done for P. Hahn and H. Weber (Atomic Institute of the Austrian Universities, Vienna, Austria) and for S. Egusa (JAERI, Japan).

A COMPARISON Oi MEASURED ANJ CALCULATED HELIUM PRODUCTION It4 NICKEL FOR FISSION REACTOR IRRADIATIONS

D. W. Kneff, R. P. Skowronski, B. M. Oliver (Rockwell International, Energy Systems Group), and
L. R. Greenwood (Argonne National Laboratory)

1.0 Objective

The objectives of this work are to apply radiometric plus helium accumulation neutron dosimetry to the measurement of neutron fluences and energy spectra in mixed-spectrum fission reactors utilized for fusion materials testing, and to measure helium generation rates of materials in these irradiation environments.

2.0 Summary

Helium generation measurements and calculations have been performed for 45 nickel samples from nine different fission reactor irradiations, representing a neutron fluence range of 0.1-8.0 x 10^{22} neutrons/cm^2. The measurements were made by gas mass spectrometry, and the calculations were based on dosimetry-adjusted neutron spectra and evaluated cross sections, including new evaluations for ^{59}Ni. The measurements and calculations agree to within ±10%, demonstrating the ability to calculate helium levels in nickel accurately for a wide range of reactor spectra and conditions.

3.0 Programs

Title: Helium Generation in Fusion Reactor Materials/Dosimetry and Damage Analysis
Principal Investigators: D. W. Kneff, H. Farrar IV, and L. R. Greenwood
Affiliation: Rockwell International and Argonne National Laboratory

4.0 Relevant DAFS Program Plan Task/Subtask

Task II.A.1	fission Reactor Dosimetry
Task II.A.4	Gas Generation Rates
Subtask II.A.5.1	Helium Accumulation Monitor Oevelopment

5.0 Accomplishments and Status

5.1 Introduction

The accurate calculation of helium production in nickel in mixed-spectrum fission reactors has been difficult in the past, because the contribution from epithermal and fast neutrons could not be readily determined. A semi-empirical technique[1] for making these calculations is available only for one reactor, the High Flux Isotopes Reactor (HFIR) at the Oak Ridge National Laboratory. It cannot be readily extended to other reactors used in the fusion materials program. The recent evaluation of the neutron cross sections for ^{59}Ni by F. M. Mann[2] now makes it possible to calculate helium production in nickel in fission reactor environments in a straightforward manner.[3]

These calculations have been tested against helium measurements for 45 samples of elemental nickel, irradiated in nine different fusion materials irradiation experiments in three fission reactors: HFIR, the Oak Ridge Research Reactor (ORR), and the Experimental Breeder Reactor-II (EBRII). This work is part of an ongoing program to characterize fusion materials irradiation test facilities using radiometric dosimetry and helium accumulation measurements. The radiometric dosimetry, performed at Argonne National

Laboratory (ANL), is used to determine the neutron fluence and energy spectra for fusion materials irradiations. The helium measurements, performed at Rockwell International, are being used to integrally test total helium production cross sections, and to develop and use helium accumulation monitors for neutron dosimetry.

The helium measurements were made by gas mass spectrometry. The helium calculations were performed by first using the radiometric dosimetry measurements to adjust calculated neutron spectra for the nickel samples in each irradiation. These adjusted spectra were in turn used to calculate spectrum-averaged cross sections for ^{58}Ni and ^{59}Ni, using the new evaluations.[2] The averages were used to calculate the helium production in each nickel sample. Direct comparisons were then made with the measured helium concentration in each sample.

5.2 Radiometric Dosimetry and Spectral Adjustments

The multiple-activation dosimetry technique[4] was used to determine the neutron fluence and energy spectrum for each irradiation. Since all of the present irradiations were of long duration (100-500 full-power days), only long-lived activities could be used to monitor the fluence. The reactions used included $^{58}Fe(n,\gamma)^{59}Fe$, $^{59}Co(n,\gamma)^{60}Co$, $^{54}Fe(n,p)^{54}Mn$, $^{46}Ti(n,p)^{46}Sc$, $^{55}Mn(n,2n)^{54}Mn$, and $^{63}Cu(n,\alpha)^{60}Co$. For EBRII, the reactions $^{45}Sc(n,\gamma)^{46}Sc$ and ^{235}U, ^{238}U, and ^{237}Np(n,fission) were also used. Dosimetry monitors were in the form of small-diameter (0.25-1.27 mm) wires, which were gamma counted following irradiation using Ge(Li) spectroscopy. Measured activities were generally accurate to ±1.5%. Long wires were segmented to determine flux gradients.

The measured activities were used to adjust calculated neutron spectra for each irradiation using the computer code STAYSL.[5] A generalized least-squares adjustment was performed to minimize χ^2, using a variance-covariance matrix derived from uncertainties and their correlations in reaction rates, cross sections, and the calculated spectrum. Adjusted spectra for the three reactors of present interest have been presented in previous reports. (See, for example, Ref. 6-8.) The adjusted thermal, resonance, and fast neutron fluxes have estimated accuracies of 5-10%. However, since the uncertainties are highly correlated, the integral quantities tend to be more accurate.

5.3 Calculation of Helium Production in Nickel

Helium is produced in nickel by the sequential reactions $^{58}Ni(n,\gamma)^{59}Ni(n,\alpha)^{56}Fe$ for thermal and epithermal neutrons, and by Ni(n,Xα) reactions for fast neutrons. Helium production by the ^{58}Ni sequential reactions is calculated as follows:

$$\frac{N(He)}{N_o(^{58}Ni)} = \frac{\sigma_\alpha\left[\sigma_T\left(1 - e^{-\sigma_\gamma \phi t}\right) - \sigma_\gamma\left(1 - e^{-\sigma_T \phi t}\right)\right]}{\sigma_T(\sigma_T - \sigma_\gamma)}$$

Here N(He) is the number of helium atoms produced at irradiation time t, $N_o(^{58}Ni)$ is the initial number of ^{58}Ni atoms, ϕ is the total neutron flux, and σ_α, σ_T, and σ_γ are the $^{59}Ni(n,\alpha)$, ^{59}Ni total absorption, and $^{58}Ni(n,\gamma)$ cross sections, respectively. All cross sections should be averaged over the neutron energy spectrum, and thus include the contributions from both the thermal and epithermal fluxes. For the present calculations, the ^{58}Ni cross section was taken from the ENDF/B-V activation library,[9] and the ^{59}Ni cross sections from the evaluations by Mann.[2] The spectrum-averaged helium production cross sections for Ni(n,Xα) reactions with fast neutrons were calculated using the adjusted neutron spectra and cross sections from the ENDF/B-V Gas Production Data File.[10]

The thermal and fast spectral-averaged cross sections for each of the nine irradiations are listed in Table 1. Total neutron fluences derived from the radiometric dosimetry for each of the irradiated nickel samples are given in Column 4 of Table 2. Total (thermal plus fast) helium production for each nickel sample was calculated from this information plus fluence gradient information provided by the dosimeters. The results are presented in Column 7 of Table 2. These calculated helium concentrations have estimated uncertainties of ±10%.

TABLE 1

REACTOR IRRADIATION PARAMETERS AND SPECTRAL-AVERAW CROSS SECTIONS

Reactor:	ORR				EBRII	HFIR			
Irradiation:	MFE1	MFE2	MFE4A-1	MFE4A-2	X287	CTR31	CTR32	T2	RB1
Reactor Position	C7	i 7	i 3	i 3	ROW 7	PTP	PTP	Target	Be
Power History (MWd)	3031	10972	5481	12176	30496	21853	10863	6616	23386
Time (days)	101	366	183	406	488	219	109	66	234
Spectral-Averaged Cross Sections (barns):									
$^{58}Ni(n,\gamma)$	2.51	1.23	1.33	1.32	0.0094	1.62	1.63	1.90	2.24
$^{59}Ni(n,\gamma)$	42.20	21.93	24.25	24.03	0.0725	29.07	29.22	33.44	38.87
$^{59}Ni(n,p)$	1.05	0.57	0.62	0.62	0.0547	0.73	0.74	0.83	0.96
$^{59}Ni(n,\alpha)$	6.25	3.25	3.59	3.56	0.0144	4.30	4.33	4.95	5.75
$^{59}Ni_{ABS}$	49.50	25.75	28.46	28.21	0.1416	34.10	34.29	39.22	45.58
Ni(n,Xα) [fast]	0.00067	0.00108	0.00119	0.00128	0.00083	0.00095	0.00092	0.00072	0.00050

5.4 Helium Measurements

The irradiated nickel samples were etched before analysis to remove all possible surface effects of helium recoil into or out of the samples. They were then segmented and analyzed by high-sensitivity gas mass spectrometry[11] for their irradiation-generated helium concentrations. Duplicate samples were analyzed for most sample locations, with excellent reproducibility. The absolute uncertainties in the analyses were ±1-2%. The averaged helium measurement results are presented in Column 8 of Table 2.

Special analysis procedures were adopted for selected samples to look at possible analysis effects of reactor tritium, through its decay to ^{3}He, and of ^{4}He diffusion from the nickel samples at the high irradiation temperatures (ranging up to 600°C). Measurable ^{3}He was observed only in the samples from HFIR irradiation T2, and corrections were made for those data. ^{4}He loss from the samples was measured in a two-step procedure using encapsulated nickel samples from ORR-MFE2, ORR-MFE4A-2, and HFIR-CTR32. The capsules were first sheared to measure the helium released from the nickel into the capsule void, and the helium remaining in the nickel was then measured by sample vaporization. The helium release during irradiation was less than 0.25% in each of the seven capsules analyzed, indicating that nickel retains all but a very small fraction of its helium even under the high-temperature irradiation conditions present.

5.5 Discussion

Comparisons between the calculated and measured helium concentrations in the 45 nickel samples are given in the last column of Table 2. The calculated and measured values generally agree within ±10%, which is within their estimated uncertainties (±10% for the calculations and ±2% for the measurements). The comparisons cover a neutron fluence range of 1×10^{21} to 8×10^{22} n/cm^2.

These comparisons demonstrate that helium production levels in nickel can be calculated quite accurately for a wide range of neutron spectra and conditions. They also provide confidence in the use of bare nickel wires as helium accumulation monitors for fission reactor applications.

6.0 References

1. F. W. Wiffen, E. J. Allen, H. Farrar IV, E. E. Bloom, T. A. Gabriel, H. T. Kerr, and F. G. Perey, "The Production Rate of Helium During Irradiation of Nickel in Thermal Spectrum Fission Reactors," J. Nucl. Mater. (to be published).

2. F. M. Mann, "^{59}Ni + n Cross Section Evaluation," in Damage Analysis and Fundamental Studies, Quarterly Progress Report October-December 1982, DOE/ER-0046/12, U.S. Department of Energy, 35 (1983).

TABLE 2

COMPARISON OF MEASURED AND CALCULATED HELIUM PRODUCTION IN NICKEL FOR FISSION REACTOR IRRADIATIONS

Irradiation Experiment	Sample	Height Above Reactor Midplane* (cm)	Total Neutron Fluence (10^{22} n/cm^2)	Helium Concentration (appm)**				Ratio
				Calculated			Measured (Average)	Calculated / Measured
				^{59}Ni(n,α)	Fast	Total		
ORR-MFE1	1	21.7	0.133	9.3	0.9	10.2	10.2	1.00
	2	10.0	0.233	27.9	1.6	29.5	30.1	0.98
	3	1.9	0.296	44.6	2.0	46.6	48.5	0.96
	4	-9.8	0.349	61.5	2.3	63.8	63.5	1.00
	5	-18.3	0.310	48.8	2.1	50.9	53.5	0.95
ORR-MFE2	1	15.4	1.16	165.9	12.5	178.4	166.0	1.07
	V9†	14.0	1.21	179.7	13.1	192.8	182.6	1.06
	2	8.5	1.40	236.7	15.1	251.8	249.3	1.01
	Y1†	0.4	1.60	304.0	17.3	321.3	338.2	0.95
	3	-5.1	1.68	332.9	18.1	341.0	380.0	0.92
	H7†	-6.5	1.69	336.6	18.2	354.8	377.5	0.94
ORR-MFE4A-1	4	-5.8	0.872	113.9	10.4	124.3	121.1	1.03
	7	-8.3	0.868	112.9	10.3	123.2	111.9	1.10
	8	-9.3	0.863	111.6	10.3	121.9	109.6	1.11
	9	-10.4	0.857	110.2	10.2	120.4	106.8	1.13
	10	-11.6	0.848	107.9	10.1	118.0	110.8	1.06
	11	-12.9	0.835	104.8	9.9	114.7	108.2	1.06
	13	-15.4	0.805	97.7	9.6	107.3	108.7	0.99
	15	-17.8	0.768	89.2	9.1	98.3	101.7	0.97
ORR-MFE4A-2	5	-5.9	1.76	421	23	444	496.7	0.89
	8	-5.9	1.88	475	24	499	566.1	0.88
	A4†	-11.6	1.71	399	22	421	423.4	0.99
	B2†	-12.1	1.82	447	23	470	515.3	0.91
	4	-14.3	1.77	425	23	448	485.1	0.92
	1	-14.4	1.65	374	21	395	401.5	0.98
EBRII-X287	9	16.2	5.14	0.12	39.6	39.7	40.10	0.97
	12	16.2	4.36	0.08	29.1	29.2	28.24	1.03
	1	15.3	5.02	0.12	37.7	37.8	38.10	0.99
	8	-0.4	6.73	0.21	55.9	56.1	56.68	0.99
	11	-0.4	6.16	0.17	43.7	43.9	43.17	1.02
	6	-11.4	5.72	0.15	30.0	30.2	28.81	1.05
	7	-17.1	5.47	0.14	25.7	25.8	27.08	0.95
	10	-17.1	5.00	0.12	20.3	20.4	20.48	1.00
HFIR-CTR31	1	20.8	5.44	3990	51	4041	4011	1.01
	5	-12.5	7.89	6824	75	6899	7286	0.95
HFIR-CTR32	1	20.8	2.78	1345	26	1371	1416	0.97
	N2†	16.7	3.50	1983	32	2015	1929	1.04
	3	4.2	4.70	3187	43	3230	3568	0.91
	4	-4.3	4.69	3176	43	3219	3694	0.87
	P4†	-8.3	4.45	2924	41	2965	3025	0.98
	6	-20.8	2.74	1312	25	1337	1515	0.88
HFIR-RB1	19	10.7	2.96	2515	15	2530	2815	0.90
	18	2.0	3.89	3865	19	3884	4397	0.88
HFIR-T2	T22	17.0	2.31	1275	17	1292	1386	0.93
	T21	7.2	3.04	2028	22	2050	2089	0.98

*Radial positions differ for some samples.

**Atomic parts per million (10^{-6} atom fraction)

†Encapsulated sample

3. L. R. Greenwood, "Fission Reactor Dosimetry - HFIR - CTR 31, 32, 34, and 35," in Damage Analysis and Fundamental Studies, Quarterly Progress Report April-June 1983, DOE/ER-0046/14, U.S. Department of Energy, 9 (1983).

4. L. R. Greenwood. "Neutron Flux and Spectral Measurements to Characterize Irradiation Facilities for Fusion Material; Studies," in Radiation Metrology Techniques, Data Bases, and Standardization, F. E. K. Kam (Ed.), Proc. Fourth ASTM-EURATOM Symposium on Reactor Dosimetry, Gaithersburg, MD, March 22-26, 1982, NUREG/CP-0029, Vol. 2 (1982), pp. 783-792.

5. F. G. Perey, "Least Squares Dosimetry Unfolding: The Program STAY'SL," ORNL/TM-6062, Oak Ridge National Laboratory (1977); as modified by L. R. Greenwood (1979).

6. L. R. Greenwood, "Fission Reactor Dosimetry - HFIR - CTR 31, 32, 34, and 35," in Damage Analysis and Fundamental Studies, Quarterly Progress Report January-March 1983, DOE/ER-0046/13, Vol. 1, U.S. Department of Energy, 17 (1983).

7. L. R. Greenwood, "Dosimetry and Damage Analysis for the MFE4A Spectral Tailoring Experiment in ORR," in Damage Analysis and Fundamental Studies, Quarterly Progress Report January-March 1983, DOE/ER-0046/12, U.S. Department of Energy, 14 (1983).

8. L. R. Greenwood, "Fission Reactor Dosimetry," in Damage Analysis and Fundamental Studies, Quarterly Progress Report July-September 1981, DOE/ER-0046/7, U.S. Department of tnergy, 8 (1981).

9. ENDF/B-V Activation File-532, National Neutron Cross Section Center, Brookhaven National Laboratory.

10. ENDF/B-V Gas Production Data File-533, National Neutron Cross Section Center, Brookhaven National Laboratory.

11. H. Farrar IV, W. N. McElroy, and E. P. Lippincott, "Helium Production Cross Section of Boron for Fast-Reactor Neutron Spectra," Nucl. Technol., 25, 305 (1975).

7.0 Future Work

Helium measurements and integral cross section testing are in progress for several other pure elements irradiated in mixed-spectrum fission reactor environments. Initial emphasis is on Cu, Fe, and Ti. The goals are the accurate prediction of helium generation in materials irradiations and the further development of helium accumulation fluence monitors for stable-product neutron dosimetry.

8.0 Publications

A paper entitled "A Comparison of Meafured and Calculated Helium Production in Nickel Using Newly Evaluated Neutron Cross Sections for ^{59}Ni, by L. R. Greenwood (ANL), D. W. Kneff, R. P. Skowronski (Rockwell International), and F. M. Mann (HEDL), was presented at the Third Topical Meeting on Fusion Reactor Materials, Albuquerque, New Mexico, on September 21, 1983, and has been submitted for publication in J. Nucl. Mater. as part of the conference proceedings.

14-MeV NEUTRON IRRADIATION OF COPPER ALLOYS

S.J. Zinkle and G.L. Kulcinski (University of Wisconsin-Madison)

1.0 Objectives

The objectives of the study are to 1) determine defect survivability in copper alloys irradiated at room temperature and the influence of solute additions, 2) determine if resistivity, microhardness and TEM analysis provide consistent results in tens of defect cluster density, and 31 determine the fluence dependence of the cluster density for a room temperature 14-MeV neutron irradiation of copper.

2.0 Summary

Resistivity and Vickers microhardness measurements have been obtained from copper and three copper alloys (Cu + 5% Al, Cu + 5% Mn, Cu + 5% Ni) irradiated at roan temperature with 14-MeV neutrons up to a maximum fluence of 3×10^{21} n/m^2. The defect cluster density appears to scale linearly with the square root of neutron fluence. Resistivity analysis indicates that about 16% of the Frenkel defects initially created in the cascade escape correlated recombination events. Good agreement has been obtained between resistivity and microhardness estimates of the defect cluster density as compared to densities actually observed by TEM methods.

3.0 Program

Title: Radiation Effects to Reactor Materials
Principal Investigators: G.L. Kulcinski and R.A. Dodd
Affiliation: University of Wisconsin

4.0 Relevant DAFS Program Task/Subtask

Subtask II.B.3.2 Experimental Characterization of Primary Damage State; Studies of Metals
Subtask II.C.6.3 Effects of Damage Rate and Cascade Structure on Microstructure; Low-Energy/High-Energy Neutron Correlations
Subtask 11.C.16.1 14-MeV Neutron Damage Correlation

5.0 Accomplishinents dnd Status

5.1 Introduction

A previous investigation[1] of 14-MeV neutron irradiated copper alloys estimated that about 70% of the defect clusters produced in copper during neutron irradiation were smaller than the normal resolution limit of an electron microscope (~ 1 nm). We have used resistivity methods, which are sensitive to these smaller defect clusters, along with TEM and microhardness measurements in an attempt to characterize the nature of the cluster size distribution. This analysis also allows a comparison to be made of the relative sensitivity of these three experimental tools at low-neutron fluences. In addition. using appropriate models. resistivity analysis yields the fraction of defects which escape correlated recombination:' This quantity is important for radiation damdge modeling.

TABLE 1

IRRADIATION DATA FOR RESISTIVITY AND TEM SAMPLES

Alloy	ρ_0 (Ω-m)	Grain Size (μm)	Control Hardness (kg/mm^2), 10g Load	Maximum Fluence (n/m^2)	
				Resistivity	TEM
cu	4.48 x 10^{-11}	13	**56.7** ± 4.3	2.9 x 10^{21}	1.9 x 10^{21}
Cu-5% Al	3.96 x 10^{-8}	23	**53.8** ± 0.9	2.9 x 10^{21}	2.1 x 10^{21}
Cu-5% Mn	1.08 x 10^{-7}	22	53.4 ± 2.5	2.8 x 10^{21}	2.0 x 10^{21}
Cu-5% Ni	5.16 x 10^{-8}	12	53.4 ± 2.8	2.9 x 10^{21}	2.2 x 10^{21}

5.2 Experimental

Foils of pure (99.99+ atom %) copper and copper alloyed with five atom percent of either aluminum, nickel or manganese obtained fran Hanford Engineering Development Laboratory[1] were cold-rolled to a thickness of 25 μm. Transmission electron microscope (TEM) disks and resistivity foils were cut from these foils, annealed in high-purity argon, and allowed to air cool. The metals were irradiated at room temperature using 14-MeV neutrons from the Rotating Target Neutron Source II (RTNS-II) at Lawrence Livermore National Laboratory. The irradiation consisted of four incremental fluences up to a maximum level of about 3 x 10^{21} n/m^2. Details of the experimental procedure have been previously described.[2]

Changes in the foil resistance were measured with standard resistivity equipment (potentiometer sensitivity = 10 nV). The pure copper sample had an initial residual resistivity ratio (RRR = $\rho_{298}/\rho_{4.2°K}$) of 380.

Vickers microhardness measurements were performed[3] using a Buehler Micromet® microhardness tester at indenter loads of 5g and 10g. A minimum of 60 indentations was made around the periphery of four different TEM disks for each metal at every fluence level. Pre-irradiation materials properties and irradiation conditions of the metals investigated are given in Table 1.

5.3 Experimental Results

Figures 1 and *2* show the respective irradiation-induced resistivity changes for pure copper and the copper alloys. The data for the pure copper sample scales linearly with the square root of neutron fluence. This fluence dependence is in agreement with previous work for both electron and neutron irradiation at temperatures where the interstitial is mobile.[4] Irradiation of the copper alloys produces an initial decrease in foil resistivity, followed by an increase in resistivity with fluence for the Cu-5% Al and Cu-5% Ni alloys. The resistivity of these alloys became greater than the pre-irradiation value at a fluence of 3 x 10^{21} n/m^2. The resistivity of the Cu-5% Mn sample remained below its unirradiated value at all fluence levels investigated. The negative resistivity changes observed in the irradiated copper alloys are believed to be due to short-range ordering.[5]

Changes in the Vickers microhardness of the four metals obtained at an indenter loading of 10 grams are shown in Fig. 3 as a function of 14-MeV neutron fluence. Results obtained at an indenter loading of 5 grams showed similar trends.[3] As is evidenced in Fig. 3, the hardness data for all four metals scale linearly with the fourth root of neutron fluence after an incubation fluence. The duration of the incubation period is on the order of 1 x 10^{20} n/m^2, and is shorter for pure copper as compared to the alloys. The Cu + 5% Mn alloy exhibited significantly larger radiation hardening than the other metals at the fluence levels investigated. All four metals in Fig. 3 have roughly equal slopes in their curve of microhardness vs. fluence.

5.4 Data Analysis

Early resistivity studies of pure metals irradiated at temperatures above 70°K provided support for a theoretical model known as the unsaturable trap model (UTM).[4] More recent developments have concentrated on

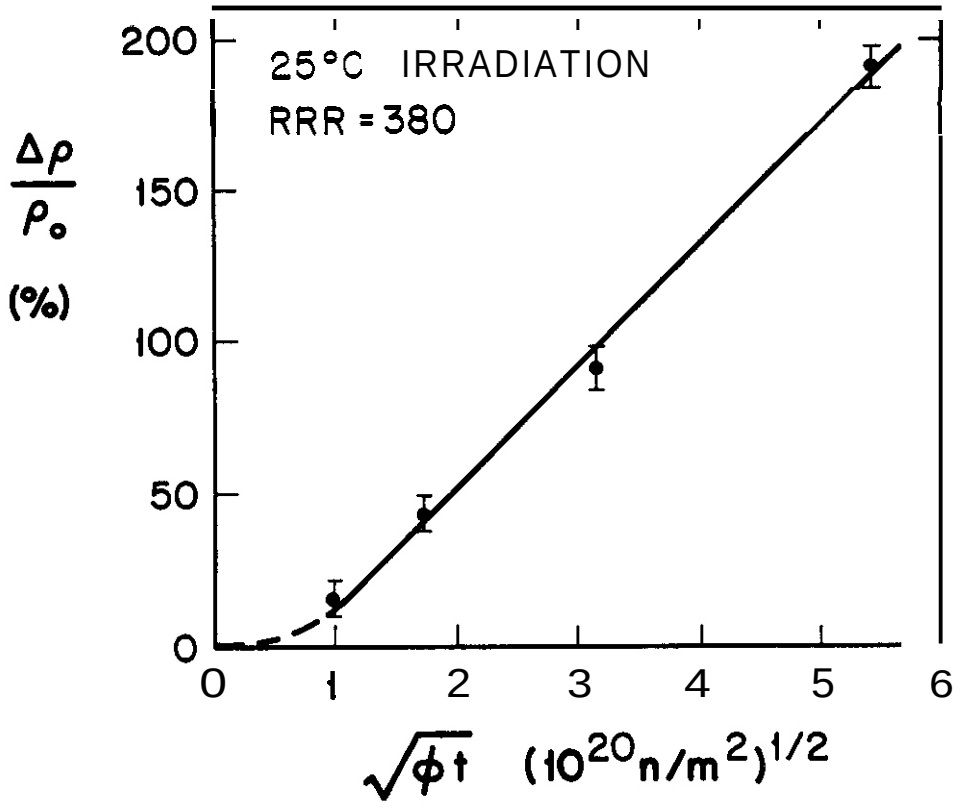

FIGURE 1. Resistance change vs. the square root of 14-MeV neutron fluence for pure copper.

examination of the reciprocal damage rate (RDR) for studying point defect interactions. Using the analysis of Dworschak et al.[6], the following result is obtained:

$$\Delta\rho = \rho_f^t \frac{r_t C_t}{r_v} \left\{ \sqrt{1 + \frac{2 f\sigma_d \Phi}{r_t C_t / r_v}} - 1 \right\} \qquad (1)$$

This may be rewritten in the form

$$\frac{\Phi}{\Delta\rho} = \frac{1}{f\sigma_d \rho_f^t} \left\{ 1 + \frac{\Delta\rho}{2 \rho_f^t C_t r_t / r_v} \right\} \qquad (2)$$

where Φ is the neutron fluence. f is the fraction of defects escaping correlated recombination, σ_d is the displacement cross section, ρ_f^t is the specific resistivity of trapped Frenkel defects, r_t and r_v are the capture radii of impurity traps and vacancies, C_t is the concentration of impurities, and $\Delta\rho$ is the radiation-induced resistivity increase. A least squares fit to the present resistivity data yields the result

$$f \sigma_d \rho_f^t = 8.4 \times 10^{-32} \ \Omega\text{-m}^{-3} \ . \qquad (3)$$

The quantity ρ_f^t depends on the amount of clustering which has occurred. To obtain a lower limit for the fraction of defects escaping correlated recombination, ρ_f^t may be taken to be equal to the isolated Frenkel pair specific resistivity in copper,[7] $\rho_{FP} = 2.0$ μΩ-cm/% F.P. Using a displacement cross section[1] of σ_d = 3690 barns then gives $f \geq 11\%$.

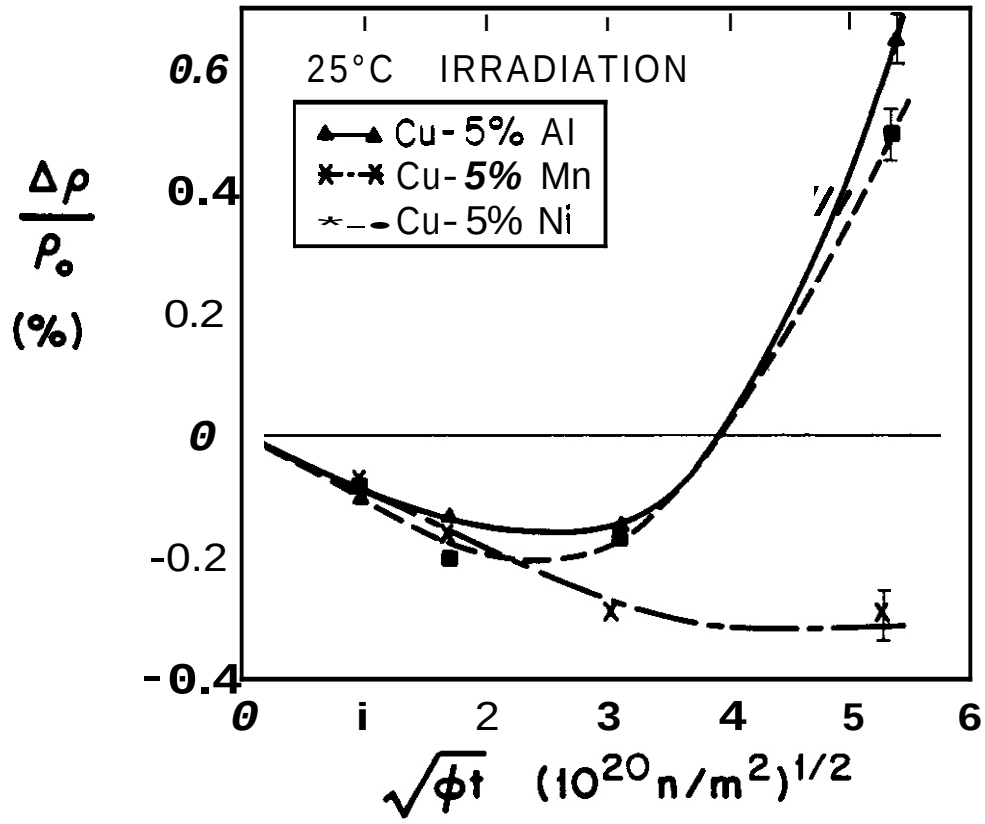

FIGURE 2. Resistance change vs. the square root of 14-MeV neutron fluence for copper alloys.

A more accurate estimation of f requires a determination of the effect of clustering on ρ_F^t. Thompson et al.[8] experimentally investigated the effect of clustering on ρ_{FP} during an electron irradiation at tern peratures where only interstitials migrate and cluster. Using his result of ρ_f^t/ρ_{FP} = 0.8 ± 0.1 along with ρ_{FD}^i = 1.4 μΩ-cm/% interstitials and ρ_{FD}^v = 0.6 μΩ-cm/% vacancies,[7] the specific resistivity of trapped Frenkel defects (where both interstitials and vacancies are clustered1 can be computed. Assuming an equivalent number of vacancy and interstitial clusters leads to a prediction of ρ_f^t = 1.4 ± 0.25 μΩ-cm/% F.P. With this value, f ≃ 16%.

Brager et al.[1] irradiated identical metals with 14-MeV neutrons up to a maximum fluence of 7.5 x 10^{21} n/m² and examined the foils with TEM. We have found that their reported visible defect cluster size distribution can be fitted very well by a log-noma1 distribution[9] with d_0 = 2.25 nm:

$$N(d) = \frac{1}{\sqrt{2\pi}\ \ell n\ \sigma} \exp\left[-\frac{(\ell n\ d/d_0)^2}{2\ (\ell n\ \sigma)^2}\right]. \qquad (4)$$

In anticipation that a large number of small defects might be invisible to TEM methods, we also fit the larger defects of the observed distribution to a log-normal distribution with smaller values of d_0. The fitted distributions are compared to the reported pure copper TEM data of Brager et al.[1] in Fig. 4. Applying the log-noma1 distribution to the resistivity data gives the result,

$$\Delta\rho = \frac{\pi \rho_F^t N_{c\ell}\ b}{8} d_0^2\ e^2\ (\ell n\ \sigma)^2 \qquad (5)$$

where b is the Burgers vector of the defect cluster and $N_{c\ell}$ is the cluster density.

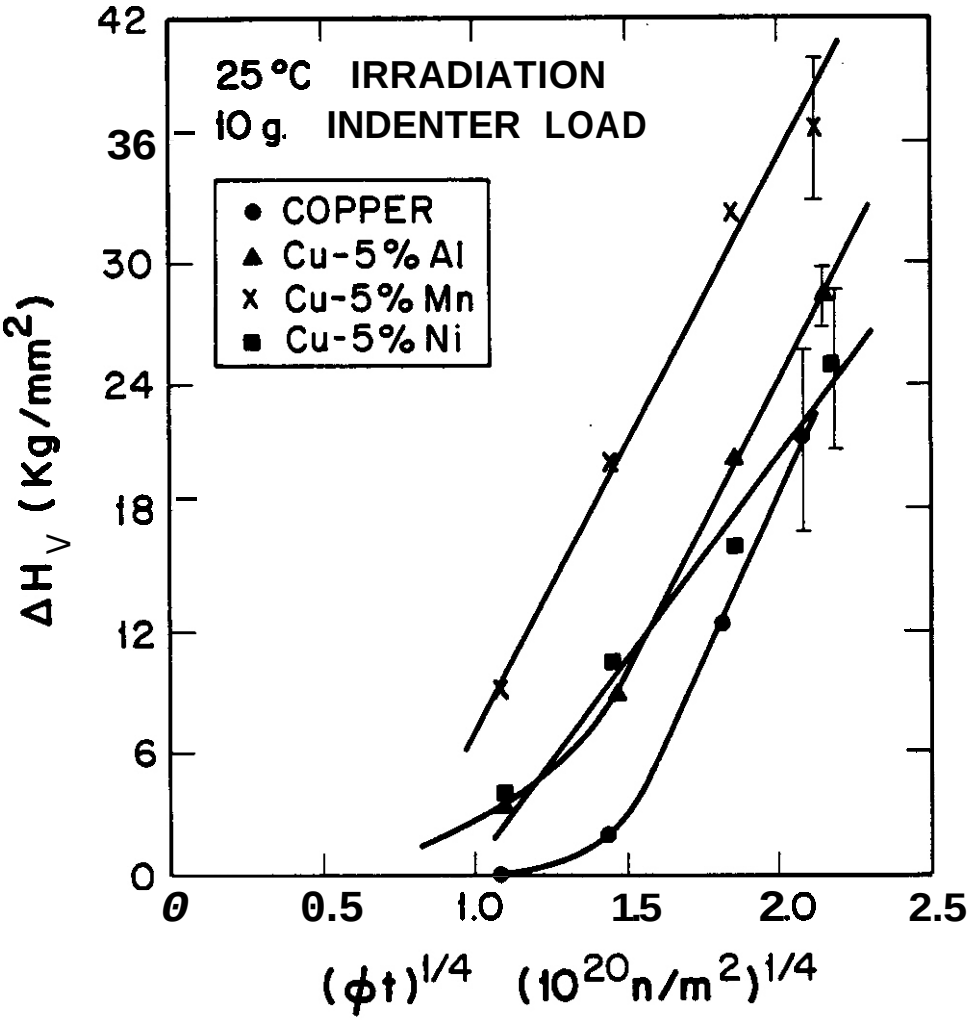

FIGURE 3. Change in Vickers microhardness vs. fourth root of 14-MeV neutron fluence.

A similar analysis can be applied to tensile data from a room temperature 14-MeV neutron irradiation of copper by Mitchell et al.[10] The hardening due to dislocation loops is given by[11]

$$\Delta\tau = \frac{\mu b}{\beta \bar{\ell}} = \frac{\mu b}{\beta} \sqrt{\sum_j n_j d_j} \qquad (6)$$

where τ = shear stress, μ = shear modulus, and 6 is a constant. Using the Von Mises criterion to relate yield strength to shear stress, $\Delta\sigma_Y = \sqrt{3}\,\Delta\tau$, and once again assuming a log-normal cluster size distribution, Eq. 6 can be solved for the cluster density:

$$N_{c\ell} = \frac{\exp\left[-(\ell n\sigma)^2/2\right]}{3\,d_0} \left(\frac{\beta\,\Delta\sigma_y}{\mu b}\right)^2 \qquad (7)$$

Vickers microhardness data can be correlated to tensile data results found in the literature, $\Delta\sigma_Y$ (MPa) = K ΔH_V (kg/mm²). A recent correlation[1] found the result K = 3.21 to be valid for irradiated pure copper and also copper alloys. As seen in Fig. 5, we have obtained a reasonable correlation between the pure copper tensile data of Mitchell et al.[10] and the 10g microhardness data for three metals (Cu, Cu-5% Al, Cu-5% Nil with K = 3.0. The Cu-5%Mn microhardness data do not agree well with the tensile data.

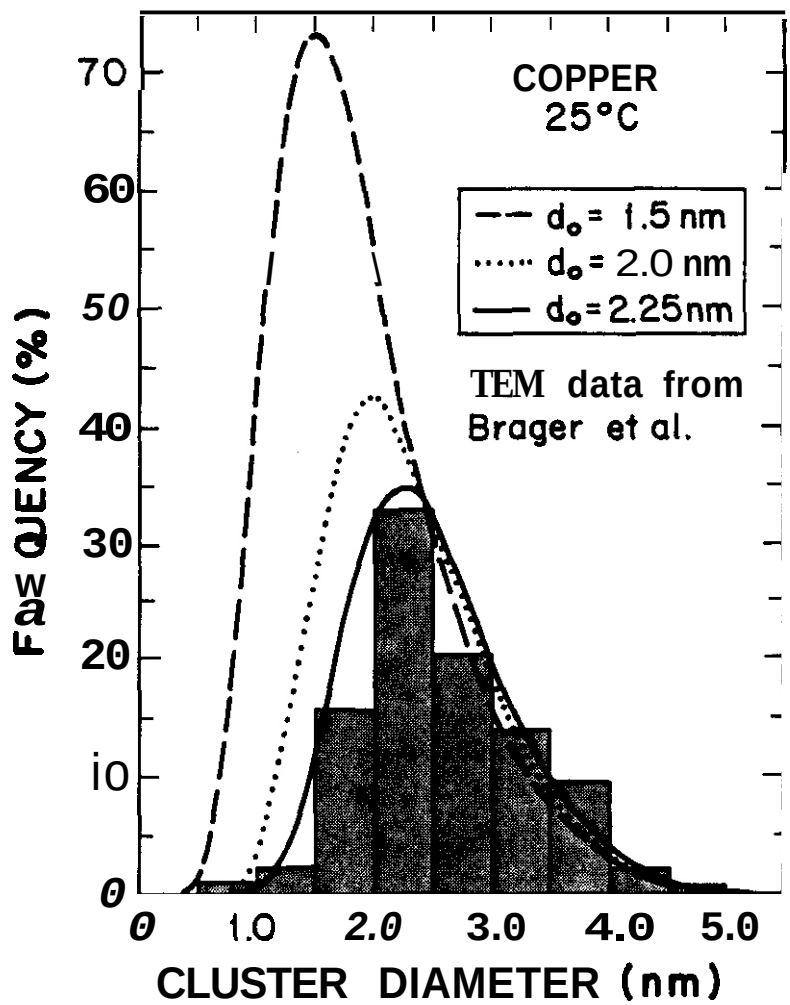

FIGURE 4. Log-normal curve (Eq. 4) fitted to observed TEM cluster data at a 14-MeV neutron fluence of 3 x 10^{21} n/m^2.

5.5 Discussion

The general fluence dependence of the radiation-induced change in resistivity and microhardness is in good agreement with theoretical models. Resistivity results for pure copper scale linearly with the square root of 14-MeV neutron fluence, indicating that the cluster density $N_{C\ell} \sim \sqrt{\phi t}$. The microhardness data of all four metals appears to be proportional to the fourth root of neutron fluence (again indicating that $N_{C\ell} \sim \sqrt{\phi t}$), but there is insufficient high-fluence data to conclusively determine the actual power law dependence. Previous experiments have found that the yield stress is proportional to the one-third power of the fluence.[12] The roughly equal slopes for all four metals in the curve of microhardness change vs. fourth root of neutron fluence (Fig. 3) may be taken as an indication that there are equivalent damage production rates in these materials following the initial transition period.

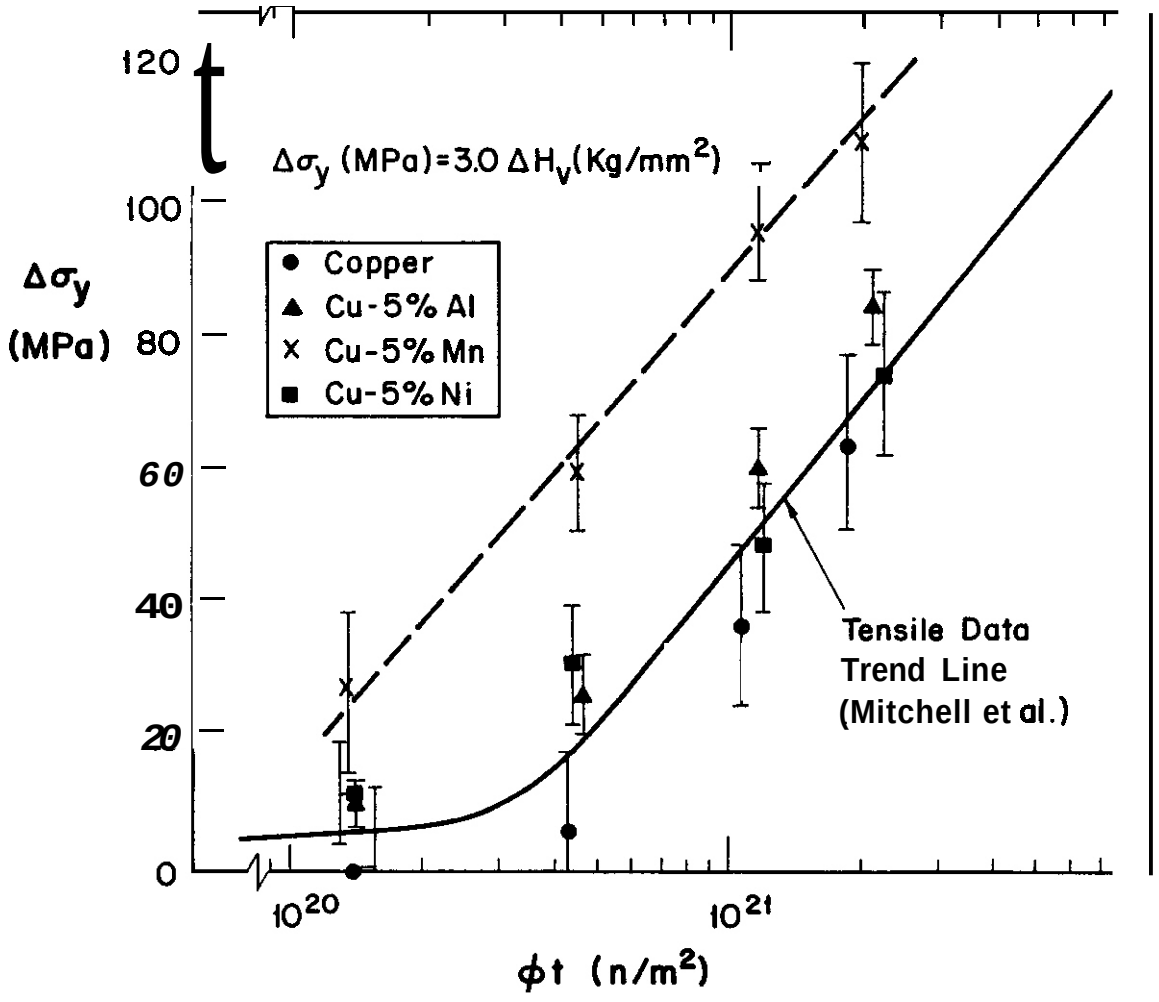

FIGURE 5. Correlated yield strength change vs. 14-MeV fluence.

Our best estimate of the fraction of defects which escape correlated recombination (16%) agrees well with the value of 15% found in the literature for electron-irradiated copper.[13]

The calculated visible defect cluster densities obtained from resistivity (Eq. 5) and Mitchell's tensile data (Eq. 7) may be compared to the density which was actually observed by TEM methods. The results of this comparison are sunmarized in Tables 2 and 3. Parameters used in the calculation were ρ_f^t = 1.4 μΩ-cm% F.P. and β = 3/7.[14] Brager et al. reported a cluster density of 1.3 x 10^{23}/m^3 at ϕ = 2.7 x 10^{21} n/m^2 for 14-MeV neutron irradiated pure copper. This value is in good agreement with the calculated densities of 1.05 x 10^{23}/m^3 (resistivity) and 1.2 x 10^{23}/m^3 (tensile), which were obtained assming perfect dislocation loops and that all of the defect clusters were visible. If one assumes that a substantial number of small defect clusters are invisible (i.e. a smaller value of d_0 in Eq. 4 and Table 2), then the calculated cluster density becomes much smaller than the observed value. Brager[1] observed significantly higher cluster densities in 14-MeV neutron irradiated copper than other researchers who irradiated to similar fluences.[10,15] One possible explanation for the discrepancy is that Brager carefully investigated defect clusters down to diameters of 1.0 nm. The size limit of the other TEM investigations is uncertain. From this analysis, it appears that it is possible to observe essentially all of the surviving point defect clusters by TEM methods if a very careful study is undertaken, investigating clusters down to diameters of 1.0 nm.

TABLE 2

CALCULATED UEFECT CLUSTER DENSITIES IN COPPER AT A FLUENCE OF 3×10^{21} n/m^2 ASSUMING PERFECT DISLOCATION LOOPS ($b = a_0/\sqrt{2}$)

	Fraction of Clusters	Predicted Visible Cluster Density (10^{22}/m^3)		
d_0 (nm)	Which are Visible (Fig. 4)	Resistivity	Microhardness*	Tensile**
1.5	0.4	8	7	7
2.0	0.7	9	9	9
2.25	1.0	10.5	12	12

*Extrapolation to $\phi t = 3 \times 10^{21}$ n/m^2 from ΔH_v vs. $(\phi t)^{1/4}$ curve (Fig. 3); assumes $\Delta\sigma_y$ (MPa) = 3.0 ΔH_v (kg/mm^2)

TABLE 3

COMPARISON OF CALCULATED AND OBSERVED DEFECT CLUSTER DENSITIES IN COPPER AT A FLUENCE OF 3×10^{21} n/m^2 ASSUMING ALL CLUSTERS ARE VISIBLE

			Visible Cluster Density (10^{22}/m^3)	
Type of Analysis	Method	Copper Type	Perfect Loops ($b = a_0/\sqrt{2}$)	Faulted Loops ($b = a_0/\sqrt{3}$)
Calculation	Resistivity	DAFS	10.5	11[+]
Calculation	Microhardness	DAFS	12	18
Calculation	Tensile[10]	LLNL/Cominco	12	18
Observed	TEM[1]	DAFS	.....	13.....

[+]Assumed stacking fault specific resistivity $\rho_{SF} = 2.5 \times 10^{-17}$ Ω-m^2 [14].

5.6 Conclusions

Approximately 16% of the defects created in copper during room temperature 14-MeV neutron irradiation escape correlated recombination events.

Good agreement has been obtained by fitting observed (TEM) defect cluster size distributions to a log-normal distribution. Using this fitted distribution, estimates of defect cluster density obtained by utilizing resistivity and tensile data have been found to agree well with TEM results. Hence, it appears that TEM may be capable of observing essentially all of the defect clusters produced if careful microscopy is performed on clusters down to sizes of ~ 1 nm.

Resistivity, tensile,[10] and microhardness data indicate that, for a room temperature 14-MeV neutron irradiation, the defect cluster density is linear with the square root of fluence up to a = 7×10^{21} n/m^2.

Finally, defect clustering during 14-MeV neutron irradiation of copper at 25°C appears to cause a substantial reduction (~ 30%) in the Frenkel pair specific resistivity.

6.0 References

1. H.R. Brager et al., J. Nucl. Matl., 103 and 104, 995 (1981).
2. S.J. Zinkle and G.L. Kulcinski, DAFS Quarterly Progress Report DOE/ER-0046/9 (May 1982), p. 93 and DOE/ER-0046/14 (1983).

3. S.J. Zinkle and G.L. Kulcinski, Proceedings of the Symposium on the Use of Nonstandard Subsized Specimens for Irradiated Testing, Albuquerque, NM, Sept. 23, 1983.

4. R.M. Walker in "Radiation Damage to Solids," Proceedings of the International School of Physics (Enrico Fermi) Course XVIII, D.S. Billington (Ed.), (1962), p.594.

5. R. Poerschke and H. Wollenberger, J. Nucl. Matl., 74, 48 (1978).

6. F. Dworschak et al., J. Physics F, 5, 400 (1975).

7. R.C. Birtcher and T.H. Blewitt, J. Nucl. Matl., 98, 63 (1981).

8. L. Thompson et al., Rad. Effects, 20, 111 (1973).

9. F. SchUckher in Quantitative Microscopy R.T. DeHoff and F.N. Rhines, (Eds.) McGraw-Hill, NY (1968) p. 205.

10. J.B. Mitchell et al. in "Radiation Effects and Tritium Technology for Fusion Reactors," J.S. Watson and F.W. Wiffen (Eds.), Gatlinburg, TN (1975) Vol. II, 172.

11. N.M. Ghoniem et al., Proc. of Eleventh International Symposium on Effects of Radiation on Materials, ASTM STP 782, Scottsdale, AZ, (1982) 1054.

12. J.J. Koppenaal and R.J. Arsenault, metallurgical Reviews, 16, 175 (1971).

13. U. Theis and H. Wallenberger, J. Nucl. Matl., 88, 121 (1980).

14. J. Polak, Phys. Stat. Sol., 11, 673 (1965).

15. J.B. Roberto et al. in "Radiation Effects and Tritium Technology for Fusion Reactors," J.S. Watson and F.W. Wiffen (Eds.), Gatlinburg, TN (1975) Vol. II, 159.

7.0 Future Work

TEM analysis of the irradiated copperfcopper alloys will be performed. Analysis will include defect cluster size distribution and cluster density as a function of neutron fluence.

8.0 Publications

S.J. Zinkle and G.L. Kulcinski, "14-MeV Neutron Irradiation of Copper Alloys," 3rd Topical Meeting on Fusion Reactor Materials, Albuquerque, NM (Sept. 19-22, 1983). Proceedings to be published in J. Nucl. Matl.

9.0 Acknowledgement

This work performed under appointment to the Magnetic Fusion Energy Technology Fellowship Program and with funds supplied by the Office of Fusion Energy, Department of Energy.

14-MeV NEUTRON RADIATION-INDUCED MICROHARDNESS CHANGES IN COPPER ALLOYS

S.J. Zinkle and G.L. Kulcinski (University of Wisconsin)

1.0 Objectives

The objective of this work is to examine the effect of a high-energy neutron irradiation on damage production in copper alloys. Specific objectives are: (1) to determine the effect of neutron fluence and solute additions on the radiation-induced Vickers microhardness nmber of copper, (2) to examine the effect of indenter load on the radiation-induced microhardness at low values, and (3) to correlate microhardness results with resistivity and TEM data.

2.0 Summary

Vickers microhardness measurements have been performed on copper and copper alloy (Cu-5% Al, Cu-5% Mn, Cu-5% Ni) TEM disks which were irradiated at 25°C with 14-MeV neutrons in incremental doses up to a maximum fluence of 2.2 x 10^{21} n/m^2. Measurements were made at two different values of indenter loading (5 g and 10 g) in order to facilitate correlations with high-load data. The radiation-induced change in microhardness scales linearly with the fourth root of neutron fluence following an incubation fluence for both values of indenter load. The copper alloys, in particular Cu-5% Mn, exhibit a shorter incubation fluence and hence a larger radiation-induced hardness increase than the pure copper samples. The 5 g microhardness data has a lower value for the radiation-induced microhardness change compared to the 10 g data due to surface effects. The 10 g microhardness data predictions of defect cluster density agree well with resistivity predictions and TEM observations.

3.0 Program

Title: Radiation Effects to Reactor Materials
Principal Investigators: G.L. Kulcinski and R.A. Dodd
Affiliation: University of Wisconsin

4.0 Relevant DAFS Program Plan Task/Subtask

Subtask II.B.3.2 Experimental Characterization of Primary Damage State; Studies of Metals
Subtask II.C.6.3 Effects of Damage Rate and Cascade Structure on Microstructure; Low-EnergylHigh-Energy Neutron Correlations
Subtask II.C.16.1 14-MeV Neutron Damage Correlation

5.0 Accomplishments and Status

5.1 Introduction

The materials properties of irradiated copper and copper alloys have been extensively studied over the past two decades (see, e.g. Ref. 1). The irradiated properties of copper and its alloys are of current interest since high-strength copper alloys have recently been considered for use as high-magnetic field insert coils in tandem mirror and tokamak fusion reactors. For these reasons, copper is an ideal material on which to investigate the effect of irradiation on low-load microhardness. Simple binary copper alloys were also studied in order to determine the effect of solutes on low-load microhardness.

This paper describes the effect of a room temperature 14-MeV neutron irradiation on the Vickers microhardness of pure copper and three copper alloys. Microhardness data was obtained at indenter loadings of 5 g and 10 g in order to determine the effect of low-indenter loads on microhardness results. This allows a determination to be made whether low-load microhardness results are representative of bulk material behavior. Since 14-MeV neutron irradiation results in relatively uniform, fine-scale damage compared to the sampling volume of a typical microhardness test, it may be argued that the irradiation-induced change in microhardness should be independent of indenter load (sampling volume). This investigation is designed to determine whether or not such an assumption is valid.

Resistivity and transmission electron microscope (TEM) data have also been obtained from these materials as a function of fluence in order to facilitate correlations.[2] These results may be compared to the microhardness predictions of defect survivability in order to determine the applicability of low-load microhardness data for modelling bulk properties.

5.2 Experimental Procedure

Foils of pure (99.99+ atom %) copper and copper alloyed with five atom percent of either aluminum, nickel or manganese obtained from Hanford Engineering Developent Laboratory[3] were cold-rolled from 250 μm down to a thickness of 25 μm. TEM disks were cut from these foils, annealed in high-purity argon, and allowed to air cool. The pure copper samples were annealed at 400°C (0.5 T_M) for 15 minutes and the copper alloys were annealed at 750°C (0.75 T_M) for 30 minutes. The metals were irradiated at room temperature using 14-MeV neutrons from the Rotating Target Neutron Source-I1 (RTNS-II) at Lawrence Livermore National Laboratory. The irradiation consisted of four incremental fluences up to a maximum level of about 2 x 10^{21} n/m^2. This was achieved by spacing the TEM disks away from the neutron source so that the disks experienced different flux levels during the irradiation. A previous investigation[3] determined that 14-MeV neutron PKA-damage events in copper were essentially independent of flux for fluences up to 10^{22} n/m^2 and flux levels of $< 2 \times 10^{16}$ n/m^2-s. Six TEM disks of each metal were irradiated to the various fluence levels. Pre-irradiation materials properties and irradiation conditions of the metals investigated are given in Table 1.

Vickers microhardness measurements were performed using a Buehler Micromet® microhardness tester. This instrument is designed for operation at indenter loads between 5 and 500 grams, with loads down to 1 gram available from the manufacturer. The indenter loading was restricted to be less than or equal to 10 grams in order for the diamond pyramid indentation depth to be less than one-tenth of the nominal TEM foil thickness of 25 μm. At this low indenter load, special care must be taken to ensure that background vibrations do not introduce errors into the measurement.[4] A simple anti-vibration test stand (shown schematically in Fig. 1) was developed which effectively isolated the microhardness tester from background vibrations down to indenter loadings of 2 grams. The 1000 kg lead brick base provides the test stand with a large inertia so that all except very low frequency vibrations are damped out. The air pad serves as a dashpot to effectively suppress most of the remaining vibrations. The other cushion materials were chosen on the basis of their different stiffness values. The use of varied materials was found to be effective in eliminating external vibrations. Also, the value of a multiple-interface design, which serves to reflect/dampen vibration waves, was found to be important. The anti-vibration stand was found to be very effective in suppressing background vibrations down to indenter loads of 2 grams as determined by various testing methods (hardness vs. load curves and reproducibility of low-load hardness results in the presence of various external vibrations).

TABLE 1

IRRADIATION DATA FOR TEM SAMPLES

Alloy	Initial Resistivity (Ω-m)	Grain Size (μm)	Maximum Fluence of TEM Disks (n/m^2)
cu	4.48 x 10^{-11}	13	1.9 x 10^{21}
Cu-5% Al	3.96 x 10^{-8}	23	2.1 x 10^{21}
Cu-5% Mn	1.08 x 10^{-7}	22	2.0 x 10^{21}
Cu-5% Ni	5.16 x 10^{-8}	12	2.2 x 10^{21}

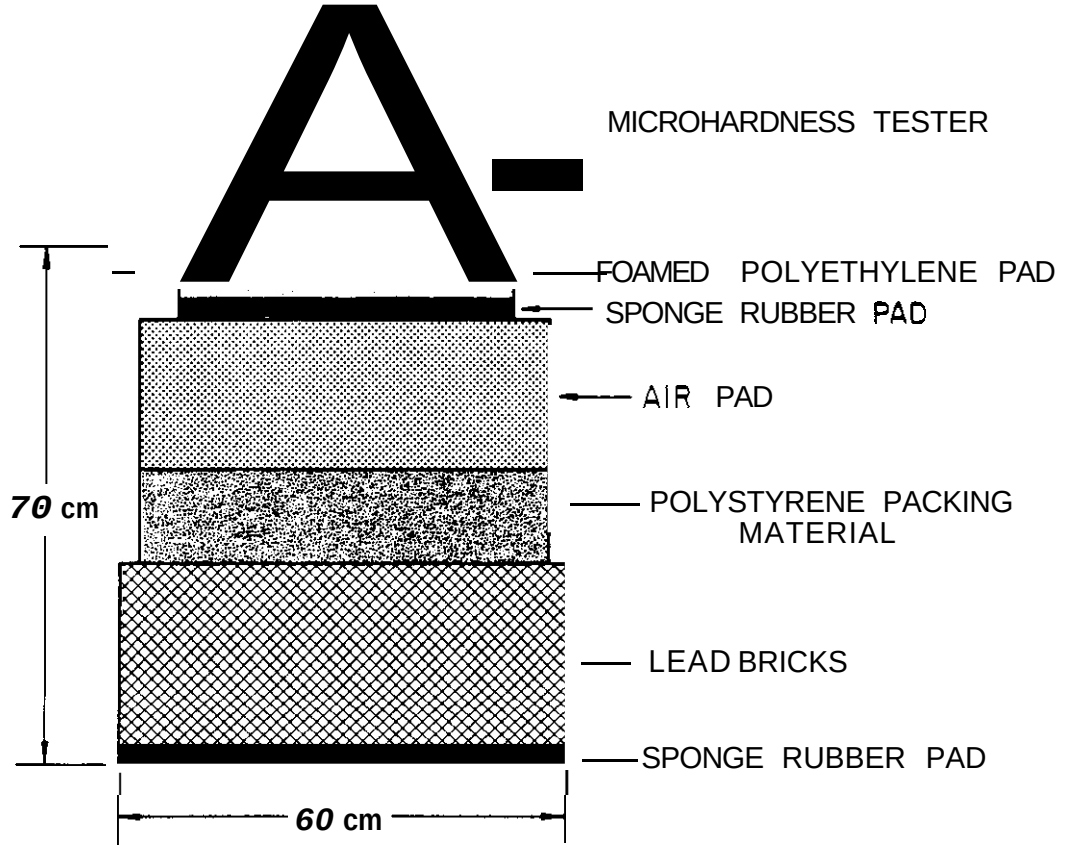

FIGURE 1. Schematic of anti-vibration test stand used to make microhardness measurements.

A standard sample preparation procedure was developed for all of the TEM disks prior to indentation. Each disk was given a light mechanical polish in a 0.3 μm alumina slurry on a rotating cloth wheel in order to remove the oxide layer and give a relatively smooth surface. The samples were then electropolished in a 33% HNO_3/67% CH_3OH solution cooled to -20°C at an applied potential of 5 V for 5 seconds. The purpose of the electropolish was to remove the work-hardened layer introduced by mechanical polishing, and also to give an optically smooth surface. The electropolish treatment removed 1-2 μm, which is expected to exceed the work-hardened surface layer in copper for the type of mechanical polishing which was utilized.[5]

A minimum of 60 indentations were made for each value of indenter load on four different TEM disks for each metal at every fluence level. All measurements were made by the same operator in order to minimize the effect of different observer's biases. The lengths of the diagonals of the indentation were measured at a magnification of 600X using a calibrated eyepiece accurate to ±0.2 μm. Both diagonals of the indentation were measured twice and the results averaged in order to minimize measurement errors. The length of the chisel tip of the Vickers diamond[4] used in this study was found to be less than 0.2 μm by SEM methods. Indentations were made around the periphery of the TEM disk so that the disk could still be used for electron microscope observations.

Several TEM disks were re-examined at different time periods and on different days of the week in order to determine the reproducibility of the results. Agreement on the Vickers microhardness (H_v) for a single disk was typically found to be within about 1 kg/mm^2 ($\lesssim$ 2% deviation). A larger variation was noticed between different TEM disks of the same metal irradiated to identical fluences -- typical standard deviations about the mean for a set of 4 disks (60 indentations) were 2-3 kg/mm^2.

TABLE 2

VICKERS MICROHARDNESS OF CONTROL SAMPLES

	Sample H_v (kg/mm^2)			
Indenter Load (g)	Copper	Cu-5% Al	Cu-5% Mn	Cu-5% Ni
5	71 ± 4	71 ± 3	70 ± 2	65 ± 2
10	57 ± 4	54 ± 1	53 ± 3	53 ± 3

5.3 Experimental Results

The Vickers microhardness numbers of the unirradiated samples at indenter loads of 5 g and 10 g are summarized in Table 2, along with the experimental standard deviation for each set of 4 disks which were examined. The 10 g microhardness values of the metals are all about 54 kg/mm^2. The result for copper is slightly higher than the alloy values. The 5 g microhardness numbers are all about 70 kg/mm^2 with the exception of a somewhat lower value for Cu-5% Ni. Therefore, it appears that addition of Al, Mn and Ni solutes does not have a significant effect on the low-load microhardness of copper, i.e. solute hardening is negligible.

Figure 2 shows the microhardness change at an indenter loading of 10 g as a function of fluence. Following a short incubation fluence, the data for all four metals scales linearly with the fourth root of 14-MeV neutron fluence. The duration of the incubation period is shorter for the alloys (in particular Cu-5% Mn) than for pure copper. As can be seen from Fig. 2, room temperature 14-MeV neutron irradiation to a fluence of 2×10^{21} n/m^2 induces significant hardening in these metals -- microhardness changes are on the order of 50% or more of the control value. The Cu-5% Mn alloy exhibited significantly larger radiation hardening as compared to the other metals at the fluence levels investigated. All four metals in Fig. 2 have roughly equal slopes in their curve of microhardness vs. fluence following the incubation period.

The pronounced load dependence of the microhardness induced by irradiation is illustrated for the four metals in Figs. 3 and 4. Figure 3 shows the Vickers microhardness as a function of the fourth root of neutron fluence at indenter loads of 5 g and 10 g, while Fig. 4 shows the change in Vickers microhardness vs. the fourth root of neutron fluence for the same indenter loads. The results at both loads are linear with $(\phi t)^{1/4}$ following an incubation fluence. The duration of the incubation fluence is slightly longer for the 5 g indenter load, and the slopes of the curves for the 5 g and 10 g loads are similar. The general differences between the alloys observed at a 10 g indenter loading are also present at a 5 g indenter loading -- Cu-5% Mn exhibits the largest radiation hardening and shortest incubation fluence of the metals investigated.

5.4 Discussion

5.4.1 10 g Data

The Vickers microhardness value of the control pure copper samples at a load of 10 g is in good agreement with the value obtained by Brager et al.[3] at an indenter load of 50 g. However, the hardness values for the alloy control samples (in particular Cu-5% Al and Cu-5% Mn) are significantly lower than their reported values. The cause of this discrepancy is uncertain, as the materials were obtained from the same lot and were given identical heat treatments. The difference in the results may be caused by the different indenter loads. Another possible source of the variance may be due to the heavily cold-worked condition of our alloys prior to annealing caused by cold-rolling the foils down from 250 um to 25 um. The pure copper grain size in the present study (Table 1) is about 13 μm, which may be compared to a grain size of 55 μm found by Brager et al.[6]

The large effect of microstructure on low-load Vickers microhardness is illustrated in Fig. 5. In this figure, the low-load microhardness of as-received copper is compared to results from the same foil after it had been annealed in air at 600°C for 1 hour. The annealed copper microhardness increases at low loads

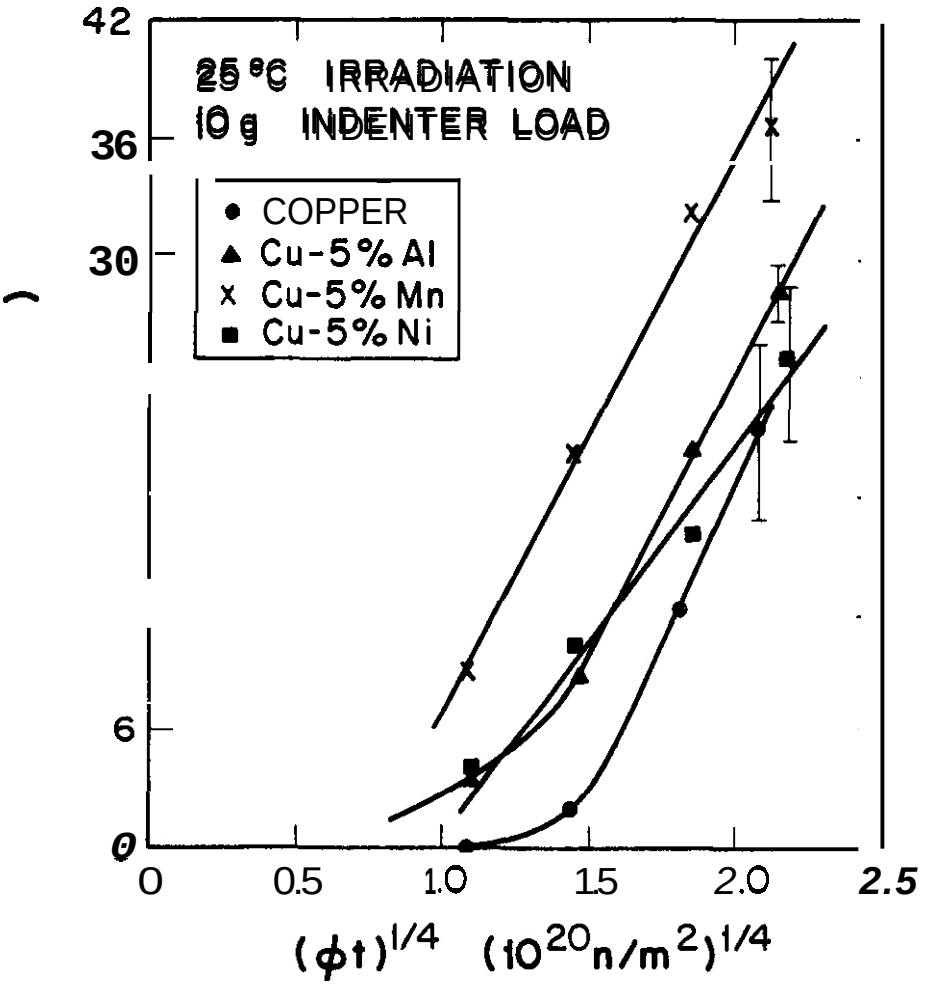

FIGURE 2. Radiation-induced Vickers microhardness change versus the fourth root of 14-MeV neutron fluence at an indenter load of 10 g.

(indicating a "hard surface")[7] while the as-received copper microhardness remains constant, then decreases rapidly with decreasing load ("soft surface" layer).[7] This hard/soft surface layer effect has been commonly observed in the past,[4,8] but the exact mechanism which causes this effect is the subject of much controversy.[7]

Figure 2 indicates that the change in microhardness appears to be linear with the fourth root of neutron fluence. The roughly equal slopes for all four metals in the curve of microhardness change vs. the fourth root of neutron fluence may be taken as an indication that there are equivalent damage production rates in these materials following the initial transition period. The shorter incubation periods of the alloys, compared to pure copper, may be caused by the solute atoms acting as trapping sites. This leads to a shorter nucleation period for dislocation loops.

The theoretical hardening due to dislocation loops can be represented by[9]

$$\Delta\tau = \frac{\mu b}{\beta \bar{\ell}} = \frac{\mu b}{\beta} \sqrt{\sum_k n_k d_k} \qquad (1)$$

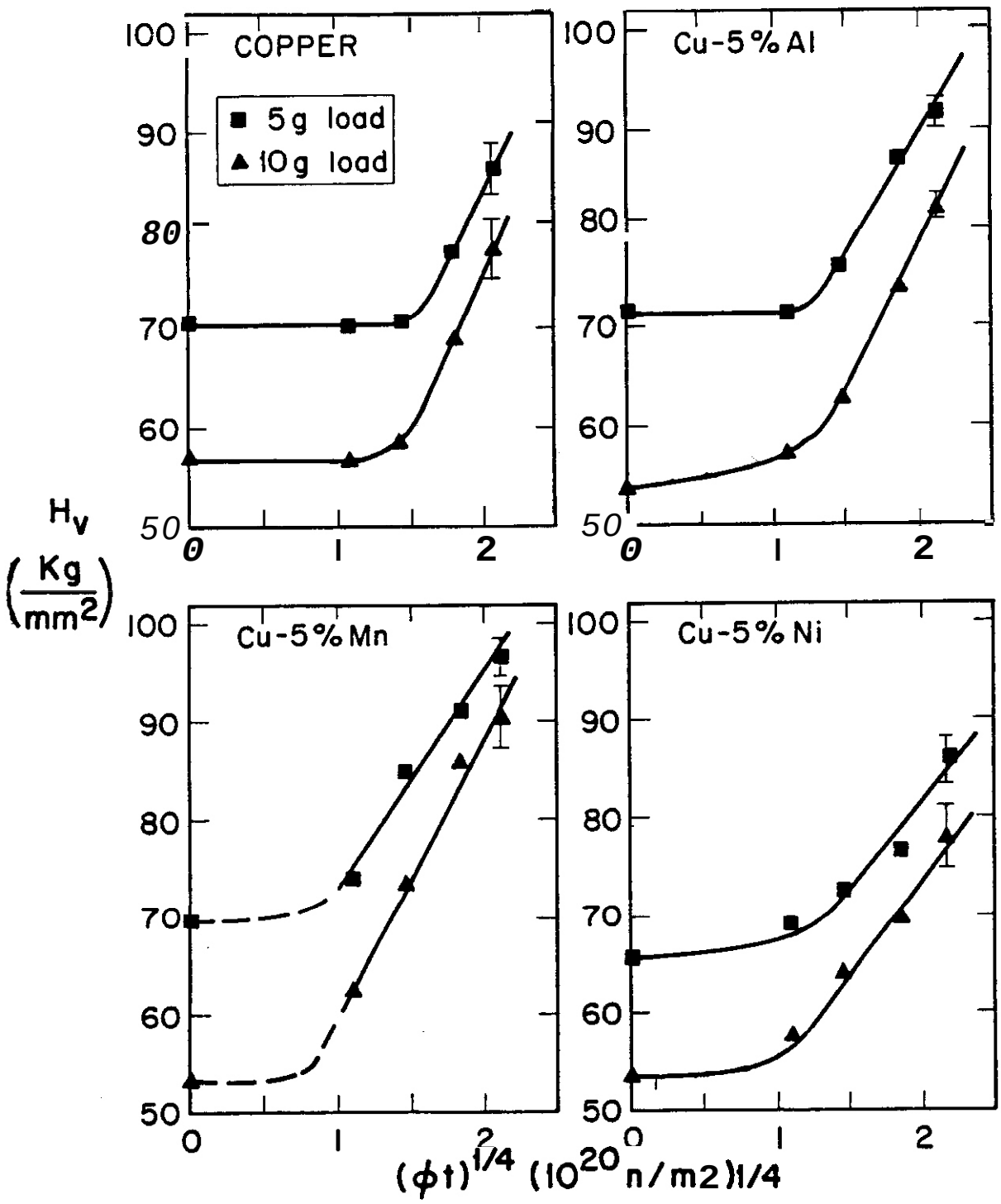

FIGURE 3. Vickers microhardness number versus the fourth root of 14-MeV neutron fluence at indenter loads of 5 g and 10 g.

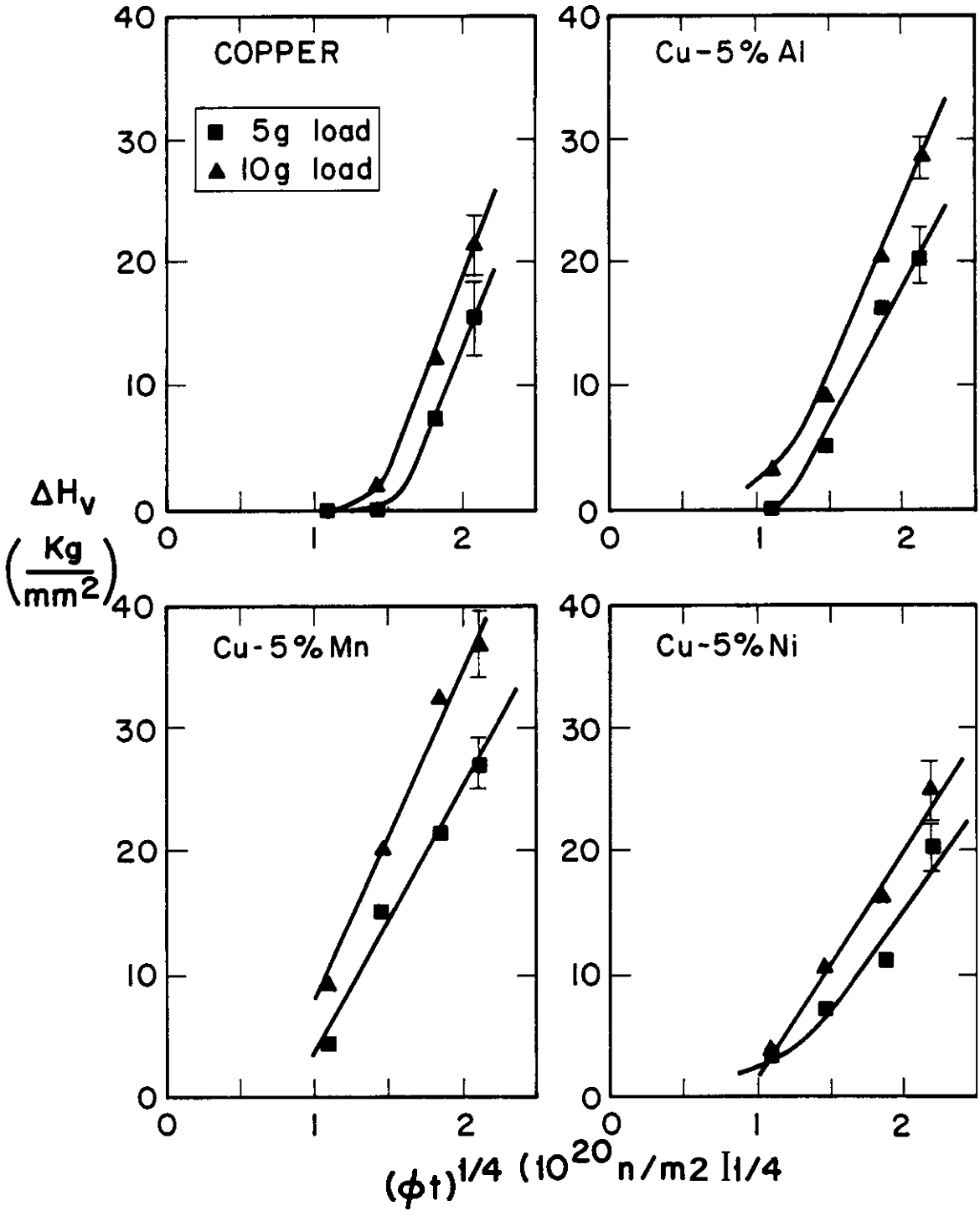

FIGURE 4. Radiation-induced Vickers microhardness change versus the fourth root of 14-MeV neutron fluence at indenter loads of 5 g and 10 g.

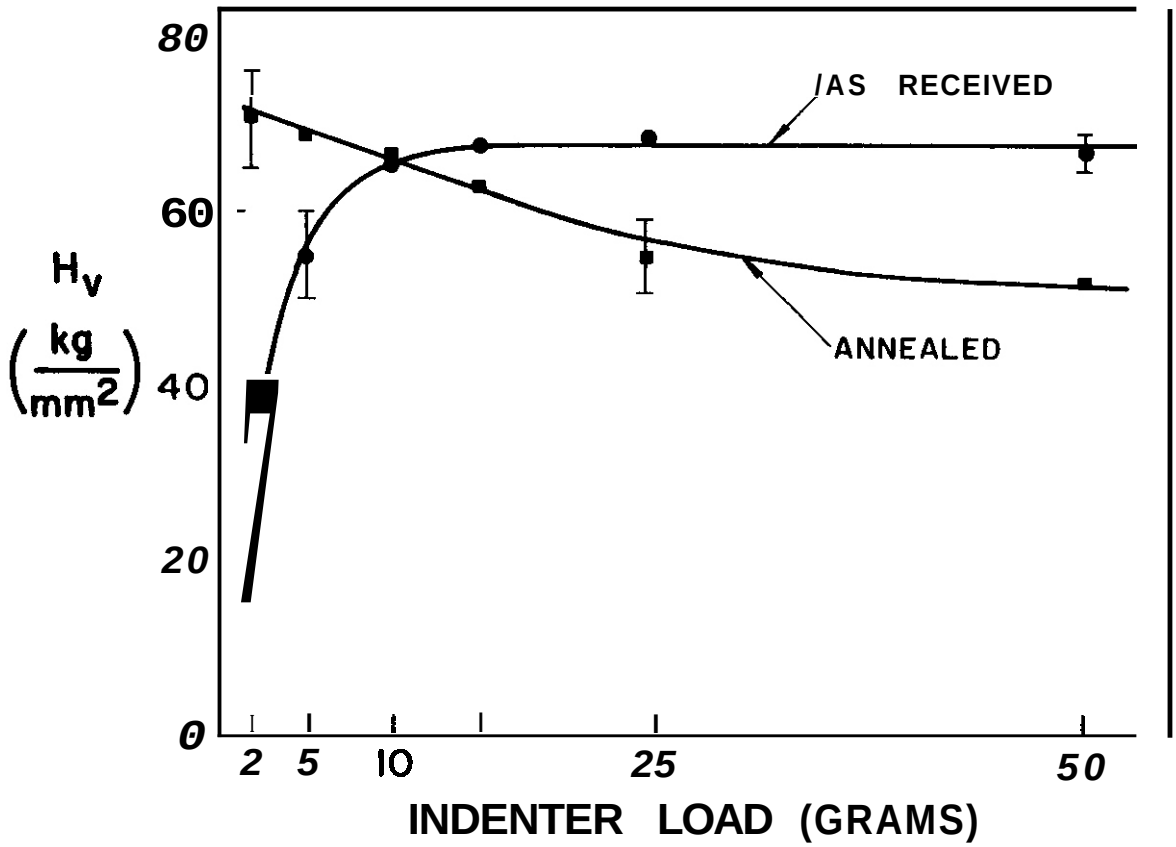

FIGURE 5. Vickers microhardness as a function indenter load for annealed and cold-worked copper.

where τ = shear stress and n is the loop density. Using the Von Mises criterion to relate yield strength to shear strength $\Delta\sigma_Y = \sqrt{3}\,\Delta\tau$, and assuming a correlation may be obtained between microhardness data and yield strength[6] (i.e., $\Delta\sigma_Y = K\,\Delta H_V$), indicates that the microhardness increase is proportional to $\sqrt{n}$. Since $\Delta H_V \sim (\phi t)^{1/4}$ this indicates that the loop density $n \sim \sqrt{\phi t}$. Analysis of the resistivity data obtained during the irradiation also predicts that the defect cluster density is proportional to the square root of 14-MeV neutron fluence.[2] In addition, good agrement between resistivity and 10 g microhardness estimates of the magnitude of the defect cluster density have been obtained.[2] The results of these calculations and the observed cluster density are compared in Table 3.

Previous experiments have found that the yield stress is proportional to the one-third power of the neutron fluence.[10] Unfortunately, there is insufficient high-fluence data in the present investigation to conclu-

TABLE 3

COMPARISON OF CALCULATED AND OBSERVED DEFECT CLUSTER DENSITIES IN COPPER AT A FLUENCE OF 3×10^{21} n/m^2 ASSUMING PERFECT DISLOCATION LOOPS (FROM REF. 2)

Type of Analysis	Method	Copper Type	Cluster Density (10^{22}/m^3)
Calculation	Resistivity	OAFS	11
Calculation	Microhardness	OAFS	12
Calculation	Tensile[1]	LLNL/Cominco	12
Observed	TEM[3]	OAFS	13

sively determine whether the present microhardness data scales as $(\phi t)^{1/4}$ or $(\phi t)^{1/3}$. The fact that the microhardness data was obtained at low loads may have an effect on the observed fluence dependence. However, the good agreement between the 5 g and 10 g results concerning the fluence dependence indicates that this is not the case. The agreement of the microhardness and resistivity data concerning the fluence dependence of the cluster density also lends credence to $\Delta H_v \sim (\phi t)^{1/4}$.

Tensile tests performed on samples irradiated with neutrons and ions show a similar dependence on fluence as the microhardness results reported here -- an incubation period which lasts until a fluence of about 2×10^{20} particles/cm^2 is followed by a monotonically increasing sample hardness. This behavior has been observed in tensile tests of a room temperature 14-MeV neutron irradiation of copper,[11] and for a 20°C irradiation of nickel by 16-MeV protons and 14-MeV neutrons.[12] A similar effect was also observed during microhardness measurements of molybdenum irradiated at 300°C with 10-MeV $^4He^+$ ions.[13]

Vickers microhardness data can be correlated to tensile data results found in the literature, $\Delta\sigma_Y(MPa) = K\ \Delta H_v(kg/mm^2)$.[14] A recent microhardness correlation[6] found the result K = 3.27 to be valid for 14-MeV neutron irradiated copper tested at an indenter loading of 50 g. As seen in Fig. 6, we have obtained a reasonable correlation between the pure copper tensile data of Mitchell et al.[11] and the 10 g microhardness data for three metals (Cu, Cu-5% Al, Cu-5% Ni) with K = 3.0. The Cu-5% Mn microhardness data does not correlate well with the pure copper tensile data using this value of K. The change in H_v at a load of 5 g during neutron irradiation is smaller than the observed change in H_v at a 10 g load for all 4 metals (Fig. 4). Therefore, the bulk microhardness change during irradiation should be greater than or equal to the 10 g hardness change, $\Delta H_v)_{bulk} \geq \Delta H_v)_{10g}$. It then follows that the result K = 3.0 should be taken as a maximum value for a correlation of bulk microhardness with tensile data. The small discrepancy (10%) in the value of the correlation constant K between the present investigation and previous work[6] may be due to a difference in initial microstructure, as discussed earlier.

In summary, it appears that the two main effects of low loads on the microhardness results of irradiated metals are: (1) a longer incubation fluence, which leads to (2) a smaller amount of radiation-induced microhardness change as compared to high-load results.

5.4.2 Implications of the Load Dependence of H_v

As is evident in Figs. 3 and 4, the choice of indenter loading at low loads can have a significant effect on the interpretation of microhardness results. At low loads, it becomes increasingly difficult to correlate observed behavior to bulk properties -- the microhardness values become very sensitive to the sample's microstructural condition. In this study the 5 g microhardness number was greater than the 10 g value at all fluences. Conversely, the change in microhardness at a 5 g load was less than the 10 g result for all fluences. The dependence of low-load microhardness on the microstructure of the irradiated samples is illustrated in Fig. 7. In this figure, it is seen that the difference between the microhardness numbers obtained at indenter loads of 5 g and 10 g decreases with increasing neutron fluence. As the neutron fluence increases, there is a higher density of small dislocation loops present which can affect the low-load H_v. Extrapolation of the observed results to higher fluence indicates that the values of H_v obtained at indenter loads of 5 g and 10 g may become equivalent for $\phi t \sim 1 \times 10^{22}$ n/m^2. For still higher fluences, it is possible that the value of H_v obtained at a load of 5 g could become smaller than the 10 g microhardness value. Therefore, it appears that low-load results may not be representative of bulk behavior since the bulk hardness (measured at high indenter loads) is known to be independent of indenter load.

Samuels and Mulhearn experimentally determined that the strain falls below 1% for a Vickers diamond indenter at a distance from the point of indentation of about 7 times the indenter depth. The indenter depths for the control samples in the present study were about 2.5 μm for an indenter loading of 10 g and about 1.6 μm for an indenter loading of 5 g. The corresponding "influence volume" (≥ 1% strain) of the indenter in this study therefore extends into the foil to a distance of about 18 μm for a load of 10 g and about 11 μm for a load of 5 g. Hence, the 5 g load is more indicative of the near-surface hardness of the foil and the 10 g load is relatively more representative of the bulk hardness. The approach of the 5 g and 10 g microhardness numbers to a common value with increasing neutron fluence may be taken as an indication that the defect clusters created during irradiation tend to decrease the value of the near-surface hardness. There is no

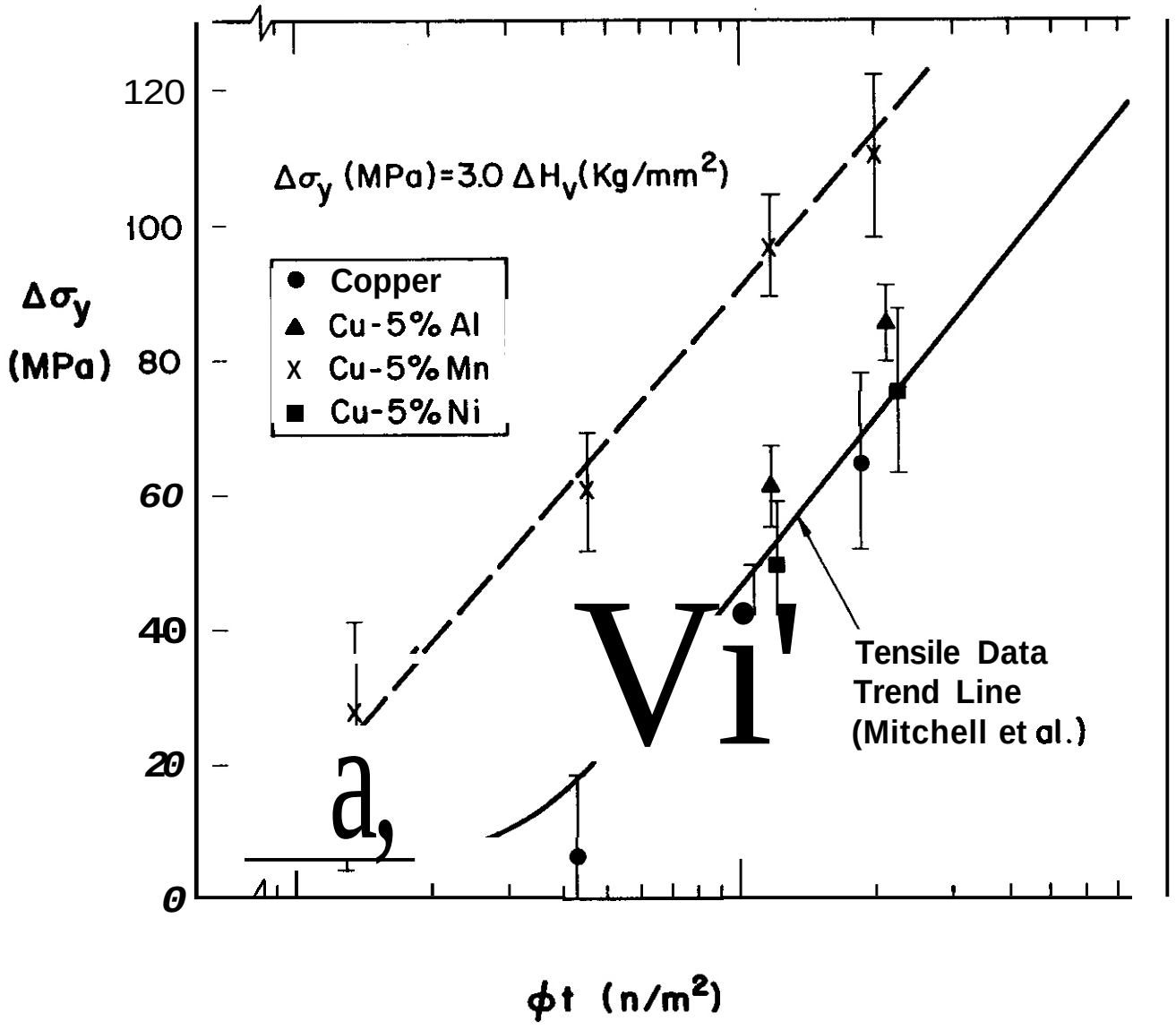

FIGURE 6. Correlation between tensile data and Vickers microhardness change as a function of 14-MeV neutron fluence. Microhardness measurements made at an indenter load of 10 g.

known theory which adequately explains the near-surface microhardness phenomenon. It appears reasonable to assume that the observed microhardness should be given by

$$H_v)_{observed} = H_v)_{bulk} + \Delta H_v)_{surface} \cdot \quad (2)$$

The bulk term increases monotonically with irradiation and at large fluences dominates the observed microhardness value. The near surface term, $\Delta H_v)_{surface}$, should depend strongly on the sample's microstructure (dislocation density) and also on the depth (x) from the surface. The surface term should become important only for indentation depths which are near the foil surface. It may be postulated that this term should be

$$\Delta H_v)_{surface} \sim \frac{1}{x^m} * f \text{ (microstructure)} \quad . \quad (3)$$

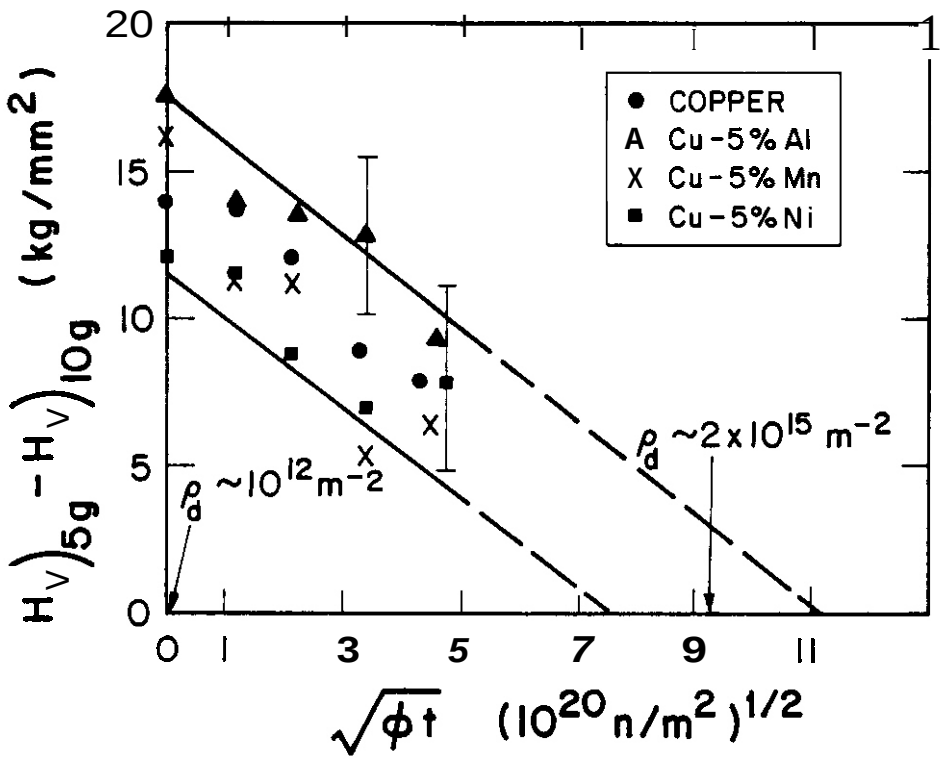

FIGURE 7. Difference in microhardness nunber measured at 5 g and 10 g versus the square root of 14-MeV neutron fluence. The abcissa is proportional to the defect cluster density (see text).

At large loads (large impression depths) the surface term becomes negligible and the microhardness approaches a constant value. At small loads, the surface term should become dominant and the measured hardness in single crystals may increase up to values comparable to the metal's theoretical shear strength. Gane[15] measured the hardness of gold under a load of about 0.1 mg and found a significant surface hardening ($\tau \sim \mu/100$, where μ = shear modulus). This value is a factor of twenty larger than the measured bulk hardness and corresponds to a shear strength[15] of $\tau \sim \mu/20$.

The microstructure factor (f) in the surface term may be positive or negative depending on the microstructure and condition of the foil surface. A negative value of f would indicate a "soft surface", whereas a positive value would indicate a "hard surface" layer. The exact cause of the hard vs. soft surface layer is unknown and is the subject of much controversy. Both work-hardened and work-softened surface layers have been experimentally observed.[7,16] it appears that in general, annealed materials exhibit readily work-hardened surface layers, while heavily cold-worked materials have soft surface layers. One known exception to this behavior was reported by Gane and Cox.[17] They found that the microhardness of gold increased at low loads for both annealed and cold-worked samples.

Application of Eqs. 2 and 3 to microhardness vs. load curves of various materials in annealed and cold-worked states gave values of the exponent m ranging from 1/2 to 7. The larger values of m were found for the cold-worked materials (with a negative microstructure factor, f). This indicates a very short-range influence of the surface term for cold-worked metals. Upit and Varchenya[8] have reported that the total observed hardness near the surface is well approximated by $H)_{observed} = c_1 X^n$. A cursory analysis of their results indicates that, by subtracting away the bulk hardness value, the surface hardness is well represented by Eq. 3. The dependence on depth of their reported results is then given by m ~ 1-2.

One possible explanation of the hard vs. soft surface phenomenon would be to consider the effect of surfaces and cold-work level on dislocation sources and dislocation multiplication. Near-surface sources began operating at lower stresses than bulk dislocation sources in a material with an initially low dislocation density.[7] If the dislocations that are produced do not readily glide out to the surface, then the near surface region will become preferentially work-hardened (Kramer's "debris layer" model).[7] On the other hand, cold-worked materials already have an ample amount of Frank-Read dislocation sources. The high dislocation density (with resulting back stresses) may tend to minimize the preferential activation of near-surface dislocation sources compared to interior sources. Near-surface dislocations would tend to move to the free surface due to repulsive interactions with interior dislocations, where they are annihilated. This results in a lower dislocation density in the near-surface region upon deformation for cold-worked metals. Figure 7 may be seen as an indication that the surface becomes softer relative to the bulk with increasing dislocation density (in this case, dislocation loops). The 5 g (surface) hardness increases less rapidly than the 10 g (bulk) hardness with increasing neutron fluence. The abscissa is plotted as the square root of neutron fluence, which is proportional to the dislocation loop density (see earlier discussion). Extrapolating to higher fluences, it is seen that the 5 g and 10 g hardness values become equivalent for a fluence of $\sim 1 \times 10^{22}$ n/m^2. This fluence corresponds to a total dislocation line density of about 2×10^{15}/m^2. This density was calculated from TEM data[3] using an average loop diameter of 2.5 nm and assuming $n = \sqrt{\phi t}$. It is seen that the calculated dislocation density extrapolated to where there is no surface hardening is typical of values for a cold-worked metal.

From the above discussion it appears that it is impossible to correlate low-load microhardness results to bulk behavior unless measurements are obtained at several different values of indenter load. With several properly chosen load values, it may be possible to ascertain the magnitude of the near-surface microhardness term and thereby determine the bulk contribution to the observed microhardness.

5.5 Conclusions

The fluence incubation period and the magnitude of the radiation-induced microhardness change at low indenter loads are in modest disagreement with bulk microhardness results. The incubation period of the radiation-induced microhardness change at 5 g loads is longer than it is at 10 g loads. This leads to a smaller irradiation-induced change in H_v at low loads compared to the change in the H_v at higher loads. Low-load microhardness results are strongly influenced by the material's microstructure.

The general fluence dependence of low-load microhardness ($\Delta H_v - (\phi t)^{1/4}$) appears to be in fair agreement with bulk results. This conclusion is based on the observation that the 5 g and 10 g load results show a similar fluence dependence following the incubation period.

Unirradiated copper alloys behave similar to pure copper with regard to low-load microhardness (i.e., no significant solute hardening). Conversely, alloying has a significant effect on the low-load microhardness of irradiated copper samples. The alloys have a shorter incubation fluence than pure copper. This is probably due to solute atoms affecting the nucleation of irradiation-produced dislocation loops. The Cu-5% Mn alloy exhibited a significantly shorter incubation fluence, and hence shows a larger radiation hardening at a given fluence compared to the other metals.

A reasonable correlation has been obtained between the 10 g microhardness data and tensile results. We have found $\Delta\sigma_Y$(MPa) = K ΔH_v(kg/mm^2) gives a good correlation with K = 3.0. The slight discrepancy with another correlation found in the literature[6] (K = 3.27) is believed to be primarily due to different initial microstructures.

The general phenomenon of an increase in microhardness at low loads appears to be related to an intrinsic materials property which depends on the sample's microstructure. It is believed that the commonly observed increase in hardness near the surface is not an experimental artifact, but rather is an indication that annealed metals are more susceptible to work-hardening in the near-surface region as compared to the bulk.

6.0 References

1. R.W. Knoll, "A Literature Review of Radiation Damage Data in Cooper" UWFDM-384, University of Wisconsin Fusion Engineering Program Report (Oct. 19801.

2. S.J. Zinkle and G.L. Kulcinski, "14-MeV Neutron Irradiation of Copper Alloys," 3rd Topical Meeting on Fusion Reactor Materials, Albuquerque, NM, Sept. 19-22, 1983. Proceedings to be published in J. Nucl. Matl.

3. H.R. Brager, F.A. Garner and N.F. Panayotou, J. Nucl. Matl., 103 & 104, 995 (1981).

4. B.W. Mott, Micro-Indentation Hardness Testing, Butterworths Scientific Publications, London (1956).

5. K.C. Thompson-Russell and J.W. Edington, Practical Electron Microscopy in Materials Science, Monographs, Phillips Technical Library (1977) p. 2.

6. N.F. Panayotou, J. Nucl. Matl., 108 & 109, 456 (19821.

7. Surface Effects in Crystal Plasticity, R.M. Latanision and J.T. Fourie (Eds.) NATO Advanced Study Institute Series, Noordhoff, Reading, MA (19771.

8. The Science of Hardness Testing and Its Research Applications, J.H. Westbrook and H. Conrad (Eds.), ASTM Symposium Oct. 18-20, 1971, Detroit (Materials Engineering Congress).

9. N.M. Ghoniem et al., in Proc. of 11th International Symposium on Effects of Radiation on Materials, ASTM STP 782, Scottsdale, AZ, (June 27-29, 19821 p. 1054.

10. T.J. Koppenaal and R.J. Arsenault, Metallurgical Reviews, 16, 175 (19711.

11. J.B. Mitchell et al., in Radiation Effects and Tritium Technology for Fusion Reactors, J.S. Watson and F.W. Wiffen (Eds.), Gatlinburg, TN, (Oct. 1-3, 19751 Vol. II, p. 172.

12. R.H. Jones et al., in Effects of Radiation on Structural Materials, ASTM STP 683, J.A. Sprague and D. Kramer, Eds., (1979), p. 346.

13. K. Abe et al., J. Nucl. Matl., 103 & 104, 1169 (1981).

14. L.E. Samuels and T.O. Mulhearn, J. Mech. Phys. Solids, 5, 125 (1957).

15. N. Gane, Proc. Royal Soc. (London), 317, 367 (19701.

16. A. Misra and I. Finnie, Wear, 65, 359 (1981).

17. N. Gane and J.M. Cox, Phil. Mag., 22, 881 (19701.

7.0 Future Work

The Vickers microhardness of selected TEM disks of copperfcopper alloys obtained from HEDL will be measured using the University of Wisconsin test assembly. Results will be compared to previous HEDL measurements to verify the compatibility of the two testing procedures.

8.0 Publications

S.J. Zinkle and G.L. Kulcinski, "14-MeV Neutron Radiation-Induced Microhardness Changes in Copper Alloys," Symposium on the Use of Nonstandard Subsized Specimens for Irradiated Testing, Albuquerque, NM, Sept. 23, 1983. Proceedings to be published by ASTM.

9.0 Acknowledgments

This work performed under appointment to the Magnetic Fusion Energy Technology Fellowship Program and with funds supplied by the Office of Fusion Energy, Department of Energy.

CHAPTER 3

REDUCED ACTIVATION MATERIALS

A COMPARISON OF ACTIVATION IN STARFIRE AND MARS FIRST WALLS

H. L. Heinisch and F. M. Mann (Hanford Engineering Development Laboratory)

1.0 Objective

The objective of this work is to determine the activation of the constituents of potential fusion materials in order to provide guidelines for the development of low-activation materialc.

2.0

Activation calculations were performed for elements in the MARS and STARFIRE first-wall positions. The seven elements considered (N, Al, Ni, Mo, Cu, Nb, Pb) are those which were found from earlier STARFIPE calculations to require restrictions in order to meet NRC disposal reoulations. The importance of the neutron spectrum is demonstrated by a comparison of MARS and STARFIRE results. In the harder spectrum of the MARS first-wall the same seven elements face restrictions, but for Ni, Mo and Nb the allowable limits are two to five times larger than in STARFIRE.

3.0

Title: Irradiation Effects Analysis (AKJ)
Principal Investigator: D. G. Doran
Affiliation: Hanford Engineering Development Laboratory

4.0 Relevant DAFS Program Plan Task/Subtask

No relevant task.

5.0 Accomplishments and Status

Interest in reduced activation materials for fusion reactors has led to calculations such as those in Reference 1. In that work, activation calculations were performed for 27 elements in the neutron flux of the STARFIRE first wall, and the results were examined in comparison to the NRC reoulations for near-surface land disposal.

The STARFIRE desiqn was chosen for the earlier study because it is conceived as a typical commercial fusion reactor. The present work was undertaken to find out how much the conclusions of the earlier work mioht be changed by using a different reactor design. In the STARFIRE calculations, seven elements were identified as facing restrictions on their concentrations in first-wall materials in order to meet NRC regulations. In the present study the activation of these seven elements, N, Al, Ni, Cu, Nb, Mo and Pb, wore calculated in the first-wall spectrum of the MARS reactor and compared with the STARFIRE calculations. The STARFIRE Tokamak has a water-cooled $LiAlO_3$ blanket, resulting in a neutron spectrum at the first-wall havino a 1/v low energy tail. The MARS mirror machine design has a PbLi blanket, which also acts as coolant. As a result, the MARS first-wall spectrum has comparatively few neutrons below 10 keV. The MARS and STARFIRE first-wall spectra are compared in Figure 1.

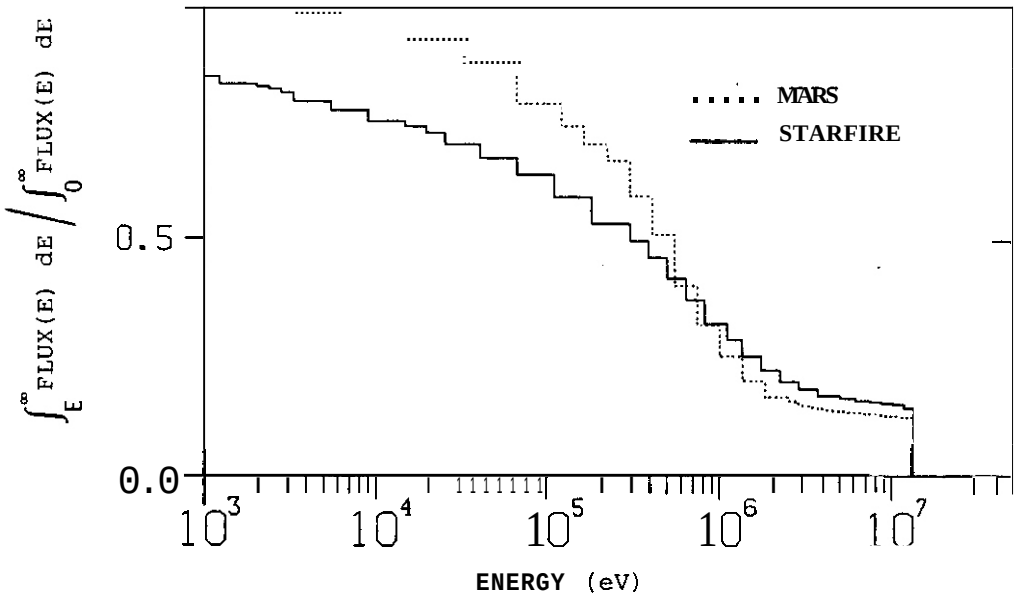

FIGURE 1. Fraction of Flux for Energy Greater than E for MARS and STARFIRE Conceptual Fusion Reactors

The MARS calculations were done with the REAC code system[2] used for the earlier STARFIRE calculationz. In both cases the irradiation was to a first-wall dose of 10 MWY/m^2, followed bv a coolino time of 3×10^3 days (~8.2 years). STARFIRE has a first-wall loading of 3.6 MW/m^2 and a neutron flux of 1.8×10^{15} n/cm^2. MARS has a wall loading of 4.3 MW/m^2 and a flux of 7.74×10^{15} n/cm^2. Thus, MARS requires less time than STARFIRE to reach 10 MWY/m^2, but this time difference has little effect on the production of long-lived nuclides. The spectral differences are much more important.

Table 1 compares decay rates of activation products from STARFIRE and MARS first walls per 10 MWY/m^2, after 3×10^3 days. A star identifies the isotope for each element which is responsible for the fractional limit of that element in first-wall materials, as determined in the STARFIRE study. In several of the elements the production of these critical isotopes differed substantially in MARS and STARFIRE. In Ni the ^{63}Ni production is a factor of 5 less in MARS, in Nb the ^{94}Nb production is a factor of 3 less in MARS, and in Mo the ^{93}Mo production is about half as much in MARS. In Cu, Al and Pb the differences between MARS and STARFIRE are slight. For N there is a 30% reduction in ^{14}C production in MARS.

The production of the critical isotopes in Ni, Nb and Mo is stronqly dependent on neutron capture (n,γ) reactions. Neutron capture cross Sections generally have strong responses in the lower neutron energy range, which accounts for the spectral sensitivity observed here.

The results for MARS do not change the primary conclusions arrived at in the STARFIRE calculations. The seven elements N, Al, Ni, Cu, Nb, Mo, and Pb face restrictions in order to meet NRC requlations for either of the conceptual fusion reactors. The particular radioactive isotopes of each element which necessitate the restrictions are the same for both reactors. The important differences are in the magnitudes of the production of the critical isotopes in these two reactors.

Table 2 summarizes the differences in restrictions imposed by the NRC requlation 10 CFR 61 for Class C disposal for the STARFIRE and MARS first walls. Only the elements with siqnificantlv different maximum allowable concentrations in the two reactors are listed. The higher limit on Ni in MARS implies that a wider range of low Ni alloys (e.g., ferritics and manganese steels) are available for that reactor desiqn. The higher limits on Mo and Nb ease restrictions on impurity content, hence lowerinp the cost of allov production. These differences in first wall alloy requirements are due primarily to the choice of a PbLi blanket over the water-cooled solid breeder.

Neutron spectral differences will be very important in the blanket region itself. Limits on alloy compositions imposed by reduced activation considerations will depend on the neutron spectrum seen by each reactor component. Activation calculations must take these spectral differences into account.

TABLE 1

ACTIVATION AI STARFIRE AND MARS FIRST WALL?

PER 10 MWyr/m^2 AFTER 3000 DAY (8.2 YEAR) COOLING

Element	Product Isotope	Decay Rate (Ci/cm^3) STARFIRE	MARS	Ratio MARS/STARFIRE
N	^{3}H	0.76	0.79	1.05
	* ^{14}C	2.45 x 10^{-2}	1.71 x 10^{-2}	0.70
A1	^{3}H	3.50 x 10^{-3}	3.81 x 10^{-3}	1.09
	* ^{26}Al	3.17 x 10^{-5}	3.41 x 10^{-5}	1.07
Ni	^{55}Fe	5.96	6.51	1.ns
	^{60}Co	2.60	?.71	I.*ni*
	^{57}Co	0.14	0.17	1.71
	* ^{63}Ni	n.77	0.16	0.21
	^{3}H	0.14	0.16	1.08
	^{59}Ni	7.67 x 10^{-3}	2.49 x 10^{-3}	0.33
Cu	^{60}Co	2.09	2.24	1.07
	^{3}ti	1.68	1.81	1.08
	* ^{63}Ni	0.55	0.55	1.on
Nb	^{3}H	0.58	0.62	1.on
	* ^{94}Nb	7.11 x 10^{-2}	7.61 x 10^{-2}	n.37
	^{93}Zr	2.22 x 10^{-5}	7.30 x 10^{-5}	1.os
	^{92}Nb	1.91 x 10^{-5}	2.01 x 10^{-5}	1.06
Mo	^{3}H	6.58 x 10^{-2}	6.92 x 10^{-2}	1.05
	^{93}Nbm	6.67 x 10^{-2}	6.34 x 10^{-2}	0.95
	* ^{93}Mo	6.01 x 10^{-2}	3.42 x 10^{-2}	0.57
	^{99}Tc	1.52 x 10^{-3}	8.27 x 10^{-4}	0.54
	^{94}Nb	4.00 x 10^{-4}	4.51 x 10^{-4}	1.13
	^{93}Zr	3.52 x 10^{-6}	3.43 x 10^{-6}	0.97
	^{90}Sr	3.24 x 10^{-7}	6.39 x 10^{-7}	1.07
	^{92}Nb	3.55 x 10^{-7}	3.75 x 10^{-7}	1.06
Pb	^{204}Tl	1.23 x 10^{-3}	1.37 x 10^{-3}	1.11
	^{3}H	7.11 x 10^{-4}	7.70 x 10^{-4}	1.08
	* ^{205}Pb	1.64 x 10^{-5}	1.72 x 10^{-5}	1.05

*isotope responsible for the fractional limit of the element in the STARFIRE first wall.

TABLE 2

ESTIMATED MAXIMUM ALLOWABLE ATOMIC CONCENTRATIONS PFR 10 MWyr/m^2, BASED ON NRC REGULATION 10 CFR 61 CLASS C DISPOSAL

Element	STARFIRE	MARS
Ni	0.9%	4.3%
Nb	2.9 ppm	7.8 ppm
Mo	30.0 ppm	53.0 ppm

6.0 References

1. F. M. Mann and W. E. Kennedy, Jr., Damage Analysis and Fundamental Studies Quarterly Prowess Report, June 1983, DOE/ER-0046/14 (1983) p. 63.

2. F. M. Mann, HEDL-TME 81-37, Hanford Engineering Development Laboratory, Richland, WA, August 1982.

7.0 Future Work

Activation calculations will be performed in the blanket regions of MARS and STARFIRE.

8.0 Publications

A paper entitled "Reduced Activation Calculations for the STARFIRE First Wall," by F. M. Mann, has been submitted for publication in the Journal of Nuclear Technology/Fusion.

CHAPTER 4

FUNDAMENTAL MECHANICAL BEHAVIOR

THE MICROMECHANICAL MECHANISMS OF CLEAVAGE FRACTURE IN MARTENSITIC STAINLESS STEELS

G.R. Odette, G.E. Lucas, R. Maiti, and J.W. Sheckherd (University of California, Santa Barbara)

1.0 Objective

The purpose of this study was to investigate the validity of the Ritchie-Knott-Rice (RKR) model for brittle cleavage failure in a specific heat of HT-9. Such a model can he useful in directing alloy development efforts in the ferritic alloy system.

2.0 *Summary*

Coupled measurements of tensile and blunt and sharp notch fracture properties were made on a prototypical heat of HT-9, which is a 12% Cr martensitic stainless steel. Based on these data, it was found that cleavage fracture is controlled by a critical stress-critical distance criteria. The microcleavage fracture stress is *2400* MPa, consistent with the observed martensite lath packet size; and the critical distance is ∿ 50 μm which is consistent with observed prior austenite grain size.

3.0

Title: Damage Analysis and Fundamental Studies for Fusion Reactor Materials Development
Principle Investigators: G.R. Odette and G.E. Lucas
Affiliation: University of California, Santa Barbara

4.0 Relevant DAFS Program Plan Task/Subtask

Subtask B Mechanical Properties

5.0 Accomplishments and Status

5.1 Introduction

Martensitic stainless steels are known to be resistant to many forms of radiation damage such as swelling[1]. However. they can be subject to irradiation embrittlement as measured by upward shifts in the transition temperature (T_o) delineating the brittle cleavage from ductile microvoid coalescence fracture mode[2]. In previous papers we suggested that it may be possible to operate safely thin fusi n structures in the lower-shelf temperature regime based on the size dependence of fracture loads and modes[3] and the possibility that radiation will not decrease lower-shelf toughness (K_{Ic}) significantly[4].

In part, this conclusion is derived from an assumption that cleavage fracture in this alloy class occurs when the applied tensile stress (a_n) exceeds a critical microcleavage stress (σ_f^*) over a critical distance (ℓ^*), after the work of Ritchie, Knott, and Rice (RKR)[5]. Such behavior has been observed in a number of carbon and low-alloy steels[6]. However, it has not been demonstrated previously for the 9–12% Cr fusion candidate alloys (e.g., HT-9).

For sharp cracks and in the small-scale yielding limit, σ_n is proportional to the yield stress (σ_o) which is temperature (T) and strain-rate ($\dot{\varepsilon}$) sensitive. The magnitude of σ_n varies with distance from the crack front increasing to a maximum of ~ 3-5 times the yield stress; the value depends on the strain hardening exponent?, where the flow stress $\sigma \propto \varepsilon^n$. The position (x) of a particular level of stress varies as $x(\sigma) = R(\sigma)K^2/\sigma^2$ where K is the applied stress intensity and R the dimensionless stress field distribution function. The critical stress intensity K_{Ic} is obtained when $x(\sigma = \sigma_f^*) = \ell^* = R(\sigma_f^*) K_{Ic}^2/\sigma_o^2$.

The material properties ℓ^* and σ_f^* are expected to be relatively insensitive to parameters such as temperature, strain rate, and fine scale matrix microstructure induced by radiation. In this case, $K_{Ic}^{\ell} \propto \sigma_f^{*1.5}\sqrt{\ell^*}$; that is, K_{Ic}^{ℓ} is not a strong function of σ_o, which is influenced by the matrix microstructure, hence irradiation. However, it should be noted that while K_{Ic}^{ℓ} is not sensitive to σ_o, the transition temperature T_d scales roughly as $\Delta T_d \sim C\Delta\sigma_o$.

The purpose of this work was to test the validity of the critical stress-critical distance model in martensitic stainless steels by measuring the yield and fracture properties $\sigma_o(\dot{\varepsilon},T)$, σ_f^* and K_{Ic}, which can in turn be used to estimate ℓ^*. In addition, we have attempted to evaluate the relations between σ_f^* and ℓ^* and the pertinent microstructural characteristics of this alloy class.

5.2 Experimental Details

The Magnetic Fusion Energy (MFE) Alloy Development for Irradiation Performance (ADIP) Electroslag Remelted (ESR) program heat of HT-9 was used in this study[7]. The steel was received in the form of ~ 25 mm hot rolled plate with a nominal composition:

C	Mn	Si	Ni	Cr	Mo	V	Cu	Fe
.23	.39	.23	.46	12.3	.99	.45	.07	bal

The final heat treatment schedule was as follows: solution anneal at 1300°C for 1800s, air cool; temper at 750°C for 3600s, air cool. Figure 1 is an optical micrograph of the microstructure showing both prior austenite grain boundaries ($\bar{d}_a$ ~ 25 μm) and subgrain martensite lath packets ($\bar{d}_m$ ~ 7 μm). In addition, transmission electron microscopy examinations showed martensite and precipitate structures typical of this alloy class[8]. We also noted that the grain boundaries were heavily precipitated.

Mechanical property specimens were all cut from the plate with a transverse orientation. Round tensile specimens 3.2 mm in diameter with a 25.4 mm gage length were tested at strain rates of 10^{-3} and 3 s^{-1} and at temperatures from 172°K to 339°K in an MTS 810 load frame. Test data were analyzed to provide yield (ε_o = .002), ultimate tensile stress, and work hardening data.

Both standard and subsized Charpy-V-notch specimens were tested over a similar temperature range on an instrumented pendulum and drop tower-, respectively, using procedures established by the Electric Power Research Institute[4]. Estimated notch stain rates varied from 100 to 300 s^{-1}. All dimensions of the subsized Charpy (SCVN) specimens were 1/3 that of standard specimens. Load-time and velocimeter measurements were used to determine test parameters such as general yield (P_{gy}) and maximum (P_m) loads and total energy absorbtion.

Blunt notch bend bars with the following dimensions were tested in four-point bending at temperatures 77°K to 298°K and effective notch tip strain rates of $10^{-4}s^{-1}$ and $50s^{-1}$: load span 63.5 mm; support span 38.1 mm, thickness 12.7 mm; width 12.7 mm; notch depth 4.23 mm, notch angle 45°. These are often referred to as G-0 bars after a detailed finite element analysis of that geometry by Griffiths and Owen[10]. This analysis provides the ratio of the maximum principal to yield stress far a range of maximum to general yield loads and permits evaluation of σ_f^*. Cleavage failures, and hence valid GO tests, were only obtained at the higher strain rate at temperatures less than 172°K.

---

*The dynamic facility used is located at Fracture Control Corporation of Goleta, CA, and their assistance is gratefully acknowledged.

Both .4T (10 mm) and 1T (25 mm) fatigue precracked bend bars were tested at notch strain rates of $\dot{e} \sim 10^{-2}$ to 10^{-1} s^{-1} at temperatures from 140°K to 213°K according to ASTM E 399 procedures to measure static toughness[11].

Examination of fracture surfaces of the various specimens was carried out using an ETEC scanning electron microscope (SEM).

5.3 Results and Analysis

Figure 2 shows yield stress data versus a strain rate temperature parameter $P_{\dot{\varepsilon},T} = T(°K)\ \log 10^{8}/\dot{\varepsilon}(s^{-1})$ for temperatures less than ~ 260°K, which is the regime of interest. The dynamic yield stress data are from CVN P_{gy} measurements[12]. However, data points near T_{d}, which are subject to both large scatter and systematic deviations are not included. The linear correlation for a_o observed in Figure 2 was used in the subsequent analysis. Ultimate tensile strengths (σ_u) were found to be $\sigma_u \sim 1.2\ \sigma_y$ for the static tests with a slight decrease in the ratio at dynamic strain rates. Work-hardening exponents (n) were observed to be $n \sim .13$.

The CVN energy absorbtion data had a 41J (30ft-lb) index temperature of ~ 300°K with the knee starting at ~ 200 °K. Linear elastic blunt notch toughness" [K_{Ic} (ρ = .25 mm)] values were found to be ~ 94 and 88 MPa $\sqrt{m}$ at -200 and -173°K, respectively. A rapid upswing to elastic plastic fracture was observed at higher temperatures [K_{Jm} (ρ = .25 mm) ~ 120 to 330 MPa $\sqrt{m}$ for T = 210 to 300°K] roughly paralleling the CVN total absorbed energy upswing. The normalized (E/b^2B) energy absorbtion of SCVN and CVN specimens had similar shapes, but the SCVN was shifted to slightly lower temperatures in the transition regime (~ 10-15°K).

Maximum load data from the GO bar testing and the yield stress correlation were used to directly compute σ_f^*, and the results are shown in Figure 3. The magnitude of σ_f^* can also be estimated from CVN P_{gy}^* and P_m data; with $\sigma_f^* = M_{CVN}\ P_{gy}^*$ at $P_m = P_{gy}^*$ or $P_m = .8\ P_{gy}^*$, where M_{CVN} = 73.1, 84.1 MPa/N depending on the notch field analysis and yield criteria (i.e., Von Mises or Tresca)[14]. Values of σ_f^* determined from CVN data are also shown in Figure 3. The linear elastic blunt notch toughness values from the Charpy data can also be used to estimate σ_f^* using an expression proposed by Wullaert, Ireland and Tetelman[15]. The results are also shown in Figure 3.

The SCVN P_{gy}, P_m data can be also used to estimate σ_f^*. However, this required adjusting for the lower general yield and maximum load-stress relations found for the SCVN compared to the CVN. An empirical correction factor of ~ 1.3 was found based on the observed general yield loads compared to those calculated from the yield stress correlation. Using this value and $M_{SCVN} \simeq 9M_{CVN}$, σ_f^* estimates from the SCVN tests were made and these are also shown in Figure 3. Notably, consistent values of σ_f^* = 2400 ± 100 MPa are found independent of temperature.

These can be used with measured K_{Ic} values to evaluate ℓ^*. Valid K_{Ic} data was obtained only at 173 and 186°K. All other measurements from 140 to 215°K had appropriate P_{max}/P_Q ratios (≤ 1.1) but had inadequate thicknesses to he classified as "valid". However, the actual value of K_Q are expected to be ~ K_{Ic} within material data scatter. Values of K_{Ic} and K_Q are shown in Figure 4.

We have previously shown that crack tip stress fields can be reasonably represented by spline fits[4] $\sigma_n/\sigma_o = A\text{-}B(K/\sigma_Y)^2$. Using the RKR model this yields an expression for toughness in the form

$$K_{I_C} = \sqrt{B}\sigma_o^2\ell^*/(A-\sigma_f^*/\sigma_o) \qquad (1)$$

Appropriate stress field parameters for this steel ($n \sim .1$ and $K_{Ic}/\sigma_o < .12$) are A = 4 and B = 100. The values of ℓ^* derived from Equation 2 (assuming $a_o = a_o(\dot{\varepsilon} = 10^{-2}s^{-1})$) are also shown in Figure 4 in parentheses next to the data points; they are found to be independent of temperature with values of $\ell^* \simeq 54$ (±10) μm. The banded region in Figure 4 shows K_{Ic} predicted by Equation 1 for ℓ^* = 50-60 μm and for σ_o values corresponding to strain rate in the range $\dot{e}$ 10^{-2}-10^{-1} s^{-1}.* The magnitude of the band width demonstrates the sensitivity of the position of the knee region to this parameter.

"Estimated upper limit of the effective notch strain rates

5.4 Discussion

The constant values of σ_f^* and ℓ^* and the general shape of the lower shelf toughness curve strongly support the applicability of a critical stress-critical distance model for cleavage fracture in this martensitic stainless steel. Further, evidence supporting this is available in the magnitudes of these properties relative to microstructural characteristics of this steel.

The value of $\ell^* \sim 54$ is approximately 2 prior austenitic grain sizes. The value of $\sigma_f^* = 2400$ is consistent with measurements of Brozzo in low-carbon martenatic steels[17] and Green and Curry[18] in low alloy steels with similar subgrain structures and sizes. In particular, these studies suggest that σ_f^* is controlled by the martensite/bainite lath packet size d varying as $\sigma_f^* \sim c/\sqrt{d}$; where $c \sim 190 \pm 20$ MPa $\sqrt{mm}$. This compares to $c \sim 200$ MPa $\sqrt{mm}$ for HT-9 ($d_M \sim 7\mu m$). These values of σ_f^* are also in reasonable agreement with the σ_f^* model proposed by Knott[19], suggesting σ_f^* is controlled by crack propagation from a cracked packet through adjoining martensite laths which fail by a ductile internal necking process. This theoretical interpretation and experience with the other steels[16-20] suggests that the cleavage facets should roughly correspond to the packet morphology. This is clearly shown in the fractograph shown in Figure 5, where the packet substructure is clearly visible in the grouping of cleavage facets. We also note that the value of $\ell^* \sim 2d_a$ may suggest that the fracture initiation site is a prior austenite grain boundary, which we have noted to be heavily precipitated.

The excellent low temperature toughness of the ESR heat of HT-9 is very encouraging and supports the possibility that these steels can be used for many fusion applications even when high transition temperatures result from significant in service irradiation embrittlement. Further, these results will assist in developing procedures to correlate radiation damage data and guide efforts to develop improved alloys through compositional and microstructural tailoring. These topics will be the subject of future research.

5.5 Conclusions

The flow and fracture properties of the MFE-ADIP program heat of ESR HT-9 were measured in the cleavage fracture regime. Analysis and evaluation of these results provided the following conclusions:

1. This heat has excellent lower shelf toughness with $K_{1c} \geq 55$ MPa $\sqrt{m}$.
2. The fundamental micromechanism of fracture is a critical tensile stress operating over a critical microstructural distance; and this mechanism can he modeled using a modified RKR formulation.
3. The critical microcleavage fracture stress is $\sigma_f^* \sim 2400$ MPa and is controlled by the martensite lath packet size.
4. The critical distance $\ell^* \sim 50$ μm and appears to he controlled by the prior austenite grain size.
5. These results can be used to both assist damage analysis and alloy development efforts.

6.0 References

1. R.W. Powell, D.T. Peterson, M.Z. Zimmerschied, J.F. Bates, J. Nucl. Mater., *103-104* (1981) 969.
2. J.R. Hawthorne, DOE/ER-0045/8 (1982) 336.
3. G.K. Odette and G.E. Lucas, J. Nucl. Mater., 117 (1983) 276.
4. G.R. Odette and G.E. Lucas, J. Nucl. Mater., 117 (1983) 264.
5. R.O. Ritchie, J.F. Knott, J.R. Rice, J. Mech. Phys. Solids, 21 (1973) 395.
6. J.F. Knott, Proc. 4th Int. Conf. on Fracture, Vol. 1, Waterloo (1977) 61.
7. T.A. Lechtenberg, "Alloy Development Irradiation Performance", Semi. Ann. Prog. Rept. 14, DOE/ER-0045/8 (1983) 363.
8. D.S. Gelles and L.E. Thomas, "Microstructural Examination of the Commercial Martensitic Steel HT-9 Following Neutron Irradiation:' submitted for publication J. Nucl. Mater. (1983).

9. W.L. Server, J.T.E.V.A. 6-1 (1978) 29.

10. J.R. Griffiths and D.R.J. Owen, J. Mech. Phys. Solids, 19 (1971) 419.

11. 1977 Annual Book of ASTM Standards.

12. W.L. Server, J. Test. and Eval., 6,1 (1978) 29.

13. A.S. Tetelman and A.J. McEvily, Jr., Fracture of Structural Materials, Wiley Sons, New York (1967).

14. G.R. Odette, W.L. Server, W. Oldfield, R.O. Ritchie, R.A. Wullaert, FCC 78-11 (1978), prepared for Electric Power Research Institute.

15. R.A. Wullaert, D.R. Ireland, and A.S. Tetelman, Irradiation Effects on Structural Alloys for Nuclear Reactor Applications, ASTM-STP 484 (1970) 20.

16. P. Brozzo, G. Buzzichelli, A. Mascanzoni, M. Mirabile, Met. Sci., 11 (1977) 123.

17. G. Green, Ph.D. Thesis Cambridge University (1975).

18. D.A. Curry, Met. Sci., 16 (1982) 435.

19. J.F. Knott, Conf. on Fracture Mechanics in Design and Service: Living with Defects (Roy. Soc. London, London, 1979).

7.0 Publications

"The Micromechanical Mechanisms of Cleavage Fracture in Martensitic Stainless Steels" by G.R. Odette, G.E. Lucas, R. Maiti, and J.W. Sheckherd, presented at the Third Topical Meeting on Fusion Reactor Materials at Albuquerque, NM, September 19-22, 1983.

Figure 1. Micrograph of the lath martensitic microstructure of the ESR heat of HT-9 (400x).

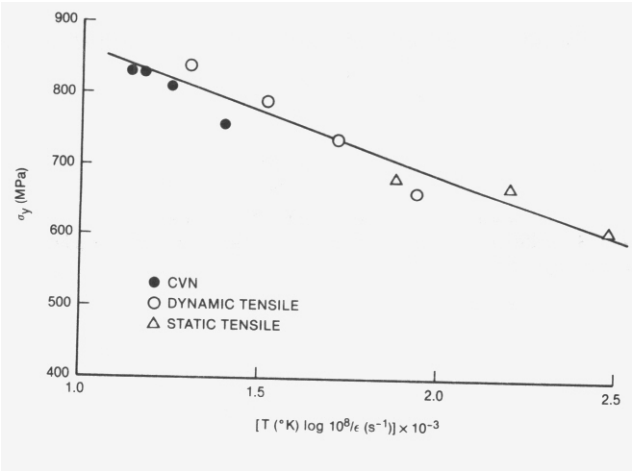

Figure 2. Variation of the yield stress with $P_{\dot{\varepsilon},T}$.

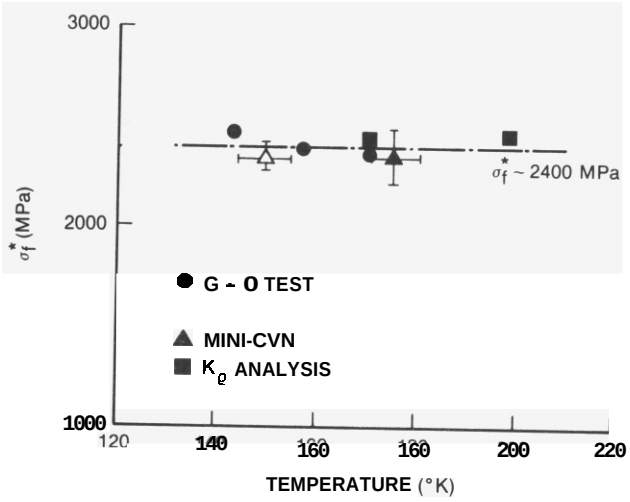

Figure 3. Variation of the critical microcleavage stress σ_f^* with test temperature.

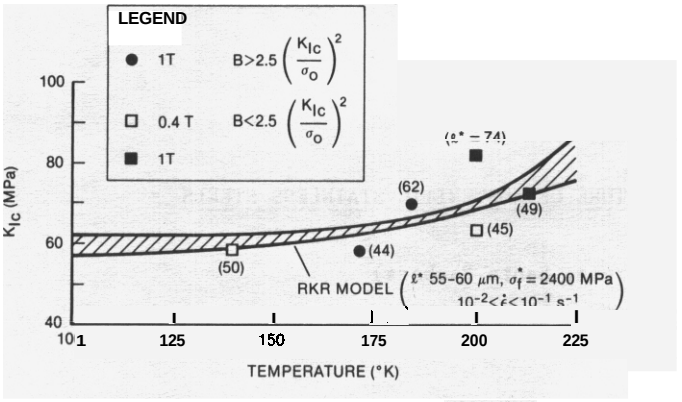

Figure 4. Variation of K_{IC} (K_Q) with test temperature.

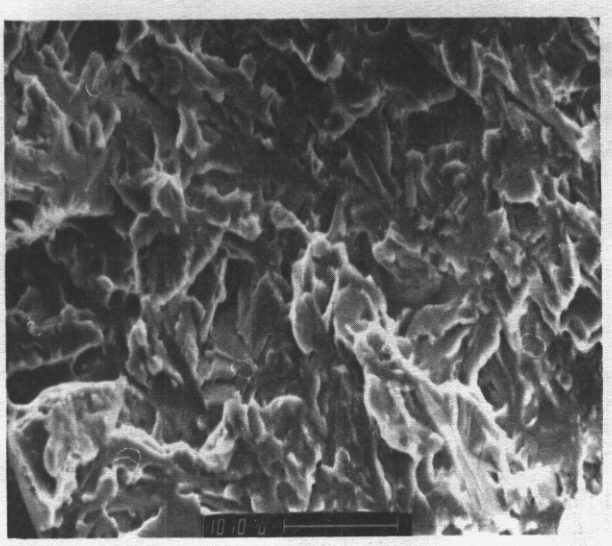

Figure 5. Scanning electron micrograph of the fracture surface of a GO bar tested at $144^{o}K$ and $50s^{-1}$.

A MODEL FOR IN-REACTOR STRESS RUPTURE OF AUSTENITIC STAINLESS STEELS

G.R. Odette (University of California, Santa Barbara)

1.0 Objective

The objective of this work is to assess tbe mechanisms controlling creep rupture and to evaluate possible changes due to irradiation.

2.0 Summary

A model for in-reactor stress rupture of austenitic stainless steels is proposed. This model is based on stress-induced creep cavity formation on a fraction of an evolving distribution of helium bubbles. Creep deformation and its coupling with creep cavity growth in the boundary, near boundary precipitate free zone and grain matrix are considered. The model is calibrated to some high temperature in-reactor data and extrapolated to lower temperatures where irradiation creep is dominant; relatively high ductilities in breeder spectra are predicted due to delocalization of microstructurally insensitive irradiation creep strains. At low stresses, the rupture exposure is predicted to scale as $a\ 1/\sqrt{He/dpa}\ \sigma^2$ and the total ductility $1/\sqrt{He/dpa}$ a.

3.0 Program

Title: Damage Analysis and Fundamental Studies for Fusion Reactor Uaterials Development
Principle Investigators: G.R. Odette and G.E. Lucas
Affiliation: University of California, Santa Barbara

4.0 Relevant DAFS Program Plan Task/Subtask

Subtask B Mechanical Properties

5.0 Acomplishments and Status

5.1 Introduction

At low stresses, creep ruptyre in austenitic stainless steels usually occurs by the accumulation of grain boundary cavitation damage. Irradiation can significantly degrade both rupture strength and ductility, although the magnitude, and even the sign, of the effect depends on a combination of material and environmental variables.[2,3]

Simple analytical models of rupture time and ductility are developed which account for the critical variables of microstructure, stress, temperature, helium content, and the creep law. These models are calibrated and tested using existing data and then used to assess scaling of creep rupture properties between various fission and fusion environments.

5.2 Background

For unirradiated austenitic alloys, the creep failure process can be divided into regimes of: cavity formation; cavity growth; and failure at a critical cavity volume.

The cavity formation process is associated with boundary second-phase particles. Independent of the detailed mechanism (i.e., prior damage, grain boundary sliding-stress amplification, etc.), creep[4] cavity number densities and formation kinetics are largely controlled by the boundary microstructure.

Stress-driven cavity growth can take place by a variety of mechanisms, ranging from unconstrained boundary diffusion to pure power law creep.[5] The controlling mechanism is a function of cavity size and spacing, distribution of cavitated facets, stress, stress-state, temperature, and the microstructure and deformation properties of surrounding regions. Indeed, cavity growth may follow a birth-to-death trajectory through a "mechanism and rate space", transgressing several regimes. However, both theory and observation suggest a close coupling of the cavity growth rate, $\dot{v}$, with the overall creep rate $\dot{\varepsilon}$, or $\dot{v} \propto \kappa\dot{\varepsilon}$.[5] The coupling parameter κ depends on both the growth mechanism and the array of variables outlined above.

Failure criteria result from a critical grain boundary area fraction of cavities.[6] In combination these concepts lead to the widely observed Monkman-Grant relation,

$$\dot{\varepsilon}t_r = C_{MG}, \tag{1}$$

where t_r is the rupture time. The parameter C_{MG} reflects both the efficiency of creep-cavity growth coupling and local ductility limits; C_{MG} generally decreases with decreasing stress and is sensitive to boundary microstructure.

Since irradiation can perturb all of these processes, tractable models require identification of dominant mechanisms. Such dominance is observed in the role of high levels of transmutant or injected helium in enhancing the number density of creep cavities and a corresponding reduction in ductility and rupture life,[2,7] viz. - helium embrittlement.

5.3 Description of the Model

The model components include:

1. Stress (σ) activates the growth of the fraction of a distribution of grain boundary bubbles containing helium in excess of a critical number m^*. When the bubble induced creep cavity density (N_c) exceeds normal values, embrittlement occurs.

The critical number m^* is a function of surface energy γ, an interface factor F_v for bubbles on precipitates, normal boundary, stress σ, and temperature T as[a]

$$m^* = AF_v\gamma^3 T^2/\sigma^2, \tag{2}$$

where, for an ideal gas, $A \sim 8.6 \times 10^{22}$ K/J. For example, at T = 1000°K and σ = 100 MPa, $m^* \sim 4.6 \times 10^4$ for $\gamma = 1.15$ J/m^2[4] and $F_v \approx 1$. If the creep cavity density is 10^{13}/m^2, which is about 10-100 times unirradiated values,[4] only a fraction of a ppm of grain boundary helium are required (e.g., 0.5 ppm at a typical grain size of 20 μm).

Some bubbles would contain less helium than m^* and others more. For in-reactor conditions, creep cavity densities would increases with time due to the accumulation of boundary helium. It is assumed that a total density of N_b^t bubbles form early and grow as a constant (self-similar) distribution $N_b(m/\bar{m})$ when scaled in terms of an average helium number $\bar{m}$.[9] Hence, the creep cavity density would represent that fraction of the bubble distribution with $m/\bar{m} > m^*/\bar{m}$ as illustrated in Figure 1. In-reactor values of $m^*/\bar{m}$ would decrease with $G'_{He}t/N_b^t$, where $G'_{He}t$ is the total grain boundary helium (per unit area). It is convenient to represent the functional dependence by a decreasing polynomial in the form $N_b(m/\bar{m}) \approx (\bar{m}/m)^Q$ in which case $N_c \approx (\bar{m}/m^*)^{(Q+1)}$. Further, assuming that N_b^t scales with boundary helium deposition rate G'_{He} as $N_b^t \approx G'^P_{He}$, and using Eq. 2, it can be shown that

$$N_c \approx (G'_{He}t)^R \sigma^{2(Q+1)} \tag{3a}$$

where

$$R = Q - PQ + 1. \tag{3b}$$

Typical values of the scaling and distribution parameters are $P \sim 1/2$[10] and $Q \sim 2$*. However, it is noted that the overall results are relatively insensitive to these values and the specific model assumptions (e.g., continuous buhble nucleation and growth leads to roughly similar conclusions).

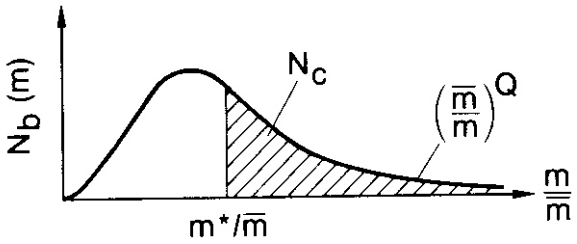

Figure 1. Schematic illustration of stress-activated creep cavity formation on a fraction of self-similar scaled ($m/\bar{m}$) bubble distribution.

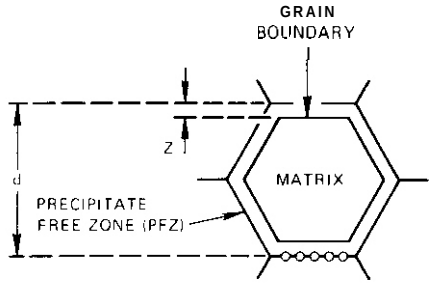

Figure 2. The three microstructural regions considered in the creep-coupled cavity-growth model.

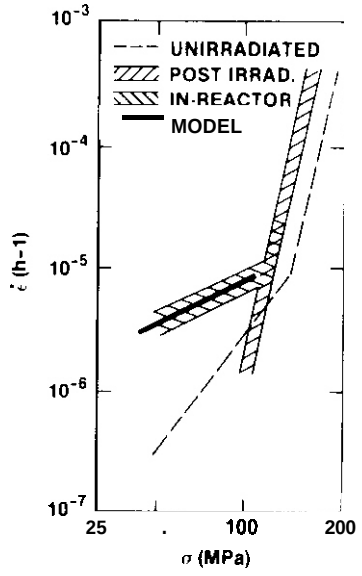

Figure 3. **Predicted creep rate due to PFZ dislocation climb-cavity growth mechanism compared to data.**

2. Cavity growth is not directly perturbed by helium, but depends on the prevailing temperature, stress and stress-state, and microstructures and deformation properties of three regions: the grain boundary, the near boundary precipitate free zone (PFZ), and the grain matrix, illustrated in Figure 2. The appropriate cavity growth model, therefore, must consider the particular set of environmental and material conditions.

3. Rupture occurs at a critical area fraction of cavities on individual grain facets. The local failure ductility, ε_ℓ, due to cavity growth is

$$\varepsilon_\ell \sim .2\ \lambda/d \sim 1/10\sqrt{N_c} \qquad (4)$$

for a coverage of 0.25, where A is the cavity half spacing and d the grain diameter.

The total ductility is equal to the critical damage strain plus the creep required to grow the cavities to critical size. Low ductility is associated with localized strains, low-critical damage strains, and efficient creep cavity growth coupling.

5.4 Calibration and Testing of The Model

A convenient data set to test and calibrate the model is due to Wassilew et al.,[11,12] for a German DIN 1.4970 stainless steel in the cold-worked and aged condition. Because of space limitations, only the low stress in-reactor condition is treated here; behavior in other regimes is discussed elsewhere.[13] The irradiation temperatures were high (T ~ 720°C) with modest total damage accumulation levels (maximum He ~ 140 appm and dpa ~ 5). Stress varied between about 40 to 150 MPa. The irradiation severely reduced both rupture time and ductility, with somewhat different behavior observed in low (< 100 MPa) and high-stress regimes.

The grain boundaries of irradiated steels are heavily precipitated (see Figure 2). Hence, boundary diffusion may be severely inhibited.[14] However, it is proposed that the surrounding PFZ can creep by operation of dislocation sources by a Herring-Nabbaro type stress induced flow of vacancies to boundary cavities. Such creep is inhibited in the hard matrix. It is further assumed that constraint effects are minimal at low strains ($\lesssim$ 1%), and as a result of factors such as relatively uniform facet cavitation (due to helium bubbles) and easy shear in the PFZ. Thus, the creep rates may be modeled for diffusion in a slab (z/d when z is the PFZ dimension) as

$$\dot{\varepsilon} \sim \dot{\varepsilon}_{PFZ}\ 2z/d \sim \frac{20\ D_s \Omega\sigma}{kTzd}\ \frac{z}{d} \sim \frac{20\ D_s \Omega\sigma}{kTd^2} \qquad (5)$$

where D_s is the lattice self-diffusion coefficient and Ω the vacancy volume. Substituting typical value of d = 20 μm and a nominal $D_s \sim \exp(-2.8\ (ev)/kT)$[15] yields the good agreement shown in Figure 4.

The creep is localized in the PFZ and due to cavity growth. Using the relations: $\varepsilon_t = d/z\ \varepsilon_\ell$, $t = \varepsilon_t/\dot{\varepsilon}$, a λ/d, A a $1/\sqrt{N_c}$ and Eq. 3 and 5 results in the expressions

$$t_r \alpha\ 1/\sqrt{G'_{He}}\ \sigma^2 \qquad (6)$$

and

$$\varepsilon_t \alpha\ 1/\sqrt{G'_{He}}\ \sigma \qquad (7)$$

for P = 1/2 and Q = 2. For different P and Q parameters or even model assumptions, the results are similar [e.g., $t_r \alpha\ 1/(G'_{He}\ (.3\text{ to }.6)\ \sigma^{(1.3\text{ to }2)}$].

The model can be calibrated to the data by matching the predicted and observed rupture ductility at one stress level; this was done at 100 MPa where $\varepsilon_t \sim 0.006$. The rupture time and ductility predictions at other stresses are shown in Figures 4 and 5; agreement is excellent. This calibration can be interpreted in terms of a cavity spacing λ ~ .5 μm. This is not only a reasonable value, but, more importantly, it is readily measurable. The alternative of calculating cavity density from first principles is certainly desirable but must be regarded as a long-term goal.

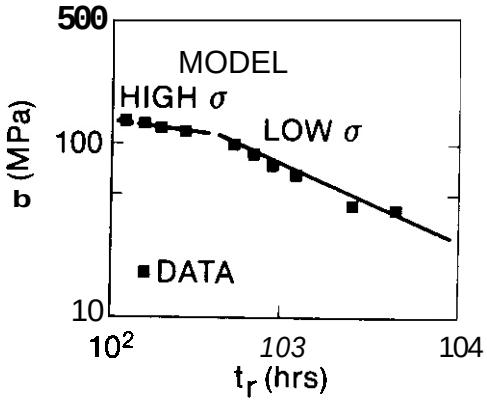

Figure 4. Predicted rupture time for PFZ diffusion creep compared to data.

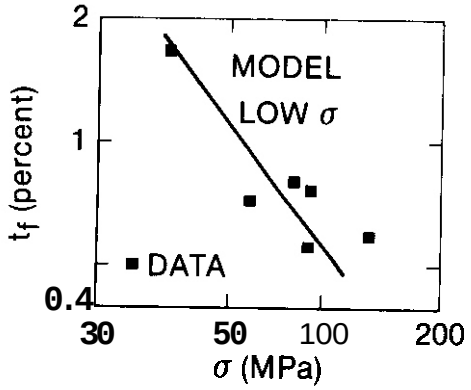

Figure 5. Predicted ductility compared to data (calibrated at 100 MPa)

5.5 Scaling of Creep Rupture Parameters

The data set modeled in Section 4 was at high temperatures associated with a dominance of diffusion creep. However, at lower temperatures more pertinent to structural applications, irradiation creep will become more important.[16] Irradiation creep is relatively insensitive to microstructure, and rates in the PFZ and matrix would be similar.[16] The net effect would be to "delocalize" the deformation from only the PFZ to the entire grain. However, the dilational component of creep local to the boundary related to cavitation damage would be similar to that experienced in the high temperature diffusion creep regime. This behavior is illustrated in Figure 6.

Hence, the rupture process can be modeled with an irradiation creep model $\dot{\varepsilon} = B\sigma$ replacing the thermal creep Eq. 5. The resulting expressions for rupture time and ductility are

$$dpa_r = I/\sqrt{He/dpa\ B}\ \sigma^2 \qquad (8)$$

and

$$\varepsilon_t = \frac{I\sqrt{B}}{\sigma\sqrt{He/dpa}}\ , \qquad (9)$$

where He/dpa is the helium to displacement ratio, assuming that the boundary concentration scales with the total helium level. At similar helium levels and stress, the ductility for the irradiation dominated creep case should be $\sim d/z$ ($\sim$ 10) times that for diffusion creep. Hence, at σ = 100 MPa, the irradiation creep ductility is $\sim$ .06 at a helium level of $\sim$ 30 appm. For a fast fission He/dpa ratio of .3, this corresponds to a rupture exposure of $\sim$ 100 dpa. Using an irradiation creep coefficient of B = 5 x 10^{-6}/MPa-dpa, I $\sim$

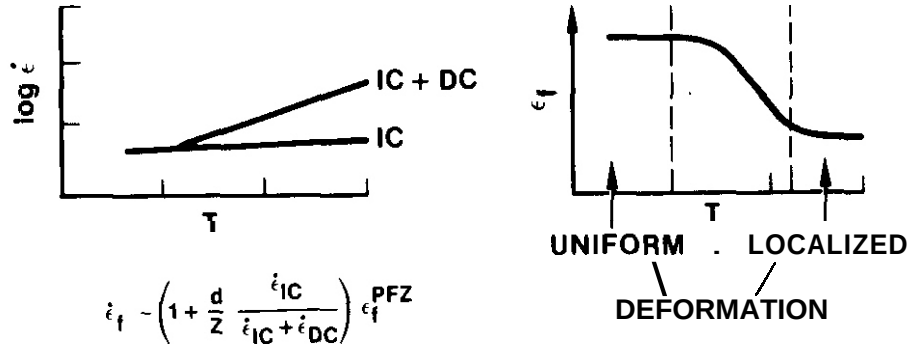

Figure 6. Schematic of how irradiation creep delocalizes strains and increases ductility at lower temperatures.

$1500/MPa^{3/2}\ dpa^{1/2}$. Figure 7 shows the predicted rupture exposures and ductilities as a function of stress for this model normalization at He/dpa ratios typical of mixed spectrum (~ 70 appm/ dpa) and fusion (~ 10 appm/dpa) spectra. The model is truncated at high-stress levels associated with a shift to unirradiated power-law creep controlled fracture.

Bath rupture strength and ductility scale as $1/\sqrt{He/dpa}$ and with $1/\sigma^2$ and $1/\sigma$ dependence, respectively. Relatively high ductilities are predicted for breeder reactors due to the uniform character of irradiation creep strains; however, even in this case the rupture life is significantly reduced by helium-enhanced boundary cavitation at low stresses.

5.6 Discussion and Conclusions

The simple models developed and calibrated in the previous sections provide a useful basis for estimating the scaling of stress-rupture parameters with factors such as helium stress, microstructure, and the creep law.

Specifically, the following conclusions obtain:

1. The microstructure and deformation behavior of the grain boundary near boundary (PFZ) and matrix regions should be considered in modeling stress rupture in irradiated stainless steels.

2. Helium embrittlement occurs when creep cavity densities formed on helium bubble sites exceed those normally induced by stress. For in-reactor condition?, this is a function of both rupture time and stress. Rupture exposure scales roughly as $dpa_r \propto 1/\sqrt{He/dpa}\ \sigma$.

3. At low stresses, diffusion or irradiation creep leads to ductility scaling as $\varepsilon_f \propto 1/\sqrt{He/dpa}\ \sigma$. However, for conditions dominated by irradiation creep, total rupture at equivalent helium levels strains are much greater then for high-temperature diffusion creep controlled rupture (by a factor ~ z/d). This rationalizes the relatively high ductility observed in breeder reactor creep experiments.

4. Either high-stress (e.g., power law creep) or low-helium environments, and particularly both, may be significantly less sensitive to helium embrittlement than low-stress high-helium conditions pertinent to fusion-service environments.

5. Alloy design efforts to reduce the flow of helium to the grain boundary appears to be the best means of controlling stress rupture in irradiated austenitic alloys.

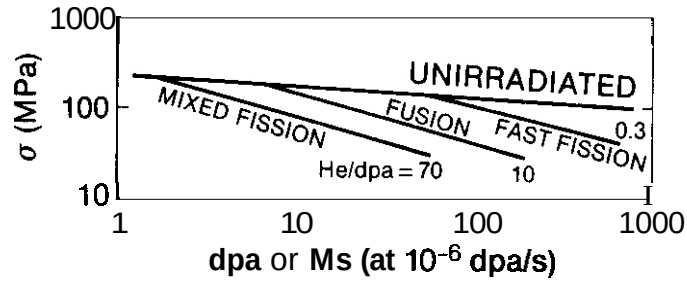

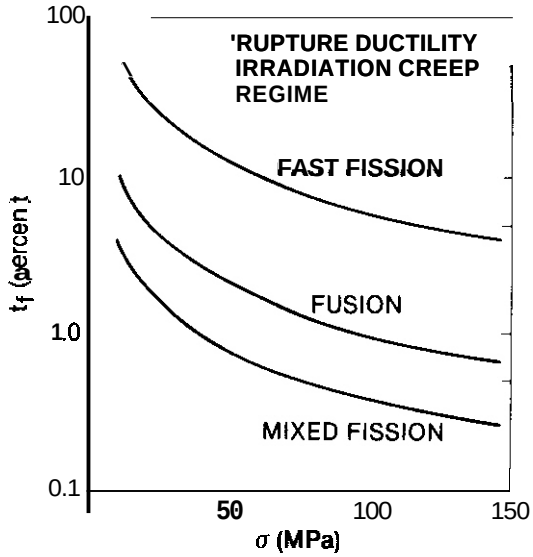

Figure 7. **Predicted creep rupture times and ductilities for various neutron spectra,**

6.0 References

1. M.F. Ashby, C. Gandhi, and D.M.R. Taplin, Acta Met. 27 (1979).699.

2. D.R. Harries, JNM, 82 (1979) 2.

3. A.J. Lovell, B.. Chin, and E.R. Gilbert, J. of Mat. Sci.

4. D.G. Morris, Met. Sci. (1978) 19.

5. W. Beere, Harwell Consultants Symp. on Inert (Rare) Gases in Metals and Ionic Solids - II, AERE-R 9733, UKAEA, S.F. **Pugh,** Ed. (1980) 439.

6. F.C. Monkman and N.J. Grant, Proc. of ASTM, 56 (1956) 593.

7. E.E. Bloom, Radiation Damage in Metals, ASM Metals Park, Ohio (1975) 295.

8. R.E. Stoller and G.R. Odette, Irradiation and Stress Induced Helium Bubble-to-Void Conversion: Real Gas and Precipitate Effects, submitted to JNM (1983).

9. A.J. Markworth, Metallography (1970) 197.

10. G.R. Odette, P.J. Maziasz, and J.A. Spitznagel, JNM, 103 & 104 (1981) 1289.

11. C. Wassilew, K. Anderko, and L. Schäfer, Proc. Int. Conf. on Irrad. Behav. of Met. Mat. for Fast React. Core. Comp., Ajaccio Corsica, France (1979) 419.

12. D.R. Harries, Harwell Consultants Symp. on Inert (Rare) Gases in Metals and Ionic Solids-II, AERE-R9733, UKAEA, S.F. Pugh, Ed. (1980) 422.

13. G.R. Odette, Submitted to JNM and in DAFS QPR-24, Oct.-Dec., 1983, DOE/ER-0046-14 (1984 - to be published).

14. B. Burton, Diffusion Creep of Polycrystation Materials, Diffusion and Defect Monograph Series-5 (1977) 62.

15. A.M. Brown and M.F. Ashby, Acta Met., 28 (1980) 1085

16. G.W. Lewthwarte and D. Mosedale, JNM 90 (1980) 205.

7.0 Publications

"A Model for **In-Reactor** Stress Rupture of Austenitic Stainless Steels" by G.H. Odette; presented at the **Third Topical** Meeting **on** Fusion Reactor Materials at **Albuquerque,** NM, September 19-22, **1983.**

CORRELATION OF FRACTURE TOUGHNESS WITH TENSILE PROPERTIES FOR IRRADIATED 20% COLD-WORKED 316 STAINLESS STEEL

M. L. Hamilton, F. A. Garner (Hanford Engineering Development Laboratory) and W. G. Wolfer (University of Wisconsin)

1.0 Objective

The object of this effort is to provide correlations between various irradiation-induced property changes in order to extend the body of data relevant to development of fission-fusion correlations.

2.0 *Sumnary*

A modified version of the Krafft correlation has been successfully employed to estimate the fracture toughness of irradiated AISI 316 using more easily obtained tensile data. It appears that fracture toughness saturates with neutron exposure at ~400°C. It also exhibits a dependence on both irradiation temperature and test temoerature.

3.0 Program

Title: Irradiation Effects Analysis (AKJ)
Principal Investigator: D. G. Doran
Affiliation: Hanford Engineering Development Laboratory

4.0 Relevant DAFS Plan Task/Subtask

Subtask II.C.14 Models of Flow and Fracture Under Irradiation

5.0 Accomplishments and Status

5.1 Introduction

It has recently been shown that a reduction in fracture toughness due to irradiation can have a significant impact on the lifetime of the first wall of a fusion reactor.[1] Both the fatigue crack growth rate and the mode of failure (leak vs. sudden crack propagation) will depend on the fracture toughness.

Experimental determination of fracture toughness for irradiated materials is hampered by several considerations. First, both standard and miniature fracture toughness specimens are rather large with respect to the limited irradiation test space available in either FMIT* or fast breeder and mixed-spectrum fission reactors. Second, selection of the minimum size for valid test specimens requires some *a priori* estimate of the expected fracture toughness. For these reasons it is desirable to explore the possibility of estimating fracture toughness from the tensile properties of irradiated specimens having a much reduced size. This possibility was discussed at some length by Wolfer and Jones,[2] and it was pointed out that the appropriate correlation between fracture toughness and tensile properties is fundamentally different for materials exhibiting homogeneous plastic flow and those experiencing localized flow.

*FMIT designates the Fusion Materials Irradiation Test Facility planned for construction on the Hanford Reservation in Richland, WA.

A limited number of toughness measurements have recently become available for 20% cold-worked AISI 316 stainless steel.[3-5] Tensile properties have also been determined on material identical to that from which the toughness specimens were constructed. It is therefore possible to test relationships which attempt to correlate fracture and tensile properties.

5.2 The Toughness Data

Huang and Fish3 performed tensile tests at 593°C on notched and unnotched specimens made from ducts irradiated at 375-415°C in EBR-II to a fluence of 7.8 x 10^{22} n/cm^2 (E > 0.1 MeV). Based on a J-integral analysis of the load-displacement curves from two notched specimens, they obtained fracture toughness values at a test temperature of 593°C ranging from 57.2 to 67.7 MPa√m for irradiation at 375-415°C.

Huang and Wire4 also made measurements on compact tension specimens fabricated from an EBR-II duct irradiated to fluences of 11.0 to 11.3 x 10^{22} n/cm^2 (E > 0.1 MeV) at temperatures ranging from 377 to 400°C. The test temperatures were 20, 232, 427, 538 and 649°C. These results have recently been revised slightly by Huang[5] and are shown in Figure 1. These authors[4,5] also showed that the Hahn-Rosenfield model6 could predict the toughness for unirradiated material but not for irradiated material.

5.3 The Tensile Data

In addition to the data on unnotched tensile specimens reported by Huang and Fish, there exist previously unreported tensile data on unnotched specimens derived from the same EBR-II ducts from which the compact tension specimens were fabricated. As shown in Table 1 these data at 10.0 x 10^{22} n/cm^2 cover a somewhat larger range of irradiation temperature (379 and 452°C) than that explored by Huang and coworkers.

5.4 The Modified Krafft Model

The model chosen most likely to relate fracture and tensile properties is that of Krafft[7] as modified by Schwalbe and Backfisch.8 This choice was based on the comparative success of this model over the Hahn-Rosenfield model in a similar analysis conducted on AISI 316 irradiated in HFIR[2]. The Krafft model considers fracture instability as occurring in small elemental fracture cells lying along the crack front.

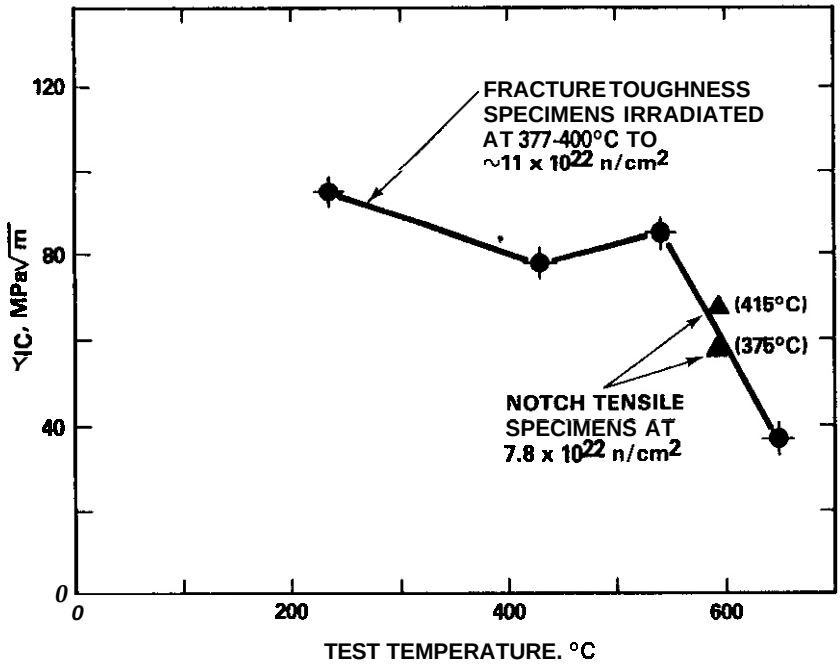

FIGURE 1. Fracture Toughness Data for 20% cold-worked 316 stainless steel, by Huang and coworkers.[3-5]

TABLE I

TENSILE PROPERTIES AND PREDICTED VALUES OF FRACTURE TOUGHNESS FOR 20% COLD-WORKED 316 DUCTS IRRADIATED IN EBR-II TO 10 x 10^{22} n/cm^2 (E>0.1 Mev)

Irradiation Temperature = 379°C

Specimen	Strain Rate (sec^{-1})	Test Temp. (°C)	Yield Strength (MPa)	Ultimate Strength (MPa)	Uniform Elongation (%)	Total Elongation (%)	Predicted Toughness, K_{Ic} (MPa $\sqrt{m}$)
M1D1	$4.4x10^{-5}$	20	793	1121	13.6	19.3	192
M1D2	$4.4x10^{-5}$	232	859	925	2.7	6.0	96.0
M2D1	$4.4x10^{-5}$	379	787	838	1.9	4.0	75.8
M2D2	$4.4x10^{-5}$	491	699	747	1.4	4.1	74.4
M3D1	$4.4x10^{-4}$	232	894	949	2.2	5.3	91.3
M4D1	$4.4x10^{-4}$	538	716	760	0.9	4.9	87.3
M4D2*	$4.4x10^{-4}$	649	501	527	1.3	3.8	59.5
M5D1	$4.4x10^{-3}$	232	880	957	2.6	5.9	97.5
M5D2	$4.4x10^{-3}$	379	782	867	1.1	3.3	75.9
M6D1	$4.4x10^{-3}$	538	673	688	0.6	3.3	66.7
M6D2*	$4.4x10^{-3}$	649	524	545	0.9	3.7	60.4
Irradiation Temperature = 452°C							
M1I1	$4.4x10^{-5}$	20	749	870	12.4	18.1	157
M1I2	$4.4x10^{-5}$	232	707	778	5.6	8.3	103.2
M2I1	$4.4x10^{-5}$	452	731	829	4.4	7.1	102.0
M2I2	$4.4x10^{-5}$	563	621	659	1.4	3.4	63.1
M3I1	$4.4x10^{-4}$	232	834	938	7.7	10.5	128.8
M3I2	$4.4x10^{-4}$	427	724	801	6.3	9.3	113.6
M4I1	$4.4x10^{-4}$	538	612	652	2.1	4.0	67.1
M4I2*	$4.4x10^{-4}$	649	414	448	1.6	3.8	55.1
M5I1	$4.4x10^{-3}$	232	832	921	6.8	9.1	118.2
M5I2	$4.4x10^{-3}$	452	728	775	2.0	4.0	73.1
M6I1	$4.4x10^{-3}$	538	633	681	4.2	6.6	88.0
M6I2*	$4.4x10^{-3}$	649	448	525	3.2	6.2	77.5

* Possibly intergranular failure.

These cells act as coherent ductile ligaments which are the last connecting links at the crack front. Instability is visualized to occur when a critical strain develops over a specific distance ahead of the crack tip. This distance is referred to as the process zone size, which is the smallest material dimension necessary for a crack propagation element. The choice of the appropriate process zone size requires some knowledge of the nature of the fracture surface and the crack nucleation sites.

The modified Krafft correlation is given by

$$K_{Ic} = \frac{\sigma_y}{(1-2\nu)} \left[\pi(1+n)d^* \left(\varepsilon_f E/\sigma_y\right)^{1+n}\right]^{/2} \quad (1)$$

where: σ_y = yield strength
ε_f = true fracture strain
E = Young's modulus
ν = Poisson's ratio
n = strain hardening exponent
d^* = size of the fracture process zone

The values of d^* and ε_f are somewhat vaguely defined, however. For irradiated austenitic stainless steels we have chosen the grain size and the total elongation, respectively. The reasons for these choices will be given in the discursion section. The average grain size of the EBR-II ducts was ~50 μm.

If power-law strain hardening is assumed,

$$\epsilon/\epsilon_0 = (\sigma/\sigma_0)^{\frac{1}{n}} \qquad (2)$$

where ϵ_0 and σ_0 are two arbitrary reference values of the unaxial strain and stress, respectively. The strain-hardening exponent n can then be obtained from the relationship

$$n = \ln(\sigma_u/\sigma_y) \; / \; \ln(E\,\epsilon_u/\sigma_y) \qquad (3)$$

where σ_u and ϵ_u are the true ultimate stress and true uniform strain. In these irradiated specimens n is small, on the order of 0.03.

5.5 Results

The values of fracture toughness predicted by Equation 1 are shown in Table 1. Some entries in Table 1 are designated by a star, representing tensile tests carried out at temperatures sufficiently high that failure is expected to be intergranular. For these cases, the correlation is not expected to be applicable. Figure 2 shows a comparison of the toughness data of Huang and Wire and the predictions of this correlation using tensile data from Table 1 for irradiation at 379°C. Also shown are predictions of toughness at 593°C for the two notched specimens reported by Huang and Fish.[3]

The agreement between actual toughness measurements and predictions based on tensile data is quite good; both exhibit a similar dependence on test temperature. The data of Huang and Fish suggest a slight dependence of toughness on irradiation temperature. The agreement of data and predictions at both 7.8 and 11.0 x 10^{22} n/cm^2 suggests that fracture toughness at 400°C saturates at relatively low fluence and does not decline thereafter.

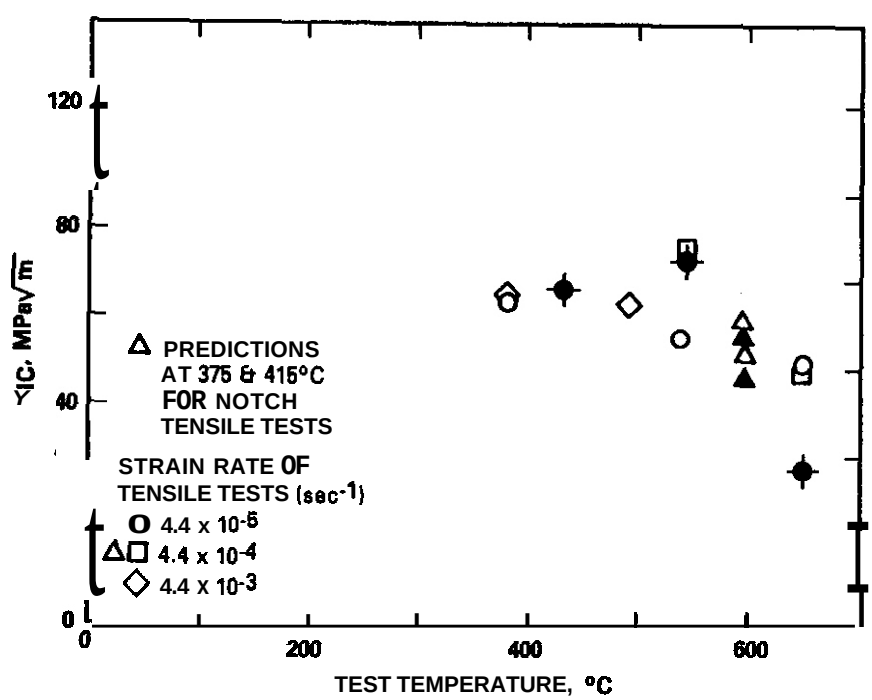

FIGURE 2. Comparison of Predictions at an Irradiation Temperature of 379°C with Toughness Data (solid symbols) at 375-415°C.

To explore the possibility of a toughness dependence on irradiation temperature, the tensile data from specimens irradiated at 452°C were used to make predictions of toughness. Figure 3 shows that a sensitivity to irradiation temperature is indeed predicted, but only for tests conducted below the irradiation temperature.

5.6 Discussion

Since toughness data are available for only a limited range of irradiation temperatures, there is no opportunity at present to test the general applicability of this correlation to a wider range of irradiation conditions. It is fortunate, however, that the successful correlation at 379°C employs two convenient and easy-to-measure parameters, grain size and total elongation. If this correlation is valid rather than fortuitous, a rationale is required for the relevance of these parameters to this model and this material.

There has been no definitive guidance for selection of these parameters. Krafft originally suggested uniform elongation but Schwalbe and Backfisch assumed that logarithmic fracture strain based on reduction of area 'represents a reasonable measure." The superiority of either of these over total elongation cannot be established, and the chief virtue of the latter is its apparent success.

Both Krafft and Schwalbe agreed, however, that whatever critical strain parameter was chosen, it should correspond to some appropriate microstructural feature which defines a process zone size. Krafft used toughness and tensile data to calculate apparent process zone sizes and concluded that for soft and medium strength materials the zone size was smaller than the grain size. For a high strength material he found the zone size to be on the order of the grain size. AISI 316 irradiated and tested at ~400°C has a yield strength of ~800 MPa[9] and therefore qualifies as a high-strength material. Schwalbe and Backfisch focused on softer materials with hard inclusions that served as void nucleation sites and specified the dimple diameter on the fracture surface as the process zone size.

In irradiated 316 stainless steel the grain interior is hardened extensively by high densities of small voids, precipitates and Frank loops.[9] Grain boundaries are relatively free of these smaller obstacles but larger n-silicide precipitates are present at the boundaries[10] which may serve as crack nucleation sites. Huang[5] notes that plate-like or "channel" fracture surfaces occur in these specimens. These surfaces are dominated by facets, which approach the grain size for tests at 538°C. Channel fracture has been observed in irradiated AISI 304[11,12] and has been shown to result from channeling of dislocation

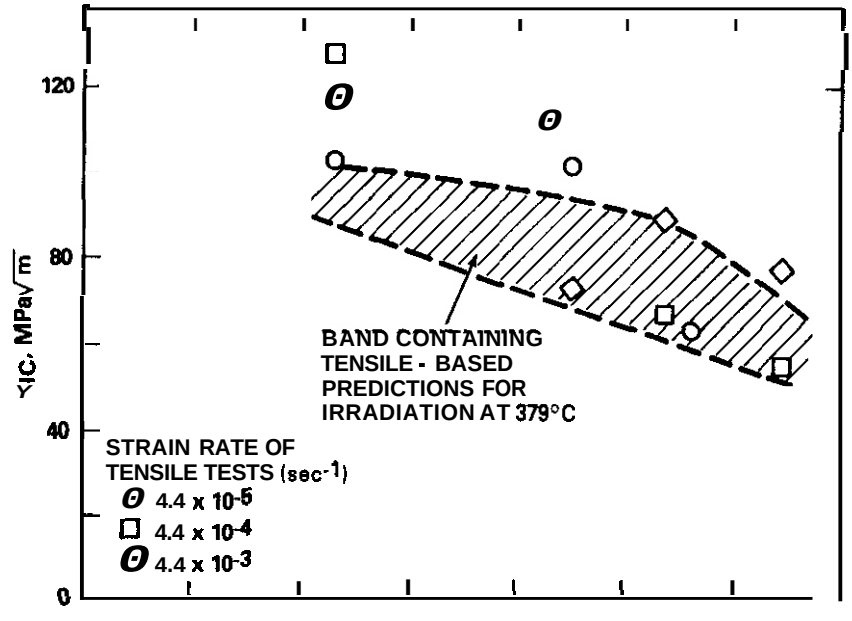

FIGURE 3. Comparison of Toughness Predictions for Irradiations Conducted at 379 and 452°C.

activity through narrow deformation zones. Distortion of irradiation-induced voids within these zones leads *to* local strain estimates of several hundred percent. When these zones intersect grain boundaries, crack nucleation is a potential consequence.

The presence of flow localization of this type apparently does not invalidate the use of a fracture model which assumes that deformation around the crack tip can be described by the macroscopic deformation law for plasticity. The reason why the Krafft model appears to work is probably that the extent of the plastic zone (estimated to be ~2 mm) is much larger than the microscopic scale of flow localization. Thus the stress relaxation invoked by this model occurs over a dimension in which only the average strain is important.

5.7 Conclusions

It appears that a correlation between fracture toughness and tensile properties may exist for AISI 316, thus allowing the use of easily obtained tensile data for estimation of toughness decreases induced by irradiation.

6.0 References

1. R. O. Watson, R. R. Peterson and W. G. Wolfer, J. Nucl. Mater, 103 & 104 (1981) 97; also J. Pressure Vessel Tech., 105 (1983) 144.
2. W. G. Wolfer and R. H. Jones, J. Nucl. Mater., 103 & 104 (1981) 1305.
3. F. H. Huang and R. L. Fish, ASTM STP 782 (1982) 701.
4. F. H. Huang and G. L. Wire, Proc. Int. Conf. on Dimensional Stability and Mechanical Behavior of Irradiated Metals and Allovs, April 1983, Brighton, England.
5. F. H. Huang, The Fracture Characterization of Highly Irradiated Type 316 Stainless Steel, HEOL-SA-2967, Submitted *to* Int. J. of Fracture.
6. G. T. Hahn and A. R. Rosenfield, ASTM STP 432 (1968) 5.
7. J. M. Krafft, Appl. Matls. Res., 3 (1964) 88.
8. K. H. Schwalbe and W. Backfisch, Fracture 1977, Vol. 2 ICF4, Waterloo, Canada (June 1977) 77.
9. F. A. Garner, M. L. Hamilton, N. F. Panayotou and G. D. Johnson, J. Nucl. Mater., 103 & 104 (1981) 803.
10. W.J.S. Yang, F.A. Garner and M.L. Hamilton, "Sluggish Phase Development and Its Consequences in AISI 316 Irradiated at Temperatures Around 400°C," DAFS Quarterly Report DOE/ER-0046/15, (Nov. 1983) in press.
11. C. W. Hunter, R. L. Fish and J. J. Holmes, Trans. Am. Nucl. Soc., 15 (1972) 254.
12. R. L. Fish, Nucl. Tech., 31 (1976) 85.

7.0 Future Work

This effort will continue, focusing on additional relevant data sets derived from HFIR, EBR-II and other reactors.

8.0 Publications

This report will be published in the Journal of Nuclear Materials and presented at the Third Topical Meeting on Fusion Reactor Materials in Albuquerque, NM, September 19-22, 1983.

THE DEPENDENCE ON NEUTRON-INDUCED DISPLACEMENT RATE OF TENSILE PROPERTY CHANGES IN ANNEALED AISI 304 AND 316

H. R. Brager, L. D. Blackburn AND D. L. Greenslade (Hanford Engineering Development Laboratory)

1.0 Objective

The object of this effort is to provide mechanical property measurements and microstructural evidence to guide the development of fission-fusion correlations that incorporate displacement rate and other important variables.

2.0 Summary

Annealed specimens of AISI 304 and 316 were irradiated in the EBR-II fast reactor at ~400°C over a range of neutron fluxes and energy spectra. Tensile tests show that the hardenina of the AISI 304 is sensitive to the displacement rate while the hardening of AISI 316 is not. However, the microstructures of both AISI 304 and 316 are influenced by displacement rate. The increase in yield strength of the specimens is correlated with the contribution of the various microstructural components produced during irradiation. The insensitivity in the hardening of AISI 316 to displacement rate arises because the strengthening contribution from precipitates increases with displacement rate, whereas the strengthening contribution from voids decreases.

3.0 Program

Title: Irradiation Effects Analysis
Principal Investigator: D. G. Doran
Affiliation: Westinghouse Hanford Company

4.0 Relevant DAFS Program Plan Task/Subtask

II.C.14 Models of Flow and Fracture Under Irradiation
II.C.17 Microstructural Characterization

5.0 Status and Accomplishments

5.1 Introduction

Fusion reactor structural materials are expected to be influenced by high-energy neutron irradiation. Predictions of component behavior for proposed reactors are based on the response of material exposed to low-flux high-energyneutron sources, high-energy ion bombardment and fission reactor neutrons. These irradiation high-energy facilities provide data in environments which are substantially different from that of proposed fusion reactor conditions in regard to neutron flux, spectra and total fluence. Very limited information exists on the influence of these variables on the evolution of tensile properties.

The design of a commercial facility will incorporate use of fission-fusion correlations which address the differences between fission and fusion reactor environments. Specimens irradiated in the EBR-II presently make up a major source of the U.S. data used in deriving these correlations. However, a problem generic to most fast reactors exists in that locations which have a high neutron flux are associated with neutrons which have higher energy. In addition, there will also be differences in other environmental variables

such as stress and temperature. In practice, it is difficult to study the impact of spectral variations without simultaneously spanning differences in temperature and/or displacement rate.

To partially compensate for differences in the effect of neutron energy on defect cluster formation, spectral-averaged damage cross sections are usually used. In general, many of the existing fission-derived correlations have not separated the individual influence of each important variable. Displacement rate variations, in particular, are usually ignored in most correlations derived from breeder reactor irradiations and the dependence on this variable is normally incorporated into the temperature dependence. For example, a correlation describing tensile properties for 20% CW AISI 316 was derived from data which spans displacement rates of roughly a factor of two. Only the variables of temoerature and neutron fluence were included in the correlation. however.[1]

The data required to confidently assess the consequences of displacement rate variations should cover the fluence range encompassing both the transient and saturation regimes of property changes and should also span a suitably large range of displacement rates. Since the data available are usually insufficient to meet these criteria, another approach is to seek guidance from the dependence of microstructure on displacement rate and use this guidance to help extrapolate beyond the range of available data.

5.2 Experimental Materials and Procedures

The materials chosen for this experiment were mill-annealed AISI 304 and 316 stainless steel tensile specimens irradiated in Row 4 of the EBR-II using sodium-filled capsules. The specimen temperatures corresponded closely to the reactor coolant and ranged from 371°C to 426°C. The cvlindrical tensile specimens were machined from 50.8 mm plate (RDT specifications M5-1T) with a lenath of 47.6 mm and shoulder diameter of 6.4 mm. The gauge section was 28.6 mn in length and 3.2 mm in diameter.

The tensile specimens were irradiated for four different times at each of six different elevations with respect to the reactor centerline. This provided a range of exposures from 0.2 to 14 dpa, of wean neutron energies from 0.75 MeV to 0.17 MeV and displacement rates varying from 8.4×10^{-4} to 0.6×10^{-7} dpa/sec. The irradiation conditions for the AISI 304 and 316 specimens were previously reported[2] and are shown in Table 1, respectively.

Tensile tests were conducted in air at a strain rate of 3.5×10^{-5} sec^{-1} with the specimens maintained at 385 $\pm$ 1°C.

The grip portion for both AISI 304 and 316 specimens was chosen for electron microscopy examination to minimize strains resulting from the post-irradiation tensile test. The selection criteria for the microscopy specimens were minimum difference in temperature, maximum difference in yield strength change, maximum difference in displacement rate but comparable total displacement levels. Stereomicroscopy was used to determine the foil thickness in order to quantify the microstructural features.

5.3 Results

5.3.1 Tensile Test Results

Figures 1 and 2 show the tensile measurements obtained for the AISI 304 and 316 specimens, respectively. For the AISI 304 stainless steel, there is clearly an effect of the displacement rate an the dpa level at which the transient regimes of yield and ultimate strength are influenced. Analogous behavior was observed in the uniform and total elongations. The saturation level of these properties has not been reached at the displacement rates studied and no conclusion can be drawn at this point concerning the sensitivity of the saturation levels to displacement rate.

The annealed AISI 316, however, shows essentially no sensitivity to displacement rate as shown in Figure 2. There is clearly very little effect of the displacement rate on the dpa level influencing the transient regime of the yield and ultimate strengths. Neither were the uniform and total elongations sianificantly affected. As with the AISI 304 data, the saturation level of these properties has not yet been reached and no conclusion can be drawn concerning the sensitivity of the saturation level to displacement rate.

TABLE 1

IRRADIATION CONDITIONS FOR ANNEALED AISI 316 IRRADIATED IN EBR-II*

Z-Coord. cm	dpa/sec (10^{-7})	E MeV	Temp. K	Total Fluence, 10^{26} n/m^2				Fast Fluence (E > 0.1 MeV) 10^{26} n/m^2				Total Displacements, dpa			
				B-257*	B-258	8-259	8-260	B-257*	B-258	B-259	8-260	B-257*	B-258	B-259	8-260
- 1.7	8.4	0.76	672	0.808	1.94	3.50	--	0.646	1.55	2.80	--	3.30+	8.W	14.4	
-18.2	5.1	0.63	651	0.610	1.46	2.64	--	0.419	1.01	1.82	--	2.00	4.85	8.73	
-30.9	2.3	0.38	647	0.389	0.932	1.69	--	0.221	0.530	0.959	--	0.91	2.21	3.97	
-45.5	1.0	0.21	645	0.249	0.596	1.08	2.06	0.120	0.288	0.521	0.994	0.40	0.97	1.75	3.33+
-55.0	0.6	0.17	644	--	--	--	1.43	--	--	--	0.549	--	--	--	2.W
+33.0	1.9	0.35	697	--	--	1.50	--	--	--	0.826	--	--	--	3.23	--

*The various irradiation capsules are designated by B-257, B-258, etc
+There two specimens were chosen for microscopy.

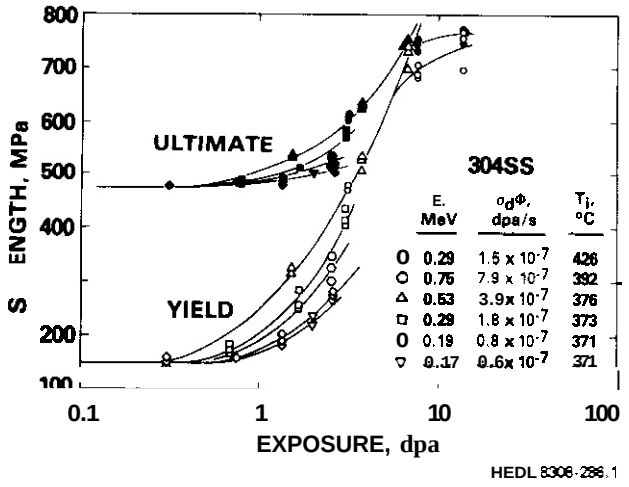

FIGURE 1. Yield and Tensile Strength Values for Annealed AISI 304 Specimens as a Function of dpa.

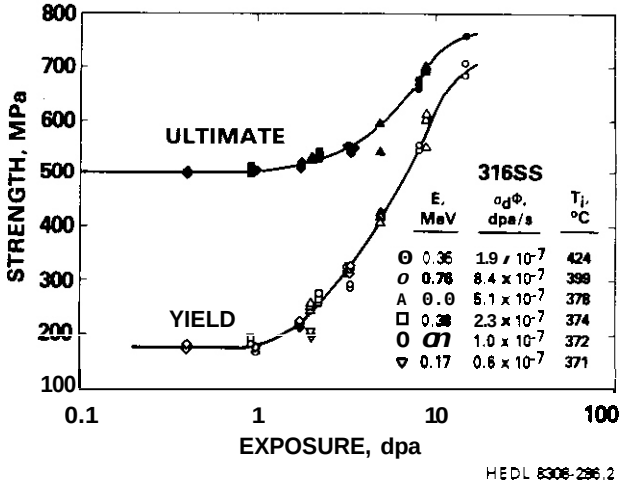

FIGURE 2. Yield and Tensile Strength Values for Annealed AISI 316 Specimens as a Function of dpa.

5.3.2 Electron Microscopy Results - AISI 304

Specimens of AISI 304 irradiated at 392" and 371°C were chosen for microscopy. These had attained 3.1 dpa at 7.9 x 10^{-1} dpa/sec, and 2.6 dpa at 0.8 x 10^{-7} dpa/sec, respectively.

Differences in microstructure were observed in the specimens irradiated at high- and low-displacement rates, as shown in Table 2 and in Reference 2. At the higher displacement rate, the densities of voids, Frank loops and dislocations were significantly higher. Small phosphorus-rich, rod-shaped precipitates were formed but their size and density did not change significantly with displacement rate.

5.3.3 Electron Microscopy Results - AISI 316

The two AISI 316 tensile specimens chosen for microscopy were irradiated at 8.4 x 10^{-7} and 1.0 x 10^{-7} dpa/sec at temperatures of 392 and 371°C, respectively. The dose levels attained were 3.3 dpa for each specimen.

TABLE 2

SUMMARY OF AISI 304 MICROSTRUCTURAL DATA

	High-Rate Specimen	Low-Rate Specimen
Total Displacements (dpa)	3.1	2.6
Displacement Rate (dpa/sec)	7.9×10^{-7}	0.8×10^{-7}
Irradiation Temperature (°C)	392	371
Test Temperature (°C)	385	385
Mean Void Diameter (nm)	5.5	5.0
Void Density (cm^{-3})	4×10^{15}	7×10^{14}
Void Volume (%)	0.03	0.005
Frank Loop Mean Diameter (nm)	17.5	16.0
Frank Loop Density (cm^{-3})	1.45×10^{16}	7.0×10^{15}
Network Dislocation Density (cm^{-2})	8×10^{9}	7×10^{8}
Total Dislocation Density (cm^{-2})	8.0×10^{10}	3.5×10^{10}
Rod Precipitate - Length (nm)	18	9
Rod Precipitate - Density (cm^{-3})	1×10^{14}	2×10^{14}

Figures 3 through 5 and Table 3 compares the Frank loop, void and precipitation microstructures of these specimens. Contrary to the expectation that no flux sensitivity would be observed, the density of voids in the high rate specimen was about two orders of magnitude lower than for the low-rate specimen. The total density for the network dislocations plus the Frank loop populations of the two specimens appears to be roughly comparable in magnitude. The high-rate specimen had about an order of magnitude higher density of both γ' precipitates and phosphorus-rich rod-shaped precipitates.

5.4 Discussion,

5.4.1 Microstructural Origins of Yield Strength

A principal goal of the present investigation was to determine the influence of neutron flux on the microstructural development and ascertain whether or not these observed features can be satisfactorily correlated with the measured changes in mechanical properties. Such an effort can only be directed toward the yield strength as other tensile properties cannot be simply related to only the radiation-induced microstructure.

The correlation in the present case of AISI 304 and 316 at low fluence should be simpler in comparison to a that of previous study on cold-worked AISI 316.3 First, the specimens in this study were mill-annealed prior to irradiation and therefore should possess little microstructure of a hardening nature. In effect, the observed microstructural and yield strength data maximize the experimental signal-to-noise ratio compared to that obtainable in cold-worked material. Second, the hardening contributions should be positive since there are expected to be few pre-existing dislocations which can reduce their density by recombination.

The yield strength changes for microstructural components can be predicted using the following equation, assuming that the von Mises criterion applies and that the Frank loops are large enouqh to be treated only as additional dislocation line length instead of as shortrange obstacles:[4]

$$\Delta\sigma = \sqrt{3}\, Gb \left[\alpha \left(N_d + N_{FL} \right)^{1/2} + \left(\frac{\rho_v d_v}{\beta_v^2} + \sum \frac{\rho_p d_p}{\beta_p^2} \right)^{1/2} \right]$$

where $\Delta\sigma$ is the yield strength change, G the shear modulus, b the Burgers vector, and N_d and N_{FL} the dislocation line lengths per unit volume for the network and Frank loop components, respectively. The voids have density ρ_v and mean diameter d_v. Each type of precipitate has a density ρ_p and mean dimension d_p. The coefficients α and β_v have values established previously4 at 0.2 and 1.0 respectively, and a value of $\beta_p = 3.0$ was established in this investigation. The hardening contribution from the phosphorus-rich rod-shaped precipitates is modified by multiplying its length in Tables II and III by $1/\sqrt{2}$ to take into account the projection of the length along <100> directions with that of the <110> motion of dislocations on {111} planes. The shear modulus at 375°C is 6.7×10^{10} Pa and the <110> Burgers vector for austenitic stainless steel is 2.5×10^{-8} cm.

TABLE 3

SUMMARY OF AISI 316 MICROSCOPY DATA

	High-Rate Specimen	Low-Rate Specimen
Total Displacements (dpa)	3.3	3.3
Displacement Rate (dpa/sec)	8.4×10^{-7}	1.0×10^{-7}
Irradiation Temperature ("C)	392	371
Test Temperature (°C)	385	385
Mean Void Diameter (nm)	~40	7.0
Void Density (cm^{-3})	$<5 \times 10^{12}$	4.3×10^{14}
Void Volume (%)	<0.02%	10.01%
Frank Loop Mean Diameter (nm)	~50	~28
Frank Loop Density (cm^{-3})	$\sim 8 \times 10^{14}$	2.1×10^{15}
Network Oislocation Density (cm^{-2})	1.9×10^{10}	1.3×10^{10}
Total Dislocation Density (cm^{-2})	3.2×10^{10}	3.1×10^{10}
γ' Precipitate Size (nm)	11	6
γ' Density (cm-3)	1.6×10^{15}	$<1 \times 10^{14}$
Rod Precipitate - Length (nm)	40	17
Rod Precipitate - Density (cm^{-3})	1.1×10^{15}	1.2×10^{14}

Assuming that the areas examined were representative of the specimen as a whole, the predicted yield strength change for the AISI 304 specimens was 304 MPa compared to the measured value of 330 MPa for the high-rate specimen, and 166 MPa compared to the measured 130 MPa for the low rate specimen. This level of agreement is a confirmation of the relationship between microstructure and .yield strenqth. The predominant components causing the hardening of the AISI 304 were Frank loops and voids in both the high- and low-flux specimens.

For the AISI 316 specimens, the predicted yield strength change for the high rate specimen, using $\alpha_p = 3.0$, was 174 MPa compared with the measured value of 147 MPa; and 156 MPa compared to the measured 172 MPa for the low rate specimen. Here, the predominant hardening components were precipitates, dislocations and Frank loops for the high rate specimen while Frank loops, dislocations and voids were the predominant hardener for the low-rate specimen.

It appears that the insensitivity of yield strength to displacement rate at ~400°C in annealed AISI 316 may arise from the fortuitous situation in which a loss in the strength contribution from precipitates as the displacement rate is decreased is offset by a concurrent gain in the strength contributions from voids. There is little likelihood, however, that this compensating effect will occur at other temperatures, displacement rates and fluences.

The two specimens of AISI 316 chosen for analysis do not have exactly the same temperature (392°C for the high-rate specimen and 371°C for the low rate specimen). However, two other specimens which have essentially the same displacement rate (2.3 and 1.9 $\times 10^{-7}$ dpa/sec) and which were irradiated at temperatures of 374 and 424°C exhibit the same amount of hardening. This suggests a relative insensitivity to temperature in this range.

5.4.2 Relationship Between Neutron Flux, Spectra and Fluence

Most studies that are concerned with irradiation damage to material properties relate the property changes with either atomic displacements or with neutron fluence above some threshold energy. Improvements have been reported for correlating changes in ductile-brittle transition temperature of ferritic steels with energy dependent damage functions (dpa) instead of (total) neutron fluence.5 The damage energy concept has also been used to relate changes in yield strength of solution annealed AISI 316 irradiated at ~60°C with fission and high energy neutrons.[6] More recently, this data has been reanalyzed and shown to more closely correlate with a cascade "lobe" production function rather than damage energy.7

For the present study, it has been assumed that the displaced atoms concept is an adequate approach for correlating variations in neutron fluence and spectra. However, the observation of displacement rate effects in both 304 SS and 316 SS means that the present results do not provide direct experimental support for the assumption that displacements per atom can adequately correlate fluence and spectra differences.

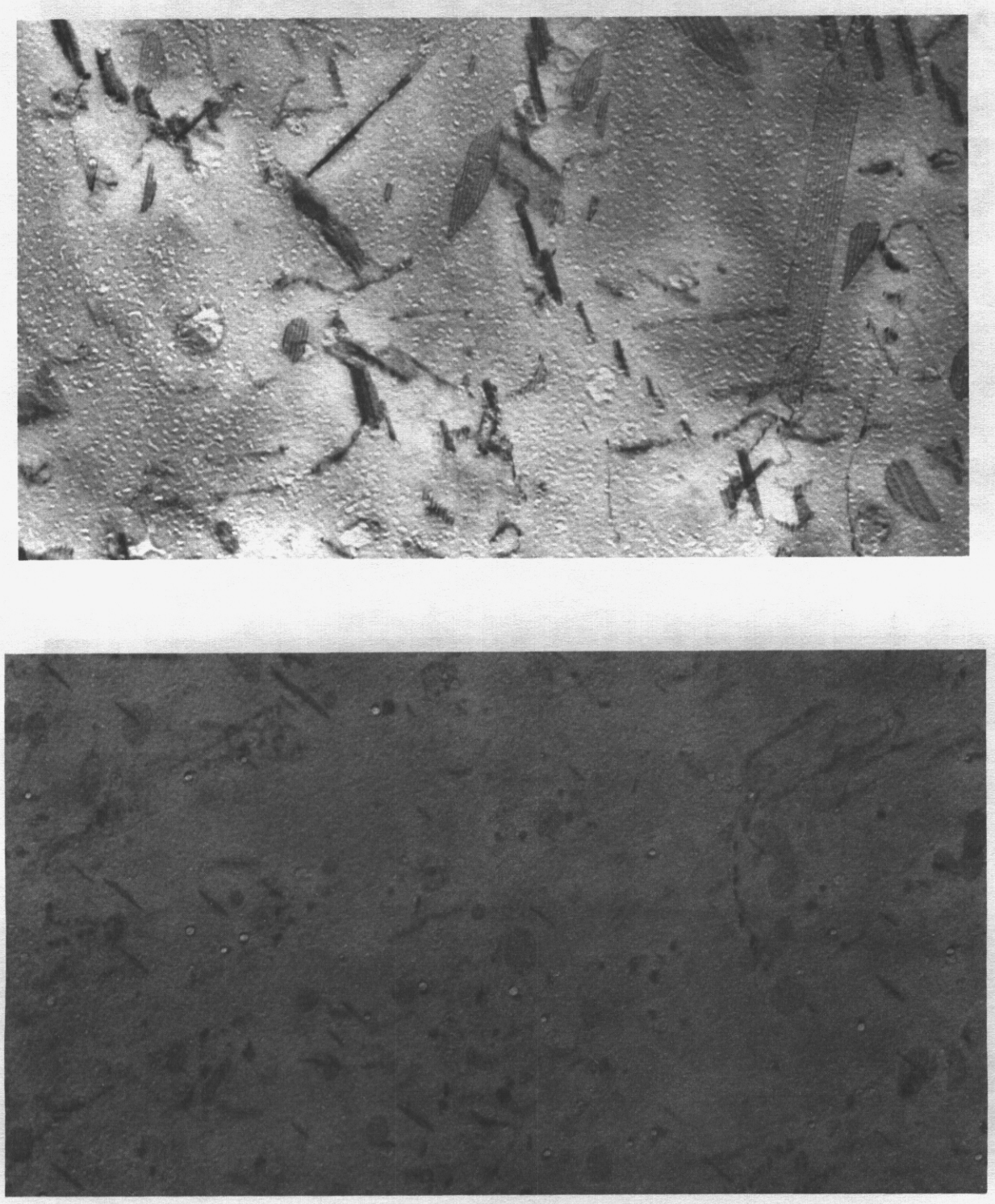

FIGURE 3

Void Microstructures Observed in Solution Annealed AISI 316 Irradiated to 3.3 dpa at the High-Rate (top) and Low-Rate (bottom) Specimens.

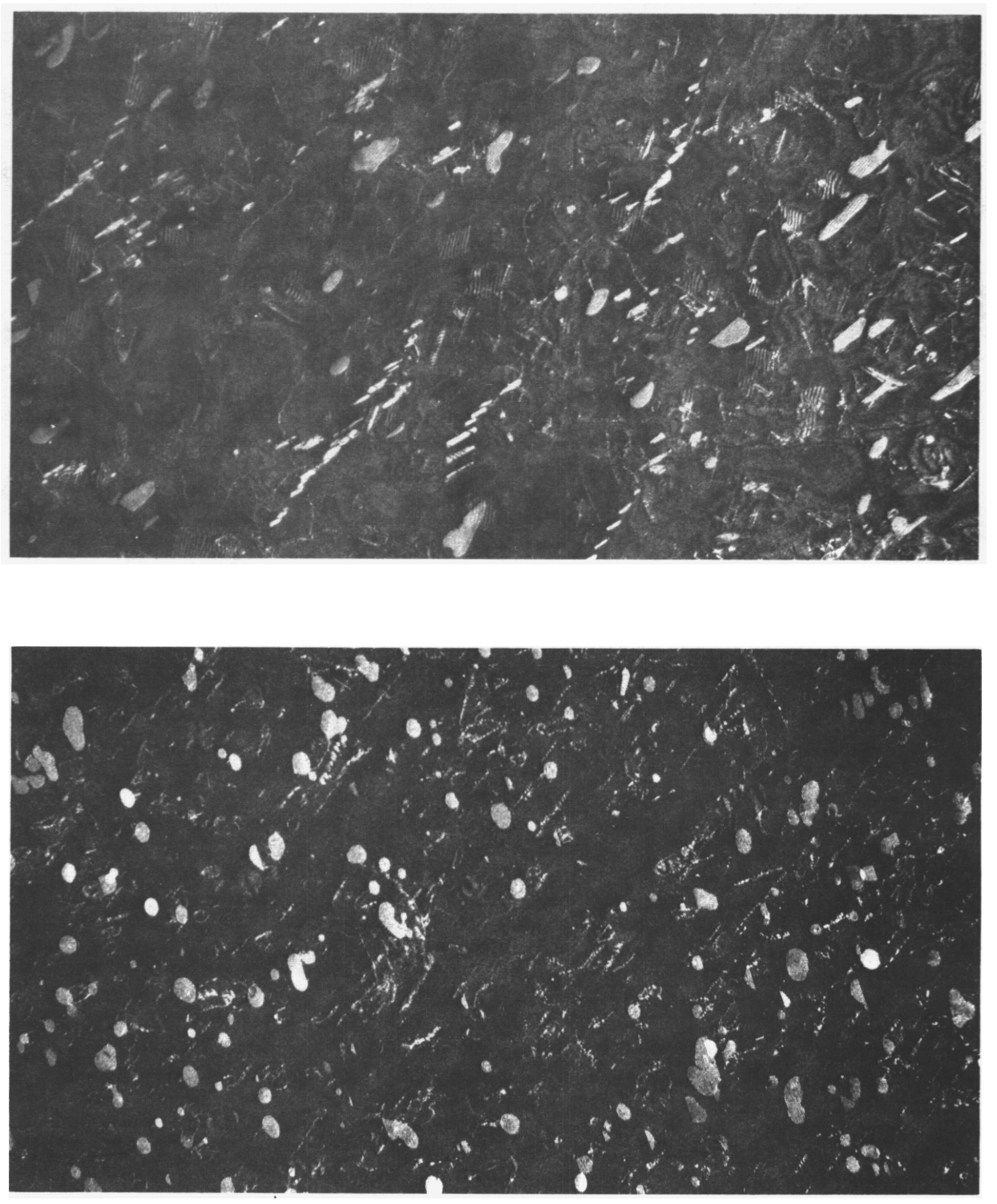

FIGURE 4

Frank Loops Observed **in** the High-Rate (top) and Low-Rate (bottom) Specimens.

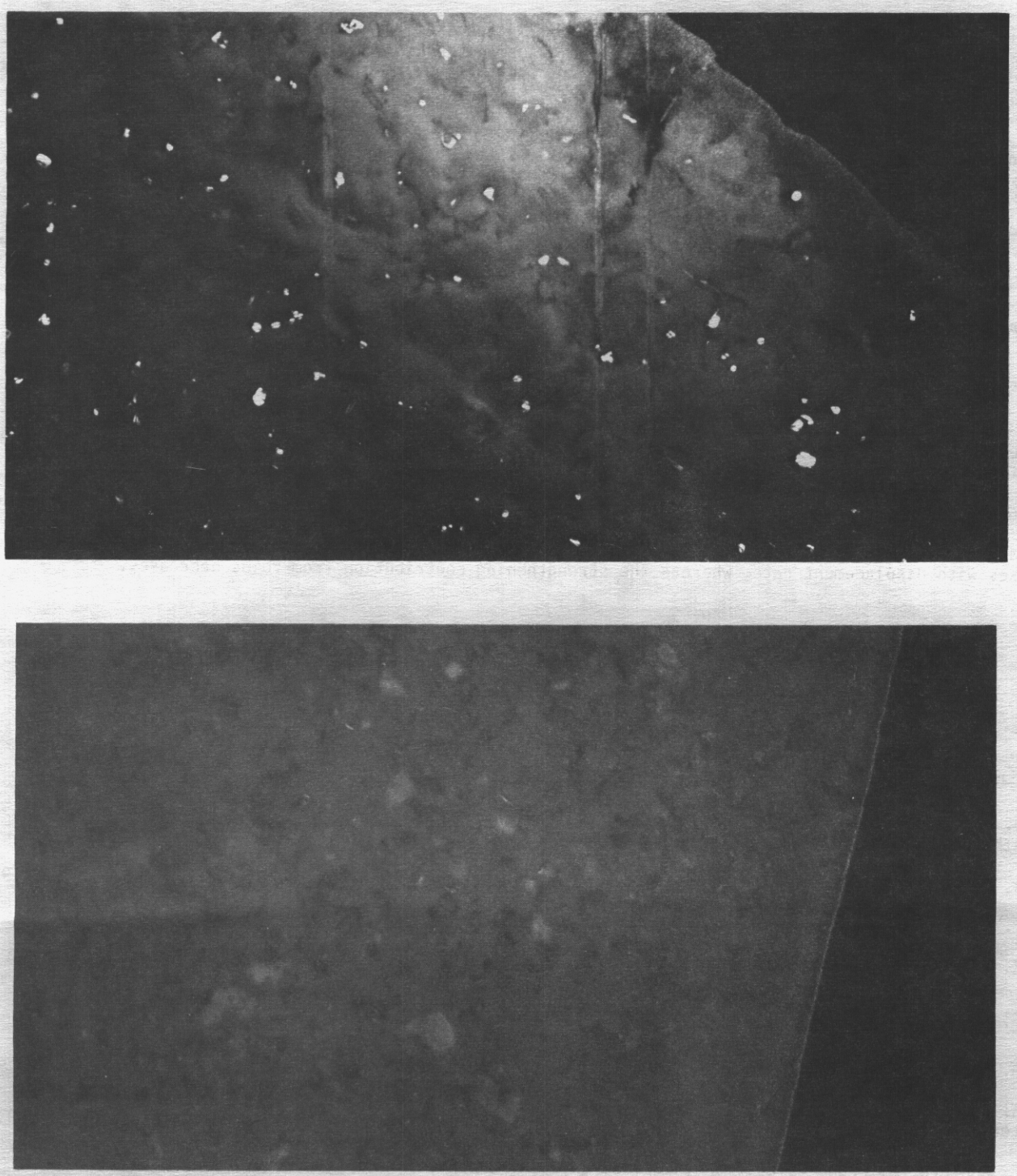

FIGURE 5

Gamma-Prime (γ') Precipitates Observed in the High-Rate Specimen But Not the Low-Rate Specimen.

5.4.3 Related Evidence

The principal microstructural difference of the AISI 304 and 316 reported here was in the formation of a high density of voids in AISI 304 and of γ' precipitates in the AISI 316. Both of these microstructural differences have been related to variations in alloy composition, namely the higher nickel concentration of the AISI 316.[8,9]

Swelling measurements of solution annealed 316 have shown at low temperature ($T \sim 400$-$430°C$) that increases in flux (and neutron energy spectra) shorten the incubation fluence for swelling.[10] At high temperatures ($T > 500°C$), the suecimens irradiated at higher fluxes have a longer incubation fluence.[11]

Recent microstructural data on cold-worked 316 irradiated at 600°C indicate an effect of flux on the Laves phase. High neutron flux and the harder spectra associated with it result in a small volume fraction of Laves phase and in its complete suppression at still higher dose rates of $\sim 2 \times 10^{-6}$ dpa/sec.[12] The cause miaht not be the high flux but rather the shorter irradiation time.

5.5 Conclusions

Annealed specimens of AISI 304 and 316 were irradiated in the EBR-II fast reactor at ~400°C over a range of neutron fluxes and energy spectra. Tensile tests show that the hardening of the AISI 304 is sensitive to the displacement rate while the hardening of AISI 316 is not. However, the microstructures of AISI 304 and 316 are influenced by displacement rate. The increase in yield strength is correlated with the contribution of the various microstructural components produced during irradiation. The insensitivity in the hardening of AISI 316 to displacement rate arises because the strengthening contribution from precipitates increases with displacement rate, whereas the strengthening contribution from voids decreases.

6.0 References

1. R.L. Fish, N.S. Cannon and G.L. Wire, Effects of Radiation on Structural Materials, ASTM-STP 683, pp. 450-465, 1979.

2. H.R. Brager, L.D. Blackburn and F.A. Garner, Damage Analysis and Fundamental Studies Quarterly, Oct-Dec. 82, DOE/ER-0046/12, pp. 101-113, 1982.

3. G.O. Johnson, F.A. Garner, H.R. Brager and R.L. Fish, Effects of Radiation on Structural Materials: Tenth Conference, ASTM-STP 725 pp. 393-417, 1981.

4. F.A. Garner, M.L. Hamilton, N.F. Panayotou and G.O. Johnson, J. Nucl. Matl.103 and 104 pp. 803-808, 1981.

5. R.L. Simons, in reference (2), pp. 178-185.

6. R.R. Vandervoort, E.L. Raymond and C.J. Echer, Rad. Effects 45, pp. 191-198, 1980.

7. H.L. Heinisch and R.L. Simons, Damage Analysis and Fundamental Studies Quarterly Jan-Mar 1982, DOE/ER-0046/9, pp. 147-152, 1982.

8. F.A. Garner, Phase Stability During Irradiation, Proceedings. TMS-AIME, pp. 165-189, 1980.

9. F.A. Garner, "Recent Insights on the Swelling and Creep of Irradiated Austenitic Alloys," J. Nucl. Material Proceedings of the Third Topical Meeting on Fusion Reactor Materials, Albuquerque, NM, 1983.

10. J.L. Boutard, G. Brun, J. Lelimann, J.L. Seran, J.M. Dupony, Irradiation Behavior of Metallic Materials for Fast Reactor Core Components, Proc., Corsica, France, pp. 137-144, 1979.

11. J.L. Seran and J.M. Oupouy, Effects of Radiation on Structural Materials, ASTM-STP 782, pp. 5-16, 1982.

12. L. Boulanger, L. LeNaour and V. Levy, Dimensional Stability and Mechanical Behavior of Irradiated Metals and Allovs, Vol. I; Proc., BNES, pp. 1-4, 1983.

7.0 Future Work

Additional specimens at higher fluence will be sought to determine whether the displacement rate affects the saturation regime. Specimens irradiated to the same dpa and mean spectral energy but at different flux will also be sought to provide single variable dependence.

8.0 Publications

H. R. Brager, L. D. Blackburn and D. L. Greenslade, "The Dependence on Displacement Rate of Radiation-Induced Changes in Microstructure and Tensile Projections of AISI 304 and 316," Accepted for publication in J. Nucl. Material (Proceedings of Third Topical Meeting on Fusion Reactor Materials, Albuquerque, NM, 1983).

SHEAR PUNCH TESTS FOR MECHANICAL PROPERTY MEASUREMENTS IN TEM DISC-SIZED SPECIMENS

G.E. Lucas, J.W. Sheckherd, G.R. Odette, S. Panchanadeeswaran (University of California, Santa Barbara)

1.0 Objective

The purpose of this study was to develop a test technique to complement microhardness in extracting mechanical properties from small volume specimens.

2.0

A shear punch test has been developed to extract strength and ductility information from thin sheet samples as small as transmission electron microscopy (TEM) disc specimens. The test is based on driving a cylindrical punch through a clamped specimen, and instrumenting the punch to obtain a load-displacement curve of the punching process. A number of correlations have been developed between features of the load-displacement curve and mechanical properties such as yield strength, ultimate tensile strength, work hardening exponent and reduction in area.

3.0 Program

Title: Damage Analysis and Fundamental Studies for Fusion Reactor Materials Development

Principle Investigators: G.R. Odette and G.E. Lucas

Affiliation: University of California, Santa Barbara

4.0 Relevant DAFS Program Plan Task/Subtask

Subtask B Mechanical Properties

5.0 Accomplishments and Status

5.1 Introduction

In the effort to develop materials for fusion reactors, a variety of requirements dictate the need for small-specimen mechanical property tests. These include limitations on space in high-energy neutron irradiation facilities, gamma heating limitations in fission reactor irradiation, and in some instances dose considerations in post-irradiation testing. Consequently, a number of efforts are in progress to develop such tests.[1]

While there are no fixed requirements on specimen geometry, it would be desirable to perform tests on samples which are relatively simple and common to other investigations. This reduces fabrication cost and facilitates irradiation capsule design and sample encapsulation. The transmission electron microscopy (TEM) disc has a geometry which is simple, and TEM discs are pervasive in past (i.e., large irradiated alloy inventories) and planned irradiation experiments for nuclear fission and fusion reactor materials development. Consequently, there is interest in developing test techniques to extract mechanical property information from TEM discs.

Microhardness and instrumented microhardness[2] techniques have been applied to TEM disc-sized specimens for this purpose; and while strength information can be obtained from these tests, measures of failure resistance, such as ductility, cannot (at least directly). In addition, the relatively small region of the specimen which is deformed during microhardness testing leads to some restriction on specimen microstructure[1] (e.g., grain size) and aggravates data scatter. Consequently, an investigation of a complementary technique was undertaken which relaxes some of the restrictions associated with sampling volume and provides an opportunity to measure parameters associated with deformation-induced failure.

5.2 Test Technique

The shear punch test is based on a blanking operation common to sheet metal forming.[3] A sheet metal sample is clamped between two dies and a flat, cylindrical punch is driven through the sample, punching a circular disc from it. The arrangement is shown schematically in Fig. 1. We have constructed punch-and-die arrangements capable of punching 6.25 mm and 1 mm and 3 mm diameter discs from sheet metal coupons. The 1 mm punch can be used on TEM discs; and, in theory, the 3 mm punch could be used to blank TEM discs from irradiated sheet stock. Results of tests from the 3 mm and 1 mm punches are reported here.

By performing the punching operation on an instrumented load frame, the load on the punch can be monitored from the load cell as a function of punch displacement. We have performed tests on both an MTS 810 servo-hydraulic machine and Instron 1122 screw-driven machine; and we have monitored punch displacement with measurements of ram displacement in the MTS, crosshead displacement in the Instron, and sample displacement with an electromechanical transducer beneath the specimen (as shown schematically in Fig. 1). Moreover, we have tried both flat-ended and cup-ended transducer arms. For reasons discussed below, load-displacement curves produced by ram/ crosshead displacement are "cleaner" and more easily analyzed.

A typical load-displacement curve is shown in Fig. 2 along with micrographs depicting the region of the sample at the punch-die interface. As can be seen, the load-displacement curve exhibits features typical of load-displacement curves produced in uniaxial tension tests of metals; that is, an initial linear portion, followed by a non-linear region in which load continues to increase with displacement, a load maximum, and a decrease in load to failure.

Analysis of the material response at the punch-die interface, as indicated in Fig. 2, has shown that the deviation from linearity corresponds to the onset of permanent indentation of the specimen by the punch. Further deformation proceeds in a process zone corresponding in width, approximately, to the tolerance between the punch and die (~ 25 μm). This results in a deformation volume of ~4×10^{-2} mm^3, considerably larger than the ~4×10^{-4} mm^3 plastic zone produced in microhardness.[4-6] A number of slip-line fields have been calculated which approximate flow in this region; and while the stress state is primarily shear, considerable tension and bending[7] also occur. Moreover, the contribution of these components increases with increasing punch-die tolerance.[7] Within this process zone the material work hardens sufficiently to compensate for the decrease in load-bearing thickness as the punch progresses, and the load increases with increasing punch displacement. However, a point of plastic instability is reached beyond which strain-hardening does not compensate for specimen thinning and the load falls with increasing displacement. Finally, the specimen fails by separation. For materials which fail in tension by microvoid growth and coalescence, this occurs primarily by microvoid growth and microcrack formation in the process zone following the onset of plastic instability and the ultimate formation of one or more macrocracks which rapidly propagate through the remaining ligament.[7-8] In addition, macrocracks may nucleate at the punch-die-specimen interfaces and propagate more slowly prior to this final failure.[9]

Consequently, there are many similarities between shear punch and tension tests manifested in similar load-displacement curves. Moreover, analogous plastic, instability and microscopic failure processes are exhibited in shear punching, providing the potential to derive useful ductility parameters. Because of the complexity of the stress and deformation fields in the process zone, however, we have initially attempted to develop empirical correlations between shear-punch data and uniaxial data for the punch and dies we have investigated.

5.3 Results and Discussion

We have performed shear punch tests on a variety of materials including stainless steel, carbon steel, low alloy steel, brass, aluminum and copper in metallurgical conditions ranging from highly cold-worked to fully recrystallized and in both the unirradiated and irradiated condition. In addition, we have obtained uniaxial tensile data on the unirradiated materials from sheet tensile specimens. Correlations between uniaxial and shear punch data are shown in Figs. 3-5, and their basis discussed below.

We have found that the following relationship correlates both the shear punch yield load P_y with the uniaxial yield stress of the material, and the maximum shear punch load P_m with the ultimate tensile strength:

$$\sigma_{eff} = \frac{P - F}{2\Pi rt} = C\sigma \qquad (1)$$

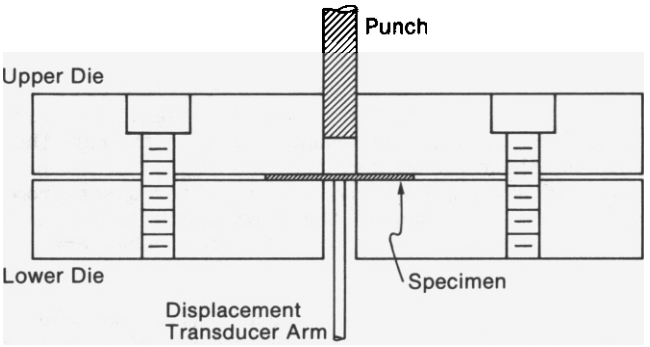

FIGURE 1. Schematic illustration of the shear punch apparatus.

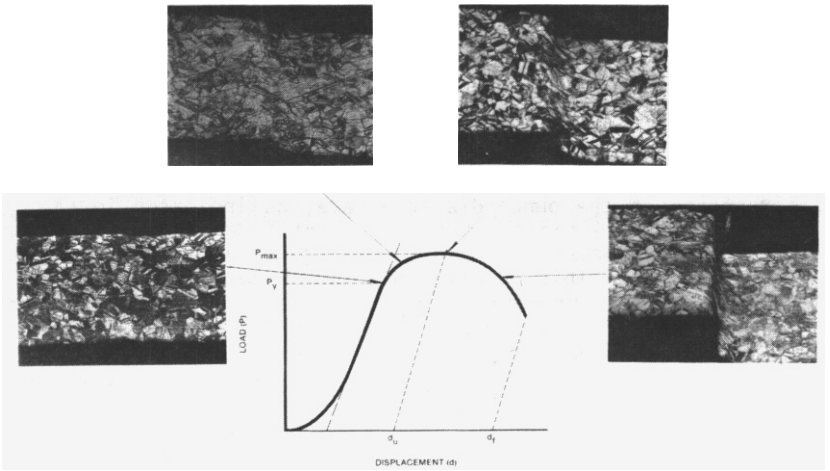

FIGURE 2. Load-displacement curve obtained in a shear punch test and micrographs showing the state of deformation in a yellow brass sample at different stages of the test.

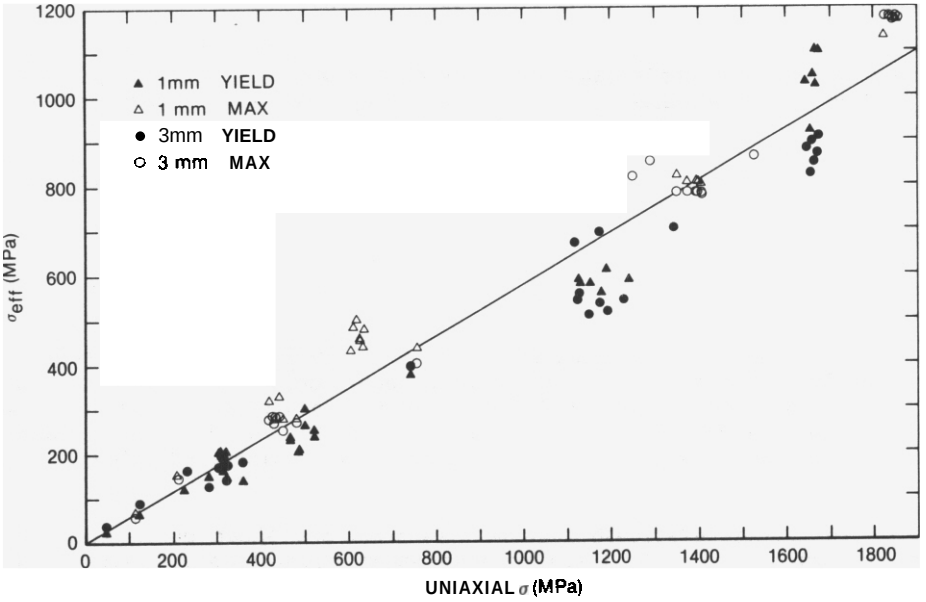

FIGURE 3. Comparison of uniaxial yield stress and ultimate tensile strength with the shear load parameter $P-F/2\pi rt$.

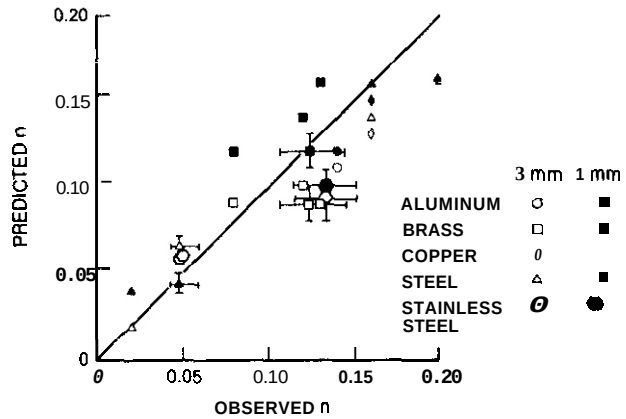

FIGURE 4. Comparison between measured values of work-hardening exponent n and value predicted from shear punch tests.

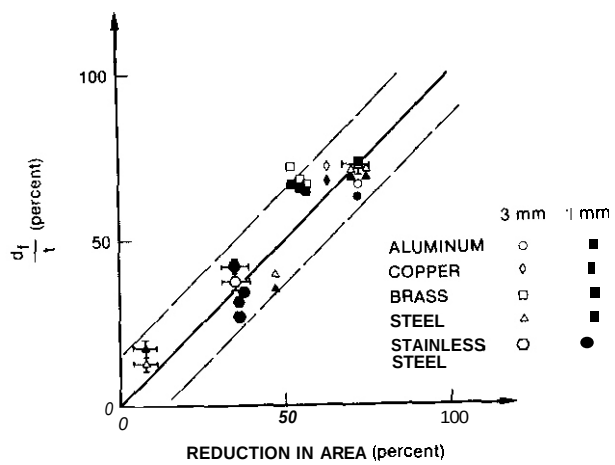

FIGURE 5. Comparison between measured values of reduction of area in tensile specimens at failure and D_f/t.

where P is the shear punch load, a is the corresponding uniaxial stress, F is the function between the punch, specimen and die (which can be determined from the load-displacement trace), r is the punch diameter, t is the specimen thickness, and C is a constant which can be determined from regression analysis. Values of σ_{eff} are plotted against a in Fig. 3 for both yield and maximum loads. We have regressed the data in several ways. Taking yield data (with a σ_Y < 1400 MPa) alone, we have found that C ~ 0.54; taking maximum load data alone C ~ 0.62; and taking yield and maximum laod data combined C ~ 0.59. The curve for this latter value of C is also shown on Fig. 3. Johnson and Slater[10] have found a similar relationship between tensile strength and maximum load for blanking operations, but we find the relationship holds for yield as well. It is interesting to note that these regression coefficients are close to 1/43, the ratio of shear to uniaxial stress in the von Mises yield criterion, suggesting that the stress state in the process zone is largely shear. However. it is clear from fractography of the punched specimens that as the post-yield strain develops, a significant hydrostatic stress develops in the process zone to drive microvoid growth and coalescence processes typical of failure in uniaxial tension tests.

The 95% confidence interval on predicted σ for a given P is ~ ± 16% for yield and ~ ± 7% for UTS. Much of the uncertainty in the yield stress correlation comes from difficulty in determining P_Y at the point of deviation from linearity. As mentioned earlier, we have tried several experimental methods to facilitate this determination. and we have found that load-displacement curves produced by ram/ crosshead displacement are easiest to analyze and provide the most reproducible results. In addition, standardized computer-aided procedures to determine yield points are under investigation, and these may reduce scatter.
By assuming a relationship of the form $\sigma = K \varepsilon^n$, and a constitutive value of $\varepsilon = .002$ at yield, n can be determined from the following relationship

$$(\frac{n}{.002})^n = \frac{P_m}{P_y} \qquad (2)$$

Figure 4 shows that this relationship works quite well for the materials we have investigated, and actually works somewhat better for the lmm than the 3mm punch . The 95% confidence interval on n for a given P_m/P_Y is approximately ± 40% of n. Again, much of this might be attributed to uncertainties in measuring n and P_Y as well as the simplicity of the empirical model.

Finally. we have found that the punch displacement to failure correlates quite well with the reduction of area (RA) at failure in the tension test with the relation RA = d_f/t. Figure 5 demonstrates this. The 95% confidence interval on RA for a given d_f/t is ~ ± 30% of RA.

5.4 Conclusion

The shear punch test is a relatively straightforward test which can be performed on specimens as small as TEM discs. The deformation and failure phenomena which occur during shear punching are similar to and related to those exhibited during uniaxial tension tests. Hence, shear punch loads and displacements have been correlated successfully with uniaxial tensile and yield strengths and with plastic instability and failure parameters such as the work-hardening exponent and reduction in area. This technique should thus be quite useful in testing irradiated material in the fusion program.

6.0 References

1. G.E. Lucas, J. Nucl. Mater., 117 (1983) 327.
2. G.E. Lucas and N. Panayotou, J. Nucl. Mater., 103 and 104 (1981).
3. T.M. Chang and H.W. Swift, J. Inst. Metals, 78 (1950) 119.
4. W. Johnson, R. Sowerby, J. Haddow, Plane Strain Slip Line Fields, London, Edward Arnold, 1970.
5. W. Dos Santos, A. Organ, Int. J. Mach. Tool Des. Res., 13 (1973) 217.
6. Y. Kasuga, S. Tsutsumi, J. Mori, Bull. Jap. Soc. Mech. Engrs. 20 (1977) 1329.
7. A.G. Atkins, Int. J. Mech. Sci., 22 (1980) 215.
8. C.F. Noble and P.L.B. Oxley, Int. J. Prod. Res. 2 (1964) 265.
9. A.G. Atkins, Phil. Mag. 43A, 3 (1981) 627.
10. W. Johnson and R.A.C. Slater, Proc. CIRP-ASTME (1967) 801.

7.0 Publications

"Shear Punch Tests for Mechanical Property Measurements in Tem Disc-Sized Specimens", G.E. Lucas, J.W. Sheckherd, G.R. Odette, S. Panchanadeeswaran, presented at the Third Topical Meeting on Fusion Reactor Materials at Albuquerque, NM, September 19-22. 1983.

CHAPTER 5

CORRELATION METHODOLOGY

A THEORETICAL ASSESSMENT OF THE EFFECT OF MICROCHEMICAL, MICROSTRUCTURAL AND ENVIRONMENTAL MECHANISMS ON SWELLING INCUBATION IN AUSTENITIC STAINLESS STEELS

G.R. Odette and R.E. Stoller (University of California, Santa Barbara)*

1.0 Objective

The objective of this work is to determine the relative influence of a variety of environmental. microstructural and microchemical variables on the swelling incubation time in irradiated AISI 316 stainless steel.

2.0 Summary

The sensitivity of swelling incubation in austenitic steels is assessed. A critical-sized helium bubble-to-void conversion model is used to evaluate the influence of helium partitioning, sink strength, surface energy and diffusion rates which mediate microchemical, microstructural and environmental effects. Several new mechanisms of precipitate-enhanced (and retarded) void formation are proposed. While such microchemical effects are important, they were not found to be dominant in all cases. The results suggest that unless fine distributions of helium can be maintained, swelling will be higher in fusion than in either fast or mixed spectrum fission environments.

3.0 Program

Title: Damage Analysis and Fundamental Studies far Fusion Reactor Materials Development

Principle Investigators: G.R. Odette and G.E. Lucas

Affiliation: University of California, Santa Barbara

4.0 Relevant OAFS Program Plan Task/Subtask

Subtask C Correlation Methodology Effects of Helium on Microstructure

5.0 Accomplishments and Status

5.1 Introduction

Neutron-induced swelling in austenitic stainless steels divides into two regimes: incubation, characterized by significant microstructural and microchemical evolution and little cavity swelling; and steady-state swelling, characterized by rapid void growth, coupled with a tendency towards saturation of a number of other microstructural and microchemical features[1]. The steady-state swelling rate appears to be relatively constant over a range of material and environmental variables[2], although the extent of this range has yet to be determined. Unfortunately, these rates are high (up to 1%/dpa), suggesting that structural lifetimes will be set by the incubation period, which is sensitive to an array of environmental and material variables.

Garner and Brager et al. propose that the incubation period is largely governed by the rate of an "inevitable" microchemical evolution "leading to an endpoint independent of most environmental and thermomechanical variables"[2]. Removal of nickel from the matrix by precipitates is suggested to be the most critical rate-controlling process governing void nucleation, with other factors such as helium and microstructure playing a "necessary but not rate-determining role". We believe that there is data which suggests that these conclusions cannot be generally applied and that there are questions concerning the empirical and analytical basis for this phenomenological microchemical model[3]. In this paper we use a

* Financial support for one of the authors (Stoller) was also provided by the Magnetic Fusion Energy Technology Fellowship Program.

physical model of swelling incubation to quantitatively evaluate the influence of a number of microchemical, microstructural and environmental factors.

Our model postulates that the incubation period is the time required for helium bubbles to grow sufficiently to undergo transition to voids. The "critical" number of helium atoms (m^*) is dictated by a number of microstructural and microchemical phenomena, while the total helium generation required to reach m^* is determined by partitioning between various sinks. The model is semi-empirical since it 1) broadly describes the observed sequence of events leading to rapid void swelling; 2) directly incorporates microstructural information as input parameters; and 3) is calibrated to swelling data. Descriptions of the basic model, including a discussion of its limitations, have been published previously[4,5].

In this work, sensitivity of m^* to variations in parameters reflecting proposed environmental, microstructural and microchemical mechanisms, and the effect of helium partitioning on swelling incubation times are evaluated.

5.2 The Critical Helium Content for Bubble-to-Void Conversion

The critical helium content m^* obtains when the bubble and void roots of the radial velocity function $\dot{r} = f(r) = 0$ are equal. For a real gas this must be found numerically, but the results are simply[6]

$$m^* = g(\ell n\ \phi)\ F_v\ (\frac{\gamma}{kT})^3\ \ (\frac{1}{\ell n\ \phi})^2, \qquad (1)$$

where ϕ is the vacancy minus interstitial impingement rate or effective supersaturation. An analytical expression for the real gas correction factor $g(\ell n\ \phi)$ has been published elsewhere[6]. The parameter F_v is related to various surface/interface energies for bubbles on precipitates and γ is the matrix surface energy.

Calculation of ϕ is based on steady-state vacancy and interstitial balance equations with whatever level of detail is appropriate, i.e. with multiple sink components, bias factors, defect traps, cascade clusters and the like. For the case with only dislocations and bubble sinks and negligible recombination,

$$\phi = \frac{G_d}{S_d D}\ (1 - (\frac{z_b}{z_d}\frac{S_b}{S_d} - \frac{z_b}{z_d})/(\frac{z_b}{z_d}\ \frac{S_b}{S_d} + 1)) + 1 \qquad (2)$$

Here the $z_{b,d}$ are interstitial bias factors (with vacancy bias factors taken as 1), $S_{b,d}$ are the sink strengths and D the self-diffusion coefficient. Hydrostatic stress σ may be treated by simply adding $\Omega\sigma/kT$ term to Eq. 2, where Ω is the vacancy volume.

5.3 The Effects of Microstructural, Microchemical and Environmental Variables on Bubble-to-Void Conversion

5.3.1 The Critical Helium Number (m^*)

Fig. 1 shows the temperature dependence of the critical number and the associated critical radius using the nominal parameters given in Reference 6. In the following sections we discuss briefly the influence on these results of possible microstructural, microchemical and environmental mechanisms as mediated by the model parameters.

Fig. 2a shows that m^* increases rapidly with decreasing values of the net bias parameter $(z_d - z_b)/z_b$ below $\sim$ -.2-.4. Steady-state swelling rates suggest values of $z_d \gtrsim 1.2$[3], which is also consistent with theoretical estimates[7]. Small bare bubbles can be biased towards interstitials ($z_b > 1$)[8]. However, Wolfer and Mansur have shown that solute segregation can reduce or even reverse this bias (i.e. $z_b < 1$); and that even for bare bubbles $z_b = 1$ at $r_b \gtrsim 2$ nm. Since stable bubbles are likely segregation sites and critical radii are generally equal to or greater than 2nm it appears that bias does not have an important effect on void swelling incubation.

We also note that bias enhancement due to radiation-induced segregation of nickel to cavities[9] does not appear consistent with the enhancement of swelling by matrix nickel depletion as proposed by Garner and Brager[2]. This obtains directly from observations that matrix nickel depletion should lower the difference

between nickel content in segregated and matrix regions; and segregation-enhanced bias effects decrease as this difference decreases.

The critical number m^* is proportional to F_v, which is expected to have values in the range from ~ .25 - 1 (matrix), and $m^* \alpha \gamma^3$, as shown in Fig. 2b. Chromium is known to be interface active in nickel and fcc iron[10], thus it may segregate and lower values of γ, perhaps even forming stable oxide surface layers. If radiation-induced segregation of nickel replaces chromium at void surfaces, increases in m^* could be expected. Such chromium depletion behavior is indeed reported.[11] This mechanism may, in part, explain the observation that increasing nickel reduces swelling.

Reliable values of alloy self-diffusion coefficients D are not available at low temperatures. Estimates range from $D \sim 10^{-20}$ to 3×10^{-19} cm^2/s at 500°C[12,13]. Self-diffusion rates are known to be sensitive to solute content; "clean" model materials have lower rates than "impure" alloys. For example, available high temperature data suggests that a few percent silicon could increase D by ~ 2[12,13]. Fig. 2c shows that such variations can have large effects on m^*. This emphasizes an important microchemical role of precipitates in acting as sinks for solutes and impurities in commercial alloys.

Fig. 2c also suggests that m^* is sensitive to the displacement rate G_d. However, in this simplified version of the model we have neglected the effect of intrinsic bulk recombination and solute trapping, which can be treated by multiplying G_d by the defect fraction reaching sinks. Coupled with reported variations in microstructure with damage rate[14] and the effect of transient subvisible defect clusters the predicted effects of damage G_d are decreased or reversed.

Fig. 2c also shows that m^* is very sensitive to dislocation sink strength S_d (note $\phi \alpha G_d/S_d D$) which typically varies by factors of ~ 3 or more. Under normal circumstances, this appears to be the major source of microstructural influence on m^*. One effect of titanium addition to 20% cold-worked 316 stainless steel may be extended incubation times as a result of TiC stabilization of the dislocation density (15).

Stress on dislocation sources is predicted to have a relatively large effect on m^* only at high temperatures, as shown in Fig. 2d. Growing precipitates may provide significant sources of internal stresses (acting on interface and near boundary dislocations). Thus, preferential void formation on phases with negative misfit strains would be expected, while precipitates with positive misfit strains would be expected to retard void nucleation.[15]

Swelling calculations usually assume dislocations are free to climb. However, bowing of pinned dislocations, resulting in lower vacancy concentrations in local equilibrium, would be expected in structural alloys. This can be modeled approximately as an alloy strength parameter acting as an "effective" negative (back) stress. This might also partly explain the swelling resistance of commercial relative to soft model alloys.

For breeder reactor conditions the bubble sink strength S_b is small and has a minor effect on m^*, as shown in Fig. 2e. However, high helium generation rates increase cavity densities[16]. When the bubble-to-dislocation sink strength approaches 1, significant increases in m^* result. This can contribute to a bifurcation in cavity evolution from void to bubble-dominated paths[15].

Assuming that they are unbiased, subvisible sinks S_s, in the form of very small gas bubbles or cascade-induced clusters, have the same effect as bubble sinks shown in Fig. 2e. The possible importance of such sinks is shown by the swelling resistance imparted by cold preimplanted helium.[17]

Fig. 2f shows m^* as a function of the strength of an equilibrium sink S_a capable of absorbing excess vacancies. Examples would be large voids ($P << \gamma/r$) or grain/ subgrain boundaries. Hence, an increase in void sink strength contributes to trapping of cavities in the bubble category leading to the "bimodal" cavity distributions which are often observed.[15]

It is well known that interphase boundaries are often poor vacancy sources and sinks.[18] However, this may not be true for interstitials; hence, precipitates may be biased towards interstitials (S_i). Negative lattice misfit precipitates would produce a similar effect. For simplicity we assume $z_i^v = 0$ bnd $z_i^i = 1$ and neglect vacancy emission. Fig. 2g shows that sinks of this type can cause a modest detrease in m^*.

Conversely, we might postulate a second type of precipitate sink, S_v, which is highly biased for vacancies, $z_v^i = 0$, $z_v^v = 1$. This might be associated with precipitates with large positive misfit strains,[19] Fig. 2h shows that a small S_v can have a very large effect on m^*.

Of course, such effects would be transient and associated with growing second-phase particles. However, they may be sufficient to boost cavities past critical sizes or, alternatively, suppress swelling for an extended period. The latter may, in part, explain the behavior of titanium-modified steels which appear to be swelling resistant when MC carbides with positive misfit strains are present.[20]

5.3.2 Helium Partitioning

It appears that most of the helium reaches sinks, including grain and subgrain boundaries and growing voids.[21] Dislocations and precipitates probably act as efficient collectors for bubbles; partitioning can be estimated based on relative time dependent (i.e., evolving) sink strengths. The number of bubbles is a particularly important partitioning parameter; previous modeling efforts have used empirical guidance to select bubble density parameters.

The bubble density N_b is known to scale with the helium generation rate G_{He}, as $N_b \propto G_{He}^p$ with $p \sim 0.5$ to 1.[17] Figure 3 shows calculated bubble-to-void conversion exposures as a function of G_{He} and P for 500 and 600°C; here we assume half the helium reaches the bubbles and a precipitate associated reduction in m^* by a factor of 0.1 at 600°C.

At moderate values of p (~ 0.5) the conversion dose I_{bv} decreases continuously with increasing G_{He}. However, at high values of p (p = 0.75 to 1), I_{bv} passes through a minimum increasing rapidly thereafter.[6,17] We have previously discussed this "bifurcation" in the path of cavity evolution as dictated by G_{He}. The primary practical implication appears to be that the very high bubble density induced by mixed spectrum reactors may, in some cases, produce lower swelling than experienced in either fission or fusion devices. In contrast, for lower G_{He} and/or values of the scaling exponent p, I_{bv} is decreased significantly. This suggests lower incubation and higher swelling for fusion environments. Note, these calculations do not directly account for the exposure required to produce the microchemical conditions assumed in the critical bubble calculations. This would be expected to reduce the absolute effect of G_{He} and p on swelling incubation.

5.4 Implications to Fission-Fusion Swelling Correlations and Alloy Development

These results show that the critical number of helium atoms required for bubble-to-void conversion is sensitive to a variety of microchemical and microstructural parameters. The relative importance of the various parameters discussed above is shown in Figure 4. It appears that precipitation of radiation-induced or enhanced phases such as η, G and laves promotes swelling in 316 stainless steel and, indeed. may be necessary at higher temperatures. There are a number of mechanisms by which precipitation can enhance void formation, and it is not possible to identify specific processes which are likely to have general dominance (i.e., nickel depletion). In addition, precipitates such as TiC which result in refined bubble microstructures may reduce swelling by lengthening incubation times. Further, the effect of helium on microchemical processes is still a subject of considerable controversy but has not been addressed here.[22]

Microstructural factors have an important quantitative effect on m^*. This is particularly significant to fission-fusion correlations if environmental differences result in large and qualitative changes in microstructure, as is observed in comparing fast-to-mixed spectrum reactor irradiation data. Helium partitioning is primarily mediated by microstructural factors such as cavity density, which is itself influenced by helium generation rates. This suggests a particularly important role of cavity density scaling laws.

We believe that most evidence suggests that the net effect of increased helium in going from fission to fusion conditions will be to reduce incubation times.

Finally, this analysis supports what has been a fundamental goal of austenitic alloy development for fusion reactors, namely setting conditions to encourage the formation and sustenance of a fine distribution of helium. If the use of tailored phases such as MC turns out to be inherently doomed because of inevitable instabilities, other approaches to forming and maintaining such distributions should be sought.

6.0 References

1. G.R. Odette, JNM 86 (1979), 533.
2. H.R. Brager and F.A. Garner, JNM 117 (1983) 159.
3. G.R. Odette and P.J. Maziasz. to be published.
4. R.E. Stoller and G.R. Odette, JNM 104 (1981) 1361.
5. R.E. Stoller and G.R. Odette, Effects of Radiation on Materials-11, ASTM-STP 782 (1982) 275.
6. R.E. Stoller and G.R. Odette, Damage Analysis and Fundamental Studies Quart. Prog. Rpt. 18, DOE/ER-0046/10 (1982) 199.
7. P.T. Heald, Phil. Mag. 31-3 (1975) 551.
8. W.G. Wolfer and L.K. Mansur, JNM 91 (1980) 265.
9. W.G. Wolfer, F.A. Garner and L.E. Thomas, Effects of Radiation on Materials 11, ASTM-STP 725 (1982) 1023.
10. L.E. Murr, Interfacial Phenomena in Metals and Alloys (Addison Wesley, Reading, Mass 1975).
11. N.Q. Lam, JNM 117 (1983) 106.
12. W. Assassa and P. Guiraldenq, Met. Sci. 12-3 (1978) 123.
13. S.J. Rothman, L.J. Nowicki, G.E. Murch, J. Phys. F-Met Phys. 10 (1980) 383.
14. L. Lenaour, M. Vouillon and V. Levy, Effects of Irradiation on Materials-11, ASTM-STP 725 (1982) 310.
15. Maziasz, P.J.. Horak, J.A. and Cox, B.L., TMS-AIME Symposium on Phase Stability During Irradiation, Pittsburgh, PA (1980) 271.
16. G.R. Odette, P.J. Maziasz and J.A. Spitnagel, JNM 104 (1981) 1289.
17. A. Hishinuma, J.M. Vitek, J.A. Horak and E.E. Bloom, Effects of Radiation on Materials 11, ASTM-STP 725 (1982) 92.
18. J.E. Harris. Met. Sci. J. 7 (1973) 1.
19. Maziasz, P.J., TMS-AIME Symposium on Phase Stability During Irradiation, Pittsburgh, PA (1980) 477.
20. P.J. Maziasz and T.K. Roche, JNM 104 (1981) 797.
21. J.A. Spitznagel, S. Wood, N.J. Doyle, W.J. Choyke. J.N. McGruer, J.R. Townsend and R.B. Irwin, JNM 104 (1981) 1463.
22. P.J. Maziasz. to be published in the Proceedings of the Third Topical Meeting of Fusion Reactor Materials, Sept. 19-22, 1983, Albuquerque, NM.

7.0 Publications

"A Theoretical Assessment of the Effect of Microchemical, Microstructural and Environmental Mechanisms on Swelling in Austenitic Stainless Steels", G.R. Odette and R.E. Stoller, Presented at the Third Topical Meeting on Fusion Reactor Materials at Albuquerque, NM, September 19-22, 1983.

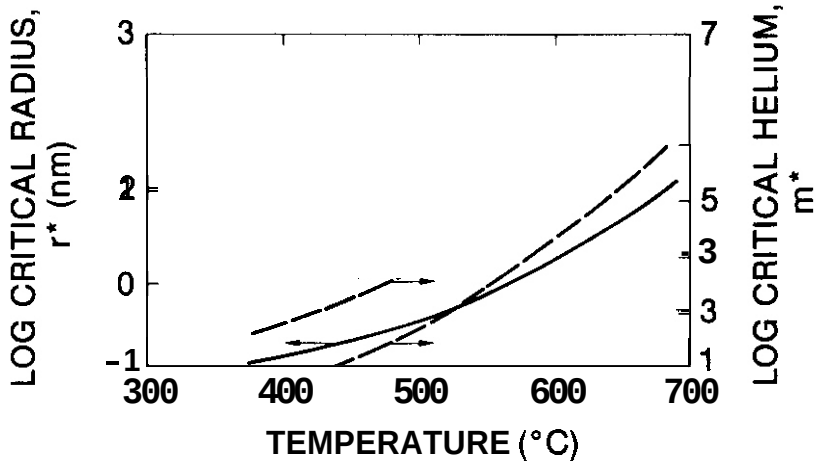

FIGURE 1. Temperature dependence of the critical helium number, m*, and the critical bubble radius, r*.

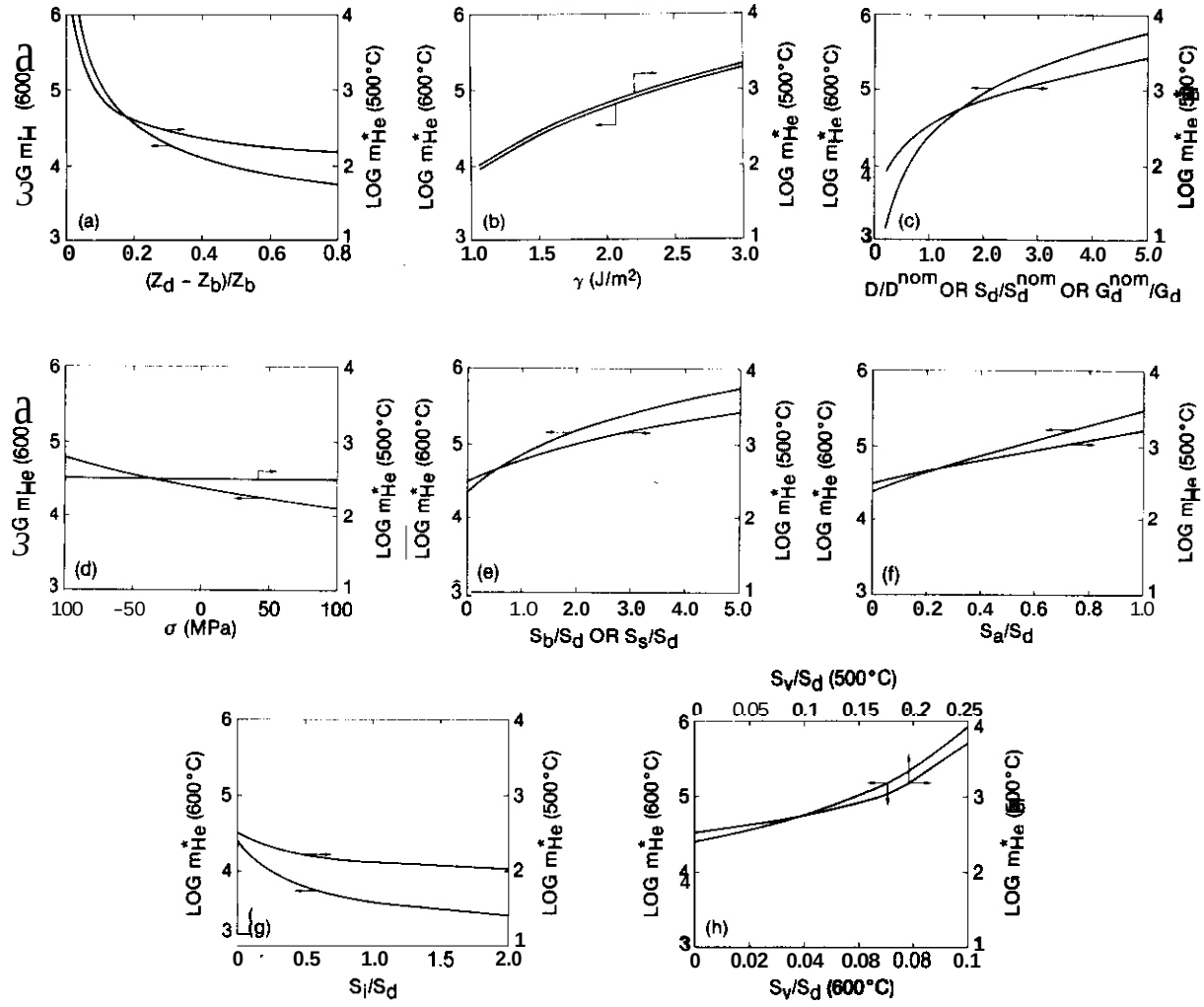

FIGURE 2. Dependence of the critical helium number for bubble-to-void conversion, m*, on various microstructural, microchemical and environmental variables (see text for an explanation of symbols).

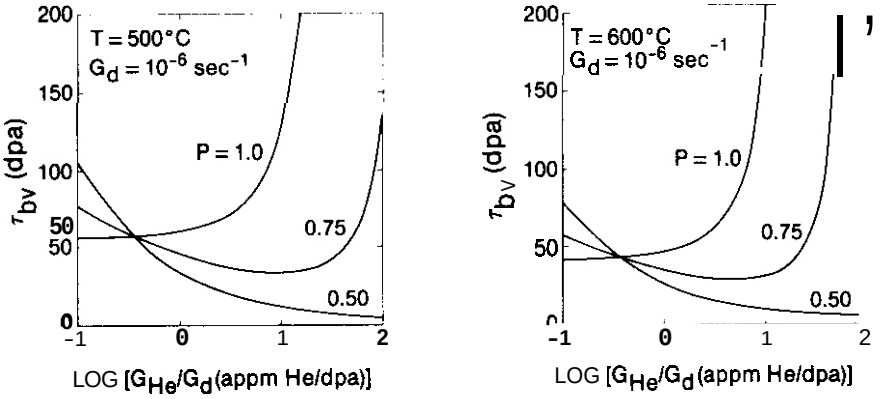

FIGURE 3. The influence of helium to dpa ratio on the bubble-to-void conversion exposure, τ_{bv}. The parameter p is the assumed scaling of the cavity density (see text).

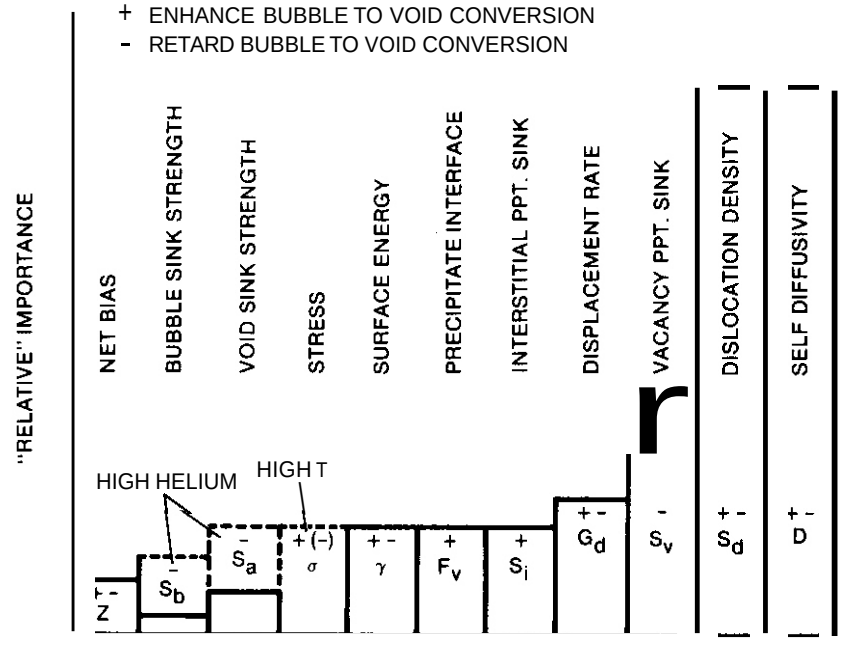

FIGURE 4. Relative influence of various model parameters on the critical number.

FACTORS THAT DETERMINE THE SWELLING BEHAVIOR OF AUSTENITIC STAINLESS STEELS

F.A. Garner (Hanford Engineering Development Laboratory) and W.G. Wolfer (University of Wisconsin)

1.0 Objective

The object of this effort is to provide models describing the behavior of irradiated alloys and use these models in development of fission-fusion correlations.

2.0 *Sumnary*

Once void nucleation subsides, the swelling rate of many austenitic alloys becomes rather insensitive to variables that control the transient regime of swelling. Models are presented which describe the roles of nickel, chromium and silicon in void nucleation. The relative insensitivity of "steady-state" swelling to temperature, displacement rate and composition is also discussed.

3.0 Program

Title: Irradiation Effects Analysis
Principal Investigator: D. G. Ooran
Affiliation: Hanford Engineering Development Laboratory

4.0 Relevant Program Plan Task/Subtask

Subtask II.C.l Effects of Material Parameters on Microstructure

Subtask II.C.16 Composite Correlation Models and Experiments

5.0 Accomplishments and Status

5.1 Introduction

Neutron-induced swelling of austenitic alloys can be characterized by a transient regime followed by a regime of essentially constant swelling rate. The latter regime is often misdesignated as "steady-state". In some alloys, the transient is rather abrupt, but in others the transient regime persists, yielding curvature to swelling levels of 20% or morel. Recently there has emerged a reasonably coherent description of the major compositional, fabricational and environmental factors which influence swelling. This paper reviews our conception of these factors, progressing from simple alloys with uncomplicated irradiation histories to more complicated alloys and histories.

5.2 Simple Fe-Ni-Cr Ternary Alloys

Johnston and coworkers first demonstrated with self-ions the sensitivity of swelling to nickel and chromium levels[2,3]. As shown in Figure la the primary influence of nickel lies in the duration of the transient regime. While it appears that the post-transient swelling rate is influenced to a lesser degree, it has recently been shown that this is an illusion which arises from the previously unsuspected distortion of swelling when determined by step-height measurements[4]. It was also shown that self-ion irradiations are dominated by injected interstitials, which distort the temperature and compositional dependence of swelling relative to that of neutron irradiations[4,5].

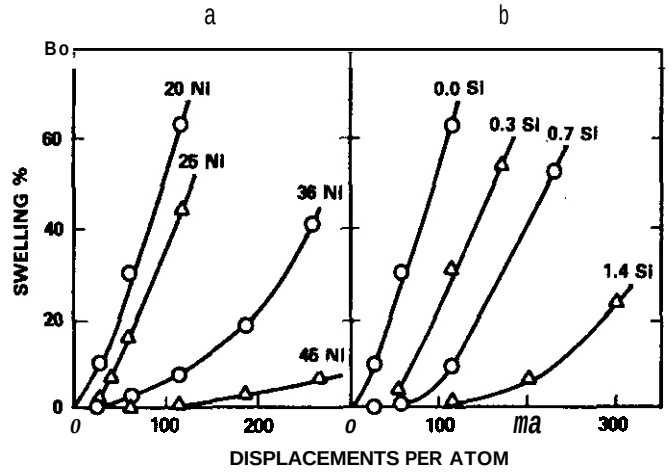

FIGURE 1. Ion-Induced Swelling of Fe-15Cr-XNi and Fe-15Cr-20Ni-XSi Alloys at 675°C.[2,3]

Neutron irradiations of Fe-Ni-Cr alloys in EBR-II have shown that nickel and chromium influence void nucleation and therefore the duration of the transient regime[6,7]. At a given temperature, however, the saturation void density is rather insensitive to composition. Unlike ion irradiations, neutron-induced post-transient swelling rates are ~1%/dpa, relatively insensitive to both composition and temperature[8,9] as shown in Figure 2. For each alloy there is a break-away temperature above which the transient is temperature-sensitive. (*See* Figure 3.) The break-away temperature itself is a function of nickel and chromium level. The longest transients occur at ~45% Ni for Fe-15Cr-XNi alloys and are even longer at lower chromium levels.

A model was earlier proposed to explain some of these observations[6,10]. While many properties of ternary alloys vary slightly with composition, the model concentrated on the compositional dependence of the void bias and the impact on the bias of the nickel segregation always observed at void surfaces. The model did not include composition-dependent dislocation biases since no data are available showing sensitivity of dislocation evolution to nickel and chromium levels. Moving dislocations also cannot segregate major elements as efficiently as can stationary voids.

Investigation of the diffusion of vacancies and interstitials in superimposed strain and composition gradients shows that drift terms arise in the void bias description as a result of segregation. These terms originate from the compositional dependence of elastic properties and lattice parameter. When compounded with forces arising from the inverse Kirkendall segregation mechanism, these terms substantially alter the void bias, providing a qualitative explanation for the dependence of swelling on nickel and chromium. At low-chromium and high-nickel levels, where voids have difficulty nucleating, loss of chromium and segregation of nickel at surfaces of the first voids not only stabilizes them against dissolution but changes the matrix composition, thus making it easier for other voids to nucleate.

Two features of this model are particularly attractive. First, it offers a rationale for the minimum in swelling observed at 35%-45% nickel[2,3]. A reversal in sign for the Kirkendall force is experienced by vacancies when the matrix nickel level is ~35%, as calculated for Fe-Ni alloys using published diffusion and thermodynamic data. Below 35% vacancies are attracted into regions of higher nickel concentration while the opposite occurs above 35%. Second, the dependence of shear modulus on nickel and chromium at void-relevant temperatures is consistent with the compositional dependence of swelling[7]. Segregation-induced increases in shear modulus at void surfaces reduce the attractive force on interstitials and thus help stabilize voids. For ternary alloys with 15% chromium, nickel segregation increases the modulus, but at 7.5% chromium there is no appreciable change in modulus with nickel segregation[11]. This extends the transient relative to alloys with 15% chromium.

This model implies a compositional sensitivity of both transient and post-transient swelling. Since only the former is observed this suggests that segregation effects are second order in magnitude (compared to temperature and displacement rate) for large voids and influence primarily void nucleation. However, there is another second order effect that has not been previously considered. Small increases (<100%) in the effective vacancy diffusion coefficient D^{V}_{eff} have been shown to strongly decrease the void nucleation rate, particularly at higher temperatures[12]. In general, the addition of nickel to Fe-Ni[13], Fe-Ni-Cr[14] and Fe-Ni-Cr-Mo[15] alloys increases the diffusivity of all alloy components, while additions of chromium decrease diffusivities[14,15]. For example, D^{V}_{eff} increases ~100% in going from Fe-15Cr-20Ni to Fe-15Cr-45Ni[14]. At temperatures where void nucleation begins to become difficult, the combined influence of these two second order compositional effects explains much of the observed swelling behavior of Fe-Ni-Cr alloys.

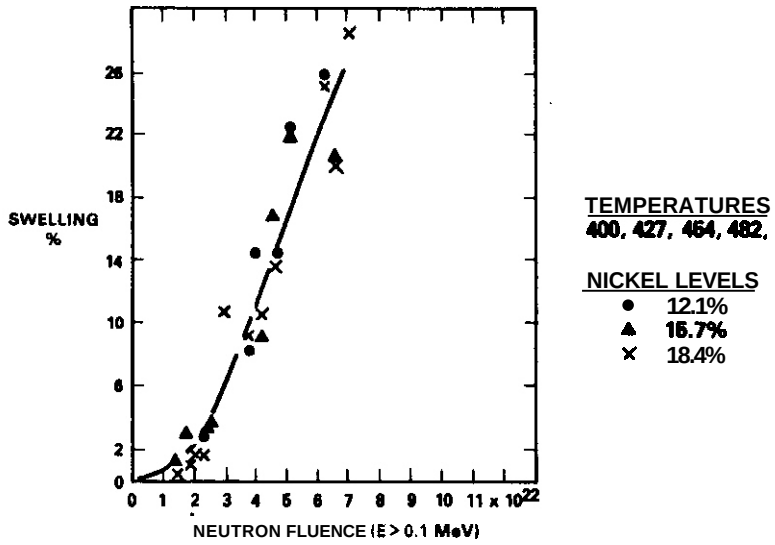

FIGURE 2. In Some Fe-15Cr-XNi Ternaries the Swelling in EBR-II is Relatively Independent of Nickel Level and Temperature Between 400 and 510°C.[8] (See Figure 3 for additional data at 25% Ni.)

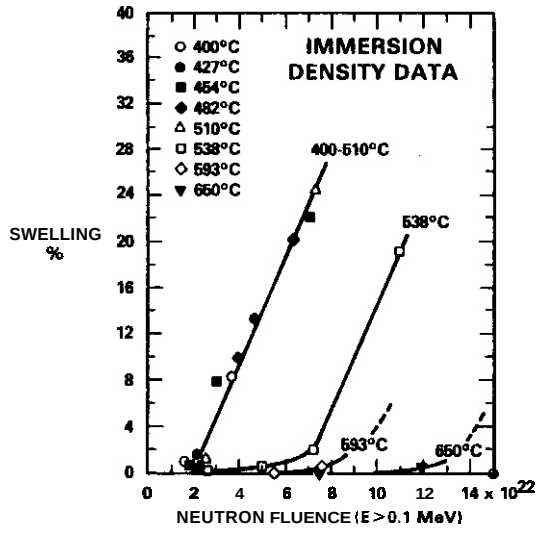

FIGURE 3. Swelling of Fe-15Cr-25Ni in EBR-II at 400-650°C.[4]

5.3 Silicon-Doped Fe-Ni-Cr Alloys

As shown in Figure lb, silicon's primary influence on swelling is also to extend the transient but it is much more effective per atom than nickel, however. It suppresses nucleation at all void-relevant temperatures[16] but the suppression is only temporary. As shown in Figure 4, Singh and coworkers have observed that void densities eventually converge at a level which is relatively insensitive to silicon content[17].

The model[12] developed to explain silicon's role in pure metals is based on its higher diffusivity compared to that of the host metal and thus its effect on increasing D^{v}_{eff}. In addition, the diffusivities of all components of Fe-Ni-Cr and Ni-Cr alloys increase substantially upon small additions of silicon[14,18,19,20] as shown in Figure 5. Rothman[14] found that the diffusivities in Fe-15Cr-20Ni increased roughly 45% when 1.4 wt.% silicon was added. D^{v}_{eff} increases even more than 45% when silicon's diffusivity contribution is included. The enhanced diffusivity of silicon-doped alloys strongly decreases void nucleation, particularly at higher temperatures.

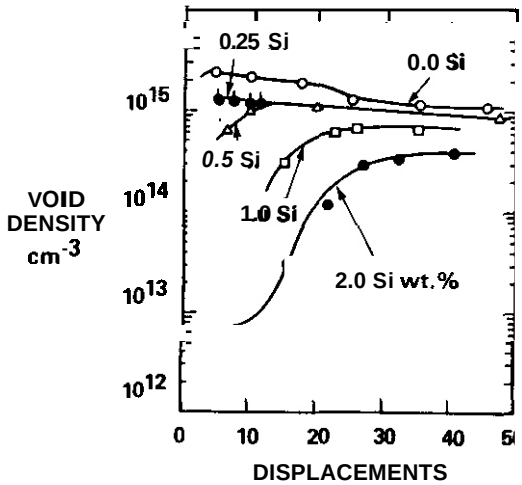

FIGURE 4. Silicon Effect on Electron-Induced Void Density in Fe-15Cr-13Ni-0.9Mn at 700°C.[17]

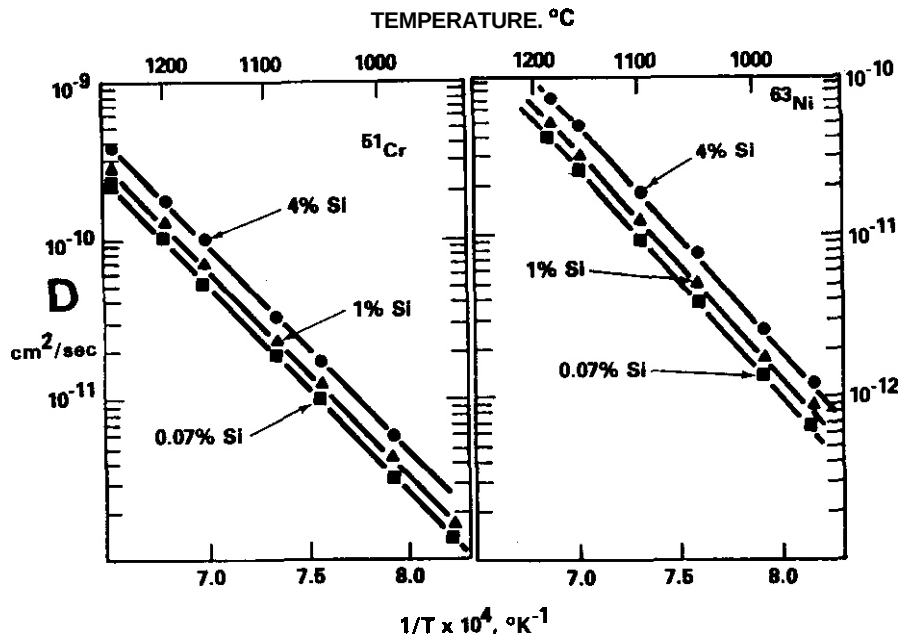

FIGURE 5. Increase in Tracer Diffusivities of Cr and Ni with Silicon Content in Fe-16Cr-14Ni.[18]

Silicon is also a smaller atom in Fe-Ni-Cr alloys[21,22] and is proposed in this model to form interstitial-solute pairs. Dimitrov and coworkers23 have recently demonstrated strong interstitial-silicon trapping in neutron-irradiated Fe-16Cr-25Ni. Silicon will thus not only drift down interstitial gradients but also UP vacancy gradients, both of which exist at microstructural sinks. The combined fast-diffusion/interstitial binding allows silicon segregation to proceed at sinks biased toward interstitials but dispenses with the requirement of unrealistically large binding energies needed for solute binding alone to suppress swelling. Nickel segregates to the same sinks by the inverse Kirkendall mechanism.

Addition of silicon inevitably causes irradiation-induced segregation of nickel and silicon into precipitates. The removal of sufficient amounts of these nucleation-controlling elements largely determines the duration of the transient. For each silicon-doped alloy there appears to be threshold levels of nickel and silicon that must be reached in the matrix before nucleation proceeds[24,25].

5.4 More Complex Fe-Ni-Cr Alloys

Addition of C, P, Mo, Mn, or Ti to Fe-Ni-Cr-Si alloys allows other phases to develop during irradiation[26]. Most, but not all, of these phases concentrate nickel and silicon, and each responds to fabricational and environmental variables in a different manner[26-30]. The combined sensitivity of the microstructural and microchemical evolutions to the many operating variables has been judged to be too complicated to model. A correlation has been established, however, between the history-sensitive phase evolution and the history dependence of transient swelling. The sensitivities of swelling to neutron flux and fluence, temperature history, stress and preirradiation thermal-mechanical treatment are mirrored in the sensitivities of the nickel-silicon removal process[27]. Details of phase identity do not appear to be as significant as are their consequences on matrix composition.

It has been shown that the eventual swelling rate of several 300 series stainless steels is ~1%/dpa over a wide range of temperature[1,31]. While the transient regime may be sensitive to temperature for some heats of steel, others are relatively insensitive to temperature. At temperatures outside the temperature-insensitive range the transients are longer but eventually the same swelling rate is reached. Applied stresses and some temperature changes can accelerate phase formation and lead to an abrupt truncation of the transient, however. Under these conditions rates of ~1%/dpa can be reached much quicker than is typical for isothermal or stress-free histories[24,29,30].

5.5 DISCUSSION

The influence of environmental, fabricational and compositional variables seems to reside in their effect on the transient regime. In addition, their action involves primarily void nucleation and is largely chemical in nature. When radiation-induced segregation is sluggish the transient regime exhibits a lot of curvature. The eventual swelling rate appears not to be very sensitive to composition or environmental variables such as displacement rate[32,33]. This implies that the temperature, composition and displacement rate sensitivities of microstructure are not as instrumental in determining the swelling rate as previously envisioned. A rationale for this insensitivity can be demonstrated using rate theory.

The swelling rate contains bias-driven and void annealing contributions[34]. The latter can be ignored if the temperature is below $0.6T_m$ or if the voids are relatively large or gas-pressurized. Thus for a system containing primarily large voids and dislocations,

$$\frac{d}{dt}\left(\frac{\Delta V}{V}\right) = \frac{S_o S_d}{(S_o+S_d)^2} \cdot \frac{Z_i^d Z_v^o - Z_v^d Z_i^o}{\bar{Z}_v} \cdot F(P,T) \quad (1)$$

The first right-hand term contains only void and dislocation sink strengths. While this term depends strongly on temperature for a microstructure dominated by one sink type, high fluence microstructures in austenitic alloys are characterized by a balance of sink strengths. Since both S_o and S_d possess similar temperature dependencies, $S_o(T) \approx S_d(T)$ over a large temperature range. For this condition, the first term equals 0.25 independent of temperature.

The second term is the system net bias and depends only weakly on temperature. The last term, however, potentially contains the major influence of temperature and displacement rate.

$$F(P,T) = \frac{S^2}{2\lambda}\left[\sqrt{\alpha^2+\beta} - \alpha\right] \quad (2)$$

where

$$\lambda = 4\pi R_c/\Omega = 32\ \pi a_o^2,\quad \alpha = 1 + \lambda \bar{C}_v^{eq}/(S\bar{Z}_i)$$

$$\text{and } \beta = 4\lambda D_v P/S^2 \bar{Z}_i \bar{Z}_v.$$

S is the total sink strength, R_c the recombination radius $2a_o$, a_o the lattice parameter, $\bar{C}_v^{eq}$ the average vacancy concentration in equilibrium with all sinks, Z_i and Z_v are bias factors for interstitials and vacancies, $\bar{Z}$ the average bias factor for the system, Ω the atomic volume, D_v the vacancy diffusivity and P the defect production rate. If we divide Eqn. (1) by P, we obtain the fractional swelling rate per dpa. Since the first two terms of Eqn. (1) are relatively insensitive to temperature, only F/P is plotted in Figure 6 to show the sensitivity of swelling to temperature and sink strength.

The activation energy for self-diffusion in nickel is known to be 2.9 eV, but the formation and migration energies that contribute to the total are not as well characterized. The value of E_v^m (and hence also E_v^f) has been revised recently[35,36]. Whereas the accepted migration energy was 1.4 eV, it now appears to be 1.1 ± 0.1 eV. Fig. 6 shows that a strong dependence on temperature occurs when E_v^m is 1.4 eV but not for 1.1 eV. Low values of sink strength also yield predictions of strong temperature dependency. In Fe-Ni-Cr alloys, however, the high fluence sink strengths (>5 x 10^{10} cm^{-2}) are sufficiently large that the swelling rate is insensitive to temperature and second-order composition effects on diffusivity.

One consequence of this treatment is that we expect a similar relative insensitivity of the eventual swelling rate to both displacement rate and helium/dpa ratio as was observed in ref. 32 and 37. This treatment decouples many of the sensitivities of post-transient swelling from the sensitivities of composition and microstructure, providing both void and dislocation sink strengths are sufficiently high.

6.0 References

1. F.A. Garner, "Recent Insights on the Swelling of Irradiated Austenitic Alloys:' Proceedinas of Third Topical Meeting on Fusion Reactor Materials, Albuquerque, NM, September 19-22, 1983 (in press).
2. W.G. Johnston et al., J. Nucl. Mater., 54 (1974) 24.
3. J.F. Bates and W.G. Johnston, Proc. AIME Conf. on Radiation Effects In Breeder Reactor Structural Materials, June 1977, Scottsdale, AZ, 625.
4. F.A. Garner, J. Nucl. Mater.. 117, (1983) 177.
5. D.L. Plumton, H. Attaya and W.G. Wolfer, Conditions for the Suppression of Void Formation During Ion-Bombardment, Proceedinas of Third Topical Meeting on Fusion Reactor Materials. Albuquerque, NM, September 19-22, 1983 (in press).
6. W.G. Wolfer, F.A. Garner, and L.E. Thomas, ASTM STP 782, (1982) 1023.
7. H.R. Brager and F.A. Garner, OAFS Quarterlv Report DOE/ER-0046/11, (Nov. 1982) 221.
8. F.A. Garner, DAFS Quarterlv Report DOE/ER-0046/14, (Sept. 1983) 133.
9. H.R. Brager and F.A. Garner, OAFS Quarterlv Report DOE/ER-0046/14, (Sept. 1983) 152.
10. W.G. Wolfer, J. Nucl. Mater., 114, No. 2&3, (1983) 292.
11. J.F. Bates, J, Nucl. Mater., 87 (1979) 409.
12. F.A. Garner and W.G. Wolfer, J. Nucl. Mater., 102 (1981) 143.
13. 8. Million et al., Mat. Sci. and Engr., 50 (1981) 43.
14. S.J. Rothman, L.J. Nowicki and G.E. Murch, J. Phys.F, 10 (1980) 383.
15. L.V. Pavlinov, Fiz. Metal. Metalloved. 41, No. 2, (1976) 344.
16. H.R. Brager and F.A. Garner, Proc. AIME Symp. on Phase Stability During Irradiation, Pittsburgh, PA, October 1980, 219.
17. B.N. Singh et al., J. Nucl. Mater., 103 & 104 (1981) 1041.
18. W. Assassa and P. Guiraldenq, Metal Science (1978) 123.
19. G.8. Fedorov, A.N. Semenikhin, Metallurgy and Metallography of Pure Metals Moscow, (1960) Vol II, 252.
20. G.R. Johnston, High Temperatures-Hiah Pressures, 14 (1982) 695.
21. J.L. Straalsund and J.F. Bates, Met. Trans., 5 (1974) 493.
22. J.F. Bates, "Partial Molar Volumes and Size Factor Data for the Fe-Ni-Cr-Si System:' HEDL-SA-2310 (1980).
23. C. Dimitrov, M. Tenti and 0. Dimitrov, J. Phys. F. 11 (1981) 753.
24. F.A. Garner, Ref. 16, 165.

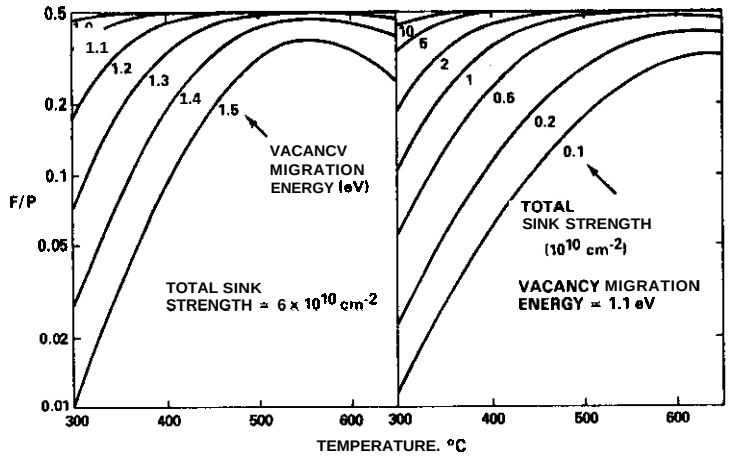

FIGURE **6.** Sensitivity of Swelling Rate Parameter F/P to Temperature, Sink Strength and E_V.

25. L.E. Thomas, 40th Ann. Proc. Electron Microscopy Soc. Amer., Wash. D.C., G.W. Bailey (ed.) 1982, 597.

26. W.S.J. Yang, H.R. Brager and F.A. Garner, ref. 16, 257.

27. F.A. Garner and D.L. Porter, ref. **6,** 295.

28. H.R. Brager and F.A. Garner, ASTM STP 683, (1978) 207.

29. F.A. Garner, OAFS Quarterlv Report DOE/ER-0046/5 (May 1981) 198.

30. W.S.J. Yang and F.A. Garner, ref. **6,** 186.

31. F.A. Garner, OAFS Quarterlv Report DOE/ER-0046/12 (Feb. 1983) 178.

32. J.L. Seran and J.M. Dupouy, ref. **6,** 5.

33. J.L. Seran and J.M. Dupouy, Proc. Conf. on Dimensional Stability and Mechanical Behavior of Irradiated Metals and Allovs, Brighton, England (April 1983) Vol I, 25.

34. W.G. Wolfer, L.K. Mansur and J.A. Sprague, (ref. 3), 841.

35. S.K. Khanna and K. Sonnenberg, Radiation Effects 59 (1981) 91.

36. L.C. Smedskjaer et al., J. Phvs. F, 11 (1981) 2221.

37. H.R. Brager and F.A. Garner, J. Nucl. Mater., 117 (1983) 159.

7.0 Future Work

The impact of second-order compositional variations on void nucleation will be evaluated using void nucleation theory.

8.0 Publications

This report will be published in the Journal of Nuclear Materials and presented at the Third Topical Meeting on Fusion Reactor Materials, Albuquerque, NM, Sept. 1983.

THE LITHIUM SHELL EFFECT AND ITS IMPACT ON MICROSCOPY OETERMINATIONS OF SWELLING BEHAVIOR

W. J. S. Vang, F. A. Garner (Hanford Engineering Development Laboratory) and A. Kumar (University of Missouri-Rolla)

1.0 Objective

The object of this effort is to determine the factors that influence the dimensional change behavior of irradiated alloys.

2.0 *Sumnary*

The heterogeneity of swelling in some irradiated alloys arises from localized enhancement of void nucleation by the "lithium shell effect" near boron-rich precipitates. It has been found that these lithium-affected volumes can be discounted in microscopy determinations of the bulk-averaged swelling rate.

3.0 Program

Title: Irradiation Effects Analysis (AKJ)
Principal Investigator: D. G. Doran
Affiliation: Hanford Engineering Development Laboratory

4.0 Relevant OAFS Program Plan Task/Subtask

Subtask II.C.2 Effect of He on Microstructure
Subtask II.C.4 Effects of Solid Transmutants on Microstructure

5.0 Accomplishments and Status

5.1 Introduction

Neutron-induced swelling in commercial alloys often occurs in a very heterogeneous manner. This nonuniformity has many origins and depends on the alloy composition, its prior thermal and mechanical history and its irradiation environment. When the bulk-averaged swelling is determined by imnersion density measurements to be rather low, microscopy is often employed in the development of predictive swelling correlations to differentiate between volume changes resulting from voids and phase changes. If a significant heterogeneity exists, however, there is often a problem in the selection of regions exhibiting representative or average behavior.

In some cases the nonuniformity requires the microscopist to resort to a time-consuming process of sampling and averaging of many areas. In other cases, however, the origin of the heterogeneity can be identified and a judgement can be made as to the consequences of ignoring the heterogeneity.

Microscopy examination sometimes shows that while the matrix swelling is close to that inferred from comparison of density changes of thermally-aged and irradiated specimens, there are some areas of the same specimen which exhibit substantially higher swelling. The possibility therefore exists that such alloys are just on the threshold of a breakdown of their swelling resistance and will shortly swell at a rate higher than predicted by extrapolation of density change data.

A conservative approach to the development of design correlations would utilize the highest levels of swelling observed by microscopy to establish the anticipated swelling rate. This approach is valid if no other rationale can be invoked to explain the local enhancement of swelling. In this paper it is shown

that in some cases there is cause to discount such enhanced swelling volumes in the development of swelling correlations.

5.2 Experimental Procedures

The specimens examined in this paper were irradiated in the EBR-II fast reactor to fluences ranging from 1.5 to 12.0 X 10^{22} n/cm^2 (E > 0.1 MeV) at temperatures between 400 and 649°C. The alloys involved were Fe-45Ni-12Cr with molybdenum, titanium, aluminum and silicon additions. The carbon and boron levels were low at 0.03 and 0.005 wt.%, respectively. After measurement of their density, the specimens were examined by conventional microscopy and energy dispersive x-ray (EDX) procedures. Ion microprobe analysis of unirradiated archive specimens was also employed in the later stages of this study.

5.3 Results

Enhanced swelling regions were found in all of the irradiated specimens and a typical example is shown in Figure 1. Outside this region the void density is much lower. The central enhanced region has relatively uniform swelling and is roughly circular in shape, having a diameter of about 3 μm.

There also appears to be an outer concentric ring of enhancement separated from the central area by a small gap. There exists no obvious correlation of these two regions with any microstructural component. The enhancement of swelling manifests itself primarily in the nucleation of a secondary set of small voids, while the primary larger voids are comparable to those observed at lower densities in the unenhanced areas.

On the basis of this micrograph alone one might be tempted to assume that a local breakdown of swelling resistance had occurred and was spreading outward. This is a particularly attractive explanation where enhanced zones were found to be surrounded by essentially unvoided material. Such an assessment was judged to be incorrect however, and will be reinterpreted in a later section of this paper.

FIGURE 1. Swelling Enhanced Region Observed at 454°C After 7.5 X 10^{22} n/cm^2 (E > 0.1 MeV).

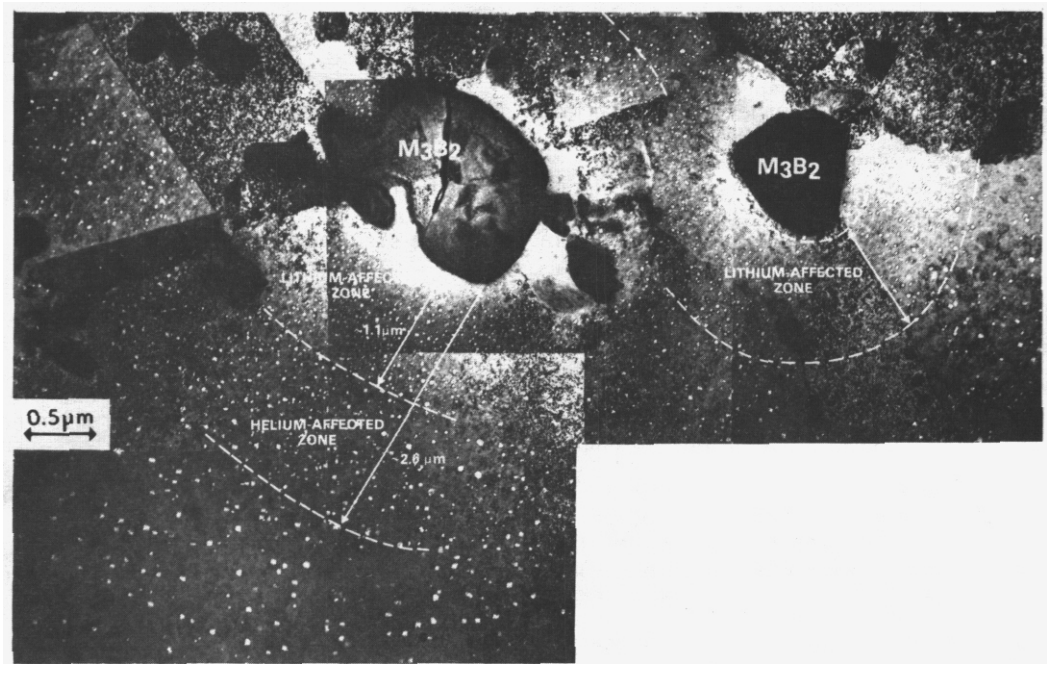

FIGURE 2. Concentric Enhanced Void Zones Due to the Products of (n,α) Reactions in M_3B_2 Particles.

Figure 2 provides clues necessary to identify the origin of the enhancement. Infrequently there were found isolated single or a few clustered precipitates which were surrounded by enhanced swelling. The large central precipitate (about 2 μm in size) clearly has two zones of enhanced swelling, each delineated by the boundaries associated with the smaller secondary voids. These boundaries are located at distances of 1.1 and 2.6 microns from the precipitate surface. Near the smaller precipitate (about 1 μm in diameter) a similar enhancement is seen but a small gap (about 0.2 μm) exists between the first enhanced region and the precipitate surface. The zone boundary distances of 1.1 μm and 2.6 μm are again observed. These are recognized to be the ranges in this steel of the products of the $^{10}B(n,\alpha)$ reaction, namely that of lithium and helium atoms, respectively. In a previous paper[1] it was shown that both lithium and helium affect void nucleation in fast reactor irradiations when these elements form atmospheres around precipitates containing boron. The influence of lithium is usually easier to observe since it is at higher concentrations than helium and also appears to exert a larger influence on void nucleation per unit concentration.[1] Detailed calculations of the concentration profiles for any precipitate1 matrix combination have been presented in reference 2.

In order to be convinced that the enhanced regions arise from the deposition of the $^{10}B(n,\alpha)$ reaction products, two conditions are necessary. First, the precipitates and their composition must be identified, particularly since the bulk-averaged boron concentration is rather low. Second, the width and spacing of the two enhanced zones (as well as the void distribution within the regions) should be checked for consistency with earlier predictions.[2,3]

The precipitate phase was determined to have a tetragonal lattice structure with $a_0 = 0.58$ nm and $c_0 = 0.32$ nm. The unit cell dimensions are close to those of the M_3B_2-type borides.[4] The composition determined by in-foil EDX analysis shows that the precipitates are enriched in Mo, Cr and Ti. (See Table 1.) Since boron is below the detection limit of the EDX technique, the concentration of boron within the precipitate phase is uncertain. Based on crystal structure and lattice parameters, the precipiate phase is most likely a M_3B_2-type boride. This phase is probably formed during fabrication prior to irradiation, since these precipitates were also observed during microscopy of unirradiated archive specimens. Furthermore, ion microprobe examination definitely confirmed the existence of boron-rich clusters in the unirradiated alloy.

It appears that the ranges of the two reaction products are nearly identical in both the precipitate and matrix phases, since the width of the enhanced regions are measured to be essentially equal to the precipitate diameters. This means that the stopping power ratio of the two phases must equal ~1.0.[1] For M_3B_2 precipitates in this alloy, the stopping power ratio was calculated to be 1.08. Using this value, it was found that predictions of enhanced zone size were in good agreement whenever the precipitates were retained in the foil and were sufficiently close to the spherical[2] or flat surface3 geometry assumed in earlier analyses.

TABLE 1

COMPOSITION (in wt.%) AND STRUCTURE OF THE PRECIPITATE PHASE

Fe	Ni	Cr	Mo	Ti	Al,Zr,Si
7.60	1.74	19.48	61.60	9.58	0

Possible Chemical Formula

M_3B_2: $(Fe_{0.29}Cr_{0.80}Ni_{0.06}Mo_{1.38}Ti_{0.43})B_2$

a_o = 0.58 nm, c_o = 0.32 nm

Reference Phase[4]

$(Fe_{0.39}Cr_{0.59}Ni_{0.21}Mo_{1.01}Ti_{0.59}Al_{0.22}Si_{0.01})B_{1.98}$

a_o = 0.578 nm, c_o = 0.313 nm

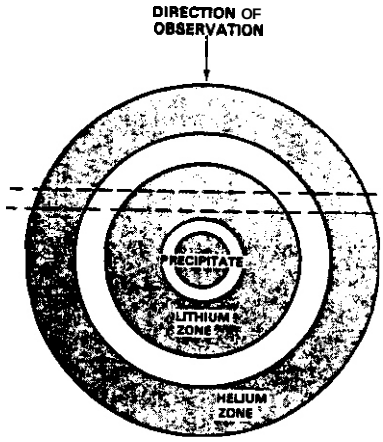

FIGURE 3. Schematic of the Relative Position of Precipitate, Microscopy Foil Section and Helium and Lithium-Affected Zones (corresponding to Figure 1).

5.4. Discussion

The enhanced region shown in Figure 1 can now be reinterpreted to be that produced by a particle large enough to produce a relatively thick lithium shell, but where the foil section was non-equatorial with respect to the precipitate and thus did not contain it. The resultant section of the lithium zone would indeed appear in projection as a nearly uniform circular region, as shown in Figure 3. One would also expect to see a concentric ring corresponding to the helium-affected zone. Even though both the particle size and the altitude of the section relative to the particle are unknown, geometrical considerations dictate that the radius of the lithium-affected zone should be roughly half that of the helium-affected zone. The helium zone can be faintly observed in Figure 1 and the relative radii of the two zones conform to the expected relationship. The helium-affected enhancement is not as pronounced as that of the lithium zone since helium exists at one quarter of the concentration of lithium.[1]

Due to the low level of boron in this alloy it must segregate to relatively few precipitates in order to yield observable rings, and this low density is confirmed by microscopy. Therefore, the enhanced regions are confined to a very small fraction of the total alloy volume and may be ignored in determination of bulk swelling rates for design equations. It has been shown elsewhere that the primary influence of most compositional variations lies in the duration of the transient regime that preceeds steady-state swelling[5-6] and it is not expected that these enhanced swelling areas will exhibit higher swelling rates than that of the unperturbed matrix.

5.5 Conclusions

The enhanced swelling observed in localized regions of some alloys arises from the deposition of lithium atoms generated by $^{10}B(n,\alpha)$ reactions in precipitates, where the lithium is deposited in halos in sufficient concentration to affect void nucleation. The affected volumes are small compared to the unaffected bulk and do not represent an incipient breakdown of swelling resistance. These lithium-affected volumes can therefore be ignored in determination of steady-state swelling rates for design equations.

6.0 References

1. D.S. Gelles and F.A. Garner, J. Nucl. Mater. 85 and 86 (1979) 689.

2. A. Kumar and F.A. Garner, "Transmutation-Induced Profiles in Halos Surrounding Spherical Precipitates: DAFS Quarterly Report DOE/ER-0046/12 (February 1983) 49, accepted for publication in Radiation Effects.

3. F.A. Garner, Rad. Effects, 66 (1982) 211.

4. H.J. Beattie Jr., Acta. Cryst., 11 (1958) 607.

5. F.A. Garner, "Recent Insights on the Swelling of Irradiated Austenitic Alloys: this volume.

6. F. A. Garner and W. G. Wolfer, "Factors Which Determine the Swelling Rehavior of Austenitic Stainless Steels:' Proceedings of Third Topical Meeting on Fusion Reactor Materials. Albuquerque, NM, September 19-22, 1983 (in press).

7.0 Future Work

None is anticipated.

8.0 Publications

This report will be published in the Journal of Nuclear Materials and presented at the Third Topical Meeting on Fusion Reactor Materials, Albuquerque, NM, Sept. 1983.

CONDITIONS FOR THE SUPPRESSION OF VOID FORMATION DURING ION-BOMBARDMENT

D.L. Plumton, H. Attaya, and W.G. Wolfer (University of Wisconsin)

1.0 Objective

Injected interstitials were recently shown to suppress void nucleation in 5 and 14 MeV self-ion bombardment. For lower-energy incident ions, the spread of the injected interstitials represents a larger fraction of the entire range so that complete suppression could occur. The effect of low-energy ions on the suppression of void nucleation is examined in both a recombination dominant loss regime and a sink-dominant loss regime.

2.0 Summary

In the region of ion deposition the number of interstitials is larger than the number of vacancies produced by displacement damage. As a result void formation can be suppressed. The following conditions must be satisfied for the suppression to occur: the distribution of injected ions and the distribution of displacement damage must overlap; within this region of overlap, the irradiation conditions must be such that recombination is a significant process. It is shown that void-free zones along the ion range can be produced bordering on regions with voids both behind and in front of the displacement damage peak. The suppression of void formation is particularly severe in low-energy ion bombardments.

3.0 Programs

Title: Effects of Radiation and High Heat Flux on the Performance of First Wall Components
Principal Investigator: W.G. Wolfer
Affiliation: University of Wisconsin-Madison

Title: Radiation Damage Studies
Principal Investigator: G.L. Kulcinski and R.A. Dodd
Affiliation: University of Wisconsin-Madison

4.0 Relevant DAFS Program Task/Subtask

II.B.2.3. Subtask C. Correlation Methodology

5.0 Accomplishment and Status

5.1 Introduction

Ion bombardment has been used to study void swelling because the higher damage rates are capable of giving, in hours, displacement doses "equivalent" to years of neutron irradiations. However, the injected ions affect void formation more dramatically than originally anticipated. Brailsford and Mansur[1] found that the injected ions would reduce the void growth rate whenever recombination was a dominant process. Lee et al.[2] experimentally verified this by Ni-ion irradiation of 316 SS that had been preconditioned by neutron irradiation to a uniform void distribution. Recently, Plumton and Wolfer[3] have shown that void nucleation can be drastically suppressed by the presence of the injected ions. This implies that the region of ion deposition and peak damage should be avoided in void formation studies.

The injected ions affect void nucleation by coming to rest as interstitials without a vacancy partner. These excess interstitials are relatively few in nmber. Therefore, they will only be important when most of the point defects produced by displacements are recombining either at sinks or in the bulk. This recombination loss is predominant at low temperatures and for large vacancy migration energies.[1,3]

The effect of injected interstitials depends on the overlap of the displacement damage and deposited ion profiles.[3] For a high energy ion, e.g. 14 MeV, there is a large ion range so that TEM work can be done in a region midway along the range far from the influence of the front surface or the injected ions. However, as the ion energy is lowered, the mutual overlap becomes an increasing fraction of the total range, until the overlap will be large enough so that no region exists free from the influence of the surface or the injected interstitials.

5.2 Theory and Results

The void nucleation theory presented previously[3] is used in this study with the modification that a surface sink term also is included. The experimental results of Garner and Thomas[4] were used to obtain the reduction in vacancy concentration due to front surface proximity. The experimentally determined average denuded zone width, L_{vf}, was found to depend on the vacancy diffusivity D_v and displacement rate P according to the relation

$$L_{vf} \sim \left(\frac{D_v}{P}\right)^{1/2} .$$

This denuded zone width was then used to reduce the value of C_v, the vacancy concentration, in the rate equations according to the equation

$$D_v C_v = D_v C_v|_{Bulk}\left(1 - e^{-2x/L_{vf}}\right)$$

where x is the distance into the sample. This approach gave denuded zones on the same order as those observed by Garner and Thomas.[4] The materials parameters used are the same as employed previously.[3]

The calculated void nucleation rates versus depth for ion irradiated nickel are presented in Figs. 1-3 for 2.5 MeV Ni ions, in Figs. 4 and 5 for 1 MeV Ni ions, and in Fig. 6 for 0.5 MeV Ni ions. The extensive parametric study on the effect of surface denuding and injected interstitials is illustrated here by two cases, namely: case 1 for E_{vm} = 1.1 eV, E_{vf} = 1.8 eV, and Q = 1 x 10^{14} m^{-2}; and case 2 for E_{vm} = 1.2 eV, E_{vf} = 1.7 eV, and Q = 5 x 10^{13} m^{-2}. E_{vm} and E_{vf} are the vacancy migration and formation energies, respectively, while Q is the total sink strength. Figures 1, 5, and 6 are for case 1 (sink dominant regime) while Figs. 2, 3, and 4 are for case 2 (recombination dominant regime). In these figures, the void nucleation rate with excess interstitials neglected is shown by a dashed line and with excess interstitials included by a solid line.

The BRICE code[5] and HERAO code[6] were used to calculate the displacement rate and excess interstitial fraction for Figs. 1, 2, 5, and 6 and Figs. 3 and 4, respectively. For 2.5 MeV Ni ions, and higher energies, the difference between the two displacement codes is evident (Figs. 2 and 31. For energies of 1 MeV and lower, the overlap between the displacement rate profile and excess interstitial fraction profile is almost complete so that differences in shapes of the profiles do not manifest themselves in the nucleation profile.

All figures illustrate the suppression of void nucleation at T = 300°C, while Fig. 1 (case 1) shows only a small decrease in the nucleation rate at 500 and 600°C. Figures 2 and 3 (case 2) both show 1-112 orders of magnitude decrease at 600°C (suppression values quoted at peak suppression). At 500°C Fig. 2 shows a 4-112 decade decrease while Fig. 3 shows almost 7 orders of magnitude decrease. Figures 2 and 3 illustrate (T = 300-500°C) the possibility of two void swelling peaks in the depth profile, one before and one after the peak of ion deposition. Figure 4 (case 1) demonstrates that as the incident ion energy is lowered, the suppression of void nucleation becomes pronounced even at high temperatures. For 1 MeV incident ions in a recombination dominated case (Fig. 5, case 2) only a band of voids nucleated just below the surface is left

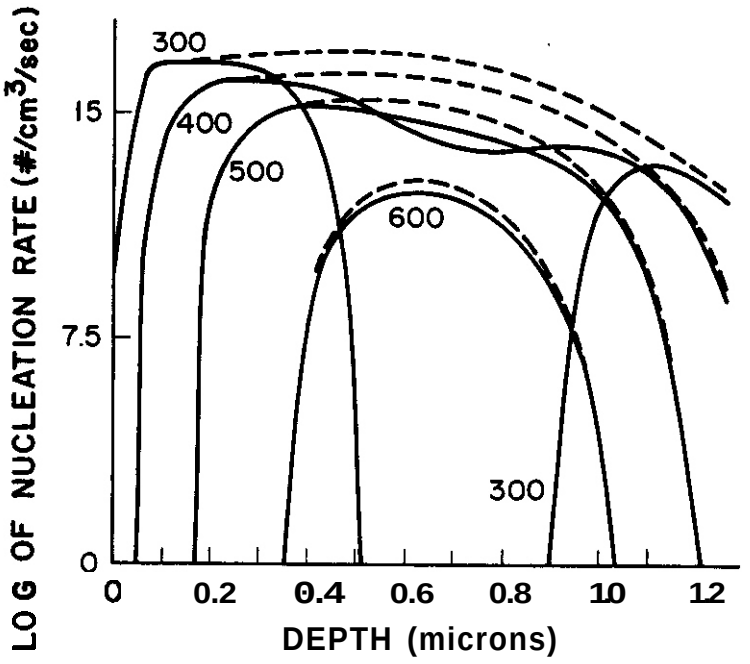

FIGURE 1. **Void nucleation rate vs. depth for 2.5 MeV Ni ions incident on Ni** (BRICE **code, case 1).**

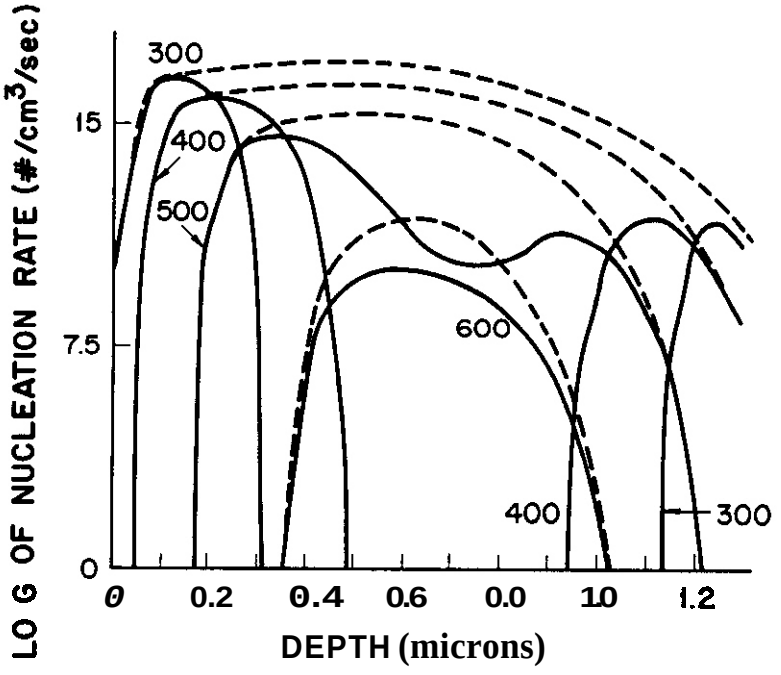

FIGURE 2. **Void nucleation rate VS. depth for 2.5 MeV Ni ions incident on Ni** (BRICE **code, case 21.**

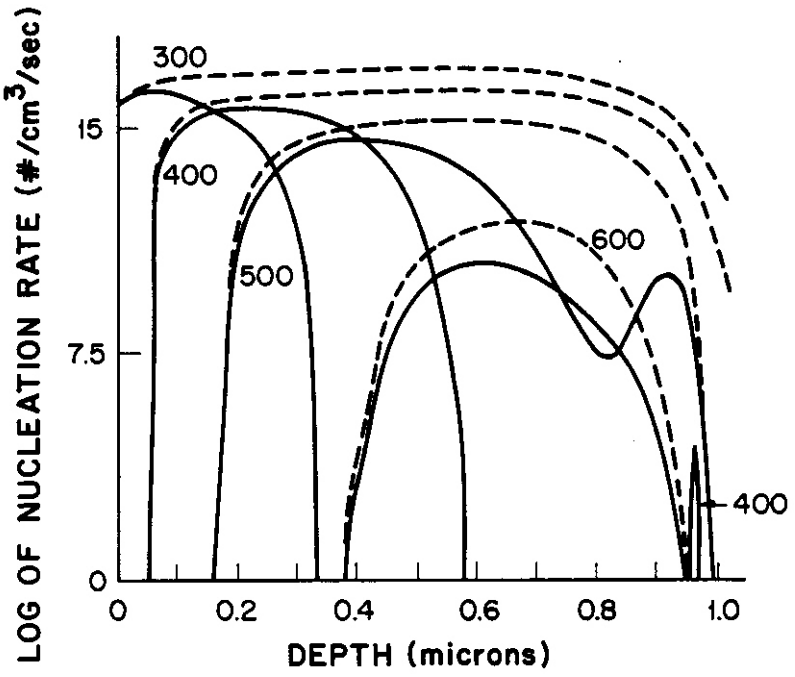

FIGURE 3. Void nucleation rate vs. depth for 2.5 MeV Ni ions incident on Ni (HERAD code, case 2).

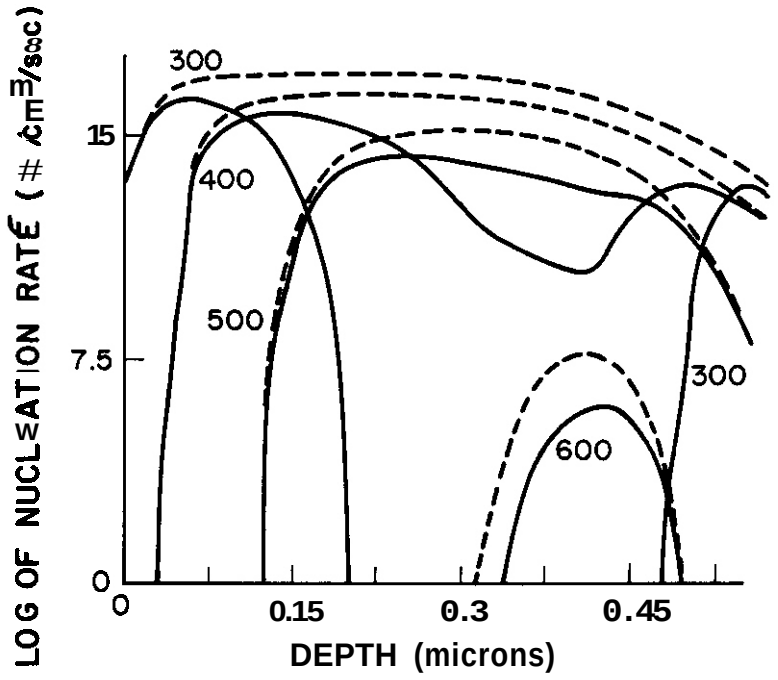

FIGURE 4. Void nucleation rate vs. depth for 1 MeV Ni ions incident on Ni (HERAD code, case 1).

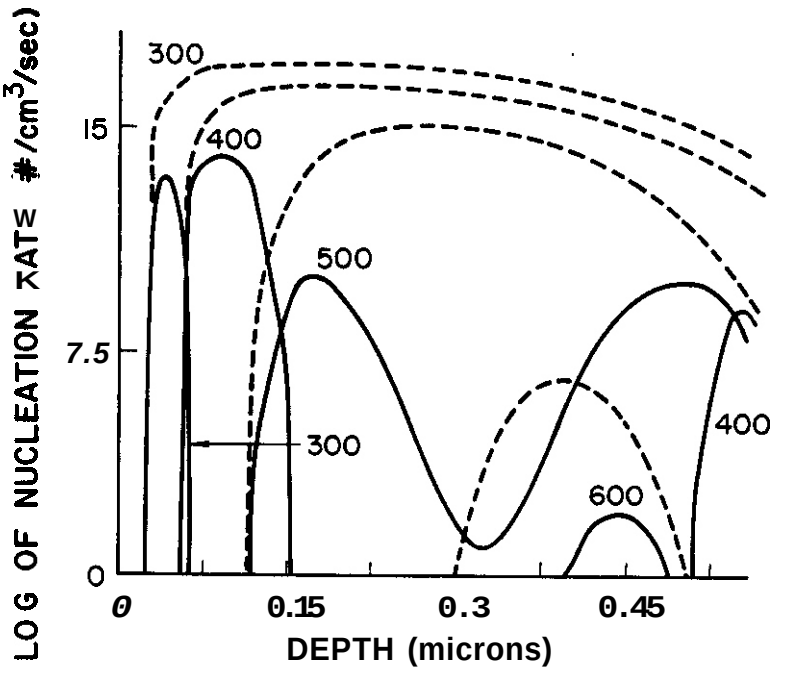

FIGURE 5. Void nucleation rate vs. depth for 1 MeV Ni ions incident on Ni (BRICE code, case 2).

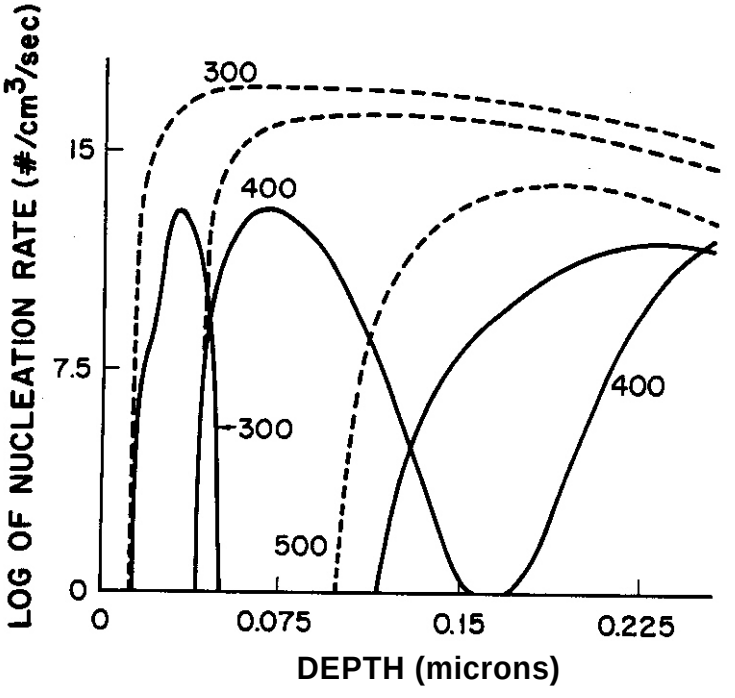

FIGURE 6. Void nucleation rate vs. depth for 0.5 MeV Ni ions incident on Ni (BRICE code, case 1).

at low temperatures. At higher temperatures, two bands of severely suppressed void nucleation occur. For 0.5 MeV ions, the surface denuding prevents void nucleation at 600°C (Fig. 6, case 11, while the suppression is again severe and leads to two peaks at 400°C, and a reduction by 4 orders of magnitude at 500°C.

5.3 Discussion

When void swelling after ion bombardment is measured either from step heights or by TEM in the peak damage region the effect of injected interstitials is present. The precipitous decline of void swelling towards lower temperatures as obtained by these two techniques[7] is possibly due to injected interstitials.

A void free gap or a reduction in swelling in the middle of the displacement depth profile has been observed by several authors. Whitley[8] observed a void free gap in the depth distribution at low temperature (400°C) in nickel. Johnston et al.[9] found a midrange swelling reduction at high temperatures (625°C) in stainless steel. Farrell et al.[10] also observed a midrange swelling reduction at 600°C in nickel. The existence of two bands of voids, one before and one after the peak of ion deposition, is in agreement with the results of the present study.

The degree and extent of the injected interstitial effect depend critically on the overlap of the profiles for displacement damage and deposited ions. The comparison between two codes for displacement damage shows that the HERAD code gives larger void suppressions in the peak deposition region than does the BRICE code at high temperatures. Since HERAD involves a more detailed modeling of the collision process, results derived from it are presumably more accurate.

The combined effect of surface denuding and injected interstitials can lead to a total suppression of void nucleation at all temperatures for heavy ion bombardment with energies on the order of 0.5 MeV or less, as found in the present study. In order to compensate for this total suppression, significant amounts of inert gases must be implanted either before or during the heavy ion bombardment.

6.0 References

1. A.D. Brailsford, L.K. Mansur, J. Nucl. Mat., 71, 110 (19771.
2. E.H. Lee, L.K. Mansur, M.H. Yoo, J. Nucl. Mat., 85 & 86, 577 (1979).
3. D.L. Plumton, W.G. Wolfer, submitted to J. Nucl. Mat., August 1983.
4. F.A. Garner and L.E. Thomas, "Effects of Radiation on Substructure and Mechanical Properties of Metals and Alloys, ASTM-STP-529, 303-325 (1973).
5. D.K. Brice, Report SAND-7500622. Sandia National Laboratories, July 1977.
6. H.M. Attaya, Ph.D. Thesis, University of Wisconsin, 1981.
7. W.G. Johnston, J.H. Rosolowski, A.M. Turkalo, T. Lauritzen, J. Nucl. Mat., 47, 155 (1973).
8. J.B. Whitley, Ph.D. Thesis, University of Wisconsin, 1978.
9. W.G. Johnston, J.H. Rosolowski, A.M. Turkalo, T. Lauritzen, J. Nucl. Mat., 62, 167-180 (1976).
10. K. Farrell, N.H. Packan, J.T. Houston, Rad. Effects, 62, 39 (1982).

7.0 Future Work

The vacancy concentration will be modified, as a function of depth, to include diffusion to the surface and diffusional spreading at the damage peak.

CORRELATION OF HELIUM CONTENT AND MICROSTRUCTURE TO BUBBLE GROWTH IN HELIUM IRRADIATED THIN FILMS OF NICKEL

M. L. Sattler and W. A. Jesser (University of Virginia)

1.0 Objective

The object of this effort is to examine in detail bubble growth during in-situ TEM annealing and to relate bubble behavior with helium content and existing microstructure.

2.0 *Summary*

Thin PVD nickel films were irradiated at 80 keV by monoenergetic helium ions to fluences as high as $10^{22} m^{-2}$. Those samples containing bubbles were subsequently annealed *in* a TEM at 550, 600, and 650°C for 90 minutes each. Individual volume changes were monitored for about 40 bubbles during the anneal. Annealing at 550 and 600°C showed all bubble sizes growing regardless of location. Annealing at 650°C showed small bubbles shrinking and large ones growing apparently via an Ostwald ripening mechanism. Finally, the films were vaporized in a mass spectrometer to measure retained helium. For the sample with visible bubbles only, 55% of the measured retained helium was needed to fill each bubble to equilibrium at 650°C. A saturation level of helium retained in the samples was found to be $8 \times 10^{20} m^{-2}$ (0.8%) for specimens with no visible bubbles and irradiated at 550°C; over twice as much retained helium was found in bubble-containing specimens irradiated at ~750°C.

3.0 Program

Title: Simulating the CTR Environment in the HVEM
Principal Investigators: W. A. Jesser and R. A. Johnson
Affiliation: University of Virginia

4.0 Relevant DAFS Program Plan Task/Subtask

Subtask II.C.2.1 Mobility, Distribution and Bubble Nucleation

5.0 Accomplishments and Status

5.1 Introduction

In view of the high helium production and high gas loads experienced by the first wall of a fusion reactor, the behavior of bubbles and the interaction of bubble evolution with microstructure is important. It is relevant to investigate bubble growth during irradiation, but it is also of interest to investigate bubble evolution during annealing because of the possible annealing of reactor components deliberately for recovery and outgassing and accidentally during coolant loss.

Previously, helium bubbles in nickel have been investigated in annealing experiments by Jager and Roth[1] who investigated helium trapping and reemission during annealing of bulk Ni foils at high temperature, Poker and Williams2 who studied low temperature release of bulk samples, and Jager, et al., [3] in an investigation of the pressurization of helium bubbles in thin films of nickel during stepwise annealing.

In this work in-situ TEM annealing experiments were conducted on a sample with a dense bubble population. In previous annealing work4 the growth of bubbles in an irradiated sample that contained no visible bubbles

was followed. This annealing was performed at a temperature well above the irradiation temperature and showed the growth exponent n to be equal to 1 for grain interior bubbles and equal to 0.6 for grain boundary bubbles. Since the largest time dependence for homogeneous growth processes was given as n = 0.55 which corresponds to Ostwald ripening, it appears difficult to establish mechanisms of growth through analysis of this growth exponent. Direct observation of growth was possible in the present experiment where individual bubbles in one region of the sample were examined at various times during the anneal. Bubble behavior was then correlated with grain boundary and dislocation microstructure. After annealing, total helium content of the specimen was measured in an effort to determine helium partitioning to the existing microstructural features.

5.2 Experimental Results and Discussion

5.2.1 Experimental Procedure

Uniformly thin films of pure Ni were obtained by the physical vapor deposition (PVD) of Ni wires onto heated rock salt. The films acquired a (100) or nearly (100) orientation of small grains averaging 170 nm across. The thickness of the films was 125 nm as determined from angstrometer measurements. Another series of PVD films was developed having an initial microstructure of small dislocation cells and a thickness of 110 nm. The films were removed by dissolution of the rock salt and mounted upon 100 mesh Mo grids for the remainder of the experiments.

The Ni samples were irradiated with 80 keV helium ions at fluences ranging from 2.1×10^{21} ions m^{-2} to 2.8×10^{22} ions m^{-2}. Those samples that were heated during irradiation to a temperature of about 750°C produced a final microstructure consisting of bubbles homogeneously located throughout the sample with larger bubbles appearing on grain boundaries and especially large bubbles at triple junctions. Those samples whose irradiation temperature remained lower than 550°C contained a final microstructure of dislocation tangles.

The irradiated sample (750°C) whose final microstructure contained a bubble population was subsequently annealed in a TEM at 550°C, 600°C and 650°C for 90 minutes each, and micrographs were taken to record bubble growth during the anneals. The pressure of the system was kept below 8×10^{-8} torr by simple LN_2 cooling of the Cu "cold finger." No oxidation of the sample was seen to occur. A control PVD Ni sample with no irradiation history was annealed at 650°C for two hours in the TEM under the same conditions and showed no bubble nucleation or impurity precipitation.

After irradiation and annealing, each sample was flash evaporated in a monopole mass spectrometer where the amount of helium (amu 4) in the sample was measured. The temperature at which the Ni films were vaporized generally did not also vaporize the Mo grid. The spectrometer was calibrated by injecting known amounts of helium at room temperature and pressure and by linearly relating the peak height to the number of atoms in the injected volume. The correlation coefficient for this calibration curve was 0.992. Experimental values of helium content were determined from the peak height obtained during evaporation by using the calibration curve and by assuming ideality at low pressure. Calculated values of implanted helium atoms were compared to these experimentally measured values of helium atoms. The calculated value of helium atoms retained in the thin films was computed using the TRIM code [6] for He ions at 30" glancing angle and 80 keV energy. For 110 nm thick films, the fraction retained was 0.21 and for 120 nm, the fraction was 0.35. Also, the value for equilibrium number of helium atoms was calculated for the sample with a bubble population using an improved reduced Van der Waals equation of state for helium at high pressures.[7]

52.2 Helium Content of Helium - Irradiated Thin Films

The thin irradiated nickel films having varying final microstructures were vaporized and found to contain more helium than that calculated from the TRIM code. Also, the amount of helium retained in samples irradiated at higher temperatures was greater than that for the lower temperature irradiations. This feature can be related to the observation that no bubbles were present in the lower temperature irradiated specimens; however, a large population of bubbles was visible in the specimens irradiated at high temperature. Thus, the bubbles apparently trap additional helium. Figure 1 gives the values for the measured and the calculated implanted densities of each sample at their corresponding irradiation temperatures.

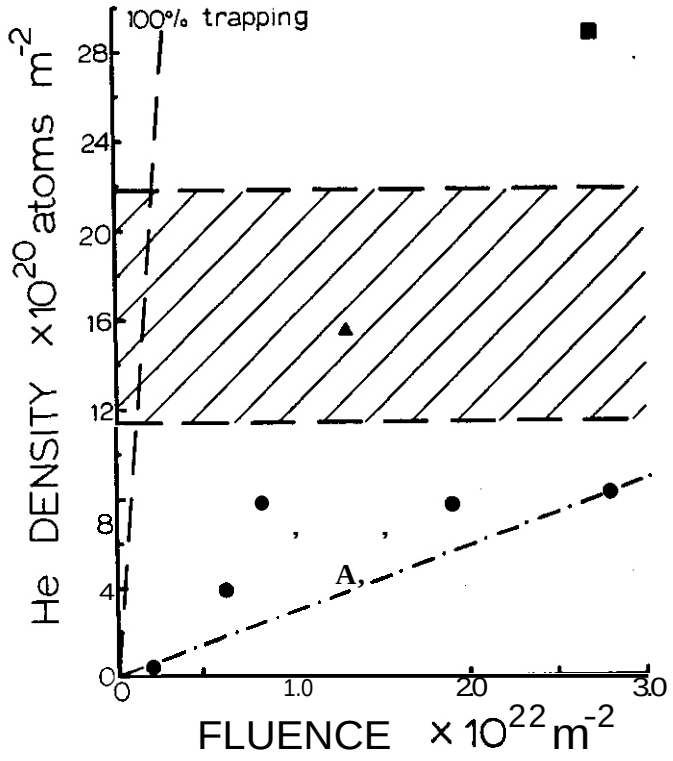

Legend: ● Measured, 110-nm thick, low-temp. irrad
■ Measured, 110-nm thick, high-temp. irrad
A Measured, 125-nm thick, high-temp. irrad
–·– Calc. implanted (TRIM), 110-nm thick
A Calc. implanted (TRIM), 125-nm thick
Jäger & Roth saturation limit band

Figure 1: Comparison of measured and calculated implanted helium densities to that of Jager and Roth[1].

Samples irradiated at temperatures lower than 550°C did display a microstructure of dislocation tangles with densities that generally increased with fluence and with helium content. The exception occurred at the highest fluence where there was a slight decrease in dislocation density. Table 1 summarizes the various samples used along with their fluences, dislocation density or related swelling, and helium content.

The data from these lower temperature irradiations suggest a saturation level at approximately 8.0 x 10^{20} He m^{-2} (0.8% He/Ni). The saturation level found by Jager and Roth [1] in their bulk Ni foils is also shown in Figure 1 along with the 100% trapping curve. This level is higher than that of the present work but the comparison here is between thin film work versus their experiments on bulk nickel. In thin film experiments completed by Jager, et al. [3] no saturation level was seen. Instead, the amount of helium retained in the sample first increased and then decreased with fluence until none was retained at higher fluences. (The described experiment was performed using lower irradiating energies.) This was not seen in the present work, but the atomic percentage of retained helium is much lower for the present case than for the above mentioned thin film case. Jager, et al.[3], also reported visible bubbles in all of the irradiated samples.

5.2.3 Helium Partitioning

For the thin films irradiated at a high temperature (~750°C) so that a bubble population was formed, the theoretical helium content was compared to the measured value. A distribution of bubble sizes was examined, as given in Table 2, and the theoretical number of helium atoms that would reside in each equilibrium bubble was calculated and totalled. Experimental measurements showed 3.0 x 10^{15} helium atoms retained in the sample, as compared to 1.7 x 1015 helium atoms calculated to be in equilibrium bubbles of the size range in the sample. By partitioning the available measured helium into these equilibrium bubbles, 1.3 x 10^{15} helium atoms remain unassigned. It seems reasonable in a sample of such small grain

size and large dislocation density that the remainder of the helium atoms are trapped at these sites as well as in point defect complexes in the matrix. This is especially plausible because there was more helium contained in traps in the samples with no visible bubbles than that assigned to other-than-bubble traps in the sample with visible bubbles. This distribution of helium atoms is comparable to theoretical calculations of helium partitioning to traps by Spitznagel, et al. [8] The calculations for the equilibrium number of helium atoms in each bubble and in the specimen are given in Table 2. In addition, the maximum number of helium atoms that a bubble can contain before loop punching occurs, as described for nickel by Trinkaus,[9] is shown in the table. The total number of helium atoms necessary before bubbles in this sample begin loop punching is 7.5 x 10^{15} atoms, which is more than twice the quantity of helium experimentally measured. It is therefore possible from this point of view for all of the helium to be in bubbles.

TABLE 1 - TEST CONDITIONS

SAMPLE DESCRIPTION	FLUENCE $\times 10^{22}$ ions m^{-2}	DISLOCATION DENSITY x 1015 m^{-2}	AMOUNT OF He PER UNIT AREA x 10^{20} atoms m^{-2} MEASURED	CALC. IMPLANTED
Dislocation - celled, 110-nm thick, low-temp. irrad. (< 550°C)	.21	1.0	.55	.44
	.63	1.6	3.96	1.33
	.84	2.6	7.80	1.72
	1.9	-	7.78	3.96
	2.8	2.1	8.20	5.20
Dislocation - celled, 110-nm thick, high-temp. irrad. (-750°C)	2.7	.2J	28.9	5.65
		SWELLING(%)		
Small - grained, 125 nm thick, 1ow-temp. irrad. (< 550") high-temp. anneal. (600")[4]	1.9	.69	-	-
Small - arained 125 nm thick. high-temp. irrad. (~750°C) lower-temp. anneal. (600, 650°C)	1.3	7.0	15.5	4.59

TABLE 2 - HELIUM PARTITIONING

AVE. BUBBLE DIAMETER (nm)	NO. OF BUBBLES PER SPECIMEN SIZE ($\times 10^{20}$ m^{-3})	EQUILIBRIUM NO. OF He ATOMS PER BUBBLE (10^5) a	b	c	TOTAL NO. OF He ATOMS PER SPECIMEN SIZE ($\times 10^{26}$ m^{-3}) a	b	c	
5.3	63.5	0.0528	0.0514	0.0807	0..334	0.326	0.511	
9.5	68.4	0.233	0.244	0.442	1.60	1.53	3.03	
16	58.6	0.819	0.779	1.96	4.78	4.58	11.46	
25	14.7	2.29	2.15	6.80	3.36	3.15	9.98	
35	29.3	4.83	4.53	16.97	14.14	13.28	49.77	Total
45	14.7	8.35	7.80	33.06	12.25	11.46	48.54	Meas. He
55	4.91	12.84	11.98	55.73	6.31	5.90	27.34	123.30
70	4.91	21.42	19.94	103.01	10.52	9.97	50.56	
95	4.91	40.62	37.71	219.64	19.92	18.52	107.79	
TOTALS					73.20	68.54	308.99	

a. T = 600°C, γ = 2.81 J m^{-2}
b. T = 650°C, γ = 2.75 J m^{-2}
c. T = 650°C, replace γ by $\gamma + \frac{\mu b}{2}$
μ = 186 GPa, b = 2.55 x 10^{-10} m

SPECIMEN SIZE
Area = 2 mm^2
Thickness = 125 nm

TABLE 3 - GROWTH CHART

BUBBLE DIAMETER nm	600°C ANNEAL		650°C ANNEAL
0 - 10	12	grow	7
	7	shrink	7
	4	unchanged	5
	4.7	$\Delta V \times 10^3$ nm^3	.54
10 - 20	5	grow	2
	2	shrink	6
	2	unchanged	5
	.64	$\Delta V \times 10^3$ nm^3	-2.9
20 - 60	4	grow	2
	2	shrink	1
	0	unchanged	2
	11.8	$\Delta V \times 10^3$ nm^3	16.8
TOTAL VOL. CHANGE	17.2	$\times 10^3$ nm^3	14.4

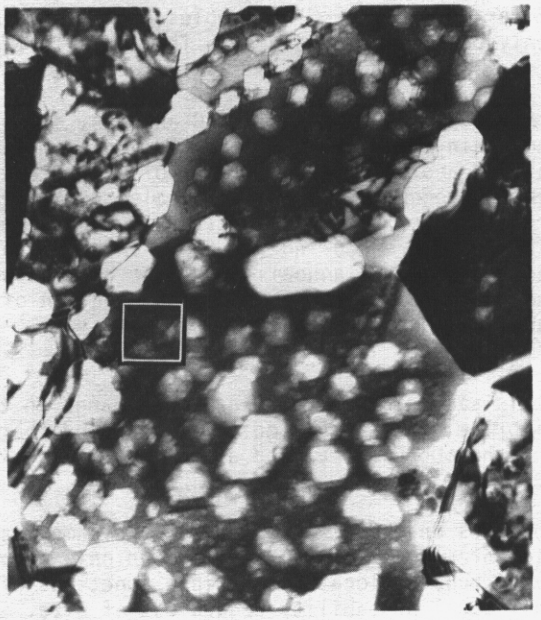

a. 0 min

b. 90 min, 600°C

c. 90 min, 650°C

Figure 2 Annealing sequence for *in-situ* TEM anneals at 600°C and 650°C after high-temperature irradiation. Small square shows area of interest.

5.2.4 Annealing of a High Temperature Irradiated Sample

After irradiation at –750°C. the specimen containing a dense population of bubbles was annealed first at 550°C for 90 minutes. The bubbles on the grain boundary and very large bubbles in the grain interior were the only bubbles seen to grow. The majority of bubbles remained the same size.

For both the 600°C and the 650°C anneals, all of the bubbles observed in an area 5.4 x 10^3 nm ^{3} in size in the grain interior were measured and analyzed. The volume changes for these 38 bubbles are recorded in Table 3 and an edited sequence of micrographs from this annealing experiment is shown in Figure 2. The table suggests a growth in bubbles regardless of initial size during the 600°C anneal and a tendency toward shrinkage in bubbles between 5 and 20 nm in diameter during the 650°C anneal. The large bubbles (20 to 60 nm) grew during the 650°C anneal. No bubbles in this grain interior region were seen to coalesce during the anneals and a few bubbles were seen to nucleate and grow during the 650°C anneal. Also, as the table shows, there is no conservation of volume between bubble size groupings during bubble growth for any annealing temperature.

For this same group of bubbles, the change in the number of helium atoms residing in the bubble, assuming equilibrium, was calculated. It was found that an additional 3.0 x 10^{15} helium atoms joined the bubbles during the 600°C anneal and an additional 1.5 x 10^5 helium atoms (9%) during the 650°C anneal.

For bubbles on the grain boundary, the same result was found as for grain interior bubbles. All sizes of bubbles grew for the 600°C anneal and only large bubbles (15 to 120 nm) grew for the 650°C anneal. However, bubbles located on triple junctions of grain boundaries were seen to shrink or to grow with roughly equal probability regardless of size. This result is different from that of Braski, et al.,[10] who observed bubbles on the triple junctions to grow at a faster rate than those on the grain boundary.

5.2.5 Ostwald Ripening Mechanism for Bubble Growth upon Annealing at 650°C

The data offer detailed measurements in support of Ostwald ripening of helium bubbles in nickel annealed at 650°C. Annealing of the specimen at 600°C showed that all bubble sizes tended to grow without coalescence. Such growth is consistent with either an overpressurized bubble population or a lattice releasing trapped helium. In view of the result that a subsequent 650°C anneal of the same specimen produced shrinking of the small helium bubbles, the overpressurization argument is less likely than the release of helium from some of the lattice traps. The overall bubble population observed by TEM during annealing showed that total bubble volume was not conserved but rather swelling increased with a net absorption of about 1.5 x 10^6 additional vacancies. Assuming that each bubble always contains the equilibrium number of helium atoms, one calculates that a net gain of about 1 x 10^5 helium atoms occurred during the 90 minutes of annealing at 650°C. This result suggests that while Ostwald ripening was occurring with a net increase of vacancies to the bubble population even at constant total helium in the bubbles even so there was an additional capture by bubbles of helium from lattice traps so that net bubble growth occurred beyond that expected from Ostwald ripening alone. Nevertheless, this data represents the first detailed observation of individual bubbles which supports the idea that helium bubbles may grow dominantly via an Ostwald ripening mechanism. This mechanism was observed only at 650°C and not at 600 or 550°C ($< T_m/2$) and hence it is not appropriate to extract an activation energy from the data over the temperature range 600-650°C.

5.2.6 Conclusions

1. There seemed to be a saturation level of helium in the films irradiated under similar conditions. This limitation was about 8 x 10^{20} He m^{-2} (0.8a%) for films 110 nm thick where no visible bubbles were exhibited.

2. High-temperature irradiation which produced bubbles in the films showed a helium retention of about twice that of specimens without visible bubbles.

3. A partitioning of helium within a specimen to visible equilibrium bubbles and to other traps showed that about half of the retained helium could reside at other traps.

4. For specimen irradiated at high temperature (750°C) and annealed at 650°C, small bubbles shrank on average while larger bubbles grew all without coalescence. This result is consistent with a growth mechanism of Ostwald ripening during the anneal.

6.0 References

1. W. Jager and J. Roth, "Microstructure of Ni and Stainless Steel after Multiple Energy He and D Implantation," Journal of Nuclear Materials, 93 & 94 (1980), 756.

2. D. B. Poker and J. M. Williams, "Low Temperature Release of Ion-Implanted Helium from Nickel," Applied Physics Letters, 40 (1982), 851.

3. W. Jager, R. Manzke, H. Trinkaus, G. Crecelius, R. Zeller, J. Fink, and H. L. Bay, "Density and Pressure of Helium in Small Bubbles in Metals," Journal of Nuclear Materials, 111 & 112 (1982), 674.

4. M. L. Sattler, J. I. Eennetch, and W. A. Jesser, "Bubble Growth Kinetics Associated with Irradiated and Post-irradiation Annealed Metals," DAFS Quarterly Progress Report, DOE/ER - 0046/7, (November, 1981), 155.

5. P. J. Goodhew and S.K. Tyler, "Helium Bubble Behavior in B.C.C. Metals Below $0.65T_m$," Proceedings of Royal Society of London, A 377 (1981), 151.

6. M. Baskes and K. Wilson, Sandia Livermore Laboratory, private communication.

7. J. I. Eennetch and W. A. Jesser, "An Improved Reduced Van der Waals Equation of State for Helium at High Pressures," Journal of Nuclear Materials, 116 (1983), 339.

8. J. A. Spitznagel, S. Wood, N. J. Doyle, W. J. Choyke, J. N. McGruer, J. R. Townsend, and R. E. Irwin, "Helium Partitioning to Extended Defects in Dual Ion Bombarded 304 and 316 SS," Journal of Nuclear Materials, 103 and 104 (1981), 1463.

9. H. Trinkaus, "Precipitation of Helium and Its Effects on Mechanical Properties of Metals," in: Point Defects and Defect Interactions in Metals, **eds.** J. Takamura, M. Doyama. and M. Kiritani (University of Tokyo Press, Tokyo, Japan, 1982), 312.

10. D. N. Braski, H. Schroeder, and H. Ullmaier, "The Effect of Tensile Stress on the Growth of Helium Bubbles in an Austenitic Stainless Steel," Journal of Nuclear Materials, 83 (1979), 265.

THERMAL CREEP AND STRESS-AFFECTED PRECIPITATION OF 20% COLD-WORKED 316 STAINLESS STEEL

R. J. Puigh, A. J. Lovell and F. A. Garner (Hanford Engineering Development Laboratory)

1.0 Objective

The objective of this effort is to provide fission-fusion correlations for dimensional changes induced by irradiation in AISI 316.

2.0 Summary

Measurements of the thermal creep of 20% cold-worked 316 stainless steel have been performed for temperatures from 593 to 760°C, stress levels as high as 138 MPa and exposure times as long as 15,000 hours. The creep strains exhibit a complex behavior arising from the combined action of true creep and stress-affected precipitation of intermetallic phases. The latter process is suspected to be altered by neutron irradiation.

3.0 Program

Title: Irradiation Effects Analysis (AKJ)
Principal Investigator: D. G. Doran
Affiliation: Hanford Engineering Development Laboratory

4.0 Relevant Program Plan Task/Subtask

Subtask II.C.1 Effects of Materials Parameters on Microstructure

Subtask II.C.14 Models of Flow and Fracture Under Irradiation

5.0 Accomplishments and Status

5.1 Introduction

Thermal creep is one of the processes that will contribute to the distortion of structural components in fusion reactors. In devices operating on the mirror principle, the blankets may be run at sufficiently high temperatures that thermal creep will supplant radiation-driven processes as the major design concern. There are some data, however, which suggest that thermal creep is altered in radiation environments.[1,2] It is also known that there are complex interactions between phase evolution, void swelling, irradiation creep and thermal creep. These four dimensional change contributions all exhibit sensitivity in their transient regimes to minor differences in composition and fabrication.[3-7]

These considerations require that the development of a thermal creep correlation for fusion application proceed using data from the same heat of steel from which irradiation creep and swelling correlations will be derived, namely that of the heats of steel commonly designated as FFTF* first core steels. The current published thermal creep equation[8] is derived from another heat of steel (V87210) whose creep, swelling and precipitation behaviors exhibit longer transients and therefore lower strains for a given exposure.

*FFTF designates the Fast Flux Test Facility in Richland, WA

This paper presents thermal creep data for the 20% cold-worked first core steel designated as heat K81581 or NICE-lot. This heat provides the majority of the data used to derive the irradiation creep correlation in Reference 2. The development of a predictive correlation based on these data will be presented in a later report.

The experimental techniques employed in this study were identical to those reported for heat V87210, and involved laser interferometer measurements of diametral strains of thin-walled helium-pressurized tubes. These tubes were maintained in inert gas within ±3°C of the nominal test temperature.

5.2 Experimental Results

The diameter changes of these tubes at four temperatures are shown in Figures 1 through 4. Table 1 contains a compilation of the strain and failure data. The stress levels quoted in these figures represent the mid-wall hoop stress, which remains nearly constant, dropping only 2% for a hoop strain of 5%.[8]

At 594 and 649°C the onset of accelerated creep is observed for all stress levels investigated. At 705°C, however, the accelerated creep regime is followed by a deceleration in creep rate after ~8000 hours. The same pattern is much more pronounced at 760°C, with the slowdown in creep rate occurring after 13000 hours.

Since earlier studies[9] (see Figure 5) had shown that a portion of the strains is due to volume changes associated with phase formation, the diameter increase of a tube held at 760°C for 14,800 hours and nominally zero stress was measured and found to be 0.70%. This implies a volume increase of 2.1% if the strains were isotropic. The measured density decrease, however, was only 1.22%. To be certain that these strains were not the result of a non-zero but small stress differential, two other tubes without end plugs (V87210, 760°C for 16,000 hours) were examined. These tubes experienced 1.33 and 1.28% density decreases and 0.97 and 0.98% diameter increases, respectively. These three sets of measurements indicate that the phase-related density decrease is distributed in a very anisotropic manner. Metallographic examination confirmed that substantial formation (>10 volume %) of large intermetallic precipitates had occurred; presumably these were mostly sigma phase.

5.3 Discussion

In previous reports[2,5] the initial acceleration of creep strain was attributed to the onset of tertiary creep. This assumption was called into question when the creep rate subsequently declined. It now appears that diameter strains on the order of >1% occur even in the absence of stress and account for the initial acceleration of strain rate. These strains saturate below 2%, however, and the larger strains attained at 705 and 760°C may be the result of recrystallization. Maziasz has pointed out that the relaxation of cold-worked dislocation densities during aging does not occur until the intermetallics form.[10]

The phase sequences in this steel initially cause a small anisotropic densification during carbide formation[11,12] followed by volume increase upon formation of intermetallic phases: laves, chi and sigma.[13] These latter phases are not fcc in structure, however. Their different structures, when compounded with the pronounced texture[9,14] of these tubes, leads to nonisotropic strains. For example, formation of hexagonal laves involves 17% compression of the crystal lattice in two directions and expansion of 24.5% in the other, resulting in a volume increase of ~10%.[15] The laves phase does not form in amounts exceeding several volume percent, however, and cannot cause the observed total strain.

The two heats discussed in this report are particularly prone to the formation of the tetragonal sigma phase, however, reaching levels as large as 10-14%.[7,9,16] Inspection of Figures 1 through 4 also shows that the nucleation and growth of these phases must be accelerated by applied stresses. This has been demonstrated experimentally for these tubes[10] and also other heats of 316.[17,18]

The late-term deceleration of creep seen in Figures 3 and 4 cannot be attributed solely to saturation of precipitate-related strains, since the strains are greater than can be attributed to phase formation alone. This deceleration may represent a hardening of the microstructure arising from dislocation cell formation and/or precipitates.

It is interesting to speculate whether the formation of intermetallic phases will be delayed by irradiation as suggested by Watkin.[19] If these phases are precursors of the acceleration of creep, then the delay shown in Figure 6 of high temperature irradiation creep (relative to thermal creep) implies that such a delay occurs. An alternative explanation is that the irradiation-induced dislocation network not only retards the elemental segregation needed to nucleate those phases but also resists the recrystallization process. In addition, radiation-produced phases form at high densities within the grains and segregate many elements known to influence the rate of sigma formation in austentics. All of these processes may contribute to the delay of accelerated creep during irradiation.

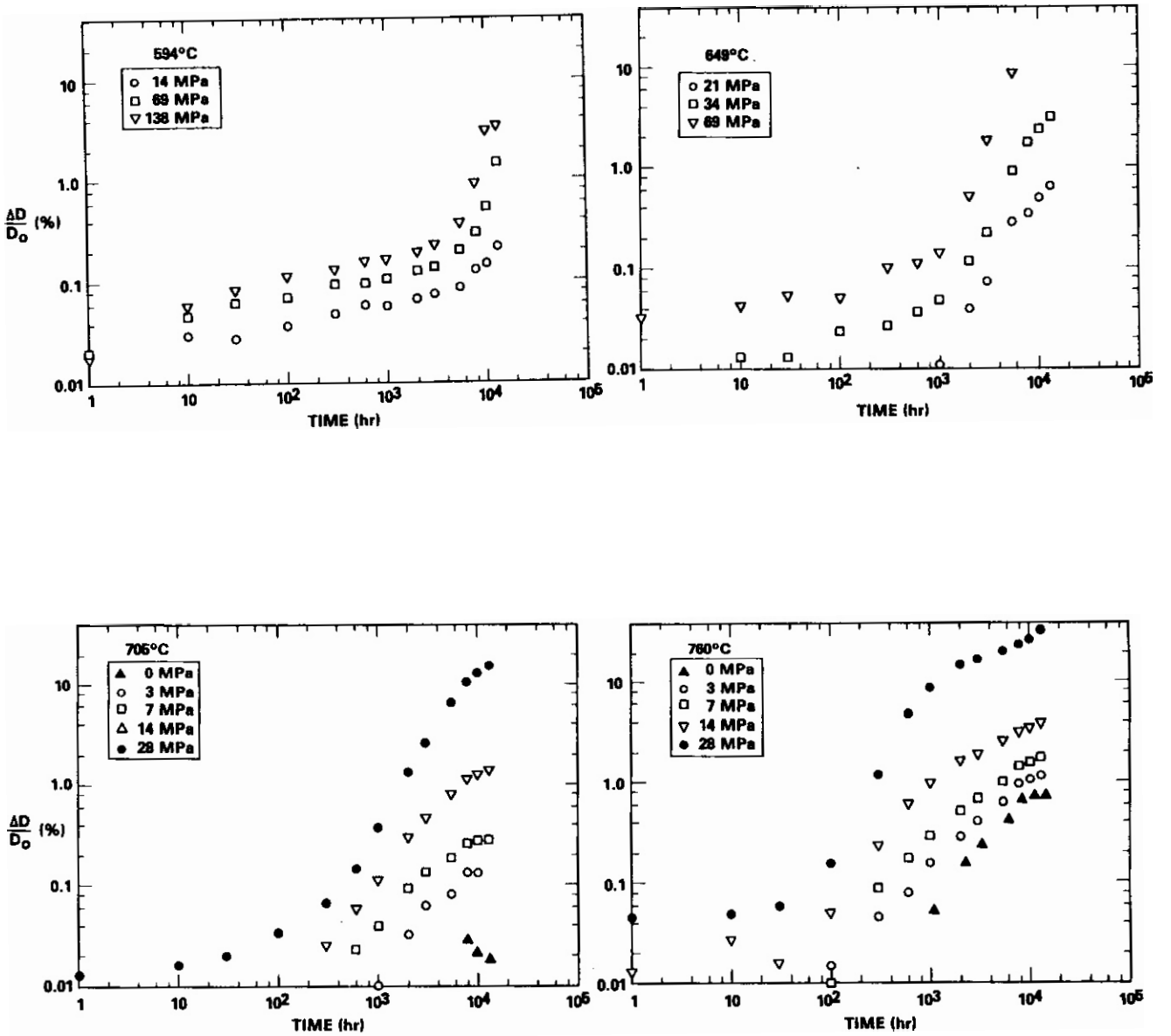

FIGURES 1-4. Thermal Creep Strains Observed in the Diameter of Gas-Pressurized Tubes Constructed from AISI 316 Heat K81581. The stresses shown are midwall hoop stress levels.

TABLE 1

THERMAL CONTROLS - NICE-LOT

$\Delta D_o/D_o$, Percent

Specimen	Stress MPa	Stress ksi	3.6 (1)	36 (10)	108 (30)	360 (100)	1080 (300)	2160 (600)	3600 (1000)	7200 (2000)	10800 (3000)	19440 (5400)	28080 (7800)	35518 (9866)	46386 kilosec (12885 hr)
							811°K (1000°F)								
L7	0	0	.003	-.008	-.013	-.022	-.012	-.013	-.021	-.014	-.010				
A2	28	4	-.004	-.007	-.001	.006	0	.003	0	.0065	.011				
A3	55	8	.001	-.002	-.011	-.013	-.002	.009	.007	.019	.023				
A4	86	12.5	-.002	0	-.003	.009	.015	.031	.037	.056	.054			-	
A5	103	15	.014	.004	.008	.016	.030	.045	.067	.079	.092				
A6	138	20	-.009	-.008	-.003	-.001	.027	.053	.068	.084	.097				
A7	172	25	.010	.011	.013	.022	.049	.096	.117	,141	.153				
L5	241	35	.009	.008	.019	.027	.088	,170	.224	.392	.330				
A9	310	45	.025	.030	.039	.054	.165	.333	,491	.718	.886				
A10	414	60	.043	.043	.065	.100	.394	1.220	failed'						
							867°K (1100°F)								
El	0	0	-.013	-,005	-.019	-.026	-.019	-.020	-.027	-.029	-.024	-.016	.073	-.022	-.029
E2	14	2	-.002	-.003	-.010	-.014	-.004	.0	-.006	-.007	.001	.003	.041	.035	.037
E3	34	5	.003	-,001	.003	-.002	.012	.011	.013	.014	.023	.036	.040	.047	.057
L4	55	8	.004	.017	.018	.015	.027	.029	,028	.077	.100	.060	,126	.099	.145
E5	69	10	.009	.030	.028	.037	.049	.058	.058	.067	.075	.086	.127	.149	.219
E6	86	17.5	.008	.029	.039	.048	.070	.071	.074	.082	.101	,136	,170	.230	.422
E7	103	15	.020	.046	.063	.070	.094	.096	.104	.126	.139	.201	.298	.522	1.46
E8	121	17.5	.020	.047	.072	.098	.121	.125	,137	.165	.186	.273	.513	1.094	3.71
E9	138	20	.018	.058	.083	.114	.136	.156	.169	.194	.233	.371	.914	3.016	3.32
E10	155	22.5	.026	.074	.106	.145	.180	.203	.223	.275	,334	.729	3.08	3.067	failed
Ell	172	25	.029	.075	.138	.170	.320	.332	.358	.464	.466	.463	.427	failed	
E12	206	30	.039	.104	.173	.243	.328	.380	.442	.635	1.229	2.193	2.172	failed	
E13	241	35	.051	.145	.250	.367	.516	.733	1.041	3.188	failed				
E14	276	40	.053	.203	.342	.620	1.071	2.151	2.892	failed					
L15	310	45	.065	.272	.555	1.248	1.945	4.200	failed						
L6	345	50	.881	,404	.977	4.177	failed								
							922°K (1200°F)								
F1	0	1	-.016	-.024	-.017	-.019	.069	-.011	-.023	-.020	-.015	-.021	-.004	.009	.007
F2	7	1	-.007	-.023	-.013	-.018	.007	-.011	-.015	-,0009	.012	.037	.074	.103	.120
F3	14	2	-.008	-.004	-.006	-.011	-.002	.003	0	.025	.053	.107	.190	.255	.305
	21	3	.003	-.010	-.001	-.004	.002	.008	,011	.040	.073	.286	.344	.490	.636
F6	28	4	,003	.007	.011	.005	.021	.023	.030	.069	.126	.383	.794	removed	
	34	5	.006	.013	.013	.024	.027	.037	.048	.116	.223	.859	1.730	2.333	3.10
F7	41	6	.014	.023	.022	,024	.043	.054	.060	.137	.287	1.202	2.482	removed	
							922°K (1200°F) (Cont'd)								
F8	55	8	,027	,041	.030	.052	,067	.083	.107	.321	.952	4.380	10.620	removed	
F9	69	10	.033	.043	.053	.051	.099	.112	.141	.517	1.826	8.545	8.514	failed	
F10	86	12.5	.034	.066	.078	.095	.129	.160	.230	1.531	6.341	6.301	6.254	failed	
F11	103	15	.062	.100	.110	.121	.199	.277	.525	5.477	failed				
F12	138	20	.081	.137	.165	.202	.318	.544	2.251	3.985	failed				
F13	172	25	.127	.228	.296	.405	.785	4.132	failed						
F14	207	30	,162	.334	.474	.777	1.246	3.896	failed						
F15	241	35	.234	.550	.855	2.061	4.125	4.292	failed						
							918°K (1300°F)								
L1	0	0	-.020	-.027	-.018	-.030	-.020	-.020	-.019	-.017	-.003	-.006	.028	.021	.018
J2	3	0.5	-.011	-.018	-.020	-.008	-.006	.003	.010	.033	.063	.081	.135	.134	1.88
J3	7		,003	-.014	-.004	-.006	.004	.023	.040	.091	.137	.187	.266	.278	.285
J4	10	1.5	-.004	-.009	.001	.009	.014	.040	.077	.178	.277	.435	.589	.632	.684
	14	2	-.007	0	-.001	.004	.026	.058	.111	.306	.475	.816	1.139	1.267	1.41
J6	71	3	.006	.010	.015	.046	.040	.094	.199	.612	1.104	2.316	3.052	4.034	4.69
J8	28	4	.013	.016	.020	.034	.067	.147	.378	1.352	2.641	6.430	10.607	13.128	15.75
	34	5	.024	.028	.043	.042	.105	.320	1.037	3.927	8.404	32.901	41.523	failed	
J9	41	6	.029	.045	.033	.066	.126	,427	1.446	6.366	18.674	25.368	failed		
J10	48	7	.047	.063	.073	.089	.208	1.017	3.585	19.321	failed				
Jll	55	8	.044	.062	.075	.102	.240	1.187	4.793	13.283	failed				
J12	69	10	.060	.097	.117	.165	.561	4.407	8.266	failed					
J13	90	13	.086	.145	.110	.302	1.945	6.850	failed						
J14	110	16	.067	.201	.277	.567	5.773	failed							
J15	131	19	.158	.278	.417	1.223	5.291	failed							
							1033°K (1400°F)								
K1	0	0	.020	-.008	.009	-.018	-.002	.002	.059	.159	.256	.428	669	.693	.73
K2	3	0.5	0	.002	-.023	.015	.046	.079	,154	.288	.412	.630	.958	1.047	1.13
K3	7	1	.013	-.004	.001	.010	.087	.175	.289	.507	.672	.990	1.420	1.546	1.71
K4	10	1.5	.007	.017	.008	.036	.145	.604	.527	.884	1.116	1.539	7.070	2.270	2.52
K5	14	2	.013	.027	.016	.050	.237	.604	.977	1.606	1.975	2.519	3.158	1.456	3.84
K6	21	3	,030	.030	.047	.092	.529	1.649	3.001	5.021	5.516	6.894	8.049	removed	
K7	28	4	.045	.049	.059	.156	1.187	4.622	8.649	14.859	16.988	20.610	24.394	27.411	34.01
K8	34	5	.061	.075	.100	.327	3.289	17.456	38.278	failed					
K9	41	6	.081	.108	.180	.868	15.148	20.318	failed						
K10	48	7	.070	.105	.144	.617	1.581	25.749	failed						

* Note: Failed specimen usually denotes benign failure mode. Specimen is considered failed when creep growth stops. The final measurement is listed in the examination tine before the "failure"note, i.e., the specimen was not present during the aging time in which "failure" occurred.

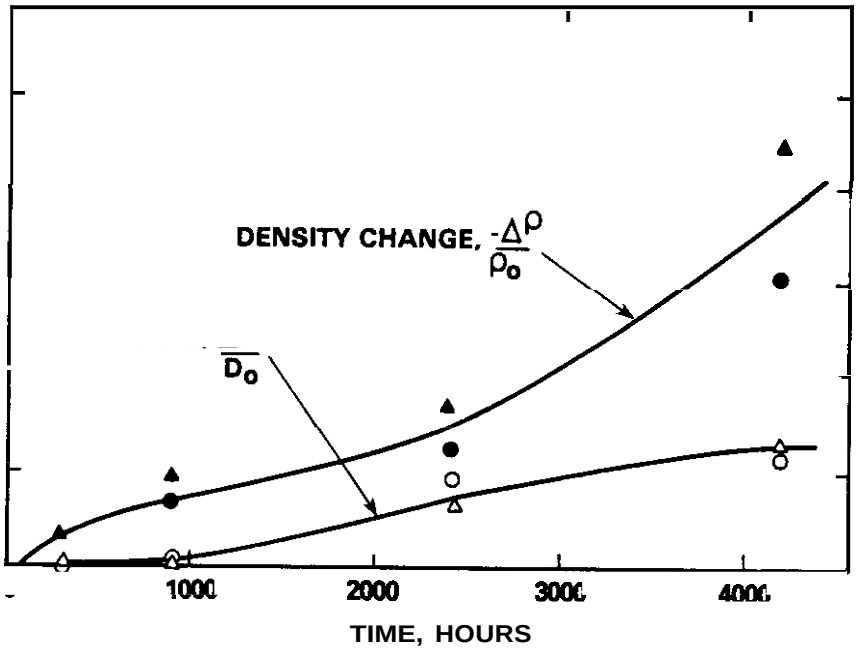

FIGURE 5. Diametral and Volume Changes Observed at 700°C in Zero-Stress Thermal Creep Tubes Constructed From Heat V87210.[10]

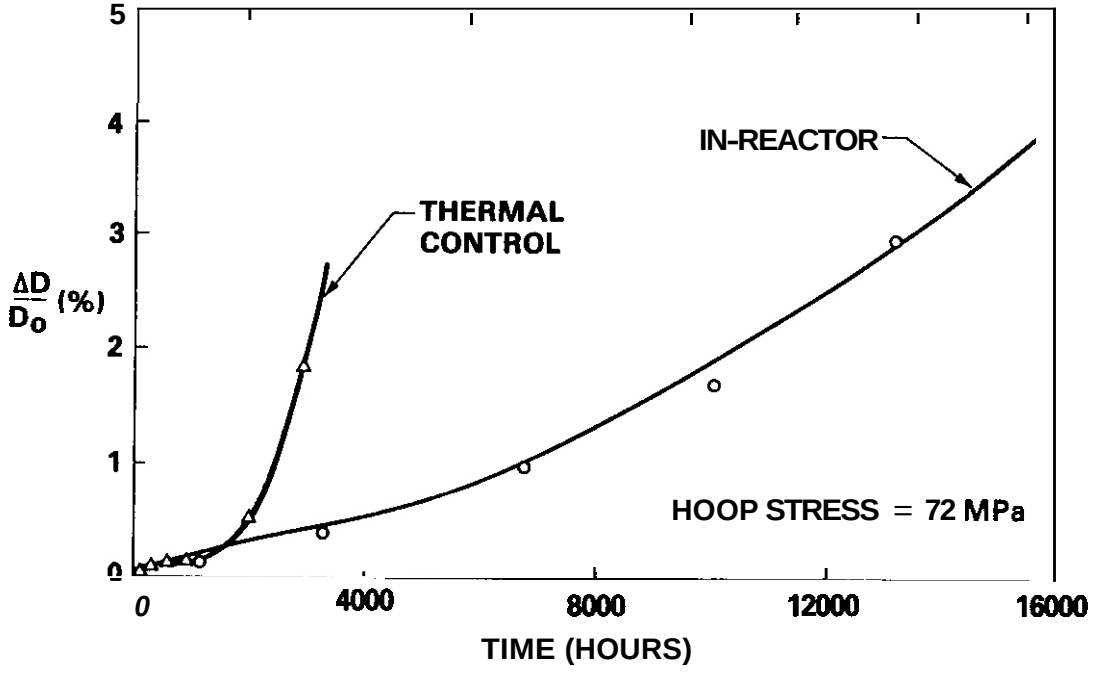

FIGURE 6. Creep Behavior Observed in 20% Cold-Worked 316 Stainless Steel at 650°C, Showing Apparent Suppression of Accelerated Strain Regime by Irradiation.[2]

5.4 Conclusions

The strains measured in thermal creep experiments on one heat of cold-worked 316 stainless steel exhibit a complex behavior arising from the interaction of creep processes with phase evolution and recrystallization, both of which are suspected to be altered by radiation.

6.0 References

1. E.R. Gilbert and B.A. Chin, ASTM STP 725 (1981) 665.
2. R.J. Puigh, E.R. Gilbert and B.A. Chin, ASTM STP 782 (1982) 108.
3. F.A. Garner, Proc. AIME Symp. on Phase Stability During Irradiation, Pittsburgh, PA, Oct. 1980, 219.
4. F.A. Garner, Recent Insights on the Swelling of Irradiated Austenitic Alloys, Proceedings of Third Topical Meeting on Fusion Reactor Materials, Albuquerque, NM, September 19-22, 1983 (in press).
5. E.R. Gilbert and A.J. Lovell in AIME Conf. on Radiation Effects in Breeder Reactor Structural Materials (1977) 269.
6. J.F. Bates, R.W. Powell and E.R. Gilbert, ref. 1, 713.
7. J.Hales, Trans. ANS, 28 (1970) 153.
8. E.R. Gilbert and L.D. Blackburn, J. of Engr. Matls. and Tech., 99 (1977) 168.
9. F.A. Garner, OAFS Quarterly Report DOE/ER-0046/5 (May 1981) 198.
10. P.J. Maziasz, J.A. Horak and B.L. Cox, ref. 3, 271.
11. B. Weiss and R. Stickler, Trans. AIME, 3, No. 4 (1972) 851.
12. F.A. Garner, W.V. Cummings, J.F. Bates and E.R. Gilbert, HEDL-TME 78-9, June 1978.
13. J.A. Spitznagel and R. Stickler, Met. Trans. 5 (1974) 1363.
14. J.F. Bates, W.V. Cummings and E.R. Gilbert, J. Nucl. Mater. 99 (1981) 75.
15. Yu.N. Sokurskii, V.S. Ageev and N.P. Agapova, Atomnava Energiva, 50, No. 4 (1981) 265.
16. R.A. Karnesky, "The Precipitation Kinetics of the Sigma Phase in 20% Cold-Worked Type 316 Stainless Steel, Masters Thesis, Wash. State Univ., 1980, also HEOL-6788.
17. D.G. Morris and D.R. Harries, Metal Science (1978) 542.
18. D.J. Chastell and P.E.J. Flewitt, Matls. Sci. and Engr., 38 (1979) 153.
19. J.S. Watkin, J.H. Gittus, A.P. Miodownik and L. Kaufman, TRG-Report-3027(S), UKAEA, 1977.

7.0 Future Work

A correlation will be developed from this data to describe the strains associated with thermal creep and precipitation.

8.0 Publications

This report will be published in the Journal of Nuclear Materials as part of the proceedings of the Third Topical Meeting on Fusion Reactor Materials, (Sept. 1983) Albuquerque, NM.

THE INFLUENCE OF IRRADIATION AND THERMAL CREEP ON STRESS REDISTRIBUTION IN FUSION BLANKETS

James P. Blanchard and Nasr M. Ghoniem (University of California, Los Angeles)

1.0 Objective

The objective of this work is to investigate the influence of creep and swelling on fusion blanket lifetimes.

2.0 Summary

Creep processes, due to thermal and irradiation fields, have generally been assumed to relax stresses resulting from the loading of structural components. However, in order to determine failure modes and mechanisms, **a** global inelastic structural analysis is required. We have recently developed the STAIRE computer program for STress Analysis Including Radiation Effects. This code is based on modified beam and arch theory far the simultaneous calculation of stresses and deflections in beams of arbitrary cross-section. The work is applied to the lifetime analysis of the Mirror Advanced Reactor Study (MARS) blanket modules. The objective of the present paper is to assess the global impact (3-dimensional) of both irradiation and thermal creep strains on the **stresses** resulting from thermal and swelling strains. The analyzed blanket consists of semi-toroidal tubes around the plasma. Thus, pipes of hollow circular cross-sections are treated as beams hanging between the inlet and outlet headers under **a** variety of boundary conditions.

3.0 Program

Title: Helium Effects on Swelling of Steels
Principal Investigator: N.M. Ghoniem
Affiliation: University of California at Los Angeles

4.0 Relevant DAFS Program Plan Task/Subtask

Subtask Group C: Damage Microstructure Evolution and Mechanical Behavior

5.0 Accomplishment and Status

5.1 Introduction

Until recently, structural analysis of fusion components has usually been divorced from radiation effects. Detailed structural models have been used without considerations of radiation induced property changes. On the other hand, estimates of lifetime limits have been performed at **a** crude level, using simple 1-D models or arbitrary design criteria. The independence and disparity of these two approaches is obviously inconsistent. In order to obtain more reliable end-of-life (EOL) estimates one requires a more thorough understanding of the effects of void swelling and thermal and irradiation creep on **a** 3-D structure. In some **cases**, the results of **a** global structural analysis could not be obtained by merely extending the results of **a** 1-D study.

In this paper, the interplay between swelling and creep is examined through the use of **a** computer code (STAIRE)[1] developed at UCLA. This code is based on classical beam theory, modified to analyze curved, thin-walled pipes including radiation effects. The basic configuration of these pipes is shown in Figure 1.

We show the applicability of this code to fusion blankets by analyzing the blanket modules of the Mirror Advanced Reactor Study (MARS) design.[2] This is a major study of a commercial tandem mirror reactor, to establish the feasibility of the mirror concept.

The basic design of the blanket is quite simple. The Li-Pb alloy is fed at 350°C to the HT-9 blanket module through a large coolant header at the top. From there, it flows (in parallel) through the rectangular HT-9 beam structure and the 10-cm-diameter circular HT-9 tube section. The tubes in the front ensure uniform flow in the regions where the neutron heating is the highest, and the rectangular sections are better suited to attain a low void fraction to increase the neutronic energy multiplication factor. At 500°C, the Li-Pb exits through a large-diameter coolant pipe to a double-walled heat exchanger. The larger pipes are necessary to reduce the MHD pumping power losses.

5.2 Theoretical Basis of STAIRE

The STAIRE code is designed to calculate the stresses and deflections in curved pipes with various end conditions. Because the pipes are indeterminate, the stresses and deflections are coupled and must be determined simultaneously. This is accomplished by setting up three equations for the deflections at the end of the pipe in terms of the inelastic strains and the unknown end reactions. For example, the equation for the radial displacement at the end (δR) is:

$$\Delta R = -\int w' x\,ds + \int \bar{e}' \sin\theta\,ds + XM\int \frac{x\,ds}{EI} + XF\int \frac{xy\,ds}{EI} + XP\int \frac{y^2\,ds}{EI}$$

where

$$w' = \frac{1}{K_{III}} \int_A (e^c + e^s + \alpha T)\,\xi\,dA$$

and

$$\bar{e}' = \frac{1}{A}\int_A (e^c + e^s + \alpha T)\,dA$$

The quantity w' is the change in curvature due to the inelastic strains and e' is the average inelastic strain over the cross-sectional area, A. Equation (1), along with equations for tha axial end displacement and end rotation, can be solved for the end reactions, XM, XF, and XP.

Once the reactions are known, the stresses in the pipe can be determined with the use of simple statics. The moment, M, and axial force, F, at any angle, θ, can be found in terms of the reactions and the axial stress can thus be given as:

$$\sigma = \frac{F}{A} + \xi(1 - K_I\xi^2)\left(\frac{M}{K_{II}I} - Ew'\right) - E(e^c + e^s + \alpha T - \bar{e}')$$

where K_I and K_{II} are constants determined by the pipe dimensions.

The pipe deflections are obtained by replacing the end reactions in equation (1) with the forces on the section at which the deflection is calculated and adjusting the coordinates to correspond to that section. This completes the analysis.

5.3 Irradiation and Thermal Creep

Irradiation creep data exists for a limited number of ferritic alloys. Odette[3] compiled such information, with a suggested correlation of the form:

$$\dot{e}^c_{irr} = A_c\,\dot{\delta}\,\sigma$$

where A_c is a constant, σ the applied Von Mises (equivalent) stress, and $\dot{\delta}$ is the irradiation dose. The values of A_c seem to be both temperature and alloy dependent. Values ranging from 7x10-7/dpa / ksi to 2x10-5/dpa / ksi were reported.

The following equation, developed by Amodeo and Ghoniem,[4] was used for thermal creep:

$$\dot{e}^c_{th} = \frac{7.4\times10^{-3}}{KT}\exp\left(\frac{-1.23}{KT}\right)(\sigma-\sigma_o)^3$$

where T is the absolute temperature and σ_o is the temperature-dependent back stress.

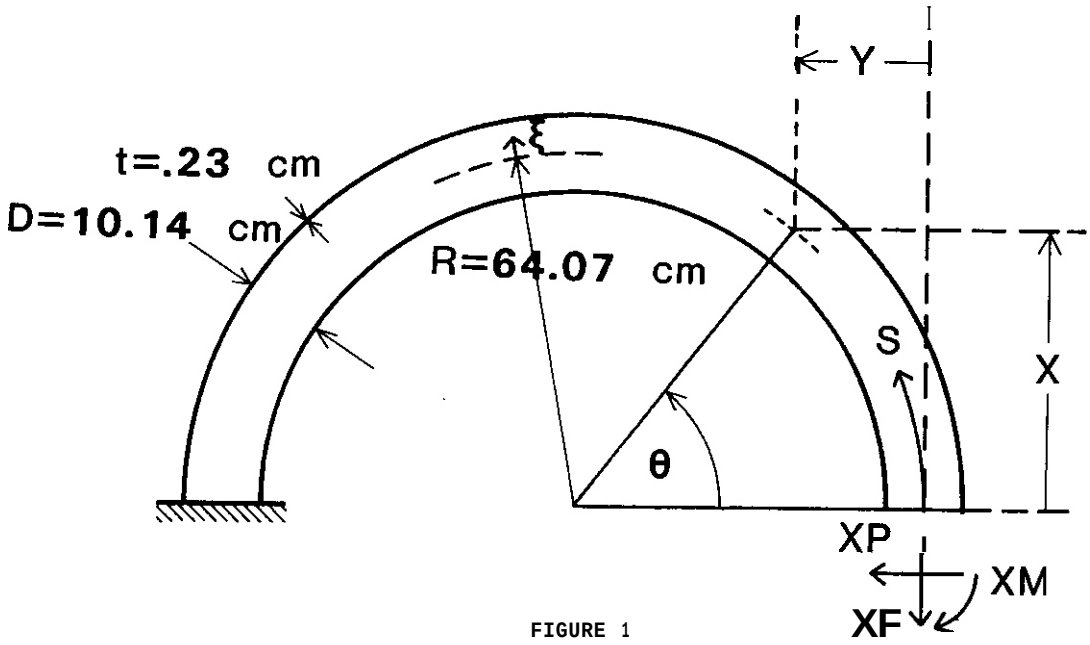

FIGURE 1
Configuration of pipe model.

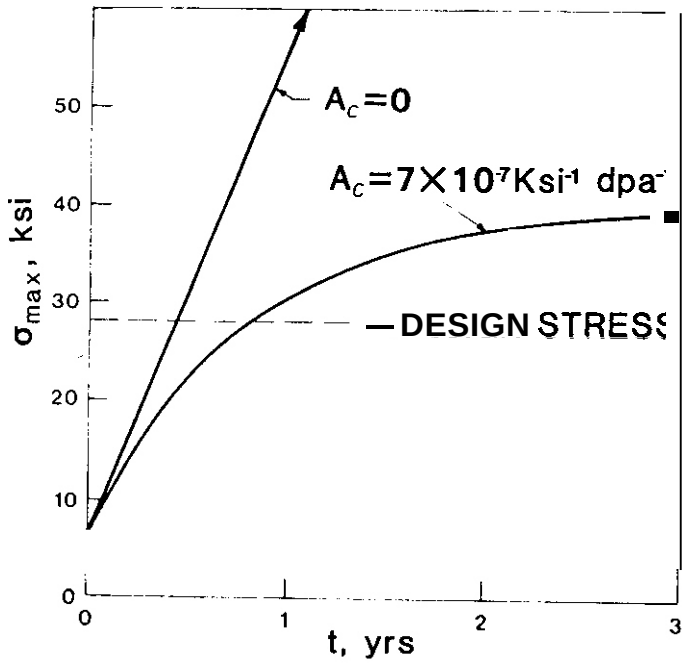

FIGURE 2
Maximum stress history with and without irradiation creep.

5.4 Influence of Irradiation Creep

In an indeterminate structure with no applied loads, the stresses result solely from restraint of the inelastic strains, so irradiation creep leads to stress relaxation, rather than an increase in the total strain as in a typical, constant load situation. In contrast, void swelling causes a substantial increase in both stresses and deflections as damage occurs. If both phenomena are considered simultaneously, one can envision the pipe reaching a steady state, in which the stress increase due to swelling is balanced by the relaxation due to creep. In Figure 2, the maximum stress due to swelling alone is seen to increase linearly with time, as the damage is accumulated at a rate of 69 dpa/year. When creep is included in the analysis, the maximum stress exhibits a less rapid increase and it reaches a steady-state value of *41* ksi. This steady-state value is determined by the creep-free elastic strain rate divided by the creep coefficient.

Contrary to what one might expect, the pipe deflections do not change when creep is included, i.e., the pipe expanded with time as if the creep coefficient is zero. This can be understood by more closely investigating the distribution of creep strains over the cross section. Because creep is proportional to the local stress and the stress is an add function over the cross section, the creep strains are negative on the inner fibers ($\zeta < 0$) and positive on the outer fibers ($\zeta > 0$). As a result, the pipe accomodates creep by decreasing the elastic strains rather than increasing the total strains. In terms of our model, the radial deflections of the clamped pipe are caused by $\bar{e}'$ alone and the creep strains do not contribute significantly to this quantity.

5.5 Damage Gradient Effects

The previous analysis has been performed under the assumption that the damage rate (69 dpa) was uniform everywhere in the pipe. In reality, 3-D neutronics Monte Carlo calculations in the MARS study found that the damage rate at the back of the pipe is about half that at the front. This affects the results in two ways. First, the swelling is taken to be a linear function of the dose, so it decreases with major radius. Second, the irradiation creep shows similar behavior, because it is proportional to the dose rate.

Figure 3 exhibits the deleterious effects of a damge gradient on the stress distribution in the pipe. Although the overall damage in the pipe has decreased, the maximum stress actually increases due to the overall decrease in the creep coefficient. Fortunately, the stress at the welds ($\theta = 0$), which will likely be the pipes' weakest points, decreases by a small amount.

5.6 Thermal Creep

From the available HT-9 data, it appears that at temperatures near or below 500°C, thermal creep can be neglected if the stress levels are below about *40* ksi. Because the Structure temperatures in the MARS blanket are limited to about 530°C by the compatibility of the LiPb coolant with HT-9 and the stresses are maintained below 30 ksi, the previous analyses will not be substantially affected by thermal creep.

In order to assess the structural response to the temperature and non-linear stress dependences of thermal creep, we will consider an illustrative case in which the inlet and outlet coolant temperatures will be 450°C and 550°C respectively. Irradiation creep will be neglected in this temperature range, so that the effects of thermal creep will be isolated. The assumed coolant temperatures might be seen in a blanket for which the designer attempts to avoid the ductile-to-brittle transition temperature (DBTT) of HT-9 and also keep the structure temperature away from the peak swelling temperature of 425°C.

The effect of thermal creep on the stress distribution in the pipe is shown in Figure *4*. The stress is redistributed by the deformation, increasing in some places and decreasing in others. This non-uniform effect results from the temperature dependence and non-linear stress dependence of the creep law. In the case of irradiation creep, the creep rate is linear in the stress and is unnaffected by temperature over the range used, so the relaxation process occurs uniformly and the shape of the stress distributions is unchanged.

Although thermal creep appears to have increased the blanket lifetime by decreasing the stresses at the welds, the increased deformation due to creep strains must also be considered as a cause of failure. If we impose a limit of one percent on the accumulated creep strains (as seen in the ASME Boiler and Pressure Vessel code), the life would be limited to less than three years by thermal creep alone. A limit of one percent on the total permanent strain would decrease the lifetime to below two years and the inclusion of

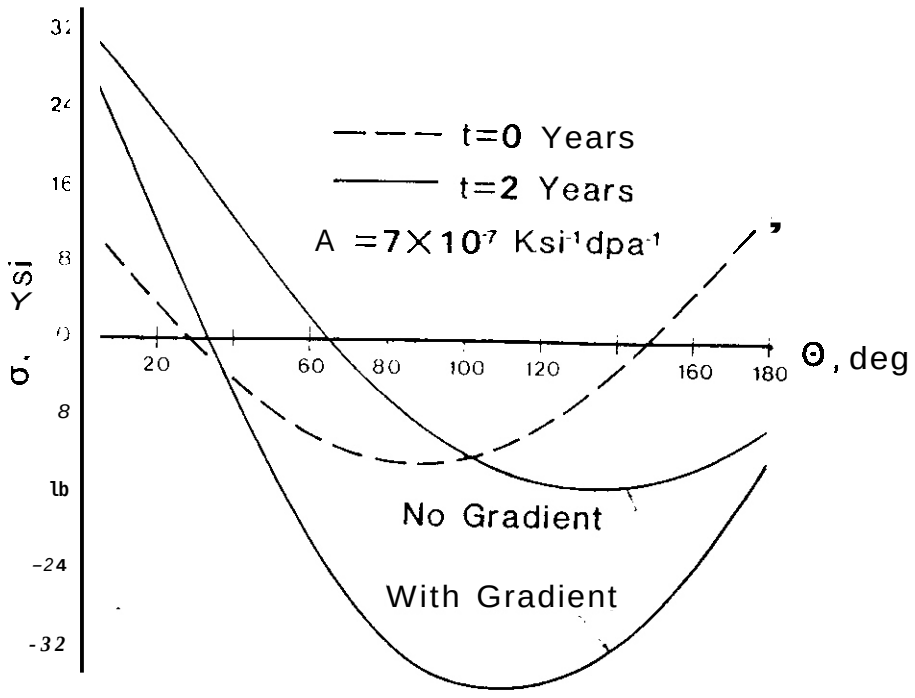

FIGURE 3
Effect of damage gradient on stress distribution

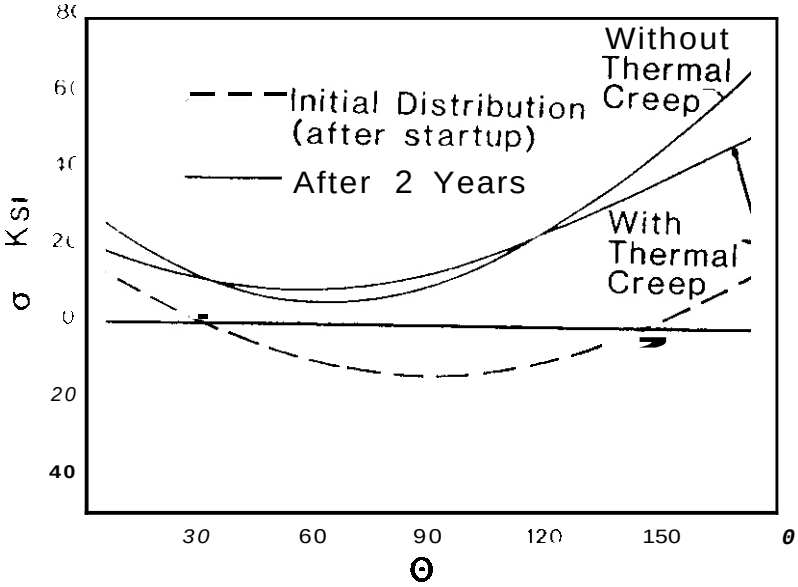

FICURE *4*
Effect of thermal creep on stress distribution.

irradiation creep will further increase the the permanent strain. Apparently, operating the blanket in this high-temperature range is not beneficial because of the onset of thermal creep.

5.1 Lifetime Prediction

Because of the uncertainties in the material properties and modeling of any structural analysis, the most realistic result is a frequency of failure, rather than an absolute failure time. In the context of this paper, we will illustrate this method by focusing on irradiation creep. We predict the failure frequency using an assumed probability of occurrence for the creep compliance, A_4. The EOL criterion will vary, depending an the extent of the analysis.

In Figure 5, the EOL is shown for a design stress limit of 28 ksi[5] and two different strain limits. Apparently, the lifetime will be primarily strain-limited and the failure will occur by loss of structural integrity or rupture.

In order to determine the frequency of failure, we will use the more conservative limit of 2% permanent strain and assume that A_4 has an equal probability of occurrence anywhere in the measured range of the available data and no probability outside that range. A more realistic assumption might be some type of normal distribution. but a uniform occurrence will be adequate for demonstration purposes. Figure 6 shows that, under the assumed operating conditions, over 90% of the coolant pipes in the MARS blanket should survive nearly three years. The abrupt change in the predicted frequency at about 2.8 years is due to the fact that the vast majority of the pipes will be in the strain-limited region, where the EOL is nearly independent of A_4.

5.8 Summary and Conclusions

Although void swelling can cause very large stresses in a structure, irradiation creep may relieve these stresses to a level that will allow an adequate lifetime for a fusion component. The stress levels in a well designed pipe will reach a steady-state value below the design stress, but this does not lead to infinite life. The swelling and creep will continue, despite the steady stress, and failure occurs because of excessive deformation.

To narrow down the prediction of a component's failure point, statistical methods can be used to calculate the probability of failure. With the use of some reasonable, simplifying assumptions, the probability of any pipe lasting about 2.8 years in the MARS blanket was found to be about 0.95. Obviously, the failure frequency will vary widely for different EOL limits or parameter distributions. More work is needed to quantify the effects of statistical uncertainties — in bath material properties and calculational methods-- an the prediction of fusion reactor component lifetimes.

REFERENCES

1. J.P. Blanchard and N.M. Ghoniem, Global Inelastic Structural Analysis of the MARS Tandem Mirror Blanket Tubes Including Radiation Effects, Proc. of the 7th Int. Conf. on Structural Mechanics in Reactor Technology, Chicago, IL, August (1983), paper N3/5.

2. B.G. Logan et. al., Mirror Advanced Reactor Study Interim Design Report, Lawrence Livermore Laboratory Report, UCRL-53333, April (1983).

3. G.R. Odette, Property Correlations for Ferritic Steels far Fusion Applications, Damage Analysis and Fundamental Studies Information Meeting, October 2-3 (1980).

4. R.J. Amodeo and N.M. Ghoniem, Constitutive Design Equations for Thermal Creep Deformation for ET-9, Third Topical Meeting on Fusion Reactor Materials, Albuquerque, NM, September (1983).

5. N.M. Ghoniem, J. Blink and N. Hoffman, Selection of Alloy Steel Type for Fusion Power Plant Applications in the 350 - 500°C Range, Proc. of the Topical Conf. on Ferritic Alloys for Use in Nuclear Technology, Snowbird, Utah, (1983).

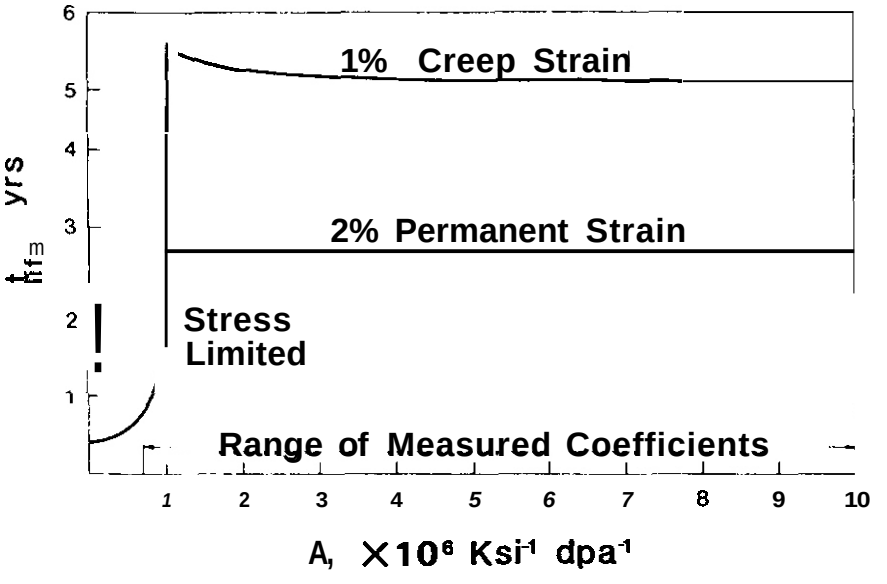

FIGURE 5
End of life for assumed failure criteria

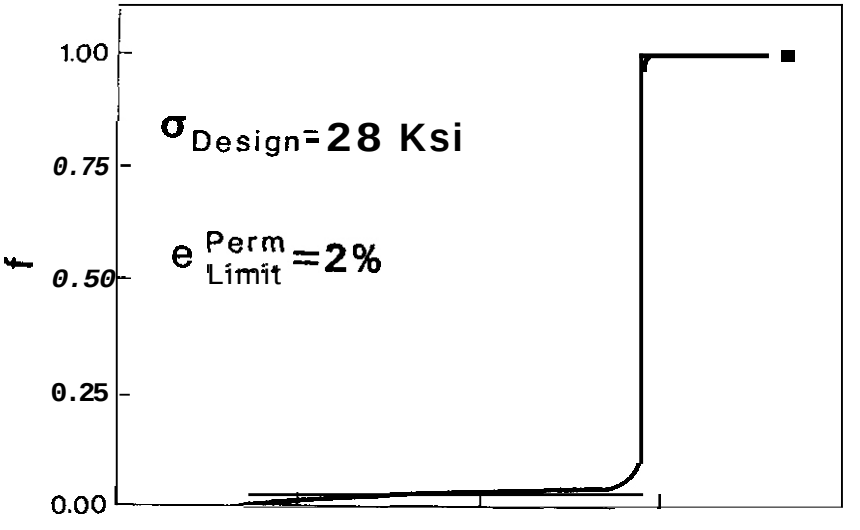

FIGURE 6
Frequency of failure for uniform A distribution

IRRADIATED BEHAVIOR OF HIGH-STRENGTH COPPER ALLOYS

S.J. Zinkle, *S.N.* Farrens, G.L. Kulcinski and R.A. Dodd (University of Wisconsin)

1.0 Objectives

To investigate the irradiated response of high-strength, high-electrical conductivity copper alloys as a function of heavy ion damage level. The microstructural evolution of candidate high-strength copper alloys under irradiation will be studied in order to determine what events may limit the useful lifetime of the material in a fusion reactor.

2.0 Summary

This report describes the initial efforts of a program designed to investigate the irradiation properties of two commercial high-strength, high-electrical conductivity copper alloys. Resistivity and microhardness measurements have been performed on as-received AMZIRC and AMAX-MZC copper alloys in order to help characterize their initial properties. In addition, 14-MeV Cu ion irradiations have been completed on 8 samples at temperatures between 300°C and 700°C (0.4 - 0.7 T_M) at calculated peak damage levels between 4 and 40 dpa. The correlated yield strength of the unirradiated alloys as obtained from microhardness measurements agrees well with values supplied by the manufacturer but the measured electrical conductivities are significantly less than the manufacturer's values.

3.0 Program

Title: Radiation Effects to Reactor Materials
Principal Investigators: G.L. Kulcinski and R.A. Dodd
Affiliation: University of Wisconsin

4.0 Relevant DAFS Program Plan Task/Subtask

Subtask II.B.3.2 Experimental Characterization of Primary Damage State; Studies of Metals
Subtask II.C.1.2 Modeling and Analysis of Effects of Material Parameters on Microstructure
Subtask II.C.6.3 Effects of Damage Rate and Cascade Structure on Microstructure; Low-EnergylHigh-Energy Neutron Correlations

5.0 Accomplishments and Status

5.1 Introduction

There has recently been a renewed interest in the irradiated properties of copper alloys as a result of design studies which call for incorporation of high-strength, high-conductivity materials in fusion reactors. Requirements of high-axial magnetic fields have led to a hybrid magnet design where a normal-conducting coil is inserted inside of a shielded superconducting coil. High-strength copper alloys have been considered for use as high magnetic field insert coils in both tandem mirror[1,2] and tokamak[3] fusion reactors. High-strength copper alloys are also being considered for use as unshielded high-magnetic field toroidal coils in a compact tokamak design.[4]

TABLE 1

COMPOSITION AND OPTIMUM PHYSICAL PROPERTIES OF AMZIRC AND MZC (FROM REF. 5)

Alloy	Zr (%)	Cr (%)	Mg	Cu (+Ag)	Electrical Conductivity @ 20°C	Yield Strength (0.2% Offset)
AMZIRC	0.13-0.20	-	-	Balance	93% IACS	410 MPa
MZC	0.15	0.80	0.04	Balance	80% IACS	517 MPa

AMZIRC® and AMAX-MZC® are precipitation-hardenable, high-conductivity copper alloys manufactured by AMAX Copper, Inc.(5) Table 1 lists the composition of these alloys, along with some typical physical properties quoted by the manufacturer. The properties of MZC are similar to those of chromium copper (Copper No. C18200). AMAX-MZC is an oxygen-free copper alloy that derives its strength from cold-work followed by aging. AMZIRC is an oxygen-free copper alloy that develops its maximum properties through solution heat treatment, cold-work and aging. The Cu_5Zr phase is precipitated during the aging of AMZIRC, thereby producing an increased electrical conductivity and ductility while raising the recrystallization temperature by retarding dislocation motion.(5) AMAX-MZC conforms to the requirements of Copper No. C18100 and AMZIRC conforms to the requirements of Copper No. C1500.

This study is intended to provide information on the irradiated response of high-strength copper alloys at anticipated fusion reactor operating temperatures. There is currently no known irradiated data base available for these high-strength, high-electrical conductivity copper alloys. Electron microscopy will be performed on ion-irradiated samples which have been thinned in cross section in order to investigate the nature of the depth-dependent evolution of the specimen microstructure during irradiation.

5.2 Experimental

Samples of MZC® and AMZIRC® copper alloys were obtained from AMAX Copper, Inc. in the form of 250 μm thick foils. The composition of these alloys is given in Table 1. Specifications given to the manufacturer for the alloy heat treatment called for obtaining the highest electrical conductivity achievable which was consistent with a yield strength of 415 MPa (60 ksi). The alloy preparation consisted of a solution heat treatment and cold-working, followed by aging at 400°C for the MZC alloy and 375°C for the AMZIRC alloy.

Resistivity samples were prepared from the as-received material by attaching the metal foils to a plexiglass base with an adhesive lacquer. A diamond saw was used to cut strips of width 200 μm. These resistivity "wires" were then floated off from the Plexiglas base by immersing the assembly in acetone, which dissolved the adhesive lacquer. This procedure has the advantage of producing uniform foils of small cross-sectional area without introducing deformation to the wire. Severe deformation would have occurred if conventional shearing methods had been used.

Resistivity measurements were performed at room temperature (23°C), 77 K and 4.2 K. Standard 4-point probe resistivity methods were followed, using a Keithley nanovolt detector and a 4-digit multimeter for the voltage readings. The gage length over which the voltage drop was measured was about 2 inches (5 cm). The current density was maintained at about 200 A/cm^2. Four samples of each alloy were measured. Readings were taken with the current going both ways through the sample and the results averaged in order to cancel the effect of thermal emfs.

Vickers microhardness measurements were obtained as a function of indenter load for both alloys. A minimum of 25 indents on 2 different foils were measured for each alloy at every value of indenter load. Measurements Were obtained using a Buehler Micromet® microhardness tester and an anti-vibration test stand. Details of the sample preparation and measurement procedure have been previously described.(6)

5.3 Results

The resistivity results obtained for the as-received AMZIRC and MZC copper alloy samples are summarized in

TABLE 2

OBSERVED RESISTIVITY VALUES FOR AS-RECEIVED AMZIRC AND MZC

Alloy	Resistivity (nΩ-m) 296 K	77 K	4.2 K	RRR = $\rho_{296}/\rho_{4.2\ K}$	Conductivity (23°C)
AMZIRC	24.0 ± 1.6	6.8 ± 0.6	4.0 ± 0.3	6.0	71% IACS
MZC	29.5 ± 1.6	14.4 ± 0.8	13.5 ± 0.8	2.2	58% IACS

Table 2. AMZIRC has about a 20% larger electrical conductivity than MZC at room temperature, with a conductivity of 71% IACS (International Annealed Copper Standard). AMZIRC also has a higher residual resistivity ratio (RRR) than MZC, which is an indication of a relatively lower impurity content (solute-free matrix). Both measured values of the alloy electrical conductivity are significantly lower (by ~ 35%) than the manufacturer's quoted optimum values.

The Vickers microhardness as a function of indenter load is shown in Figure 1. The microhardness number of both alloys is relatively constant for indenter loads greater than 25 g. The MZC alloy hardness is about 20% greater than the hardness of the AMZIRC alloy. The average microhardness numbers for indenter loads above 25 g are 143.5 kg/mm^2 (AMZIRC) and 174 kg/mm^2 (MZC).

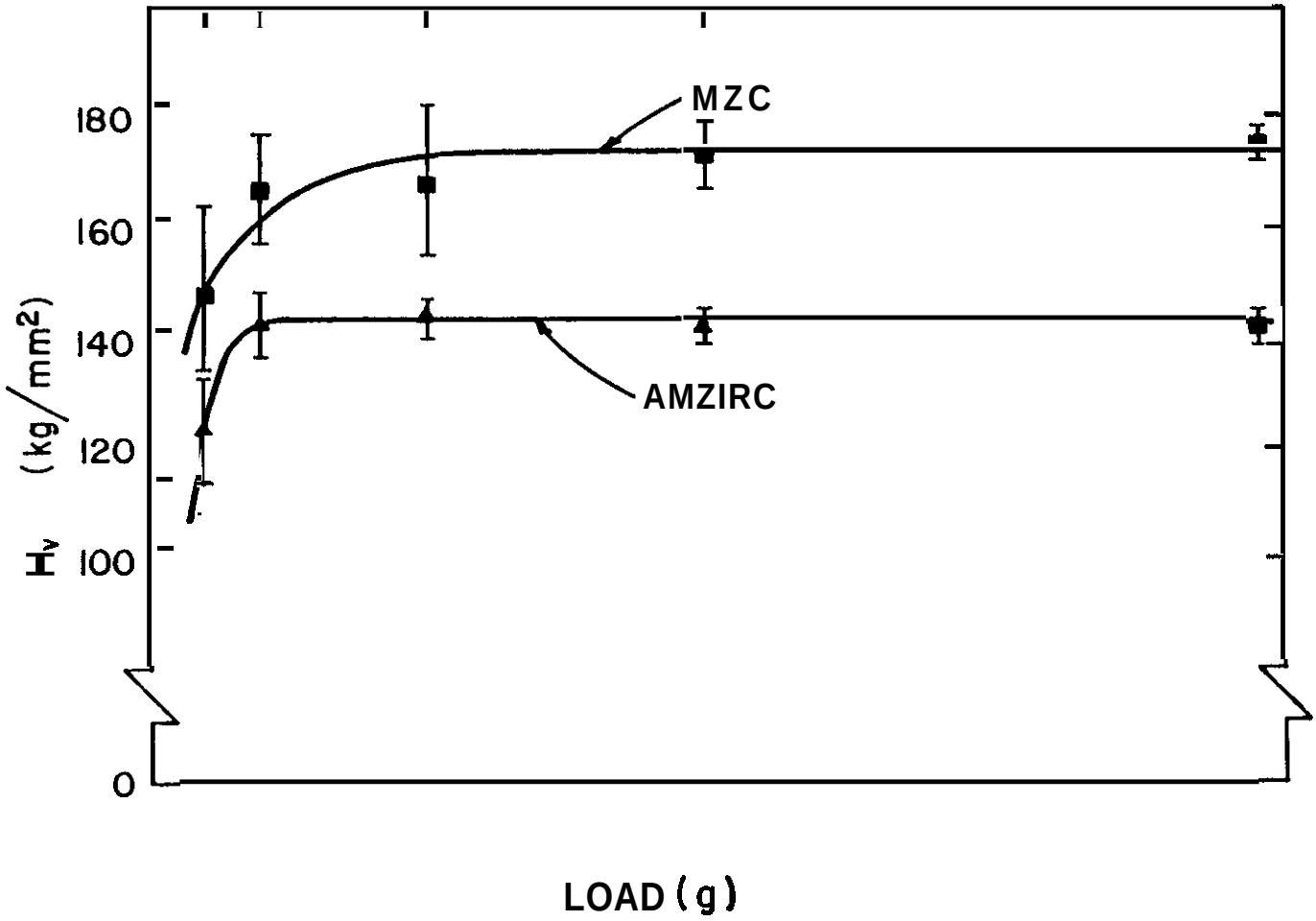

FIGURE 1. Vickers microhardness vs. indenter load for AMZIRC and MZC copper alloys.

TABLE 3

IRRADIATION PARAMETERS OF ION-IRRADIATED AMZIRC AND MZC

Alloy	Irradiating Ion	Irradiation Temp.	Ion Fluence	Calculated Damage 1 μm	Peak
AMZIRC	cu	300°C	$3 \times 10^{19}/m^2$	1	4
AMZIRC	cu	300°C	$3 \times 10^{20}/m^2$	10	40
AMZIRC	cu	500°C	$3 \times 10^{19}/m^2$	1	4
AMZIRC	cu	500°C	$3 \times 10^{20}/m^2$	10	40
MZC	cu	300°C	$3 \times 10^{19}/m^2$	1	4
MZC	cu	300°C	$3 \times 10^{20}/m^2$	10	40
MZC	cu	700°C	$3 \times 10^{19}/m^2$	1	4
MZC	cu	700°C	$3 \times 10^{20}/m^2$	10	40
MZC	Ni	500°C	$3 \times 10^{20}/m^2$	10	40

Ion irradiations have been completed on 9 AMZIRC and MZC samples using 14-MeV Cu or Ni ions from the University of Wisconsin Heavy Ion Irradiation Facility.[7] Table 3 lists the irradiation parameters obtained for these foils. The incident particle flux was maintained within ± 10% of a value of 6.6×10^{16} ions/m^2-s.

5.4 Discussion

Correlations which are available in the literature[8,9] may be used to relate the observed Vickers microhardness to a yield strength. Cahoon[8] derived an expression relating yield strength (σ_Y) to Vickers microhardness (H_V) which was shown to be consistent with the ultimate tensile strength correlation developed by Tabor:[9]

$$\sigma_Y = (H_V/3)\,(0.1)^n \quad , \tag{1}$$

where n is the strain hardening coefficient. The value of n varies with the amount of cold-work present in the metal. Typical values for copper are[9] n = 0.1 and n = 0.45 for cold-worked and annealed conditions, respectively. Using the average of the microhardness numbers obtained at indenter loads above 25 g, an estimate of the AMZIRC and MZC copper alloy yield strengths may be obtained by assuming that the strain hardening coefficient (n) equals 0.1. This appears to be a reasonable assumption since both alloys have been precipitation-hardened. The results of this correlation are plotted along with the experimentally observed electrical conductivity results in Figure 2. For purposes of comparison, the materials parameters of a high-strength, high-conductivity copper alloy being developed by INESCO, Inc.[4] are shown in this figure along with the material properties of cold-worked and annealed copper. The yield strength of annealed pure copper was derived fran reported microhardness data[6] assming a strain hardening coefficient of n = 0.45. The cold-worked copper yield strength value was derived from microhardness data[6] assuming n = 0.1. It is evident from Figure 2 that the correlated yield strength of the two comnercial copper alloys is in good agreement with the manufacturer's specifications. However, the observed electrical conductivity is substantially below the quoted optimum value. This decrease in electrical conductivity could lead to severe economic consequences in proposed fusion power reactors in the form of increased dissipative power consumption by the copper alloy magnets.

6.0 Acknowledgments

The authors would like to acknowledge the assistance of Dr. H.T. Hartwig. This work performed under appointment to a Magnetic Fusion Energy Technology Fellowship and with funds supplied by the Department of Energy.

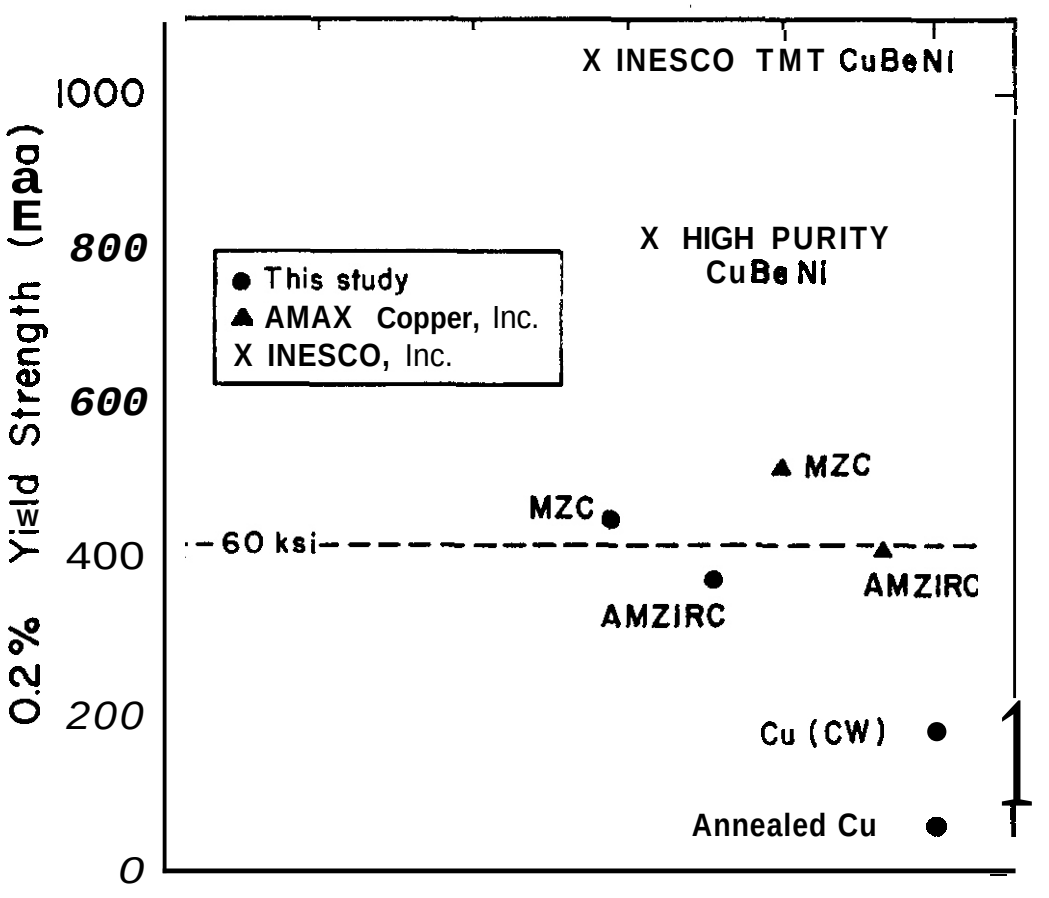
0.2% Yield Strength (MPa)
1000
800
600
400
200
0
X INESCO TMT CuBeNi
X HIGH PURITY
CuBeNi
● This study
▲ AMAX Copper, Inc.
X INESCO, Inc.
▲ MZC
MZC
60 ksi
AMZIRC
AMZIRC
Cu (CW)
Annealed Cu

7. H.V. Smith and R.G. Lott, Nucl. Instr. Methods, 143, 125-132 (1977).

8. J.R. Cahoon, W.H. Broughton and A.R. Kutzak, Met. Trans., 2, (1971) 1979.

9. O. Tabor, J. Inst. Metals, 79, 1 (1951).

8.0 Future Work

An investigation of the microstructural evolution of the AMZIRC and MZC copper alloys during 14-MeV Cu ion irradiation is being planned. Irradiated samples are currently being electroplated with copper so that the entire damage region may be viewed in cross section. Analysis of the radiation damage will be assessed by electron microscopy techniques utilizing a JEUL 200 CX electron microscope. Results obtained on the irradiated samples will be presented in the next quarterly progress report.

9.0 Publications

An abstract has been submitted to the Twelfth International Symposium on Effects of Radiation on Materials, Williaiosburg, VA, June 18-20, 1984.

EXTERNAL DISTRIBUTION

UC-20 (108)

uc-2oc (73)

DOE-HQ/Office of Breeder
Technology Projects
Nt-53
Washington, DC 20545

PB Hemmig, Asst Director,
Reactor Physics Tech

DOE-HQ/Office of Fusion Energy (2)
Washington, DC 20545

JF Clark, ER-70
JF Decker, ER-54, G-256

Argonne National Laboratory (5)
9700 South Cass Avenue
Argonne, IL 60439

LR Greenwood
A. Taylor
KE Nygren
BA Loomis
H. Wiedersich

Battelle
Pacific Northwest Laboratory (3)
P.O. Box 999
Richland, WA 99352

JL Brimhall
DA Dingee
TU Chikalla

Brookhaven National Laboratory
Associated Universities
Upton, Long Island, NY 11973

Chairman, Nuclear Energy Dept

Columbia University
Plasma Physics Laboratory
New York, NY 10027

RA Gross

Commission for the European Communities
200, Rue de la Loi
B-1049 Brussels, Belgium

J. Darvas

Energieonderzoek Centrum Nederland (2)
Netherlands Energy Research Foundation
Westinghouse 3
Postfach 1
NL-1755 ZG Petten, The Netherlands

B. vanderSchaaf
W. vanWitzenburg, Materials Dept

EURATOM
Joint Research Center Ispra
Materials Science Division
1-21020 Ispra, Varese, Italy

P. Schiller

General Atomic Company (2)
P.O. Box 81608
San Diego, CA 92138

GR Hopkins
JR Gilleland

Hahn-Meitner Institute fur Kernforschung
Glienickerstrasse 100
D-1000 Berlin,
Federal Republic of Germany

H. Wollenberger

Hokkaido University (2)
Metals Research Institute
Kita-hu, Sapporo, 060 Japan

Mihio Kiritani, Precision Eng
Taro Takeyama

INESCO
11077 N. Torrey Pines Rd
LaJolla, CA 92037

RD Stevenson

EXTERNAL DISTRIBUTION (Cont'd)

Japan Atomic Energy Research Institute (2)
Physical Metallurgy Laboratory
Tokai Research Establishment
Tokai-mura, Naka-gun, Ibaraki-ken, Japan

Shuichi Iwata, Physics
Kensuke Shiraishi, Nucl Fuel Research

Kernforschungsanlage Julich GmbH
Postfach 1913
D-517 Julich 1,
Federal Republic of Germany

H. Ullmaier

Kernforschungsanlage Karlsruhe
Institüt fur Reaktorbauelemente
Postfach 3640
D-7500 Karlsruhe 1,
Feoeral Republic of Germany

K. Ehrlich

Kyushu University
Research Institute for Appl Mechanics
6-10-1 Hakozaki, Higashi-ku,
Fukuoka, 812 Japan

Kazunori Kitajima

Lawrence
Livermore National Laboratory (3)
P.O. Box 808
Livermore, CA 94550

WL Barmore
MW Guinan, L-396
CM Logan

Lawrence
Livermore National Laboratory
P.O. Box 5511
Livermore, CA 94550

EC Dalder, L-643

Los Alamos National Laboratory (3)
P.O. Box 1663
Los Alamos, NM 87544

DJ Dudziak
CR Emigh
J. Fowler, E-546

Massachusetts Institute of Technology (4)
77 Massachusetts Avenue
Cambridge, MA 02139

I-W Chen, 13-5118
NJ Grant, 8-305
L. Lidsky
JB vanderSande, 13-5025

Massachusetts Institute of Technology (2)
Nuclear Reactor Laboratory
138 Albany St
Cambridge, MA 02139

OK Harling, NW12-204

McDonnell-Douglas Astronautics Co.
P.O. Box 516
St. Louis, MO 63166

D. Kummer

Mound Laboratory
P.O. Box 32
Miamisburg, OH 45342

Manager, Tech Appl & Dev

National Bureau of Standards
Gaithersburg, MD 20760

JA Grundl

National Research Council
Montreal Road
Ottawa, Canada

EV Kornelson

EXTERNAL DISTRIBUTION (Cont'd)

National Research Institute for Metals
Nuclear Materials Division
1-2-1 Sengen, Sakura-mura,
Niihari-gun, Ibaraki-ken, 305 Japan

Naoki Kishimoto

Naval Research Laboratory (3)
Washington, DC 20375

I. Manning, Code 6672
JA Sprague, Code 6395
LE Steele, Code 6390

North Carolina State University
Dept of Nucl Engineering
Raleigh, NC 26707

JR Beeler Jr

Oak Ridge National Laboratory (12)
P.O. Box X
Oak Ridge, TN 37830

Director
K. Farrell
ML Grossbeck
PJ Maziasz
LK Mansur
NH Packan,
FG Perey,
M. Roberts
J. Sheffield
JO Steigler
C. Weisbin
FW Wiffen
Bldg 9204-1
Bldg 9201-2

Osaka University (2)
2-1, Yamada-oka, Suita,
Osaka, 565 Japari

Kenji Sumita, Dept of Nucl Eng
Toichi Okada, Institute of
Scientific & Industrial Research

Princeton University (2)
Plasma Physics Laboratory
Forrestal Campus
P.O. Box 451
Princeton, NJ 08544

ti. Furth
K. wakefield

Risφ National Laboratory
Postfach 49
OK-4000 Roskilde, Denmark

B.N. Singh

Rockwell International
8900 DeSoto Ave
Canoga Park, CA 91304

D. Kramer

Sandia National Laboratories (2)
P.O. Box 5800
Albuquerque, NM 87185

FL Vook, Org 5100

Sandia National Laboratories
Livermore, CA 94550

W. Garrison, Div 8314
WD Wilson

Science Applications, Inc.
P.O. Box 2351
LaJolla, CA 92037

Dr. H. Gurol

Science University of Tokyo
Engineering Dept
Kagurazaka, Shinjuku-ku,
Tokyo, 162 Japan

RR Hasiguti

Studiecentrum voor Kernenergie
Centre d'Etude de 1'Energie Nucleaire
Boeretang 200
B-2400 Mol, Belgium

J. Nihoul

Swiss Federal Institute
for Reactor Research
CH-5303 Wuerenlingen, Switzerland

WV Green

EXTERNAL DISTRIBUTION (Cont'd)

Tokyo Institute of Technology
12-1, 2-Chome, O-Okayama
Meguro-ku, Tokyo, Japan

Kensutaka Kawamura

United Kingaom Atomic Energy Authority
Atomic Energy Research Establishment
Metallurgy Division
Builaing 388
Oxfordshire, OX11 ORA, UK

DR Harries

University of California (2)
Los Angeles, CA 90024

RW Conn
NM Ghoniem

University of Michigan
Dept of Nucl Engineering
Ann Arbor, MI 48109

T. Kammash

University of Missouri
Mechanical & Aerospace Eng
1006 Engineering Bldg
Columbia, MO 65211

M. Jolles

University of Missouri
Dept of Nucl Engineering
Rolla, MO 65401

A. Kumar

University of Tokyo (3)
7-3-1 Hongo
Bunkyo-ku, Tokyo, 113 Japan

Naohira Igata, Met & Mater Science
Shiori Ishino, Nuclear Eng
Taijiro Uchida

University of Virginia
Dept of Materials Science
Charlottesville, VA 22901

WA Jesser

University of Wisconsin
1500 W. Johnson Drive
Madison, WI 53706

WG Wolfer

Westinghouse
Advanced Energy Systems Division
Fuels Materials Technology
P.O. Box 158
Madison, PA 15663

A. Boltax, Manager

Westinghouse
Research and Development Center (2)
310 Beulah Road
Pittsburgh, PA 15235

JA Spitznagel
S. Wood

INTERNAL DISTRIBUTION

DOE-RL/AMPF (2)
FMIT Project Office
FED/642-F

GM Chenevert, Proj Mgr

DOE-RL/AMAR
Breeder Technology Division
Technology Development Branch
FED/242

KR Absher, Chief

HEDL (32)

SD Adkin	W/A-58
TK Bierlein	W/A-1
HR Brager	W/A-64
LL Carter	W/D-1
DG Doran	W/A-57
EA Evans	W/C-23
FA Garner	W/A-57
DS Gelles	W/A-64
R. Gold	W/C-39
JV Hagan	W/B-43
HL Heinisch	W/A-57
DL Johnson	W/A-4
GD Johnson	W/A-65
FM Mann	W/A-4
WN McElroy	W/C-39
EK Opperman	W/A-58
NF Panayotou	W/A-65
RW Powell	W/A-64
RJ Puigh	W/A-58
FH Ruddy	W/C-39
FA Schmittroth	W/A-4
WF Sheely	W/C-44
RL Simons	W/A-57
JL Straalsund	W/A-61
HH Yoshikawa	W/C-44
Central Files (3)	W/C-110
Publ Services (2)	W/C-115
Document Services	W/C-123
Microfilm Services	W/C-123

*GPO 794 - 290 (1984)